Kyoto Meteor Radar and its Application to Observation of Atmospheric Tides(Dissertation_全文)

AUTHOR(S):

Tsuda, Toshitaka

KYOTO METEOR RADAR
AND
ITS APPLICATION TO OBSERVATION
OF ATMOSPHERIC TIDES

by

TOSHITAKA TSUDA

January, 1982

KYOTO METEOR RADAR

AND

ITS APPLICATION TO OBSERVATION OF ATMOSPHERIC TIDES

by

TOSHITAKA TSUDA

January, 1982

Radio Atmospheric Science Center

Kyoto University

Uji 611, Japan

ACKNOWLEDGEMENT

The author wishes to express his sincere and hearty appreciation to Professor Susumu Kato for his continual guidance, inspiration and stimulating supervision throughout the present work and for his careful reading of the manuscript.

The author is deeply indebted to Dr. Takehiko Aso for his guidance and helpful discussion during the course of the present work.

The author wishes to express his deep appreciation to Professors Toru Ogawa and Iwane Kimura for their useful discussions and enlightening criticism on the attitude and methods of a research. The author is also grateful to Professor Hiroshi Maeda for his questions and comments which stimulated the investigations of lunar tides at meteor heights.

The author wishes to thank Drs. Hiroshi Matsumoto, Tsutomu Yabuzaki, Kazuaki Takao and Shoichiro Fukao for their helpful discussions.

The author is deeply thankful to Dr. Kozo Hashimoto for his support to acquire the authorization of operation of Kyoto meteor radar by the Ministry of Posts and Telecommunications.

The author is indebted to all associates in the Ionosphere Research Laboratory, particularly to Messrs. Yoshio Karasawa, Shoji Matsuda and Yoshiro Yoneda for their discussion and co-works for construction of Kyoto meteor radar, and Messers. Yosuke Takashima, Fumito Watanabe, Rei Ito and Jun Tanii for their discussion and co-studies including their master thesis investigations. He is also profited from Dr. Tsuyoshi Ishimine and Mr. Shoji Kainuma of the Radio Research Laboratory, the Ministry of Posts and Telecommunications for their colaborative works. Thanks are also due to colleagues in the Radio Atmospheric Science Center and the Department of Electrical Engineering of Kyoto University for their discussion and help for radar operation.

Kyoto meteor radar had been constructed under financial support of IMS (International Magnetospheric Study) project managed by the Ministry of Education, Research and Culture. A computer installed in the radar was contributed from the Toray association for the advancement of science. Numerical computations in the present work were all performed at the Data Processing Center of Kyoto University.

PREFACE

The thesis is concerned with the study of atmospheric tides observed by the Kyoto meteor radar in the altitude range from 80 to 110 km. According to a gradient of atmospheric temperature, the earth's atmosphere surrounding our life environment is divided into four layers such as troposphere, stratosphere, mesosphere and thermosphere. Although characteristic properties of atmosphere are different in each layer, the whole atmosphere is dynamically connected with each other by various kind of atmospheric waves. Among these waves, atmospheric tides are the most regular and distinguishing phenomena which are mainly generated in the troposphere and stratosphere by solar radiation energy and lunar and solar gravitational attractions, and propagate into the mesosphere and thermosphere.

Development in radio remote-sensing techniques in the last three decades have made it possible to give us great deal of information on atmospheric properties. In recent years, the time is getting ripe for constructing model atmosphere by using these data together with those observed by direct measurement techniques. When one is trying to develop a model for atmospheric motions, data are urgently needed above the mesosphere. A meteor radar has been proven to appropriate for study on regular wind component, when observations are carried out over prolonged periods of time.

The Kyoto meteor radar was constructed in 1977, and has been continuing observations. In the following chapters, characteristics of both solar and lunar atmospheric tides observed at Kyoto in 1978 - 1980 are examined in comparison with theoretical investigations.

Background of the present study is reviewed in Chapter I. Fundamental condition of the earth's atmosphere and general concepts of atmospheric tides are described. In the chapter, shown are histrical developments of meteor radar techniques.

In Chapter II, brief survey and applications of tidal theory are described. The classical tidal theory was put to practical use for two

subjects of the diurnal tide. One is latitudinal asymmetry of the diurnal tide with respect to the equator attributed to the asymmetric distribution of ozone heat source. The other is the behaviour of non-migrating diurnal tide generated by nonuniformly distributed heat source.

Chapter III is devoted to the system description of Kyoto meteor radar which is a monostatic coherent pulse doppler radar. A sensitive radio interferometer is put in operation to measure an arrival angle of meteor echo precisely. A general purpose small computer is installed in the radar to supervise the whole system, including radar control, echo validation and real time data analysis.

In Chapter IV, preliminary results of meteor radar observations are shown. Basic feature of meteor echo distribution with time and altitude is examined. Ambipolar diffusion coefficient is deduced from a decay rate of meteor echo intensity.

Chapter V describes the observation of solar atmospheric tidal wind by the Kyoto meteor radar. Height profiles of both diurnal and semidiurnal tide are delineated in the period from 1978 to 1980. Average behaviours of tidal winds are shown, and are compared with theoretical investigations described in Chapter II. Day-to-day variability of tides were larger in diurnal tide than in semidiurnal tide.

In Chapter VI, shown is the lunar tide at meteor heights which is much smaller than the solar tide. Height profile of lunar semidiurnal and diurnal luni-solar tidal winds were detected. The observed results suggests an influence of mean zonal wind effect in the course of propagation of the lunar tidal wind.

We hope that the present study on the atmospheric tides by the Kyoto meteor radar will more or less contribute to the advance of constructing the model atmosphere in the future. It is also unexpected pleasure if the present work should stimulate the further studies on remote sensing of the atmosphere by radars.

CONTENTS

List of Tables

List of Illustrations

Chapter I

GENERAL INTRODUCTION

Section 1. Atmospheric Tides

The earth's atmosphere is divided into various layers according to their thermal structure. Troposphere is the layer nearest the surface of the earth, characterized by an approximately constant lapse rate of temperature with altitude. Most weather occurs in this layer where exists a human life environment. The troposphere ends at the tropopause whose altitude varies around 15 km with latitude, season and weather situation. The stratosphere, the layer above the troposphere, is confined to a region up to 50 km, and possesses the property that on a broad scale temperature no longer decreases with altitude. This sudden reversal in temperature gradient is due in particular to absorption of ultraviolet solar radiation (2000-3000 A) by ozone. The mesosphere extends upward to an altitude of 80 to 90 km above the stratosphere, and is the region of decreasing temperature. The mesopause defines the upper edge of the mesosphere and the beginning of the thermosphere, whose upper limit is undefined.

Four basic properties of the upper atmosphere are pressure, density, temperature and composition. Among temperature, pressure and density, the hydrostatic equation and equation of state for perfect gas are established. Diffusion separation of atmospheric species becomes dominant in the thermosphere, although turbulent mixing makes atmospheric composition constant below mesopause.

Upper atmospheric motion contains various waves excited by thermal and gravitational energy, and are superimposed on mean zonal and meridional circulation. Atmospheric tides, the subject of the present study,

is one kind of those waves, which have periods of integral fractions of a lunar or solar day with integral longitudinal wavenumber. The atmospheric tides are produced by the solar radiation energy and the gravitational forces of the moon and the sun, so that those are called solar and lunar tide, respectively. Periodic excitation sources and atmospheric responses to those are the main subjects of studies on atmospheric tides.

Solar tide has a period of solar 24 hrs or a submultiple of it, and is generated principally by the daily cycle of heating and cooling, the mechanism being absorption of solar radiation by ozone and water vapor. Tidal periods less than 24 hrs occur because the heating cycle is more square-wave than sinusoidal and is therefore rich in harmonics. The first harmonic component is called the diurnal tide, and the second one is the semidiurnal tide. Although higher harmonics are theoretically possible, those amplitudes are small relative to the fundamental components.

The existance of the solar tides in the upper atmosphere was earlier found in the geomagnetic data observed at ground as S_q (Solar quiet day) variation [e.g. Kato, 1956]. The phenomenon is explained by ionospheric tidal dynamo originally motivated by motions of neutral particles in the ionospheric E layer. Advances in acquisition of new kind of data on atmospheric tides have been made in the last decades. Below 30 km, meteorological rawinsonde provides wind velocity. Various kind of rocket borne instruments can measure snapshots of wind profiles beyond 30 km up to 120 km. Indirect methods such as a meteor radar, a partial reflection technique and an incoherent scatter radar can carry out continuous observation of wind velocity in time. Chapman and Lindzen [1970] reviewed solar atmospheric tides as revealed by meteorological data until 1969. Tidal motions in dynamo region and thermosphere are discussed by Kato [1971]. Recent observations in the 1970's are summerized by Kato [1980].

Amplitude of lunar tides is about one-twentieth of that of the solar tides. Lunar tides are primarily attributed to tidal potential of the moon and secondarily to that of the sun. Their complicated contribution to the forcing of lunar tides gives many variations in oscillation frequency. The lunar tides are generated chiefly near the ground where excitation by gravitational forces is large because of large atmospheric

density. The lunar semidiurnal tide is the most fundamental component, and has period of lunar 12 hrs. The secondary component is the diurnal luni-solar tide whose period is approximately lunar 24 hrs. Although lunar tide is small in amplitude, it has been determined in many atmospheric data obtained in a prolonged period of time [Chapman and Lindzen, 1970], because their tide-generating source and their frequency is well known. Lunar pressure tide at the ground have been most extensively determined by Haurwitz and Cowley [1966, 1967, 1968a, 1969a]. Geomagnetic lunar tides were studied by Chapman and Miller [1940], Maeda and Fujiwara [1967], Tarpley [1971] and Winch [1970, 1971]. Haurwitz and Cowley [1968b, 1969b] used a large amount of data to determine the lunar tidal wind at the ground. Radio techniques have made it possible to detect lunar tides in columnar electron content [Bernhardt et al., 1976], phase height of the E region [Butcher and Weeks, 1969], group height of E layer [Rodgers and Butcher, 1976] and E_s parameters [Matsushita 1962; Tarpley and Matsushita, 1971, 1972]. The statistical method used to analyse the lunar variations has been worked out by Bartels [1932], Chapman and Miller [1940], and Malin and Chapman [1970a, b].

Theoretical investigations on the atmospheric tides originated by Newton in 17th century have been continued by many theoretical physists [e.g. Kato, 1980]. The classical tidal theory has been established by the correct understanding of the Laplace's tidal equation by the discovery of negative modes by Kato [1966] and Lindzen [1967]. Those modes characterized by negative eigenvalues play a large part in the behaviour of the diurnal atmospheric tides. The classical tidal theory has successfully explained many general features of the observations on atmospheric tides. Improved treatment of the atmospheric tides has been done by many authors who have taken account of dissipation process or electromagnetic effect [e.g. Kato, 1980]. One of the major developments in the tidal theory in recent years was an inclusion of the mean zonal wind effect on the propagation of the tidal waves. Lindzen and Hong [1974] examined the interaction between zonal wind and semidiurnal atmospheric tides. Main effect by the process is to give rise to significant mode coupling between the main semidiurnal mode and higher modes; leading to an enhancement of the latter. Walterscheid et al. [1980] used

improved heating rates for calculations of the semidiurnal atmospheric tides at solstices including the influence of mean zonal wind. They concluded the improved agreement with observations of their results with respect to wavelengths and amplitudes of the semidiurnal tidal oscillations in the meteor region (80-100 km) is primarily attributable to the improved heating rates, although effects of mean-wind related generation are discernible. Clearly, much work is to be done both theoretically and observationally before a global pattern of solar and lunar tidal motion can be established.

Section 2. Meteor Radar

Meteoric particles drifting in the interplanetary space are sometimes attracted by the gravitational force of the earth, and penetrates into the earth's atmosphere. Meteor velocity usually ranges from 11.2 to 72 km/sec, whose lower limit is decided by the second astronautical velocity for the earth's gravitational field, while its upper limit is the sum of the escape velocity of the solar system (42 km/sec) and the earth's revolution velocity around the sun (30 km/sec). Meteors are seemed to belong to the solar system, because impinging velocities for almost all meteors do not exceed this upper limit.

On the morning side of the earth, meteors are overtaken by the forward motion of the earth. On the other hand, only meteors which can overtake the earth reach the earth on the evening side. Thus hourly rate of meteors shows regular diurnal variation with a maximum around 6 a.m. and with a minimum near 6 p.m.

A meteor is classified into either shower meteors or sporadic meteors. Shower meteors are associated with intersteller matters which were spreaded by comets in those orbits. These orbits are intersected by the earth at a specific time every year. Sporadic meteors are those which are not members of recognized meteor showers, and exceed shower meteors in total number. Mean values of basic parameters for sporadic meteors are studied by Verniani [1973], and are summerized in Table 1.1. Those for shower meteors do not differ significantly from the corresponding

ones for sporadic meteors. It is known experimentally that number of meteors is inversely proportional to their mass [Manning, 1959].

Table 1.1 Basic parameters of sporadic meteors

Mean original mass	;	0.1 mg
Mean apparent velocity	;	34 km/sec
Mean value of computed density	;	0.8 g/cm^3
Mean maximum electron line density	;	$10^{12.5}$ /m

Ionization columns formed by the passage of meteoric particles through the lower ionosphere move with surrounding neutral particles. Back-scatter radar echoes are obtained from these meteoric ionization trails at HF and VHF frequencies. The magnitude and sign of the doppler shift in the received echo frequency provides a measure of the radial drift velocity of the meteor trail with the neutral wind.

The meteor radar method for measuring upper atmosphere winds was first applied by Manning et al. [1950] at Stanford University, although radio observaiton of astronomical properties of meteors was accomplished earlier at Ottawa [McKinley and Millman, 1949]. In the last two decades, more than forty meteor radars had been constructed in the world for observations of upper atmospheric motions. Improvements of the system have been done especially in height resolution by adopting a radio interferometer and echo discrimination by introducing an on-line small computer.

Because collaboration of meteor radar observation promotes the study on atmospheric waves largely, those are organized internationally as Global Radio Meteor Wind Studies Project(GRMWSP) whose participants are shown in Fig. 1.1 and also listed in Table 1.2. The group was organized as Division V, Working Group 2 (Meteor Observations) of IAGA, and has

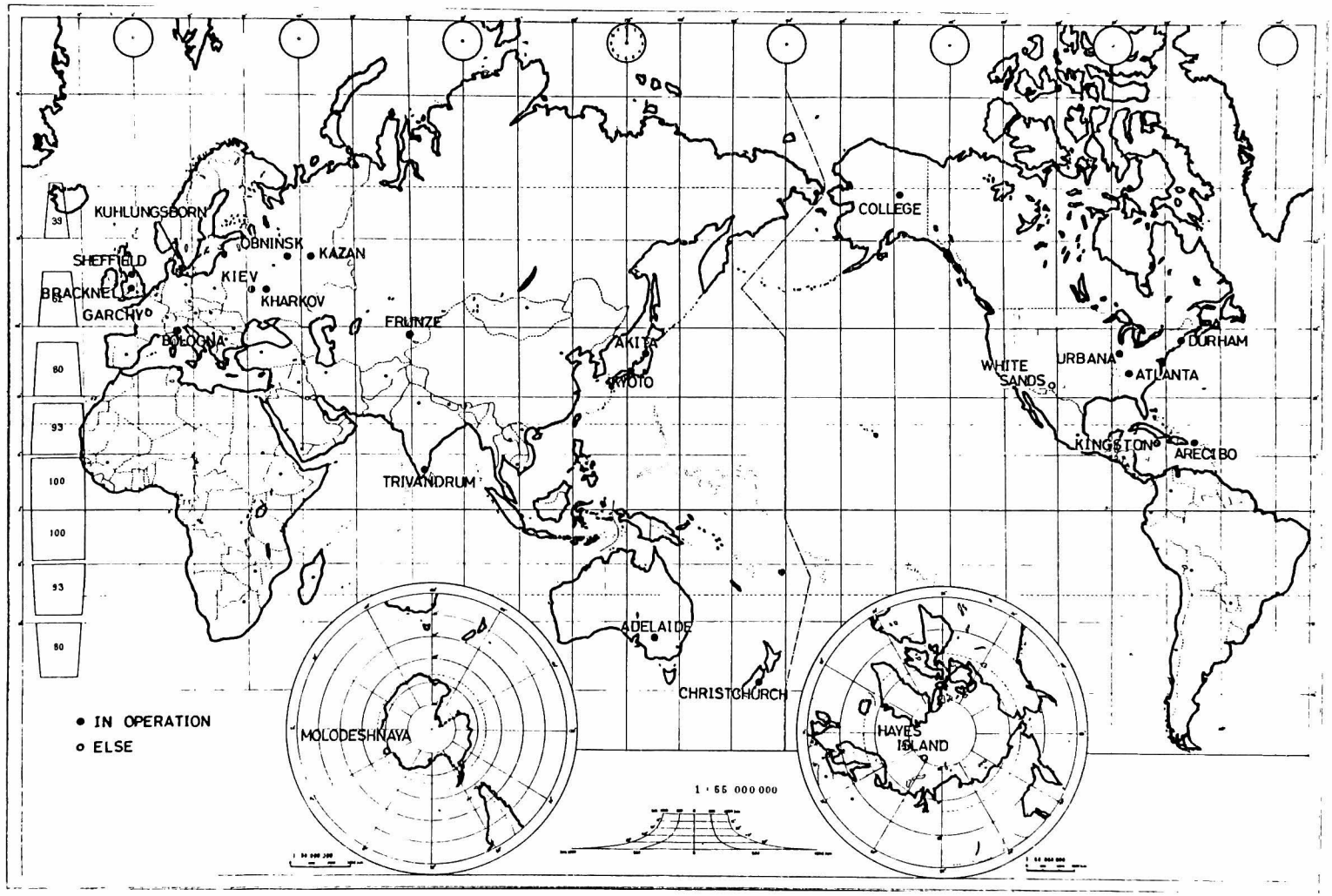

Fig. 1.1 GRMWSP network.

Table 1.2 List of meteor radar stations

Station	Location		Status	Frequency (MHz)	Peak Power (kW)	Pulse width/CW (microsec)
Hayes Island	81 N	55 E	S	33.5	75	20
Kiruna	68 N	20 E	S	30		CW
College	65 N	148 W	S	30.2	(750 W)	CW
Moscow	59 N	37 E	U	33	100	10
Stornoway	58 N	6 W	S	36.3	20	25
Tomsk	57 N	85 E	S	30	50	5
Obninsk	56 N	38 E	R	25.2	75	20
Gorky	56 N	44 E	U	36.9	75	10
Kazan	56 N	49 E	R	33.5	120	5
Kuhlungsborn	54 N	12 E	U	32.55	40	30
Jodrell Bank	53 N	2 W	SN	36.3	100	20
Sheffield	53 N	1 W	R	36.3	200	25
Bracknell	51 N	1 W	S	36.3	20	30
Eindhoven	51 N	5 E	U	40		
Ondrejov	50 N	14 E	R	37.5	25	10
Kiev	50 N	31 E	R	34.5	10	10
Kharkov	50 N	36 E	R	36.9	100	15
Garchy	47 N	3 E	R	29.7968	(5 kW)	CW
Pullman	47 N	117 W	P			
Mayaki	47 N	33 E	U			
Simferodol	45 N	34 E	U			
Montpazier	44 N	1 E	R	30		CW
Bologna	44 N	11 E	R	42.7	50	10
Florence	44 N	11 E	N	39.5	15	16
London,Ontario	45 N	81 W	R	40	(100 W)	CW

Table 1.2 (continued)

Station	Location	Status	Frequency (MHz)	Peak Power (kW)	Pulse width/CW (microsec)
Durham	43 N 71 W	R	36.8	30	40
Frunze	43 N 75 E	R	39.5	40	8
AFCRL	42 N 71 W	SN	36.8	30	40
Havana	40 N 90 W	SN	40.9	3 MW	5
Urbana	40 N 88 W	R	40.9	3 MW	5
Dushanbe	38 N 69 E	S	37.4	75	10
			17.6	20	100
			73	50	10
Accomack	38 N 76 W	N	36.8		CW
Stanford	37 N 122 W	SN	30.14	5	280
Ashkabad	37 N 59 E	S	33.7		
Tokyo	36 N 140 E	R	37.46	20	10
Kyoto	35 N 135 E		31.57	10	280
Atlanta	34 N 84 W	R	32.5	(1.7 kW)	CW
White Sands	33 N 106 W	S	32.8	50	
Eglin	31 N 87 W	SN	36.8	5	280
Ramey	18 N 67 W	R	30		CW
Kingston	18 N 77 W	R	36.4	20	35
Andhra	18 N 84 E	S	36.3	20	25
Trivandrum	8 N 78 E	P			
Mogadishu	2 N 45 E	S	36.9	40	40
Gan	1 N 73 E	P	36.3	20	25
Adelaide	35 S 139 E	R	26.773	(1.5 kW)	CW
Christchurch	44 S 172 E	R	27.1	40	
Molodezhnaya	67 S 45 E	S	33	35	
Mawson	68 S 67 E	SN	34	15	10

N = no longer operation; P = Proposed; R = Regular operation;
S = Some data available; U = Unknown

been coordinated by Dr. M. Glass, of CNET, France and Dr. R.G. Roper, School of Aerospace Engineering, Georgia Institute of Technology, Atlanta, Georgia, USA. The Cooperative Tidal Observation Program (CTOP) was proposed at Division V, Working group 2 of IAGA from Commision III of the International Union of Radio Science (URSI) at Kyoto in September, 1973. The program has been undertaken as collaborative observations by the incoherent scatter radar network and the GRMWSP. Proposed goal of the program is

i) definition of a synoptic meteorology;
ii) delineation of tidal wind parameters, and their variation with latitude, longitude, height and time;
iii) determination of the variation of the random wind component, also with latitude, longitude, height and time.

Application of the measurements is

i) prediction of the wind field, and its probable variations;
ii) inference of temperature and density from wind field for input to global model of the general circulation of the atmosphere.

Although detailed vertical wind profiles are obtained from rocket chemical trail methods, this method is necessarily limited by the intermittent nature of the observations. In addition, systematic observations with rockets is a relatively expensive method. Meteor radar observations of upper atmospheric winds have been proven to be consistent and economical, particularly for the regular wind components such as atmospheric tides, because they are capable to be carried out over prolonged periods of time.

CHAPTER II

Theoretical Studies on Atmospheric Tides

Section 1. Classical Tidal Theory

1.1 Basic Equations and Assumptions

The classical tidal theory treats the atmospheric tides as perturbations in a shallow spherical atmosphere which is assumed to be compressible perfect gas in both local thermodynamic and hydrodynamic equilibrium. We neglect dissipative effects such as turbulence, molecular diffusion of heat and momentum, infrared cooling and ion drag. In this thin fluid layer, the mean molecular weight and the acceleration of gravity can be regarded as a constant. The basic equations for the atmospheric tides are described below [e.g. Kato, 1980]. The southward and eastward components of the equation of motion including Coriolis force on a spherical earth:

$$\frac{\partial W_\theta}{\partial t} - 2\Omega W_\phi \cos\theta = -\frac{1}{a}\frac{\partial}{\partial \theta}\left(\frac{P_1}{\rho_0}\right) \tag{2.1}$$

$$\frac{\partial W_\phi}{\partial t} + 2\Omega W_\theta \cos\theta = -\frac{1}{a \sin\theta}\frac{\partial}{\partial \phi}\left(\frac{P_1}{\rho_0}\right) \tag{2.2}$$

The hydrostatic equation:

$$\frac{\partial p_1}{\partial z} = -g\rho_1 \tag{2.3}$$

The equation of continuity:

$$\frac{\partial \rho_1}{\partial t} + W_z \frac{d\rho_0}{dz} + \rho_0 \chi = 0 \ , \tag{2.4}$$

where χ is div W.

The energy conservation law of the thermodynamics:

$$\frac{\partial p_1}{\partial t} - g\rho_0 W_z + \rho_0 C^2 \chi = (\kappa-1) Q \rho_0 . \tag{2.5}$$

We assume each perturbation term varies with time as

$$\chi = \chi_\omega \exp(i\omega t) \tag{2.6}$$

where ω is the angular frequency of the oscillation.

The equations (2.1) to (2.5) can be deduced to a second order partial differential equation with respect to z, θ and ϕ :

$$C^2 \frac{\partial^2 \hat{\chi}_\omega}{\partial z^2} + \left(\frac{dC^2}{dz} - \kappa g\right)\frac{\partial \hat{\chi}_\omega}{\partial z} + \frac{g}{4a^2\Omega^2} F\left[\left(g(1-\kappa) - \frac{dC^2}{dz}\right) \hat{\chi}_\omega\right]$$

$$= - \frac{g^2}{4a^2\Omega^2} F\left[\frac{Q_\omega}{C_p T_0}\right] . \tag{2.7}$$

where $\hat{\chi}_\omega$ and F are a new variable and an operator defined as follows

$$\hat{\chi} = \chi - \frac{Q}{C_p T_0} = - \frac{1}{\rho_0 C^2} \frac{Dp}{Dt} \ , \tag{2.8}$$

$$F = \frac{1}{\sin\theta}\frac{\partial}{\partial\theta}\left[\frac{\sin\theta\left(\frac{\partial}{\partial\theta} - i\left(\frac{\cot\theta}{f}\right)\left(\frac{\partial}{\partial\phi}\right)\right)}{f^2 - \cos^2\theta}\right]$$

$$+ \frac{i\left(\frac{\cot}{f}\right)\left(\frac{\partial^2}{\partial\theta\partial\phi}\right) + \left(\frac{1}{\sin^2\theta}\right)\left(\frac{\partial^2}{\partial\phi^2}\right)}{(f^2 - \cos^2\theta)} . \qquad (2.9)$$

The equation (2.7) is solved by the method of separation of variables by assuming a form of $\hat{\chi}_\omega$ and Q_ω as

$$\hat{\chi}_\omega = \sum_{m,n} Y_{\omega,m,n}\,\Theta_{\omega,m,n}\exp(im\phi) ,$$

$$Q_\omega = \sum_{m,n} q_{\omega,m,n}\,\Theta_{\omega,m,n}\exp(im\phi) . \qquad (2.10)$$

where $Y_{\omega,m,n}$ is a solution of the Wilkes' vertical structure equation:

$$C^2\frac{d^2Y_{\omega,m,n}}{dz^2} + \left(\frac{dC^2}{dz} - \kappa g\right)\frac{dY_{\omega,m,n}}{dz} + \frac{Y_{\omega,m,n}}{h_{\omega,m,n}}\left[\frac{dC^2}{dz} + g(\kappa-1)\right]$$

$$= \frac{gq_{\omega,m,n}}{h_{\omega,m,n}C_pT_0} \qquad (2.11)$$

and $\Theta_{\omega,m,n}$ is an eigenfunction known as a Hough function of the Laplace's tidal equation:

$$F_{\omega,m}\,\Theta + \frac{4a^2\Omega^2}{gh}\,\Theta = 0. \qquad (2.12)$$

A separation constant, $h_{\omega,m,n}$ of the equation (2.7) is named as an equivalent depth which is inversely proportional to the eigenvalue $\beta_{\omega,m,n}$,

of the equation (2.12) as

$$h_{,m,n} = \frac{4a^2\Omega^2}{g} \frac{1}{\beta_{\omega,m,n}} . \qquad (2.13)$$

A subject in the classical tidal theory can be reduced to solve the eigenvalue problem of the equation (2.12), and to investigate a periodic heat source which governs the non-singular equation (2.11).

1.2 Eigenvalue and Hough Function of Laplace's Tidal Equation

Kato [1980] described the deduction of the eigenvalue for (2.12) and the Hough function. In his monograph, shown are tables of the equivalent depth, the eigenvalue and expansion coefficients of the Hough function with respect to associated Legendre functions of unnormalized Neuman-type for the migrating diurnal and semidiurnal tides. He has also shown Hough functions and the related functions, Φ_θ and Φ_ϕ which determine latitudinal distribution of southward and eastward tidal wind velocity as follows

$$W_{\theta,\omega} = -ia\omega \left(\frac{p_{\omega,m,n}}{\rho_0 g h_{\omega,m,n}}\right) \left(\frac{m}{f}\right)^2 \Phi_\theta \exp(im\phi) ,$$

$$W_{\phi,\omega} = a\omega \frac{1}{m} \left(\frac{p_{\omega,m,n}}{\rho_0 g h_{\omega,m,n}}\right) \left(\frac{m}{f}\right)^2 \Phi_\phi \exp(im\phi) \qquad (2.14)$$

This subsection is especially concentrated on the eigenvalues and Hough functions including the non-migrating diurnal tide which does not oscillate synchronously with the motion of the sun. Figure 2.1 shows the distribution of eigenvalues of the diurnal oscillation for various longitudinal wavenumber, m. A cross and an open circle correspond to a symmetric and an antisymmetric mode, respectively. The variation of

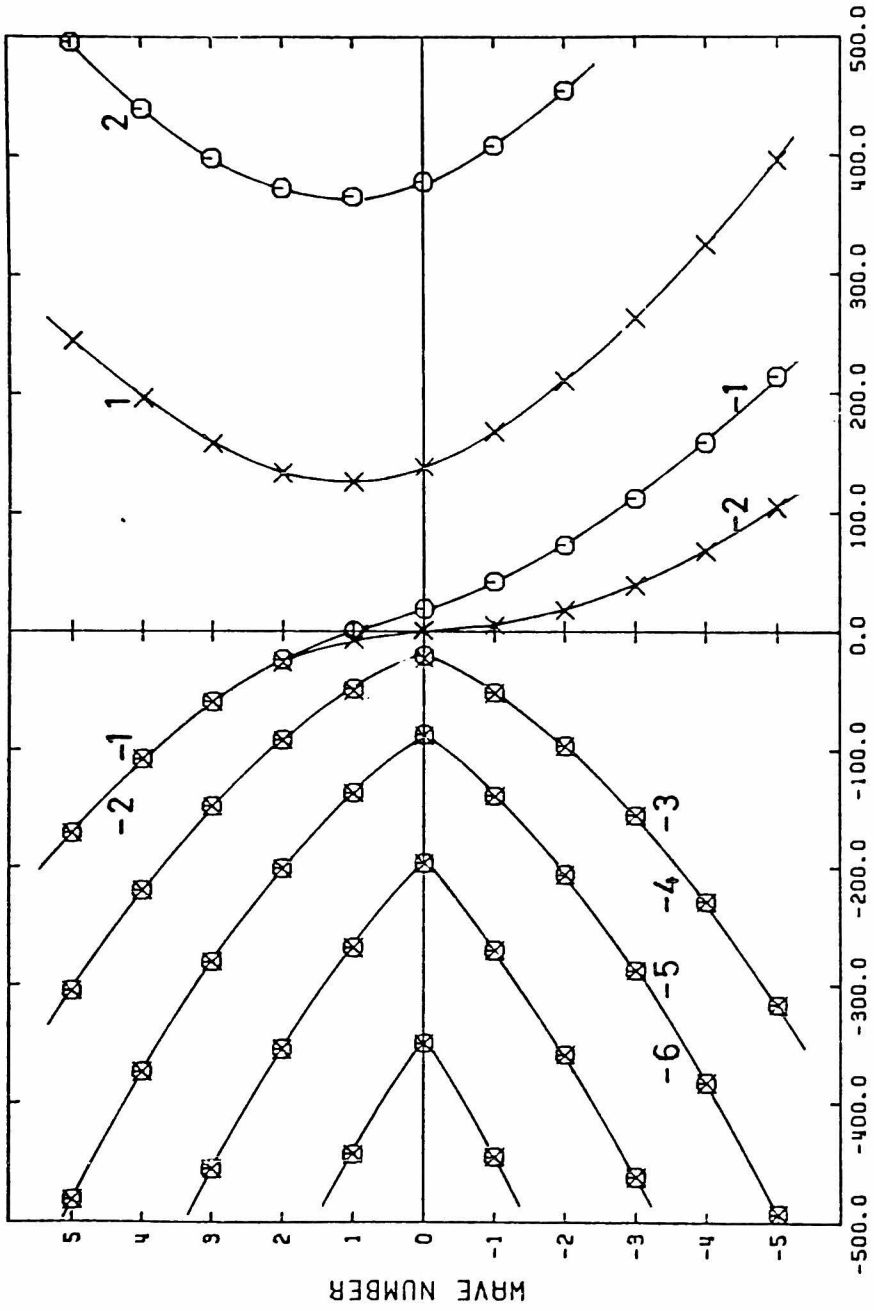

Fig. 2.1 Distribution of eigenvalue of the diurnal oscillation for various longitudinal wavenumber, m.

the eigenvalue for a fractional wavenumber is drawn as a curve which is named after the nomenclature for the mode of the migrating diurnal tide. As for the positive mode, the distribution of the eigenvalues is symmetric with respect to a line, m = 1. It seems that the earth's rotation shifts the distribution of eigenvalue with m westward by one, because the propagating mode is essentially free from the Coriolis force. Those for evanescent modes distribute symmetric with respect to the horizontal axis, except for two fundamental modes named -1 and -2. The eigenvalues for a pair of a symmetric and an antisymmetric evanescent mode are almost equal for the branch less than -3. The modes -1 and -2 play a large part in making an asymmetric distribution of eigenvalues with respect to the line m = 0. In Fig 2.2, fundamental Hough functions of the first westward propagating wave (m = 1) which corresponds to the migrating tide and eastward propagating wave (m = -1) are shown for the modes from -6 to 4. As for the propagating modes, only a little discrepancy can be seen in the shape of Hough functions for the corresponding modes, although the symmetric modes are phase-reversed with each other. Similar argument can be done for the evanescent mode, except for modes -1 and -2. The first symmetric negative mode for the case m = -1 is simpler, and seems to be more fundamental than that of the case m = +1.

Considering equation (2.14), we can recognize that the wind vector of the westward propagating wave rotates clockwise in the northern hemisphere, when the values of both Φ_θ and Φ_ϕ are in the same sign. As for the eastward propagating wave, the signs of Φ_θ and Φ_ϕ must be different to produce the clockwise rotation of the wind vector. Figure 2.3 shows the Φ_θ and Φ_ϕ for the fundamental modes of the longitudinal wavenumber of 1 and -1. Except for $S_{1,-1}$ and $S_{-1,-1}$ mode, the sign of Φ_θ and Φ_ϕ are same and different for westward propagating wave and eastward propagating wave, respectively, in the greater latitude ranges. With the exception of these two cases, the phase reversal of both Φ_θ and Φ_ϕ occurs at close point in colatitude, so that, the anticlockwise rotation is possible only in a limited narrow latitudinal range. The $S_{1,-1}$ mode shows anticlockwise rotation in the region from the equator to around 60° in colatitude. As for the $S_{-1,-1}$ mode the wind vector rotates anticlockwise in the whole northern hemisphere. So that, this mode may cause

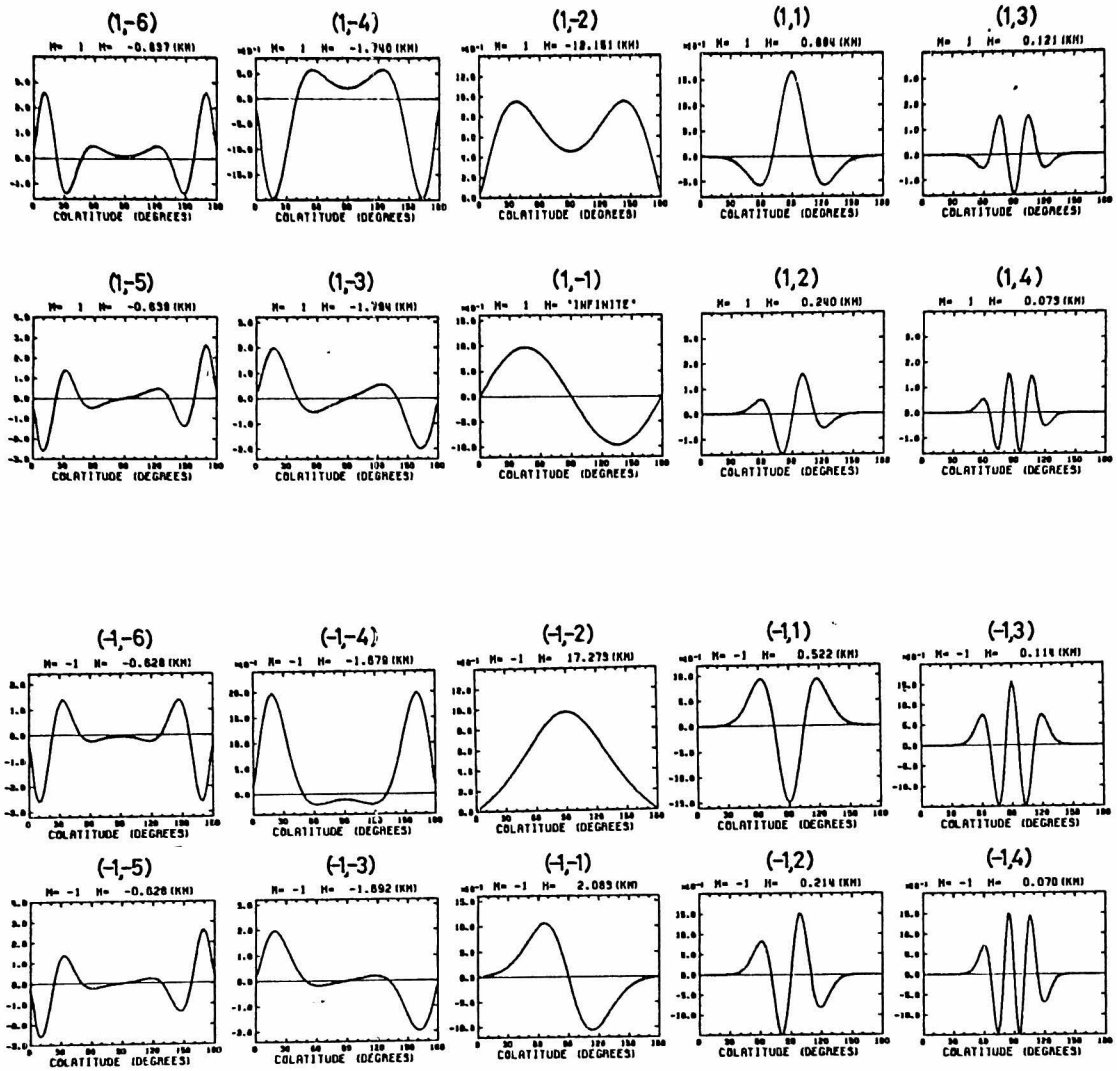

Fig. 2.2 Hough functions for longitudinal wavenumber of 1 and -1. Parameters (m,n) correspond to the longitudinal wavenumber and order of the Hough mode.

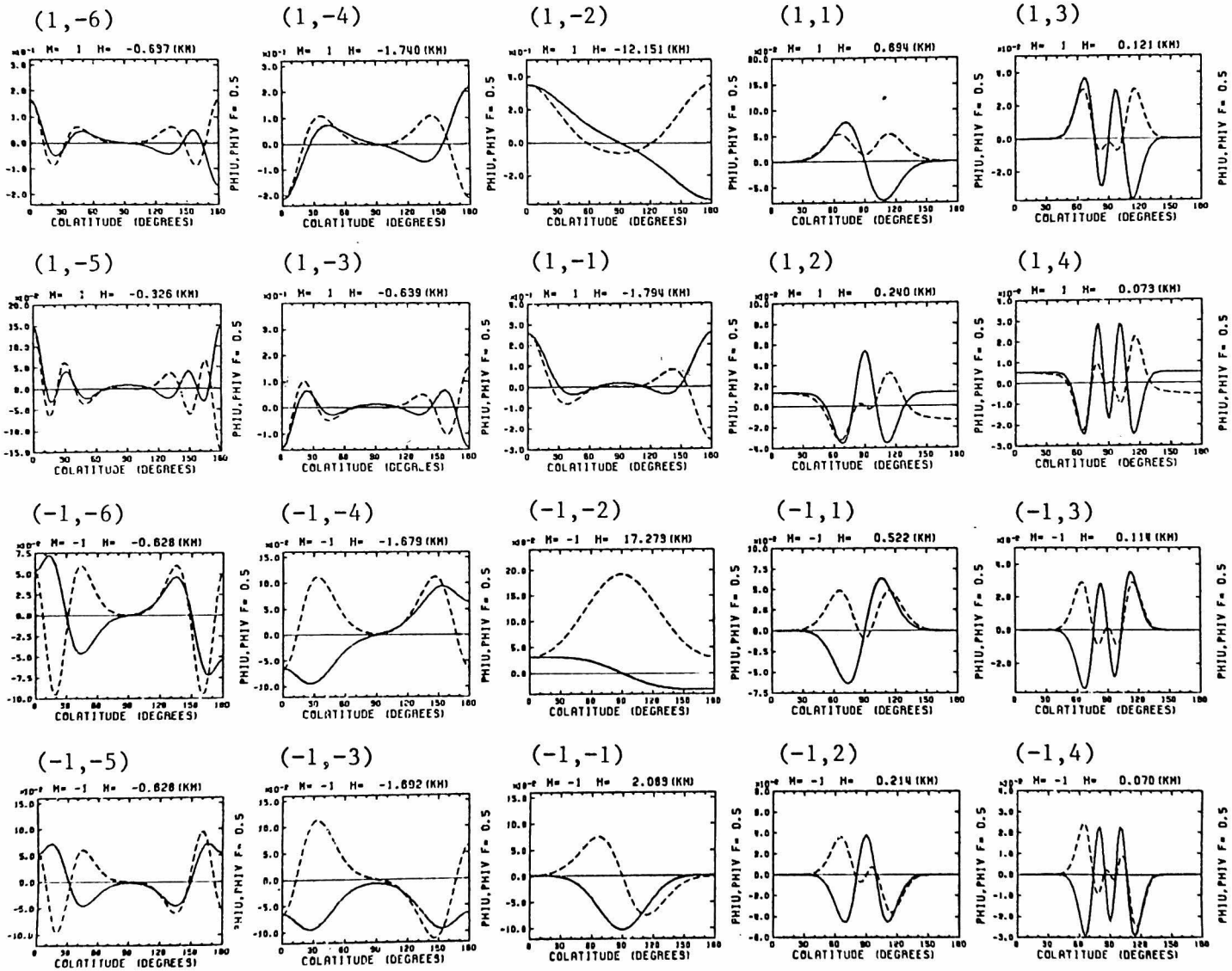

Fig. 2.3
Latitudinal distribution of the wind amplitude for m=1 and -1. Solid and broken line correspond to Φ_θ and Φ_ϕ, respectively.

anticlockwise rotation of the tidal wind.

1.3 Excitation Source of Atmospheric Tides

Excitation source of the atmospheric tides is separated into the gravitational and thermal one. The gravitational attraction of the earth's atmosphere by the moon and the sun produces lunar tides [e.g. Siebert, 1961]. Thermal excitation source is mainly due to absorption of solar incident flux by stratospheric ozone and tropospheric water vapor, latent heat release by the rainfall and heat conduction at the ground, and is much larger than the gravitational one. This subsection describes the thermal excitation source of solar tides.

(a) Absorption of Solar Incident Flux

A parameterization for the absorption of solar incident flux has been done by many authors for many species in the atmosphere. Ozone in the stratosphere and mesosphere absorbs the Hartley and Huggins band in the ultraviolet and the Chappuis band in the visible (4000 - 7600A). As for the water vapor in the troposphere and lower stratosphere, it absorbs the infrared bands. The heat source q due to ozone or water vapor absorption of solar radiation is basically stated as shown below

$$q = E(z)\int I(\lambda,z)\sigma(\lambda)n(z)d\lambda \ , \qquad (2.15)$$

$E(z)$: effectiveness of conversion to heat,
$I(\lambda,z) = I(\lambda,\infty)\exp(-\tau(\lambda,z,\xi))$: solar radiation flux,
$I(\lambda,\infty)$: solar radiation flux at the top of the atmosphere,
$\tau(\lambda,z,\xi) = \sec\xi\int\sigma_a n_a \, dz$: optical depth,

where z, λ, ξ, σ_a and n_a are altitude, wavelength, zenith angle of the sun, absorption cross section and number density of the absorber. We could obtain the heat source, if we integrate the equation (2.15) in the appropriate range of spectrum of solar flux. The knowledge on absorption

cross section and distribution with altitude and latitude for each composition are needed, while the solar radiation flux outside the earth's atmosphere has been well established [e.g. Pettit, 1951]. The cross sections for molecules of aeronomic interest were experimentally determined by many authors, and a critical review of them at wavelenghts less than 3000 A has been done by Hudson [1971]. The distribution of the absorbers is the urgent subject in estimating the heat source.

Water Vapor: The altitude distribution of the water vapor has been measured by a balloon-borne infrared radiometer up to the lower stratosphere [Williamson and Houghton, 1964; Hilsenrath et al., 1977; Murcray et al., 1962; Chaloner et al., 1975]. The mass mixing ratio of the water vapor decreases from $10^{-2}gg^{-1}$ at ground to $2 \times 10^{-6}gg^{-1}$ at tropopause, and remains close to this value, then increases at heights in excess of 25 km. A considerably large value around 10^{-5} to $10^{-4}gg^{-1}$ can be seen at the higher altitude than 30 km. In recent days, a satellite borne spectrometer for the 18 - 30 km region of the rotational water vapor band is developped for the measurement of the tropospheric water vapor distribution [Smith and Howell, 1971]. A ground-based microwave observation of mesospheric water vapor was achieved by Radford et al.[1977]. Recent observations of stratospheric water vapor profiles are illustrated in Fig. 2.4 which is reproduced from the bulletin reports of the Upper Atmospheric Programs [1979]. In spite of all these earnest studies, the three dimensional world-wide distribution of the water vapor has not been satisfactrily clarified yet. Tuller [1968] determined the world distribution of precipitable water which is larger in the tropical region and small near the poles. Topography affects the distribution such that the precipitable water is greater over the oceans.

Distribution of the heat source due to direct absorption of insolation of the water vapor was deduced by Siebert [1961] by use of an empirical formula of Mügge and Möller which is stated as follows

$$B = B_0 U (\sec\xi)^{0.3} \cos\xi \,, \qquad (2.16)$$

$$B_0 = 0.172 \text{ cal/min g}^{0.3} \text{ cm}^{1.4}$$

where B, ξ and U are the energy absorbed, a zenith angle of the sun and precipitable water in a unit of cm which is related to the density of the water vapor ρ_w as

$$U = \int_{z_0}^{z} \rho_w(z') \frac{p\ (z')}{p\ (z)}\, dz' \tag{2.17}$$

The value of B becomes zero at night. The heat source is deduced as

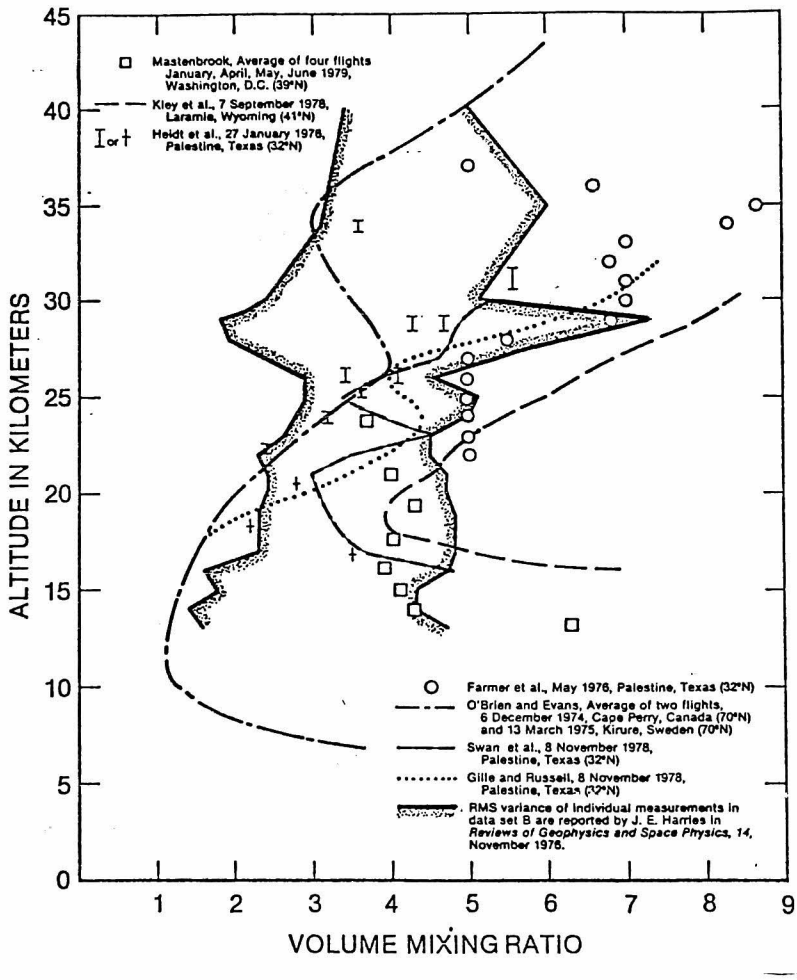

Fig. 2.4 Stratospheric water vapor profiles taken from recent observations in Bulletin of the Upper Atmospheric Program [1979].

$$\frac{1}{\rho_0}\frac{\partial B}{\partial z} = 0.3\, B_0 \frac{\rho_w p_0}{\rho_0 p_0(0)} U^{-0.7} (\cos\xi)^{0.7} . \qquad (2.18)$$

Lacis and Hansen [1974] involved multiple scattering process in the computation of the tropospheric heat source due to water vapor. The absorption varies with the amount and type of clouds, the humidity, the zenith angle of the sun and the albedo of the earth's surface. Forbes and Garrett [1979] showed the vertical distribution of the water vapor heat source decomposed into several Hough modes of the diurnal and semidiurnal tides. The maximum heating rates were 10^{-2}J/(kg sec) and 4.5×10^{-3} J/(kg sec) corresponding to the $S_{1,-2}$ and $S_{2,2}$ mode, respectively. These heat sources rapidly decrease above about 10 km, and almost disappear at around 20 km.

Ozone: Chapman [1930] explained the basic idea of the ozone layer such that ozone is produced by the photodissociation of a molecular oxygen and a subsequent recombination of an atomic and diatomic oxygen in the presence of a third body. Although the ozone is destroyed by photodissociation and recombination, various reactions between ozone and other species, however, occur in the earth's atmosphere [Nicolet, 1975]. Observation by a Dobson spectrometer has given a seasonal variation of total ozone content [Dütsch, 1971]. The vertical distribution of ozone at high altitude has been measured by a satellite borne ultraviolet radiometer at a spectral range near 2500 A [Rawcliffe et al., 1963, Hays and Roble, 1973]. Satellite observations deduced the global distribution at different altitudes in the middle and upper stratosphere [London and Fredrick, 1977]. Observations show a maximum concentration of ozone at around 20 km, minimum value of around 2×10^8 cm^{-3} at 75 km, and a small increase at around 90 km.

The heat source due to ozone is attributed to its radiative process which is closely related to its photochemical process and motion, so that the self-consistent formulation of the process becomes complicated. A radiative equilibrium due to ozone was studied by Leovy [1964] neglecting a dynamical process. Vertical distribution of heating rates due to ozone has been studied by many authors [Lindzen, 1968; Park and London,

1974; Schoeberl and Strobel, 1978; Lacis and Hansen, 1974; Strobel, 1978], and are shown in Fig. 2.5 in a unit of K/day to which the energy input per unit mass per unit time is converted by multiplying a factor Cp/(1 day). Maximum heating rate ranges from 10 to 20 K/day at around 50 km. Enhancement of the ozone concentration above 80 km which were reported by many observers mentioned above gives secondary peak of the heat source. The latitudinal structure of the heat source is important, because it determines the dominant modes of the atmospheric tides. It is mainly determined by the inclination angle of the sun, although the global distribution of ozone is needed to improve the heat source model.

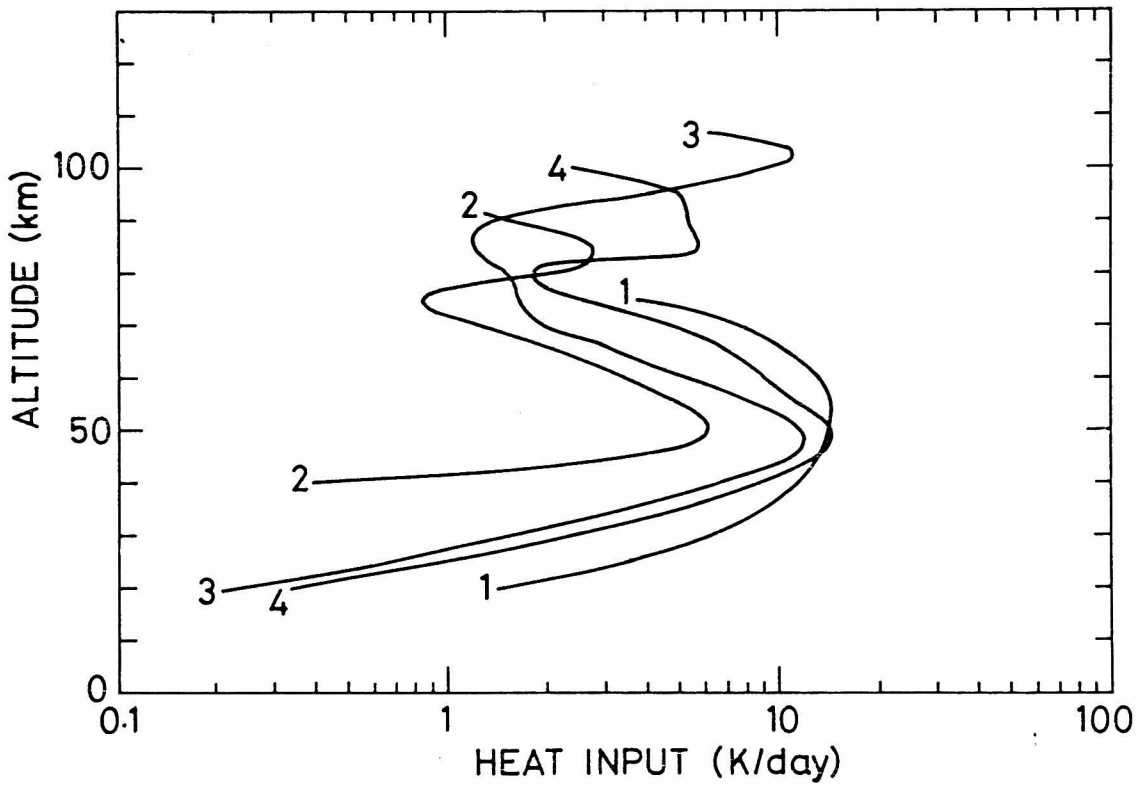

Fig. 2.5 Various models of vertical distribution of heat source due to ozone. 1: Lindzen [1968]. 2: Strobel [1978]. 3: Schoeberl and Strobel [1978]. 4: Park and London [1974].

(b) Latent Heat Release

The excitation of tides by the periodic component of the latent heat release is considered to be smaller than that of solar incident absorption. Its magnitude, however, seems to depend on topographical inequality such as a land-sea distribution, so that it might be an important source of non-migrating tides.

When an unsaturated air ascends, the relative humidity increases as it cools, although the mixing ratio of water vapor remains constant. At last surplus water vapor over the saturation level is condensed to liquid water releasing latent heat, L, which is calculated as

$$L = T(S_v - S_l) \tag{2.19}$$

where S_v and S_l are entropy of the water vapor and liquid water, respectively. Brier and Simpson [1969] reported the diurnal periodicity and superimposed semidiurnal periodicity in the tropical cloudiness and rainfall. In the United States, the diurnal variation in precipitation was found by Wallace [1975] which falls most later in the night. Lindzen [1978] adopted the semidiurnal variation of tropical rainfall as an additional heat source of the migrating semidiurnal tide. If the amplitude of the diurnal component of the precipitation is 1 mm, it may produce latent heat over unit area of $2.3 \times 10^6 J/m^2$. If this heat is distributed uniformly in a column of mass $\rho_0 H(kg/m^2)$ the heat source per unit mass becomes as

$$\frac{L}{C_p \rho_0 H} \cong 0.18 \text{ K} \tag{2.20}$$

It corresponds to a heat source of 1.1 K/day. The heat source region might be concentrated at around condensation altitude, so that it could become a little larger.

(c) Temperature Wave

Absorption of solar incident flux is a small fraction relative to those absorbed by the ocean and land. The energy received by the earth's

surface is transmitted partly into the atmosphere, so that the temperature variation on the surface is transferred upward due to eddy diffusion. This phenomenon is called a temperature wave whose periodicity is fundamentally diurnal. The temperature wave is a composed effect of radiation, turbulence diffusion and thermal conduction. Goody [1960] treated this waves including first two effects. Kuo [1968] approximated the propagation of the temperature wave as a diffusion process, and showed a good agreement between the theoretical calculations and observations. He showed that a difference in temperature from a maximum to a minimum was about 15 K at ground and 5 K at elevation of 400 m.

The temperature wave T(z) can be written as follows

$$T(z) = T(0) \exp(-kz) , \qquad (2.21)$$

$$k = \sqrt{\omega/K} \exp(i\pi/4) ,$$

where K is eddy conductivity. As for the diurnal oscillation, an e-folding depth of the temperature wave becomes 830 m when K is estimated as 50 m^2/sec as has been reported recently [Zimmerman and Murphy, 1980]. The temperature wave may become a considerable heat source of tides in the boundary layer, if the turbulent diffusion of the atmosphere is enough large.

Section 2. Latitudinal Asymmetry in Diurnal Tide at Meteor Heights

2.1 Latitudinal and Vertical Distribution Model of Heat Sources

Latitudinal asymmetry in the heat source could produce the antisymmetric modes of the atmospheric tides. Teitelbaum and Cot [1979] investigated the excitation of the antisymmetric semidiurnal modes by ozone heating under equinoctial conditions. They have shown good agreement between radar data and their results from 100 to 115 km using ozone profiles obtained from the Nimbus IV satellite. Forbes and Garrett [1976, 1978] have shown the seasonal and latitudinal structure of the diurnal tide in the thermosphere excited by in situ absorption of solar

UV and EUV flux. The latitudinal asymmetry of the diurnal tide in the mesosphere, however, has not been practically studied [Tsuda and Kato, 1980]. In this section the latitudinal variation of the diurnal tide is investigated in a classical way by using a simple ozone heat source model whose asymmetric distribution about the equator is mainly taken into consideration.

If we treat the excitation of tide in the range of the classical tidal theory, we must make the heat source separable in altitude and colatitude. The heat source is assumed to be proportional to a multiplication of total ozone content $n(\theta)$, solar radiation flux $I(\theta,t)$ and a vertical distribution function $f(z)$ as follows:

$$q \propto n(\theta)\, I(\theta,t)\, f(z) \ , \tag{2.22}$$

where we suppose the same vertical distribution model of ozone heat source as used by Lindzen [1968]. Bojkov [1969] showed a correlation between vertical ozone distribution in the stratosphere and the total ozone content. So that, equation (2.22) can approximate the latitudinal variation of ozone, although we use the total ozone content observed by Dobson spectrometer [Dütsch, 1971] as shown in Fig. 2.6 for four seasons instead of precise global ozone distribution. Maximum concentration of ozone can be seen in the high latitude region in spring. A simplified relation of solar radiation flux against colatitude and local time is written

$$\begin{aligned} I(\theta,t) \propto \cos\xi &= \cos\theta \sin\delta + \sin\theta \cos\delta \cos t \ ; \text{ daytime} \\ &= 0 \ ; \text{ night} \ , \end{aligned} \tag{2.23}$$

δ; declination angle of the sun,

θ; colatitude,

t; local time ($t=0$ at noon).

From the expression (2.23), we extract the diurnal component of the solar radiation by a Fourier transformation. From (2.22) and (2.23), we have the resultant diurnal heat source Q

$$J = \frac{i\omega R_a}{\gamma} f(z)g(\theta)\exp(i(\omega t + \phi)) \ , \qquad (2.24)$$

R_a; gas constant for air,

$\gamma = \frac{\kappa-1}{\kappa}$, κ; specific heat ratio,

ω; angular frequency of oscillation,

where

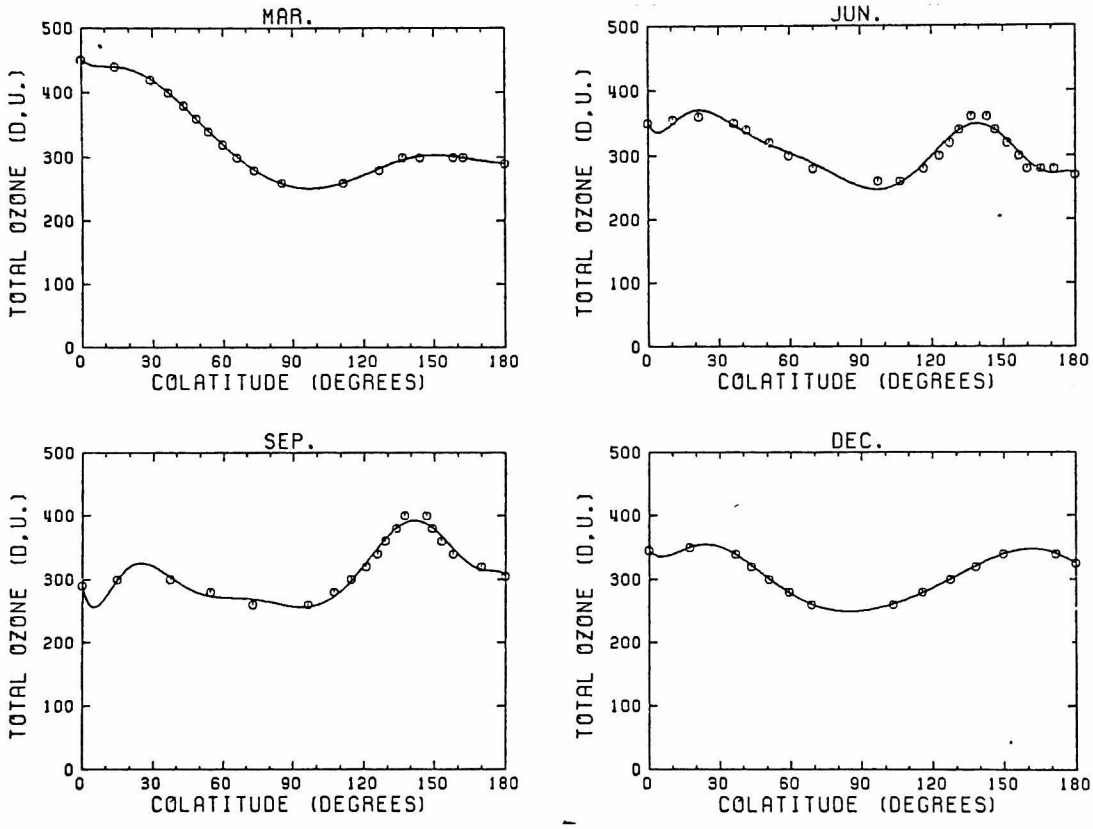

Fig. 2.6 Latitudinal distribution of total ozone content for four seasons observed by Dobson spectrometer [Dütsch, 1971]. Vertical axis is plotted in a Dobson unit.

$$g(\theta) \propto \frac{1}{\pi}(t_0 \cos\delta \sin\theta + \sin\delta \cos\theta \sin t_0)n(\theta), \qquad (2.25)$$

$$x = -\frac{\sin\delta \cos\theta}{\cos\delta \sin\theta} ,$$

$$t_0 = \pi; \quad x>1,$$

$$t_0 = |\arctan x|; \quad 1>x>-1 ,$$

$$t_0 = 0; \quad x<-1 .$$

Broken lines in Fig. 2.7 show the diurnal heat source calculated as described above for March, June, September and December, respectively. These results were expanded in a series of Hough modes as usual. Solid lines in Fig. 2.7 are those which are reproduced by taking finite number of terms in the expansion. We used 20 positive modes and 21 negative modes in the expansion. In the winter polar region, the heat source beocmes zero. Because of this fact, a large asymmetry in the heat source is introduced. Even at the equinox, small asymmetry is seen because ozone distributes asymmetrically about the equator as shown in Fig. 2.6 [Dütsch, 1971]. In Fig. 2.8, the coefficients of heat source expanded in diurnal Hough modes are shown for four seasons. The most dominant mode is $S_{1,-2}$ mode throughout a year; a fundamental symmetric evanescent mode. Among the propagating modes, $S_{1,1}$ mode has a large expansion coefficient. As for the antisymmetric modes, $S_{1,-1}$ has a large expansion coefficient in June and December. Generally, symmetric modes have larger expansion coefficients than anti-symmetric modes, and almost the same value of coefficients around a year. There is a large seasonal variation in the expansion coefficients of anti-symmetric modes. From these expansion coefficients, we can know a general behaviour of the diurnal tide. In the heat source region, evanescent modes such as $S_{1,-1}$ and $S_{1,-2}$ are dominant, while the propagating $S_{1,1}$ mode becomes dominant outside the heat source region. We could expect to see the asymmetry of the diurnal tide only in the stratosphere and mesosphere. Seasonal variation of the diurnal tide in the stratosphere and mesosphere is caused mainly by antisymmetric evanescent modes such as $S_{1,-1}$ and $S_{1,-3}$ modes.

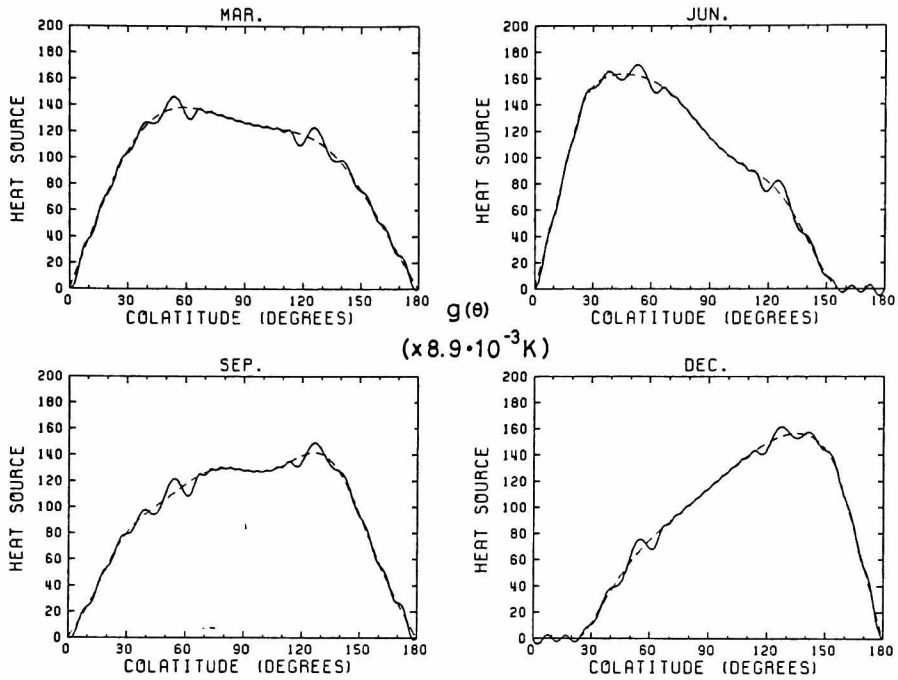

Fig. 2.7 Diurnal ozone heat source distribution against colatitude for March, June, September and December. Solid lines are results theoretically calculated, broken lines are those recomposed by taking finite number (20 positive and 21 negative modes) of Hough modes.

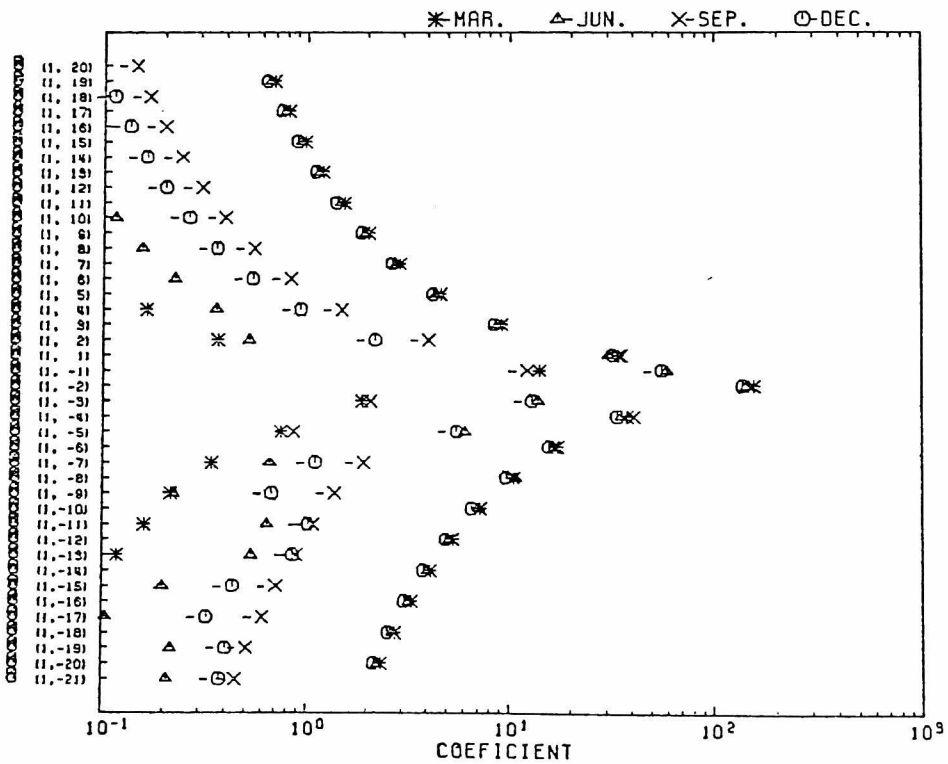

Fig. 2.8 Expansion coefficients of the diurnal heat source shown in Fig. 2.7 for four seasons.

2.2 Numerical Computations on Seasonal Variation of Diurnal Tides

The amplitude of the diurnal pressure variation divided by the static atmospheric pressure is shown in Fig. 2.9 at seven altitudes up to 121 km from the ground. The results in June shown in the right hand of Fig. 2.9 has a large asymmetry with respect to the equator between the altitude of 41 km and 98 km such that the amplitude is large in the

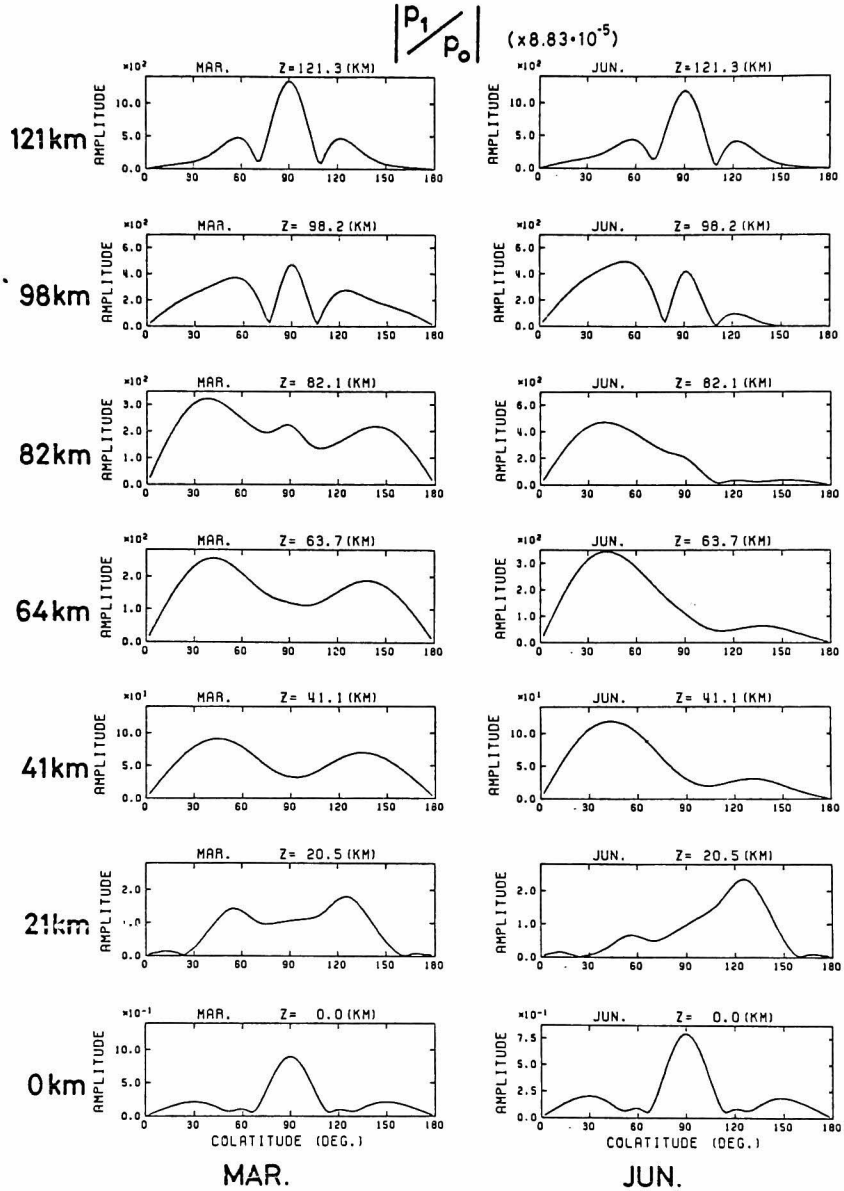

Fig. 2.9 Amplitude of diurnal pressure variation divided by the static pressure versus colatitude for March and June.

northern hemisphere. At an altitude of 121 km and at the ground, the distribution is almost symmetric and agrees with that for $S_{1,1}$ mode; the fundamental symmetric propagating mode. As for the pressure variation in March, slight asymmetry can be seen from 21 km to 98 km. These asymmetries would be produced by evanescent modes, because they are dominant only in the altitude region corresponding to the heat source. Figure 2.10 (a) and (b) shows the seasonal-latitudinal variation of the northward and eastward component of the diurnal tidal wind at 98 km, respectively. In June and December, asymmetry in the amplitude can be seen; especially in middle and high latitudes, although that in the phase is relatively small. Thus, in the meteor region we could expect asymmetry of the diurnal tide due to evanescent modes, however the dominant modes are symmetric recognized from the phase variation along latitude.

2.3 Discussion

We have shown that the evanescent antisymmetric modes produce the asymmetry in the diurnal tide about the equator in the stratosphere and mesosphere. Because the $S_{1,1}$ mode is most strongly excited among the propagating modes in each season, it dominates outside the heat source region, and overwhelms the evanescent $S_{1,-1}$ mode from which the asymmetry is mainly derived. The meteor region is the transient height for the dominant modes from the evanescent one to the propagating one, so that relatively complicated phenomena occur. Recent studies have been developed the ozone heat source model as shown in Fig. 2.5 such that it has secondary peak at around 95 km. This is proved not to affect the latitudinal variation of the diurnal tide substantially from numerical calculations which, however, are not shown here. A question might arise if the asymmetry in the water vapor heat source at ground produces the asymmetry in the diurnal tide in the mesosphere. A uniform water vapor distribution along colatitude with a constant scale height of 10 km is applied to $n(\theta)$ in the equation (2.22). Although this is far from the actual condition, the heat source becomes asymmetric because of the seasonal variation of the inclination angle of the sun. Figure 2.11 shows the diurnal pressure variation excited by the water vapor heat

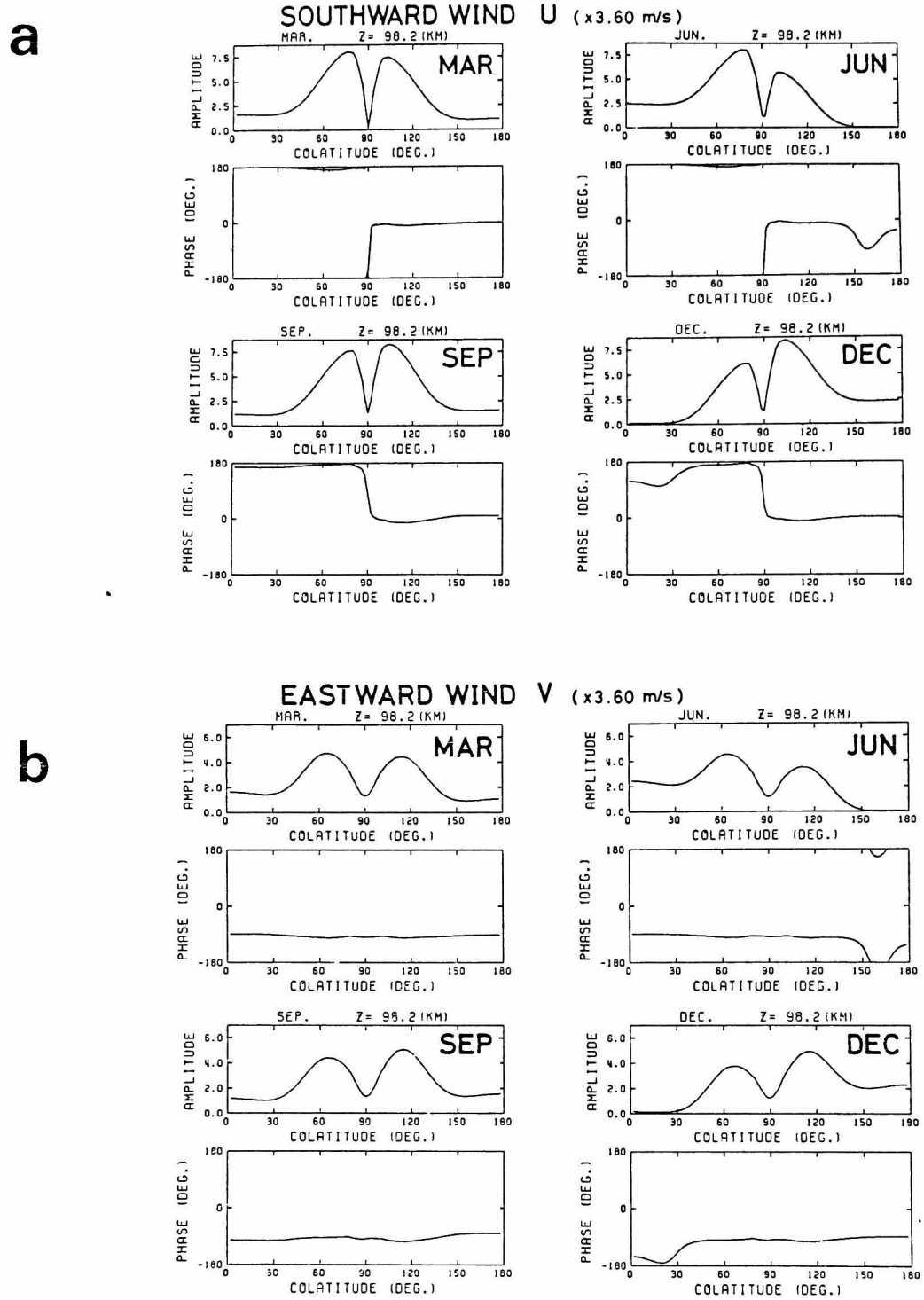

Fig. 2.10 Latitudinal variation of amplitude and phase of the diurnal wind velocity at an altitude of 98 km for four seasons. (a): southward component. (b): eastward component.

source in solstices and equinox similar to the ozone case. Below 32.5 km, the asymmetric pressure distribution about the equator can be seen, but is not recognized in the mesosphere. If there were a large asymmetry in the water vapor distribution near the equator exists, antisymmetric propagating modes could be generated, and might affect the diurnal tide in the mesosphere. It, however, could not give a large asymmetry in diurnal tide in the high latitude region, because its amplitude is small outside the equatorial region recognized easily from Figs. 2.2 and 2.3. In Chapter V, the seasonal and latitudinal variation of the northward component of the diurnal tide will be compared with the meteor radar observations.

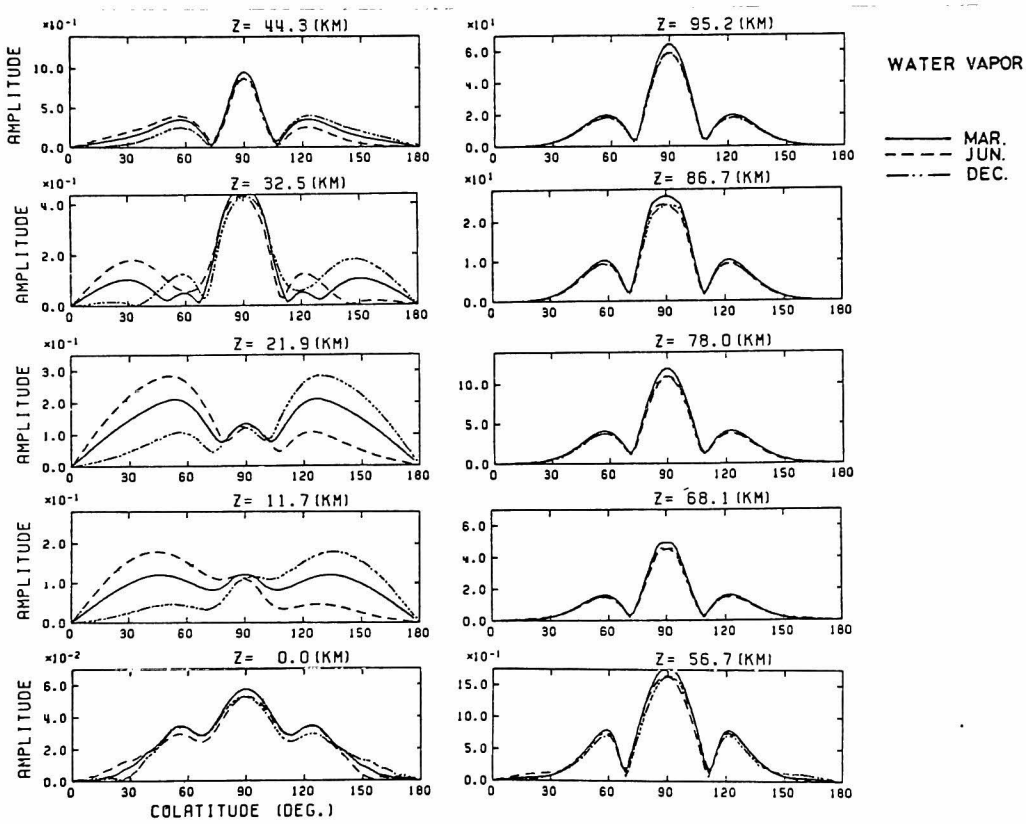

Fig. 2.11 Diurnal pressure variation generated by water vapor heat source.

Section 3. Non-migrating Diurnal Tide Excited by Localized Heat Source

3.1 Localized Heat Source Model

When some part of the earth is heated more than the surrounding area, an excess portion of the heat source can be considered to be a heat source fixed on the earth. This is mainly caused by differences in the heat conduction and the water vapor distribution over the ocean and the land. So that, topography may affect tidal winds and produce waves with tidal period which do not travel westward with the sun. Such waves called non-migrating tides are associated with positive and negative longitudinal wavenumbers. Very little work has been done on the theoretical investigation of the effects of topography on the atmospheric tides, although observations have shown an existence of non-migrating tidal waves.

A spherical harmonic analysis of the diurnal surface pressure oscillations was done by Haurwitz [1965] who showed a strong influence on these oscillations by the land-sea distribution, such that the value was larger on the lands than that on the oceans as illustrated in Fig. 2.12. The fact means an existence of a standing wave along longitude due to components with various wavenumbers, however the dominant one among those component is the migrating wave, as shown in Fig. 2.13.

Wallace and Tadd [1974] examined daily rawinsonde data and gave a diurnal tidal wind as a difference of the wind field of the observations taken at two local times 12 hrs apart. They have shown large and systematic departures from the simple zonal wavenumber 1 pattern, and assumed that those might be attributed to a horizontal inhomogeneities in the diurnal heating cycle within the boundary layer mainly due to land-sea distribution.

Nitta and Esbensen [1974] deduced the diurnal variation of wind in the troposphere by use of the rawinsonde data obtained during the BOMEX (Barbados Oceanographic and Meteorological Experiment). Their results were one order larger than the theoretical value obtained by Lindzen [1967], and also showed fairly short vertical wavelength as described in Fig. 2.14.

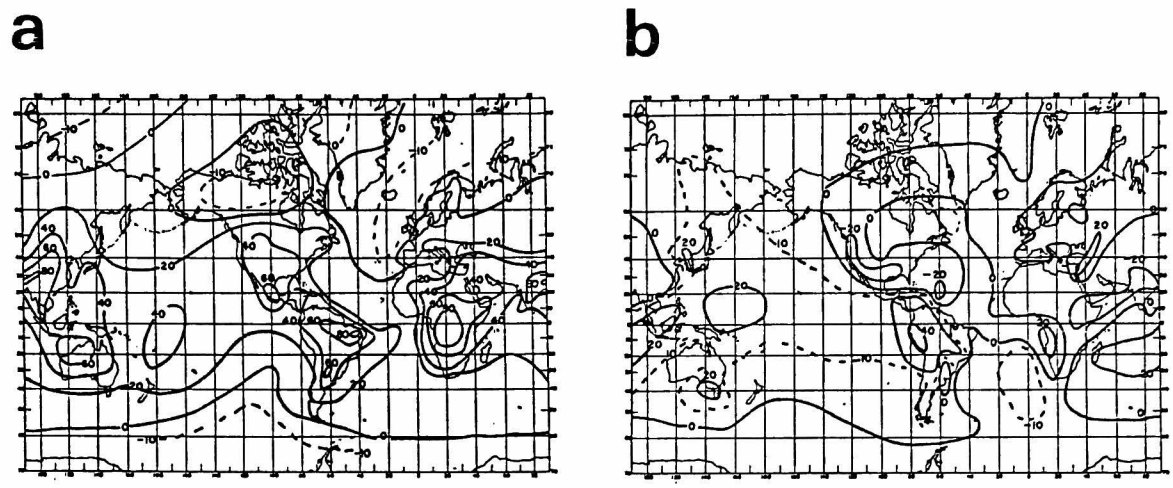

Fig. 2.12 Spherical harmonic analysis of diurnal pressure variation [Haurwitz, 1965]. (a) and (b) correspond to factors of cosine and sine term, respectively, in a unit of 10^{-2} mmHg.

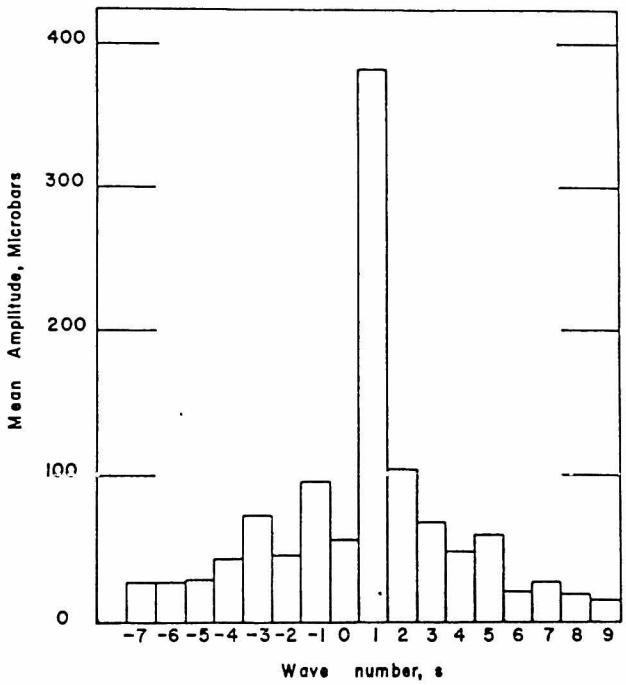

Fig. 2.13 Spectrum of the diurnal pressure tides [Haurwitz, 1965].

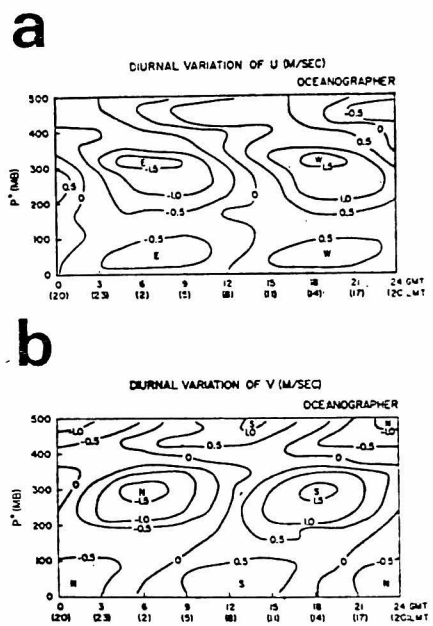

Fig. 2.14 Diurnal variation of wind component during BOMEX [Nitta and Esbensen, 1974]. (a): eastward. (b): northward.

We may expect that the horizontal inhomogeneity of the heat source such as land-sea distribution is essential in generating non-migrating tides. We assume that a localized heat source, Q, is originally produced by solar radiation which is absorbed and transfered by a matter having inhomogeneous distribution, so that Q can be written as

$$Q = S(\theta,\phi,z)\ \exp(i(\Omega t + \phi)) \tag{2.26}$$

where S is a spatial distribution of the absorber. We treat S as being separable in each variables, accordingly it is expressed by a multiple of three functions which can be independently determined with longitude, latitude and altitude.

The topography in question is expanded into Fourier series, and further decomposed into a truncated series of Hough functions as follows

$$S(\theta,\phi,z) = \sum_m \left(\sum_n q_{\omega,m,n}(z)\ \Theta_{\omega,m,n}(\theta)\right)\exp(im\phi) \tag{2.27}$$

where $q_{\omega,m,n}(z)$ is a vertical heat source distribution which includes an expansion coefficient with respect to both longitude and colatitude. Note that S is a real function, although the phase of the heat source, Q, varies with longitude.

Longitudinal distribution

Three models of the longitudinal distribution of S are assumed. The widest spread of the distribution along longitude is represented by a function $1/2(1+\cos\phi)$ which is shown in Fig. 2.15. This is composed of a stationary wave and fundamental eastward and westward propagating wave. Other two models are represented by truncated series of the Fourier expansion of a rectangular distribution whose width is 120° and 5° as shown in Fig. 2.16 (a) and (b), respectively. The former contains wavenumber of -2 to 2, while the latter contains -20 to 20.

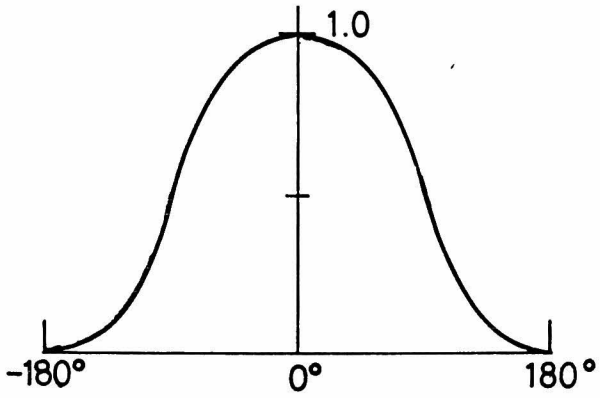

Fig. 2.15 Longitudinal distribution model of the heat source represented by a function $0.5x(1+\cos\theta)$.

a

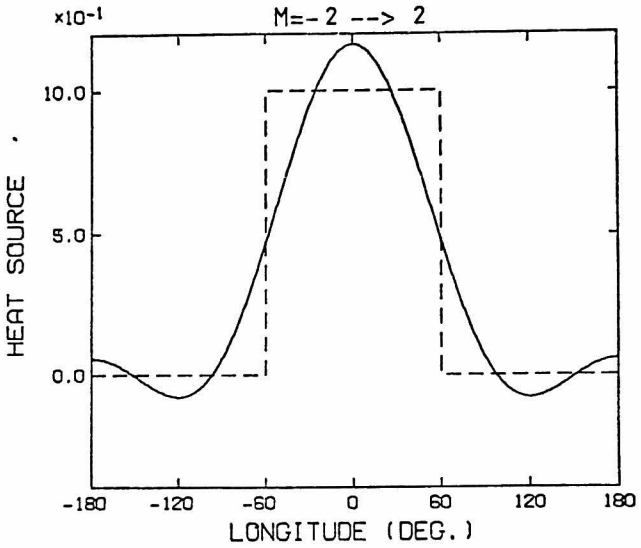

Fig. 2.16 Rectangular distribution (broken line) with a longitudinal width of (a) : 120° and (b) : 5°, and composed function of them (solid line) by using waves with wavenumbers of $|m| \leq 2$, and $|m| \leq 20$ for (a) and (b), respectively.

b

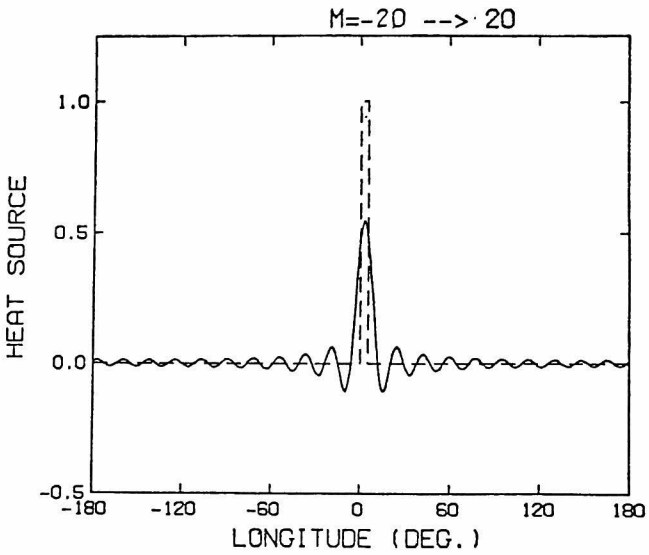

Latitudinal distribution

We assume that the heat source is confined in the tropical region so as to simulate the observations carried out at Jicamarca VHF radar (11.9°S, 76.0°W). The spread of the heat source in colatitude is considered to be narrow and wide ones which lie in the colatitude range of 100° to 102° and 85° to 115°, respectively.

The latitudinal distributions are expanded in terms of the Hough functions corresponding to the longitudinal wavenumber of -19 to 20, and their expansion coefficients are shown in Fig. 2.17 (a) and (b) for the narrow and wide latitudinal heat source distributions, respectively. From Fig. 2.17, the distribution is fairly well approximated, even though finite number of Hough functions ranging from -20 to 20 are used. The evanescent modes do not affect largely in the case of the narrow heat source. As for the wide one, a few fundamental propagating modes are dominant, and the evanescent modes can not be neglected.

Altitude distribution

The function $q_{\omega,m,n}$ in (2.27) is simplified by using a common e-folding depth of H_s for every modes as follows

$$q_{\omega,m,n}(z) = C_{m,n} \exp(-z/H_s) \tag{2.28}$$

where $C_{m,n}$ is a constant for each m, n which can be decided by expansion coefficient along longitude and colatitude. We assume the scale height H_s as 10 km and 1 km for those due to water vapor absorption and the temperature wave, respectively. An intermediate situation is considered by setting H_s as 5 km. The phase of the maximum amplitude of the heat source is assumed to be at local noon, and not to vary along height.

As listed in Table 2.1, six cases are considered as the localized heat source by combining above-mentioned distributions with longitude, latitude and altitude. Four different cases of horizontal distributions are assumed as shown in Fig. 2.18 (a)-(d). Among those, Fig. 2.18 (d) corresponds to the most localized heat source. Vertical distribution is varied in Case 3-5 so as to H_s is 10 km, 5 km and 1 km, respectively,

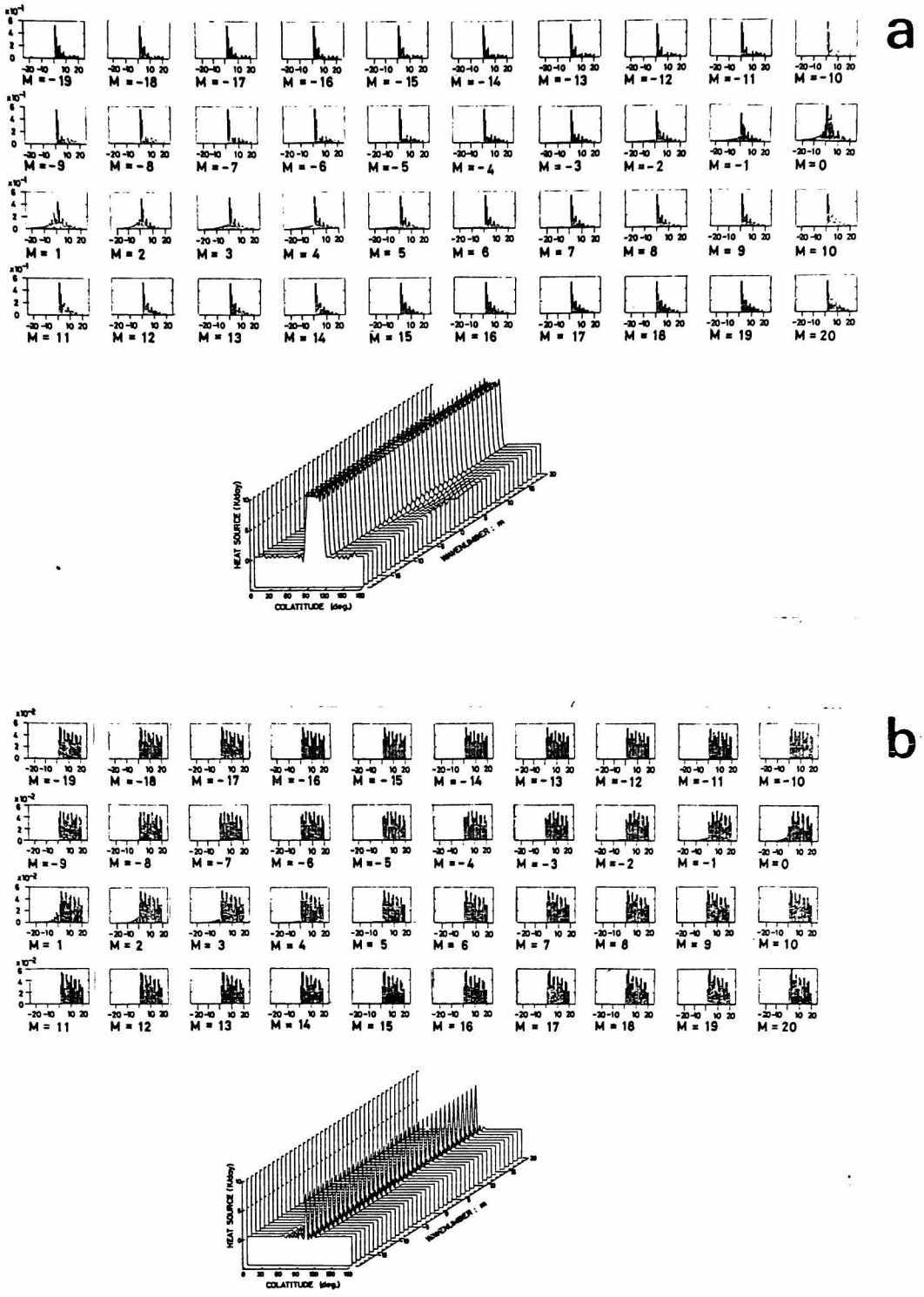

Fig. 2.17 Expansion coefficient of the latitudinal distribution of (a): wide and (b): narrow heat source, accompanying a composed function for each longitudinal wavenumber.

Table 2.1 Heat source S

Case	θ-dependence	ϕ-dependence	H_s (km)
1	const in $100<\theta<102$, 0 outside, $\|n\| = 1 - 20$ in expansion.	$0.5*(1+\cos\phi)$.	10
2	const in $85<\theta<115$, 0 outside, $\|n\| = 1 - 20$ in expansion.	as in Case 1.	10
3	as in Case 2.	const in $-60 <\phi< 60$, 0 outside, $\|m-1\| = 0 - 2$ in expansion.	10
4	as in Case 2.	as in Case 3.	5
5	as in Case 2.	as in Case 3.	1
6	as in Case 1.	const in $0<\phi < 5$, 0 outside, $\|m-1\| = 0 - 20$ in expansion	10

m: longitudinal wavenumber
n: order of the Hough mode

while the horizontal distribution is not changed. A magnitude of the heat source at the ground is normalized to 10 K/day, where K/day is defined to be 2π times the amplitude of the temperature variation.

3.2 Numerical Computation on Non-migrating Diurnal Tide for Six Cases of Heat Source Models

The vertical heat source distribution described in the preceding sub-section is substituted into the Wilkes equation (2.11) according to the classical tidal theory. The solution for the non-dissipative atmosphere is obtained by the difference method from ground to an altitude of 199.8 km with a step distance of 40 m. The boundary conditions are the vanishing vertical velocity at surface and the radiation condition which permits only outgoing energy flux at the upper boundary. The behaviour

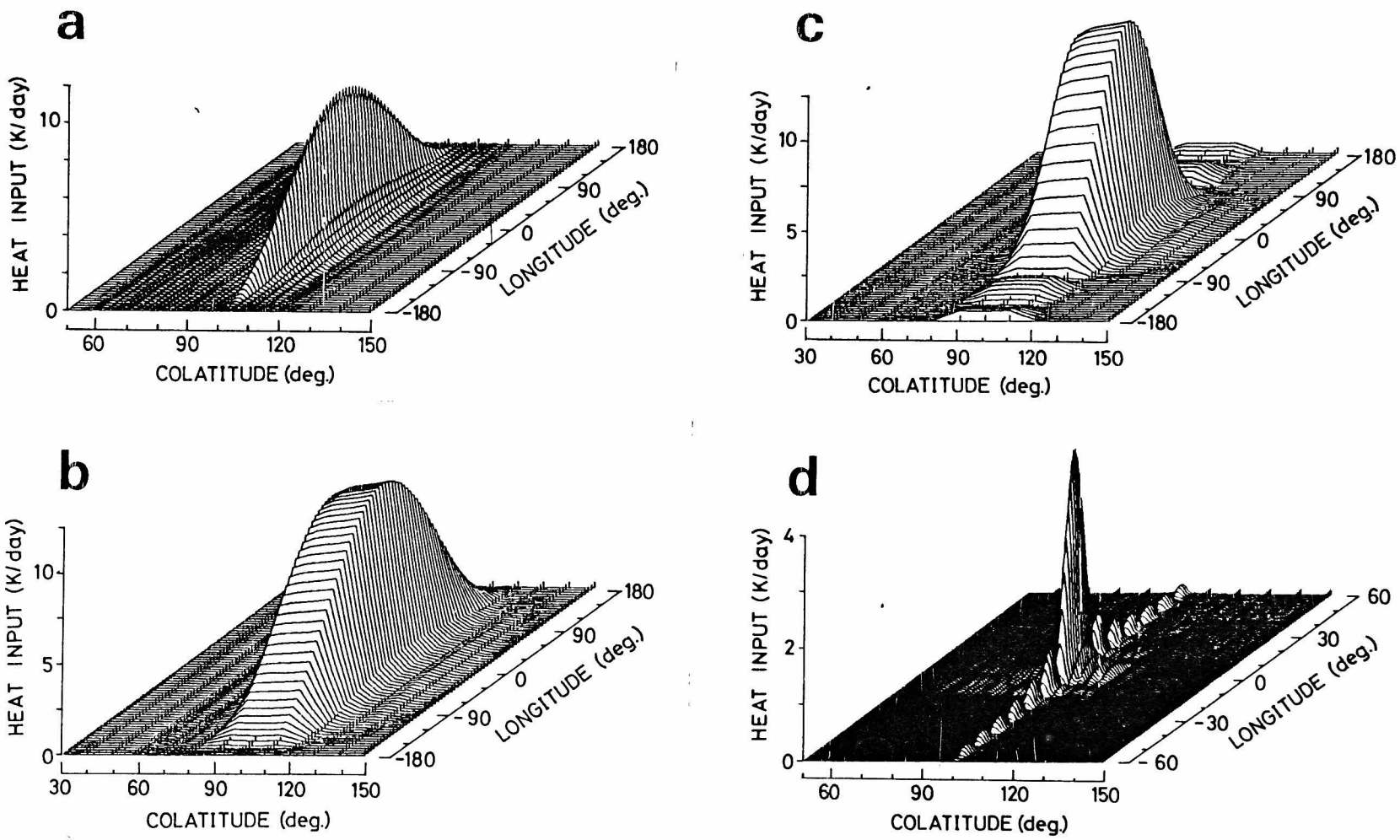

Fig. 2.18 Four models of horizontal distribution of the function S.
(a): Case 1. (b): Case 2. (c) Case 3, 4 and 5.
(d): Case 6.

of the non-migrating diurnal tide can be known, when we sum up each solution for a single mode taking the relations (2.10), (2.26) and (2.27) into account.

At first, we will investigate an accuracy of our numerical computation. For the most complicated case 6, examination is done on the

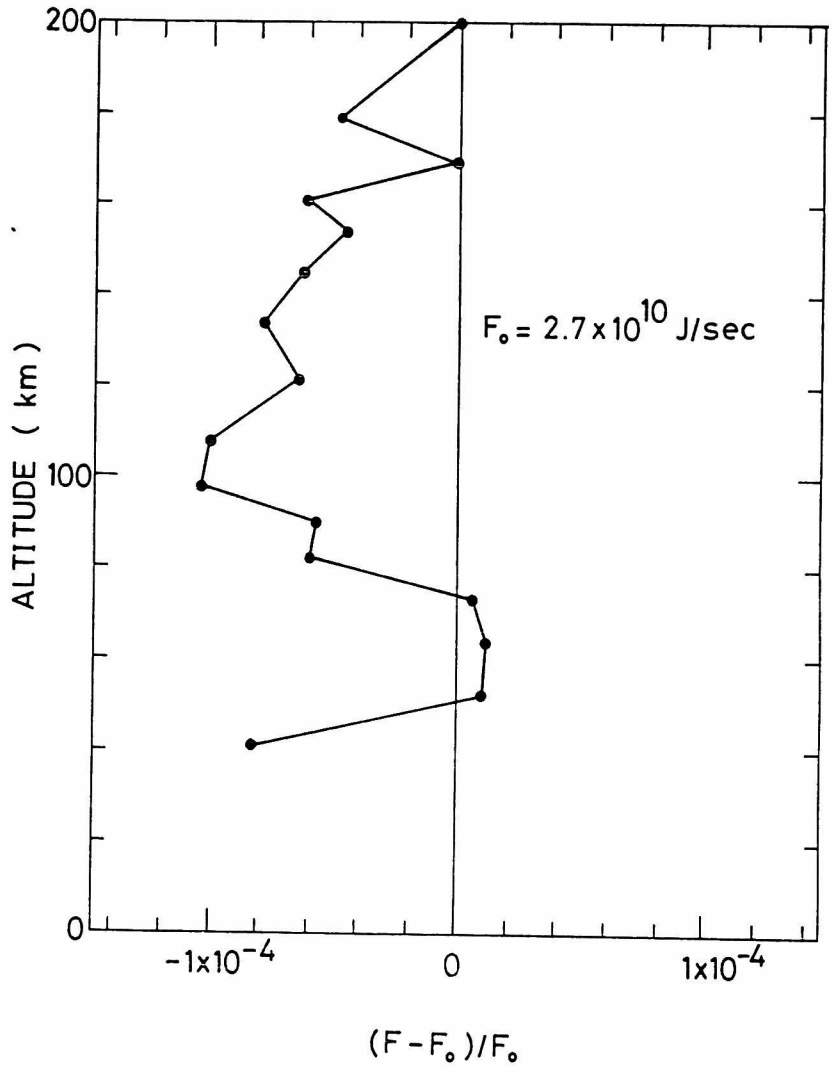

Fig. 2.19 Constancy of energy flow above the heat source for Case 6.

conservation of the total vertical energy flux, F, defined as

$$F = \int_0^{2\pi}\int_0^{\pi} \mathrm{Im}(W_z p_1^*)a^2 \sin\theta \, d\theta d\phi \qquad (2.29)$$

where Im means an imaginary part, and a is earth's radius. An asterisk which is a superscript of p_1 means taking a complex conjugate value. From the result shown in Fig. 2.19, the conservation is satisfied above 40 km to an accuracy of 2×10^{-4} to the total flux, F_0, at the upper boundary.

The amplitude of the perturbed pressure, p_1, at six altitudes is plotted in Fig. 2.20 (a)-(d) corresponding to the heat source model in Table 2.1 (a), (b), (c) and (f), and also plotted in Fig. 2.21 (a) and (b) for the heat source model in Table 2.1 (d) and (e). The illustrations of p_1 in Fig 2.20 and Fig 2.21 are shown similar to a perspective, because p_1 for non-migrating tide is a function of both longitude and co-latitude at a given altitude differing from the migrating one. The altitudes are chosen so as to a distance is equal in the pressure coordinate.

When we compare the distribution of p_1 with that of the heat source, one can easily recognize that the heat source is fairly well reproduced for the case 1 and 6, while others do not. Latitudinal distribution of p_1 varies considerably with altitude. Except for the case 6, longitudinal distribution of p_1 seems to be stationally, and its maximum remains near the region of the heat source. The amplitude and phase of the perturbed pressure divided by the surrounding static density, ρ_0, at longitude of 0° and colatitude of 100° is shown as a function of height in Fig. 2.22 (a)-(e) for each case, where the phase is defined as a local time of the maximum perturbed pressure. The amplification of 10^3 times can generally be seen in the p_1/p_0 at an alitude of 100 km in comparison with it at the ground. The phase variation suggests fairly short vertical wavelength, and that the phase velocity is generally downward. Considerable fluctuation in amplitude can be seen especially in cases 1 and 6.

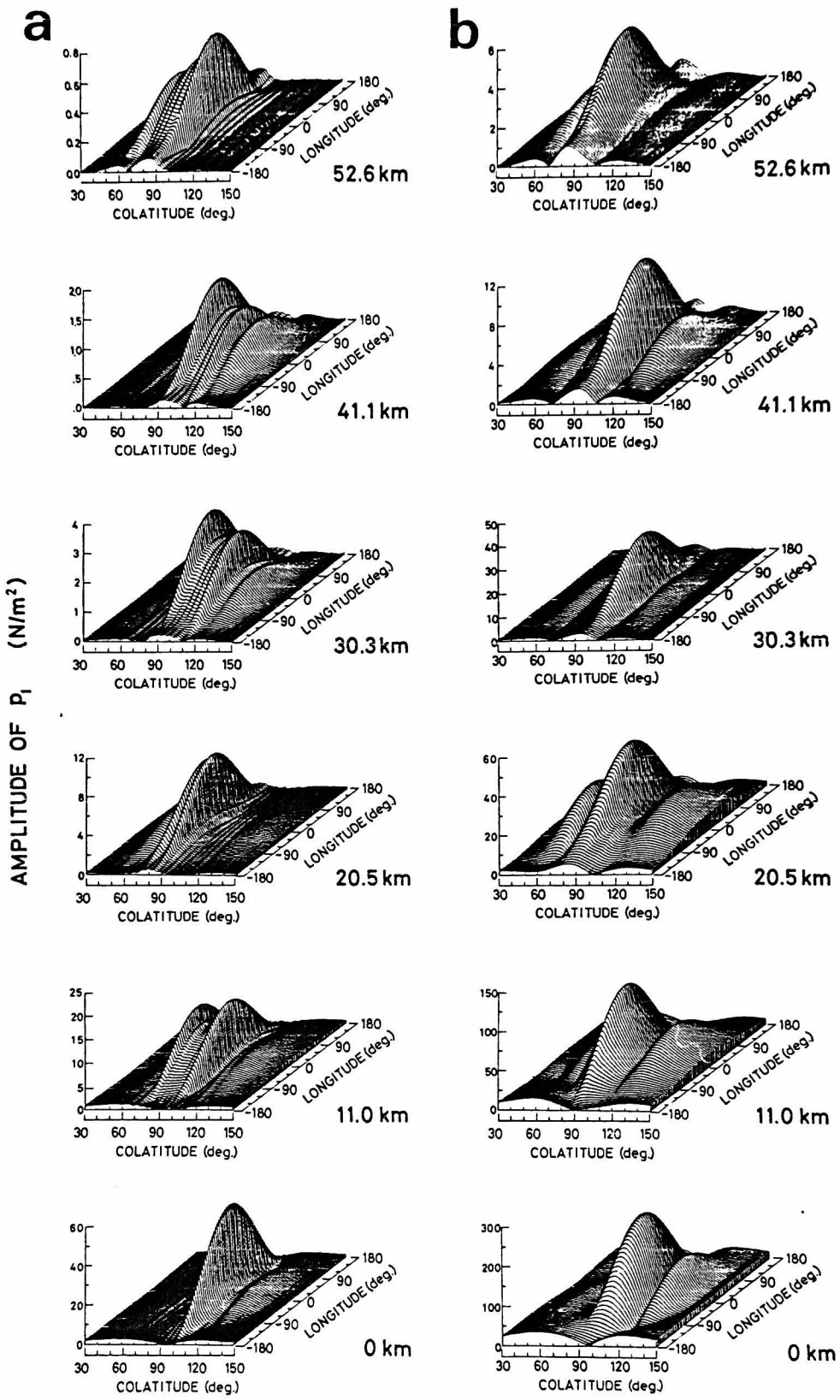

Fig. 2.20 The perturbed pressure amplitude distribution, p_1 at an altitude of 0, 11.0, 20.5, 30.3, 41.1 and 52.6 km.
(a): Case 1. (b): Case 2. (c): Case 3. (d): Case 6.

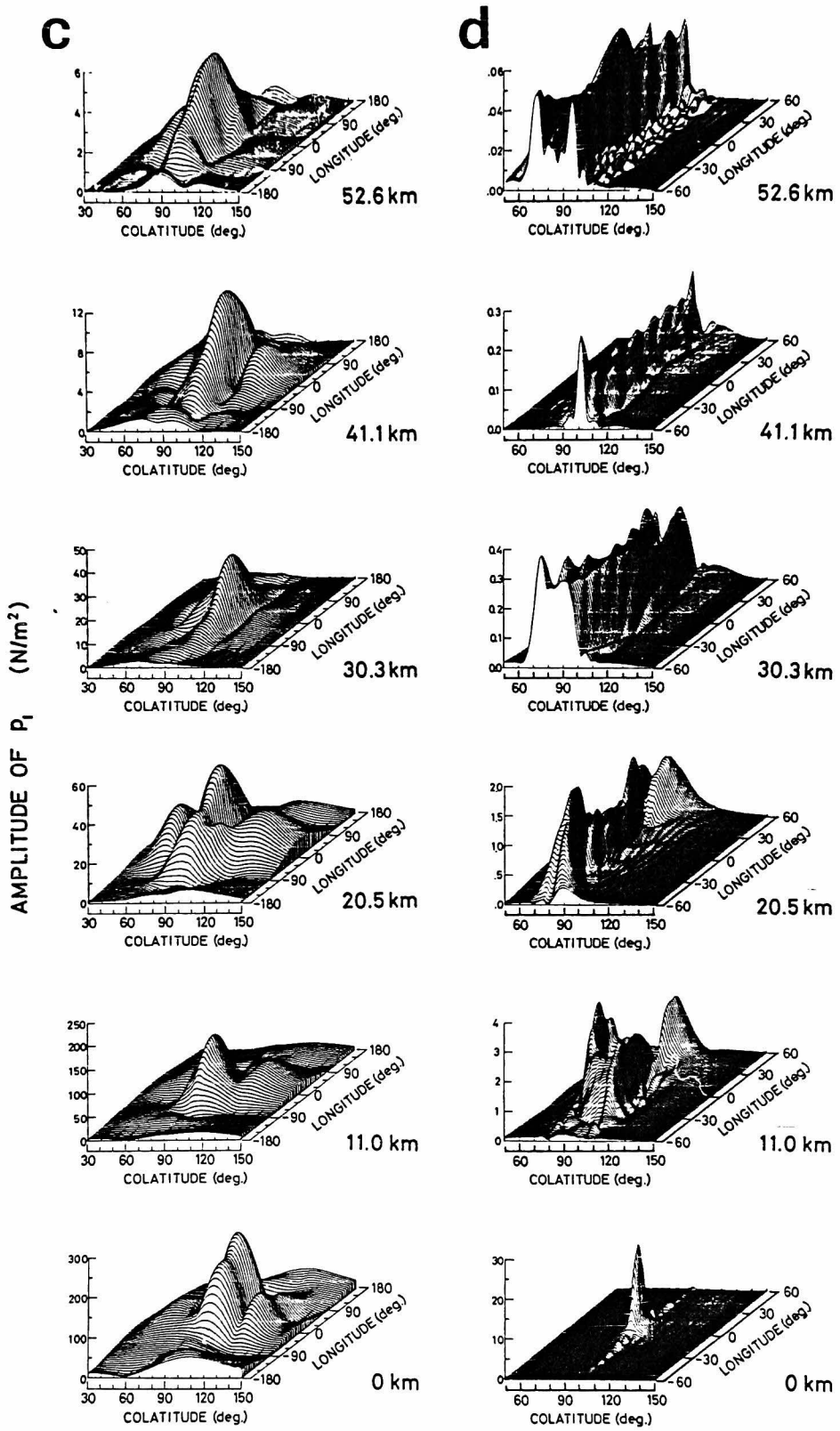

Fig. 2.20 (Continued)

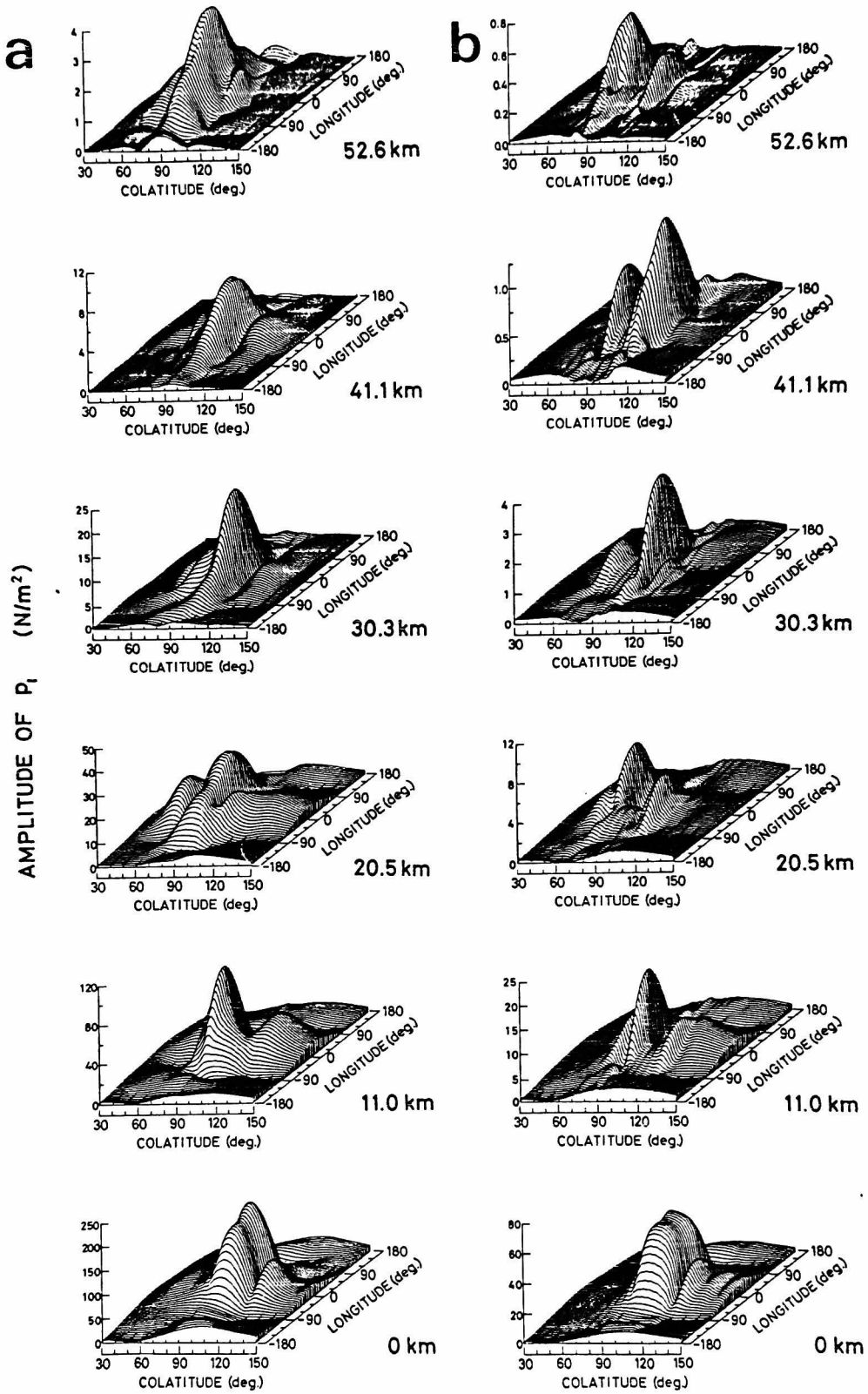

Fig. 2.21 The same as Fig. 2.18 except for (a): Case 4 and (b): Case 5.

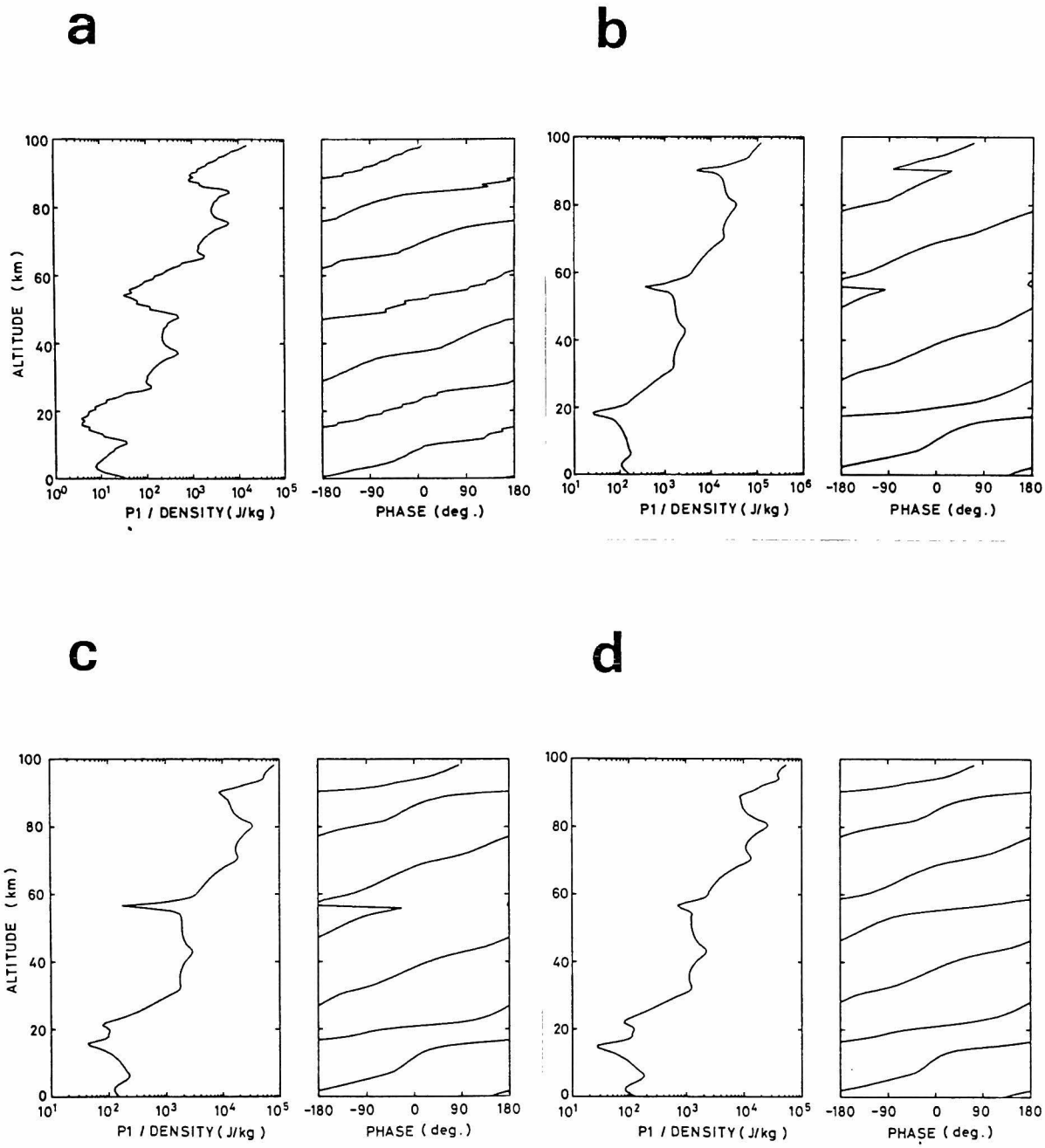

Fig. 2.22 The perturbed pressure p_1 divided by the surrounding static density at a longitude of 0° and a colatitude of 100°. Diagrams (a) - (f) correspond to Cases 1 - 6, respectively.

Fig. 2.22 (Continued)

e f

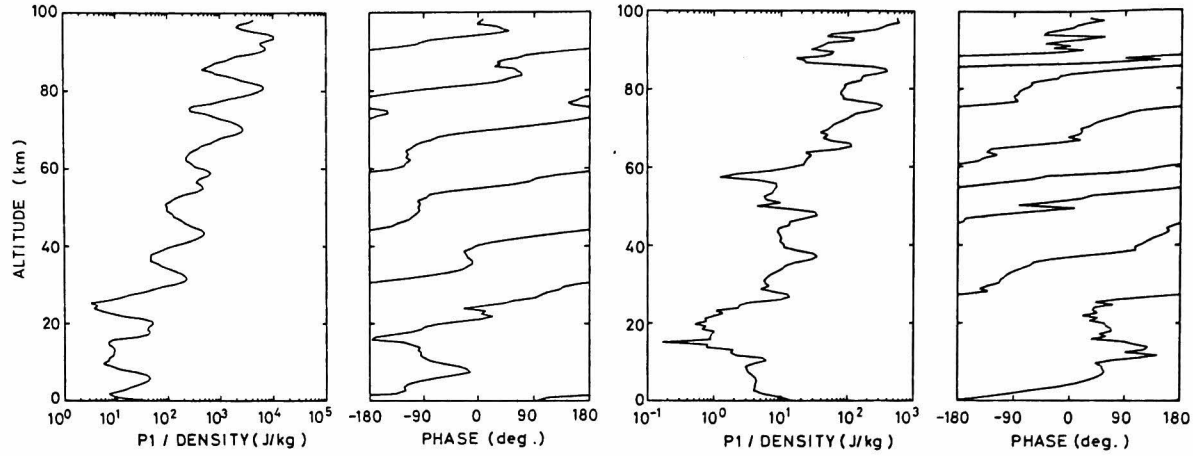

3.3 Discussion

The non-migrating diurnal tide due to locarized heat source has been examined numerically. It has been found that the non-migrating tide varied not only with the colatitude but with the longitude, and is essentially related to the universal time.

The perturbed region shown in Fig. 2.20 and 2.21 spreads as the wave propagates upward. The amplitude of p_1 generated by heat sources with the narrow latitudinal width such as Cases 1 and 6 can reproduce the shape of the heat sources. This is attributed to the different response to the excitation between the positive and the negative modes [Kato et al., 1981].

As for Case 1, the perturbed region is confined around the heat source in the southern hemisphere at ground, but it moves to the equator and the northern hemisphere at an altitude of 11 km and 20.5 km. Then, the region again moves into the southern hemisphere at an altitude of 41.1 km. It seems that the perturbation goes to and back in the range from the heat source region to a conjugate one with respect to the equator. The wave energy is apparently transfered from the source region to other, although any single mode of the tidal waves can not transport energy latitudinally. Because of differences in the vertical propagation properties of each mode, a balance among modes collapses, although it is kept critically at ground to confine waves in the heat source region.

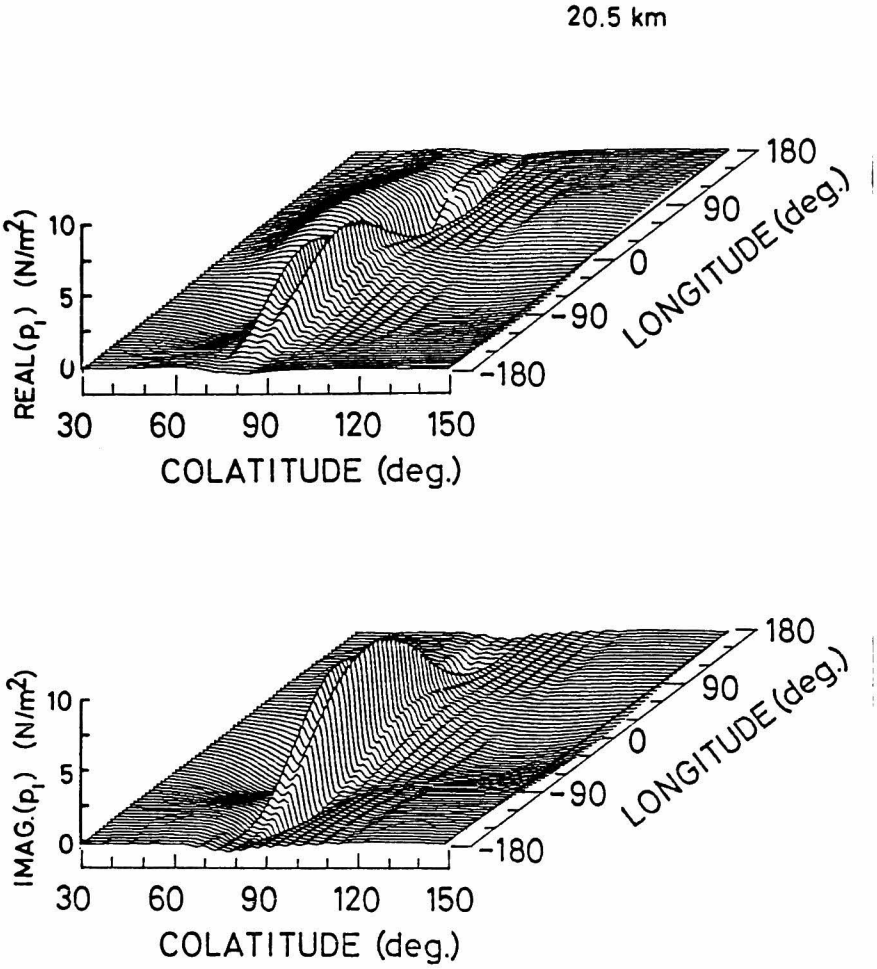

Fig. 2.23 Real and imaginary part of p_1 at an altitude of 20.5 km. top: real part. bottom: imaginary part.

Except for Case 6, the perturbed wave almost remains near the heat source region in longitude, so that it looks as a standing wave. A real and an imaginary part of the p_1 at an altitude of 20.5 km for the Case 1 is plotted in Fig. 2.23. Those correspond to an instantaneous distribution of p_1 while the imaginary part delays 6 hrs to the real one. From Fig. 2.23, the wave is seemed to be stationary along longitude, which confirms the argument done above. However, the region is recognized to move slightly westward as it propagates upward when we investigate the Fig. 2.20. Excluding the stationaly component with m=0, the non-migrating wave in question can be treated as a superposition of both westward and eastward waves as follows

$$P_{1,|m|} = p_{1,m}\exp(i(m\phi + \psi_m)) + p_{1,-m}\exp(i(-m\phi + \psi_{-m})) \tag{2.30}$$

where $p_{1,\pm m}$ and $\psi_{\pm m}$ are, amplitudes and phases of the westward and eastward propagating wave, respectively. When we assume $p_{1,m}<p_{1,-m}$, the equation (2.30) becomes as

$$P_{1,\ m} = 2p_{1,m}\exp(i\alpha_m)\cos(m(\phi+\beta_m)) + p'_{1,m}\exp(-i(m\phi-\psi_{-m})) \ , \tag{2.31}$$

where $p'_{1,m} = -p_{1,m} + p_{1,-m}$,

$\alpha_m = (\psi_m + \psi_{-m})/2$,

$\beta_m = (\psi_m - \psi_{-m})/2$.

The first term corresponds to a standing wave along longitude, while the second one a propagating wave. If $|P_{1,m}|<<|P_{1,-m}|$, $|P_{1,-m}|$, the first term becomes dominant, so that the wave becomes a standing wave, although it moves longitudinally westward at a velocity of β_m. This slight phase variation is attributed to the asymmetries in the distribution of eigenvalues between westward and eastward propagating waves shown in Fig. 2.1. If $|P'_{1,m}|>>|P_{1,m}|$, the wave becomes a propagating one whose amplitude does not vary along longitude. Cases 1 to 5 correspond to the former condition. Case 6 approximately corresponds to the latter case above 30 km, although the standing wave component can be recognized as a superposed fluctuation of p_1 in Fig. 2.20 (d).

As for Cases 3,4 and 5, the vertical scale height of the heat source is different from each other as 10 km, 5 km and 1 km, respectively, although its horizontal distribution is the same. At ground, the distribution of p_1 for Case 5 shown in Fig. 2.21 (b) differs from those for Cases 3 and 4, and it reproduces the heat source distribution better than other two cases. Maximum amplitude of p_1 is approximately 250 N/m^2,

200 N/m^2 and 60 N/m^2 for Cases 3,4 and 5, respectively. Above an altitude of 11 km, a ratio of P_1 among Cases 3,4 and 5 becomes approximately constant value of 15:10:2, and is much different from the ratio at the ground. This is caused by an excitation of the evanescent modes in the heat source reigon. Total energy input is proportional to $H_s T(0)$, so that a ratio of total heat input is 20:10:2, for Cases 3,4 and 5. Only propagating modes seem to be able to reach an altitude of 52.6 km. The amplitude of the propagating modes is not always proportional to the total heat input, but might be connected with the size of equivalent depth relative to the value of H_s. When we examine Fig. 2.22 resemblance in the vertical propagation properties for Cases 3 and 4 can be recognized. Considerable fluctuaiton with small vertical wavelengths is overlapped for Case 5, which is recognized from the phase variation. The horizontal distribution of p_1 resembles each other among Cases 3,4 and 5. Especially, those for Cases 3 and 5 are exactly alike troughout the entire altitude range. As for Case 5, the distribution seems to change steaply, and has small values outside the equatorial region. However, the horizontal distribution of p_1 may be determined by that of heat source, and less related to the vertical distribution of heat source.

The amplification of the forcing function p_1/p_0 from ground to an altitude of 100 km approximately falls in 5×10^2 to 10^3. It becomes large in Case 1 which contains mainly positive modes in comparison with them for Cases 2 and 3, becasue the amplificaiton does not occur in the case of negative modes as is well known. The fluctuation in both amplitude and phase can be explained by an interference of waves with defferent wavelengths [Kato et al., 1981]. Short vertical wavelength is generally seen for the non-migrating tides as shown in Fig. 2.22. This is attributed to the generation of higher order modes by the latitudinally restricted heat source.

Further investigations must be needed to clarify the overall picture of the non-migrating tides by use of knowledge of the actual heat source. This study will be developed if an established model can be achieved on the land-sea differences of the water vapor distribution, eddy diffusion and latent heat release.

Chapter III

KYOTO METEOR RADAR

Section 1. Design Consideration of Kyoto Meteor Radar

Kyoto meteor radar shall be a compact economical system which can provide large amount of data on upper atmospheric winds for statistical analysis. The doppler shift in the observed frequency must be measured to give the radial velocity of the trail with the neutral wind to an accuracy of approximately 0.5 m/sec. Coordinates of meteor echo reflection point must be determined by measuring azimuth and elevation angle, and range. Especially, the height assigned to each trail should be accurate to within 2 km.

The major alternatives of meteor radar are a pulse radar and a continuous wave one. Advantages and disadvantages of the two modes of operation are summerized in Table 3.1. In the case of pulse radar, the signal to noise ratio is smaller than that for CW one, since the receiver is gated open for longer time than the signal lasts. This problem can be gotten off if system installed computer controls receiver gate. In the case of continuous wave radar, the receiving equipment must be sent away from the transmitting site to be able to detect a faint echo whose intensity is much smaller than the transmitted power. The serious disadvantage in continuous wave radar is that it sometimes suffers an interrupt of observation because of interference echo from close range targets, e.g. airplanes. The Kyoto meteor radar was chosen to be a pulsed system for this reason in addition to its simplicity in site location.

Meteor radar is recommended to operate at VHF frequencies in the range 15 to 60 MHz. The radar at lower operation frequency can receive

meteor echo for long interval because the echo duration time is squarely proportional to radio wavelength [e.g. McKinley, 1961]. Further, it can detect short enduring meteor echo at high altitude for the same reason. Below about 15 MHz, strong absorption in the ionospheric D region occurs.

Table 3.1 Advantages and disadvantages of pulse and CW meteor radar

	Pulse radar	CW radar
Transmitter	high peak power (several kilowatts).	peak and average power are equal (a few hundreds watts).
Band width	wide.	narrow.
Doppler shift measurement	--	good resolution.
Ranging	counter.	complicated method with phase moduration.
Interference	--	clutter from close range targets (airplane).
Site location	monostatic.	bistatic.

On the other hand, the height resolution is better for the radar at higher operation frequency because the first Fresnel zone is short. Operation at around 30 MHz is a good compromise in choice of frequency. Kyoto meteor radar operates at 31.57 MHz with half occupying frequency width of 115 kHz authorized by the Ministry of Posts and Telecommunications.

Radar site was settled at Shigaraki (34°51'N, 136°06'E) where tests on radio frequency interference measurements at the frequency of interest before the final site selection proved to be satisfactory: Noise level at the site is -117 dBm in 11 kHz bandwidth at a frequency of interest.

The general techniques of phase coherent pulse doppler radar have been well established by Greenhow and Neufeld [1961] and Muller [1966]. Kyoto meteor radar is a transportable system whose basic design is a duplication of Stanford station [Nowak, 1967; Nowak et al., 1970]. But the detailed circuit is, in general, original. Several modifications

were made to update the system with an improvement in efficiency.

Table 3.2 Characteristics of the Kyoto meteor radar

Site	Shigaraki, Shiga prefecture (35°N, 136°E).
Type	coherent pulse doppler radar.
Items	echo amplitude, range, doppler shift and arrival angles.
Frequency	31.57 MHz.
Peak power	10 kW.
Pulse length	280 μ sec with 10 μ secx28 bits phase code modulation.
Pulse repetition	variable (maximum duty factor of 10%).
Antenna	5-element Yagi.
Dynamic range	50 dB.
Echo height	interferometer/ decay height method.
Computer	radar control and real time data processing.
Remarks	mobile on board a trailer.

Parameters of the Kyoto meteor radar are summerized in Table 3.2. A phase sequenced interferometer [Rudman et al., 1970] was added for attaining good resolution in direction finding of a meteor trail. General purpose small computer was also installed in the system for radar control, and it facilitates effective automatic operation, and real time data processing. A general view of the Kyoto meteor radar is drawn in Fig. 3.1. Instruments except for antennae were taken on board a trailer.

Section 2. Hardware System of Kyoto Meteor Radar

2.1 Block Diagram

The overall diagram of the Kyoto meteor radar is shown in Fig. 3.2. in terms of hardware, we can divide the Kyoto meteor radar into six subsystems; (1) a radar director subsystem, (2) a synthesizer subsystem, (3) a transmitter subsystem, (4) a receiver subsystem, (5) a signal processing subsystem and (6) a computer and peripherals. The signal

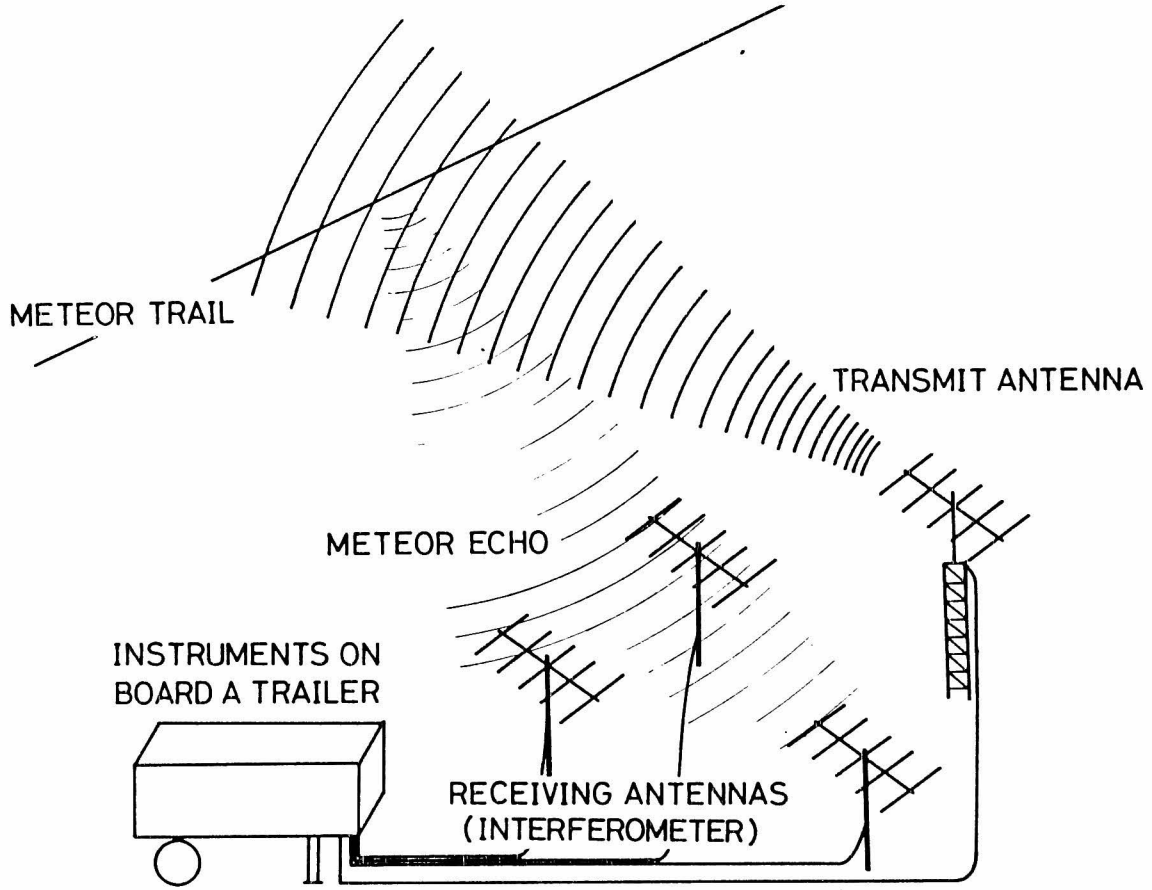

Fig. 3.1 A perspective view of the Kyoto meteor radar.

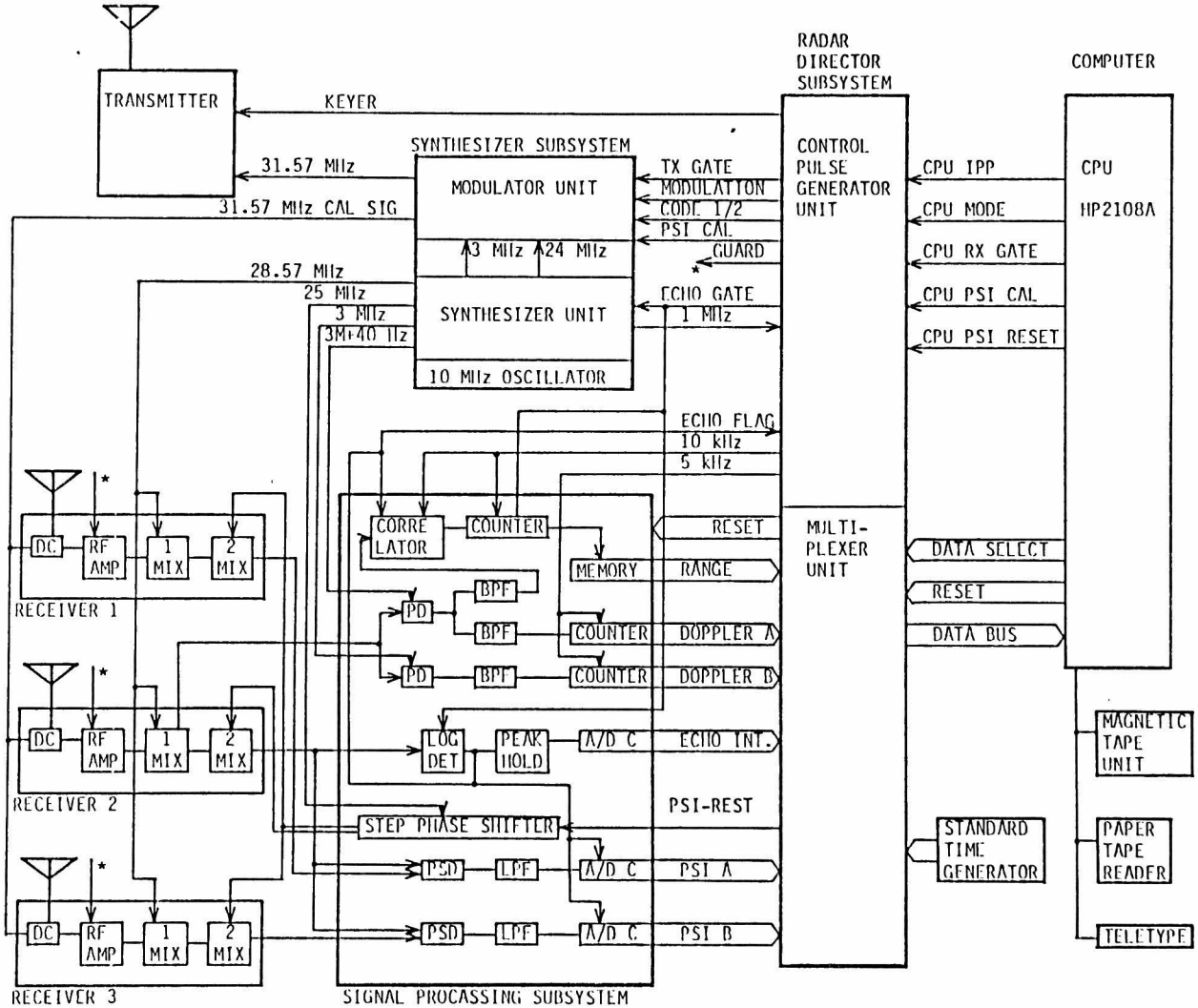

Fig. 3.2 A block diagram of the Kyoto meteor radar.

processing subsystem is further divided into four sections: (5-a) a doppler measurement section, (5-b) a phase sequenced interferometer (PSI) section, (5-c) a ranging section and (5-d) an echo intensity measurement section.

Almost all frequencies for the transmitter and receivers are derived from the synthesizer subsystem, and are phase coherent. Signals for a transmitter keying, phase code modulation of a transmit pulse, and a receiver gate are generated by the radar director subsystem under instruction of the computer. The intermediate frequency outputs and detected signals are fed to the signal processing subsystem, where signals are prepared for entry into the computer for accomplishing real-time data reduction. These subsystems will be discussed individually in the sections which follow.

2.2 Radar Director Subsystem and Computer

The radar director subsystem is composed of a control pulse generator unit and a data multiplexer unit. The control pulse unit generates the timing of an observation which is programmed by software, however, this unit prohibits a time sequence which may give a damage to the radar system by an illegal transmission. According to data select signals, the multiplexer unit controlls traffic of data bus line to the computer from the signal processing subsystem where data are converted to digital values.

Figure 3.3 shows a relation between the radar director subsystem and other subsystems, and meaning of the signals appeared in the figure are summerized below.

CPU-IPP : to produce an inter-pulse period (variable).
CPU-MODE : to modulate the transmit signal by a 28-bit pseudo random code.
CPU-RX-GATE : to control GUARD.
CPU-PSI-CAL : to control ECHO GATE.
CPU-PSI-RESET: to control PSI-START.
1 MHz : to generate a basic 100 kHz clock in the radar director.
RX GATE : to gate the 31.57 MHz transmit signal for the transmitter

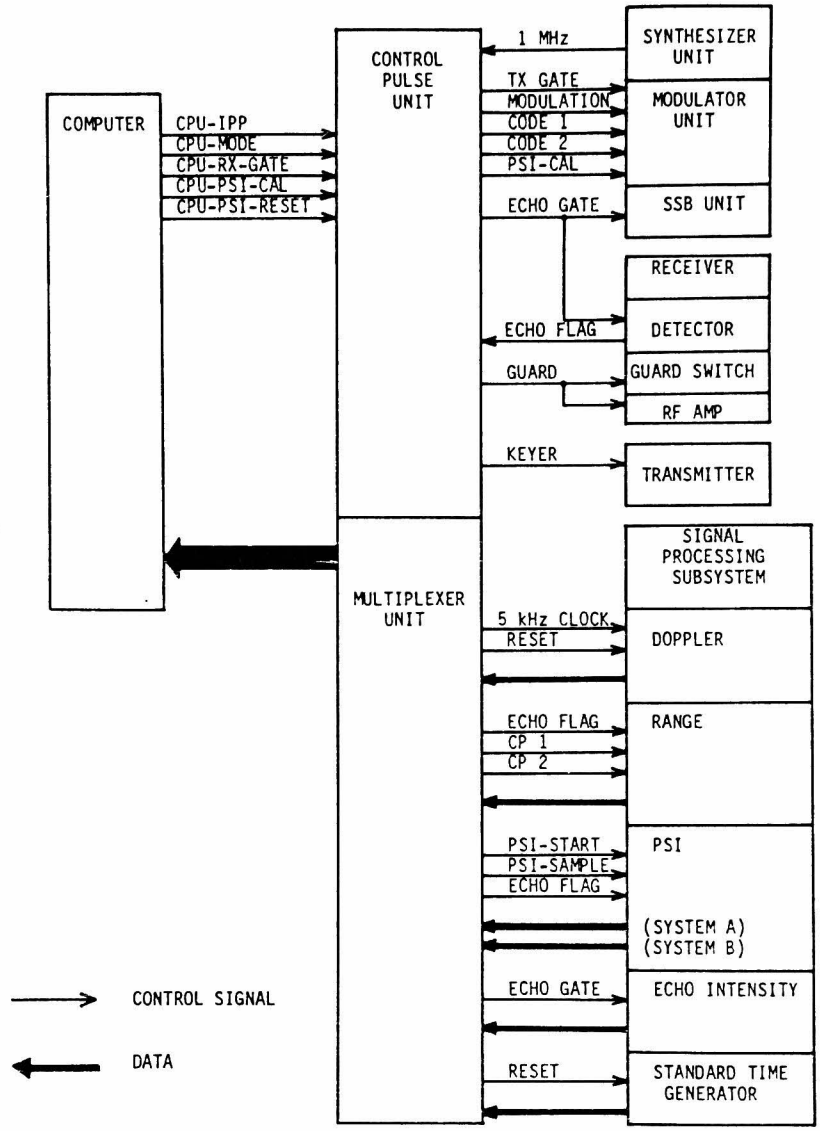

Fig. 3.3 Control signals (thin arrow) and data (thick arrow) exchanged between the radar director subsystem and others.

at the synthesizer subsystem.

MODULATION: to activate a modulator unit in the synthesizer subsystem to generate the 31.57 MHz frequency.

CODE 1/2 : to generate a 28 bit pseudo random code.

PSI-CAL : to gate the 31.57 MHz calibration signal for the receiver at the synthesizer subsystem.

ECHO GATE : to perform blanking of the detector, the echo intensity section and an offset signal unit of the synthesizer to discriminate a received echo from the calibration signal.

GUARD : to perform blanking of the receiver during the transmission pulse.

KEYER : to activate the final stage amplifier of the transmitter.

5kHz clock: to give a clock signal to the doppler counter.

CP 1/2 : to give a 100 kHz clock signal to the range counter.

ECHO FLAG : to be set by a rising edge of the received echo.

PSI-START : to give a synchronous signal for the PSI section every 11 transmissions.

PSI-SAMPLE: to give the sample timing for the PSI section.

A small general purpose computer, Hewlett Packard (HP) model 2108A, is incorporated into the system to supervise the observation and to process data taken by the radar. A 16-bit input-output interface board installed in the computer exchanges control signal outputs and data with the radar director subsystem. A time base generator, HP model 16180A, supplies fundamental time interval for the observation sequence. A magnetic tape unit, HP model 7970B, provides a medium-speed bulk storage with a density of 800 byte/inch for data recording. Other basic peripherals are a paper tape reader, a digital cassette tape recorder and a terminal. A standard time code generator gives BCD codes of Japanese standard time and a reset signal at transition of a day.

2.3 Synthesizer Subsystem

All frequencies exclusive of second stage local oscillator for the receiver are derived from this subsystem by several divisions, multiplications and additions as shown in Fig. 3.4.

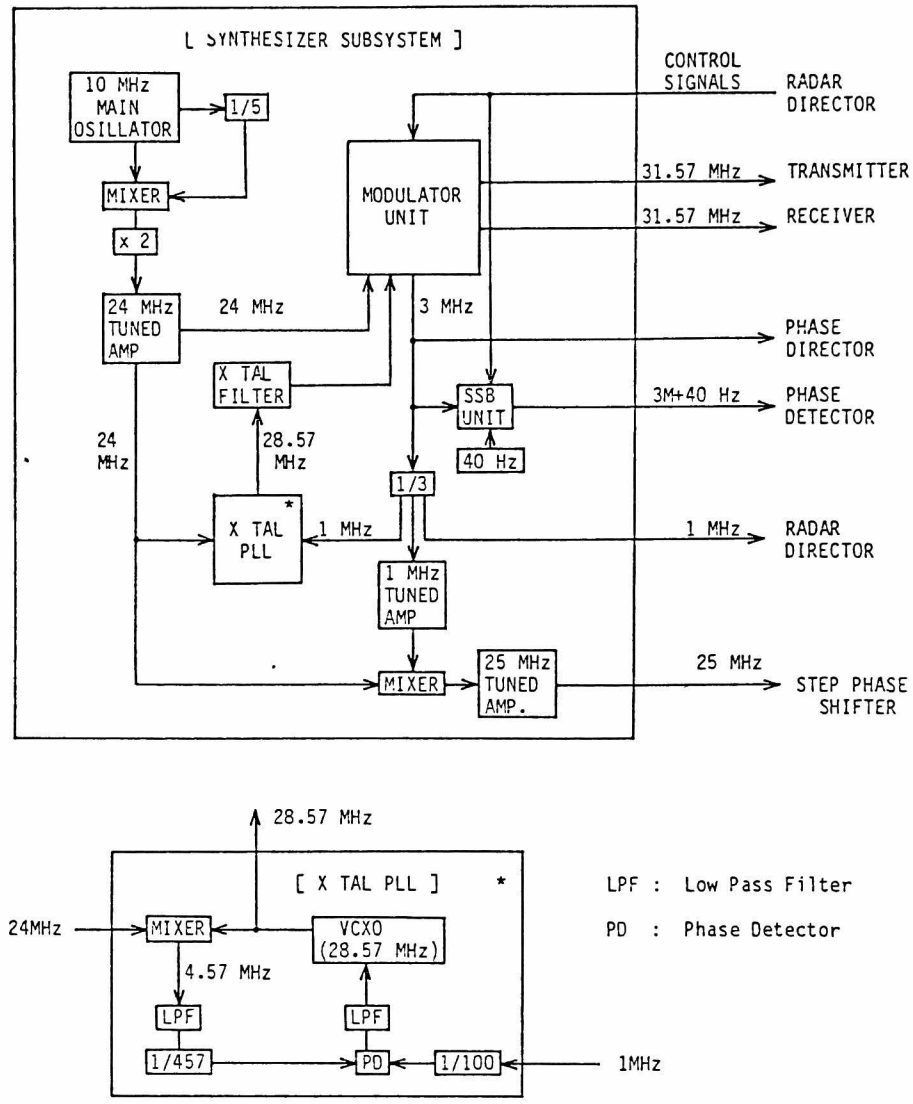

Fig. 3.4 Block diagram of the synthesizer subsystem. Crystal PLL is especially shown bottom.

The main 10 MHz oscillator with oven (HP model 10544B) from which the fundamental 24 MHz signal is produced, is characterized by the high stability of 10^{-11}, and by the high suppression of spurious signals over 50 dB. The required frequencies in the Kyoto meteor radar are listed in Table 3.3.

Table 3.3. Frequencies used in the Kyoto meteor radar

Frequency	Destination	Output level	Objective
28.57 MHz	receiver.	-10 ± 10 dBm	first stage local oscillator.
25 MHz	PSI section of signal processing subsystem.	+ 10 dBm	generation of step phase sifted 2.5 MHz reference signal for phase sensitive detector.
3 MHz 3M+40 Hz	ranging section & doppler section of signal processing subsystem.	+ 7.5 dBm	reference signal.
1 MHz	radar director subsystem.	TTL	clock signal.
31.57 MHz	transmitter.	0 dBm	pulsed CW signal for transmission.
31.57 MHz	receiver.	-50 - -120 dBm	calibration signal for phase sequenced interferometer.

The 1 MHz signal is fed to tuned amplifier and further mixed with the 24 MHz signal by a doubly balanced mixer whose output gives 25 MHz signal through three stage tuned amplifier by using a dual gate FET. The 1 MHz signal is also divided by 100, and multiplied by 2857 to give 28.57 MHz by a crystal-phase-locked-loop with a voltage controlled crystal oscillator as shown in Fig. 3.4. Before utilization, the signal passes through crystal filter with 60 dB attenuation band width of 26.5 kHz before utilization.

Single side band moduration whose block diagram is shown in Fig. 3.5 is applied to generate 3 MHz plus or minus 40 Hz frequency for the reference signal of the doppler measurement. The 3 MHz signal and $\pi/2$ phase shifted signal of it are multiplied by outputs of 40 Hz two-phase oscillator, and are added to generate 3 MHz $\pm$ 40 Hz signal.

The pulsed CW signal at a frequency of 31.57 MHz is produced by multipling the 28.57 MHz by the 3 MHz signal which is phase code modulated when necessary. To avoid interference into receivers, the frequency is intermittently generated during either the transmitter is operated or PSI calibration is made. These timings are controlled by signals MODULATION, TX-GATE and PSI-CAL as shown in Fig. 3.6 from the radar director subsystem. Input signals CODE 1 and CODE 2 decide the polarity of the phase moduration for 3 MHz signal whose phase shift value can be selected with a step of $\pi/4$.

All frequencies were proved to be sufficiently stable for use in the Kyoto meteor radar system. Some output signals of the synthesizer subsystem are passed through buffer amplifier so that interactions between the different frequencies are held to a minimum.

2.4 Transmitter Subsystem

The transmitter subsystem is composed of a transmitter and a transmitting antenna: a horizontally porallized 5-element Yagi Uda antenna. Although its radiation pattern was not measured, the antenna beam width is approximately the same one as a receiving antenna which will be shown later. The antenna is raised at a height of about 16 m, and pointed geographic north with inclination of beam axis at 45° to the horizontal.

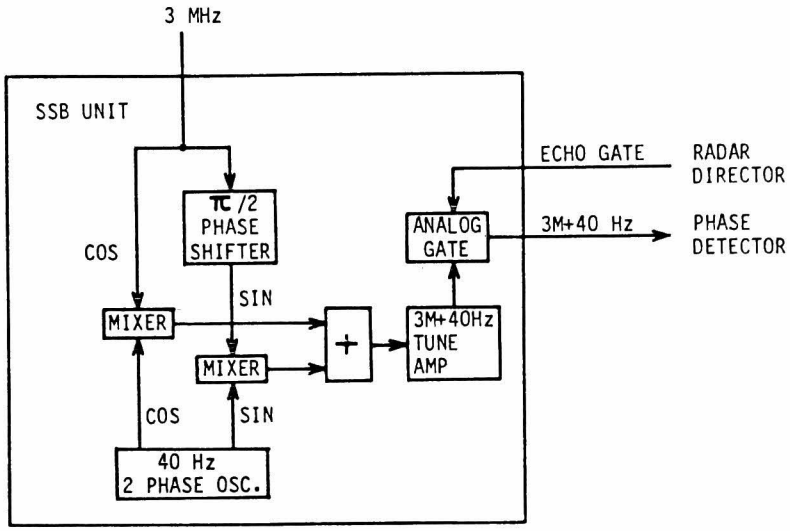

Fig. 3.5 Block diagram of the single side band unit which generates a reference signal for doppler measurement.

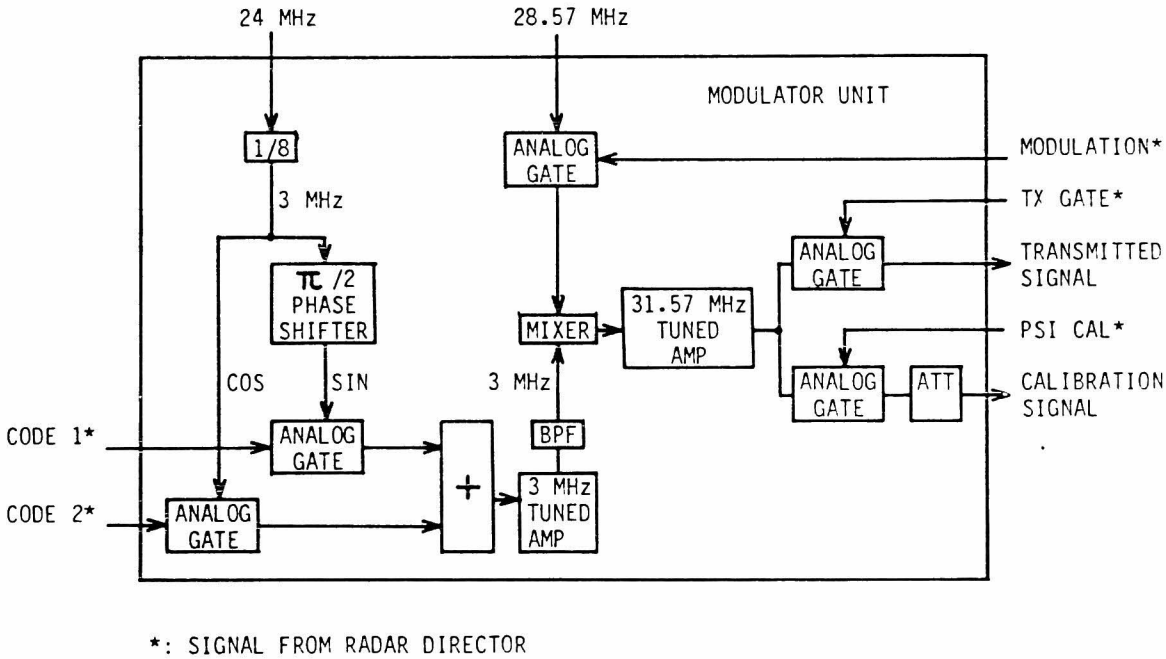

*: SIGNAL FROM RADAR DIRECTOR

Fig. 3.6 Block diagram of the modulator unit.

Illuminating area by the radar at an altitude of 100 km is illustrated in Fig. 3.7.

The transmitter amplifies the 31.57 MHz signal supplied from the synthesizer subsystem through a band pass filter which suppresses the signal outside of 31.57 MHz $\pm$ 115 kHz, the authorized range, as shown in Fig. 3.8. The transmitter is divided into three stages, a solid state linear amplifier with 50 dB gain, a driver and final tube amplifier. A screen grid tetrode is used in the final stage B-class amplifier to radiate nominal peak output of 10 kW. A keyer signal gives a trigger to activate these amplifiers. A transmitted pulse length is 280 μ sec with a maximum duty factor of 10 %. Low pass filter is inserted between the transmitter and the antenna to reject harmonics of the center frequecy.

2.5 Receiver Subsystem

The subsystem is composed of three receivers and three antennae connected to them. The antenna is a five element Yagi-Uda type one whose radiation pattern gives -3 dB half beam width of 30° in horizontal plane, and 35° in vertical plane as shown in Fig. 3.9. A vlotage standing wave ratio was 1.44 that caused miss matching loss of 0.14 dB. Three antennae are arranged nearly orthogonal as shown in Fig. 3.10. Distances of baselines are 9.9 m (1.04λ) and 19.5 m (2.05λ) for east-west and north-south row, respectively. The receiver is divided into six components as shown in Fig. 3.11: a guard switch, a radio frequency (RF) amplifier, an attenuator, a first mixer, a second mixer, a logarithmic amplifier and a detector. Specifications of the receiver is listed in Table 3.4. The signal from the antenna is gated by the guard switch, a high frequency diode switch, to protect the receiver front end from damage during the transmit pulse. The RF amplifier is not activated during the transmit pulse.

Blanking for the detector is achieved to reject the calibration pulse for the PSI, and is controlled by ECHO GATE signal from the radar director subsystem. Output signal of the first mixer is partly fed to the next stage, and partly to phase sensitive detectors in the signal processing subsystem through a buffer amplifier.

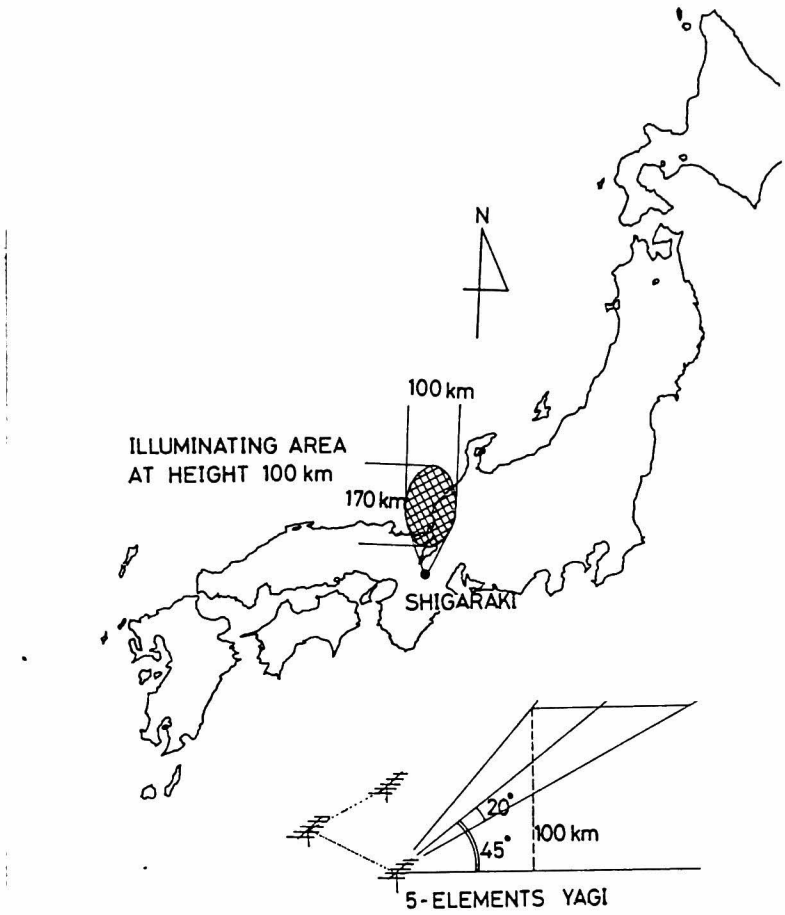

Fig. 3.7 Location of the Kyoto meteor radar station and its illuminating area at an altitude of 100 km.

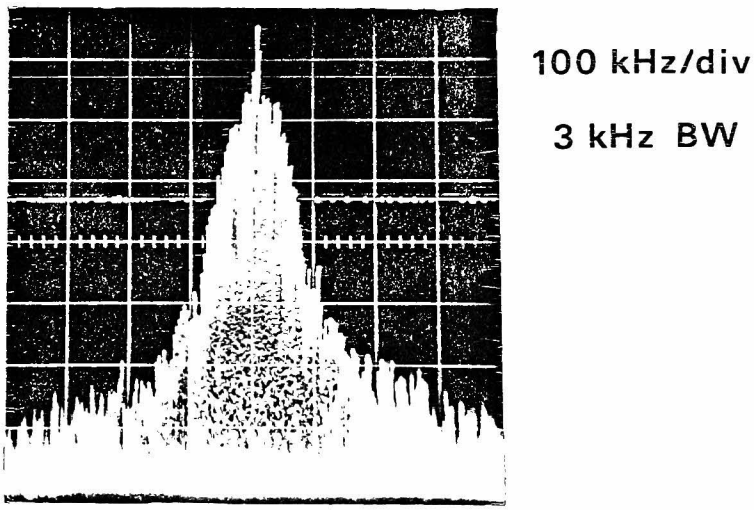

Fig. 3.8 A power spectra of the transmitted signal.

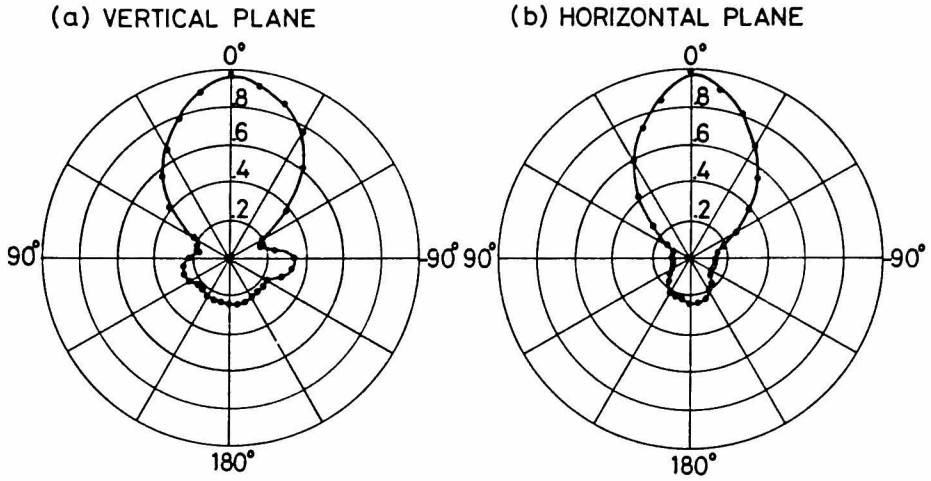

Fig. 3.9 Gain pattern of the receiving antenna. (a): vertical plane. (b): horizontal plane.

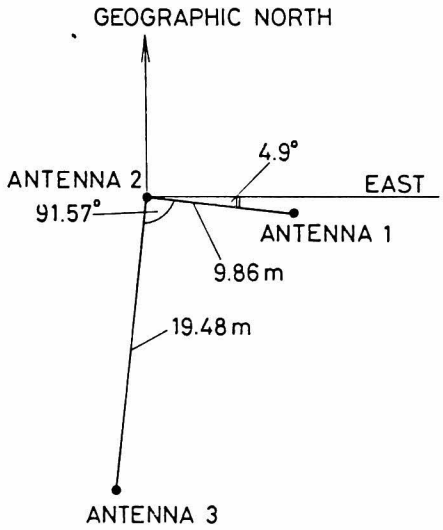

Fig. 3.10 Arrangement of three receiving antennae.

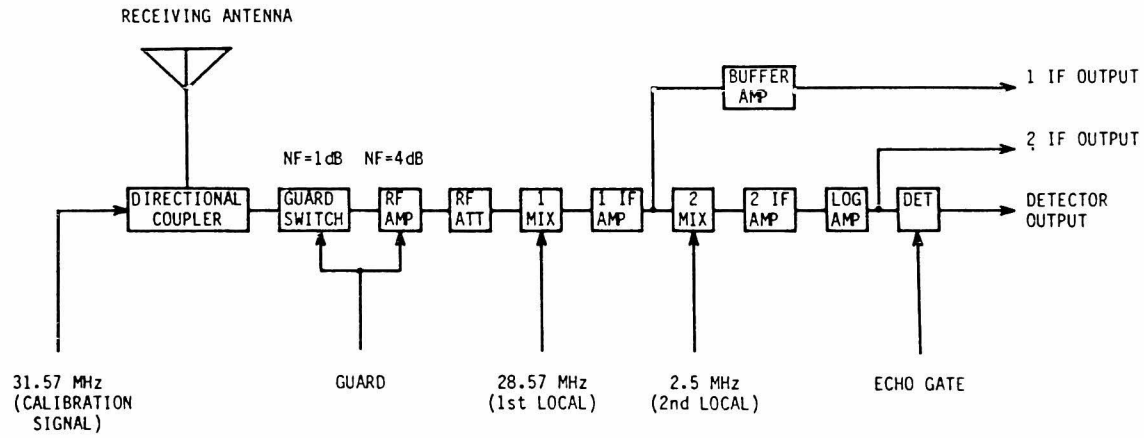

Fig. 3.11 Block diagram of the receiver.

Table 3.4 Characteristics of receivers.

center frequency	31.57 MHz
RF bandnwidth	1.2 MHz
noise figure for the RF amplifier	4.5 dB
first intermediate frequency	3 MHz
second intermediate frequency	500 kHz
IF bandwidth	300 kHz/11 kHz
dynamic range	60 dB

2.6 Signal Processing Subsystem

(1) Doppler section

The received signal frequency f_r is slightly different from the transmitted one because a doppler frequency shift due to meteor trail motion is imposed on reflected radio wave. The amplitude of a radial wind velocity of the trail is related to the doppler frequency Δf as

$$|v| = \frac{\lambda \Delta f}{2} , \qquad (3.1)$$

where λ is a radio wavelength of the transmitted signal. The sense of the radial wind velocity can be detected when the received signal is mixed with a reference signal f_t+f_d, because a residual frequency is above or below f_d depending on the sense of velocity:

$$-(f_t + \Delta f) + (f_t + f_d) = -\Delta f + f_d . \qquad (3.2)$$

This method also has an advantage in determining doppler frequency for short durating echoes because many cycles of the doppler output appear when f_d is chosen large enough. A block diagram of the doppler section is shown in Fig. 3.12 (a). The first intermediate frequency output of the receiver is fed to the phase detector and compared with the reference

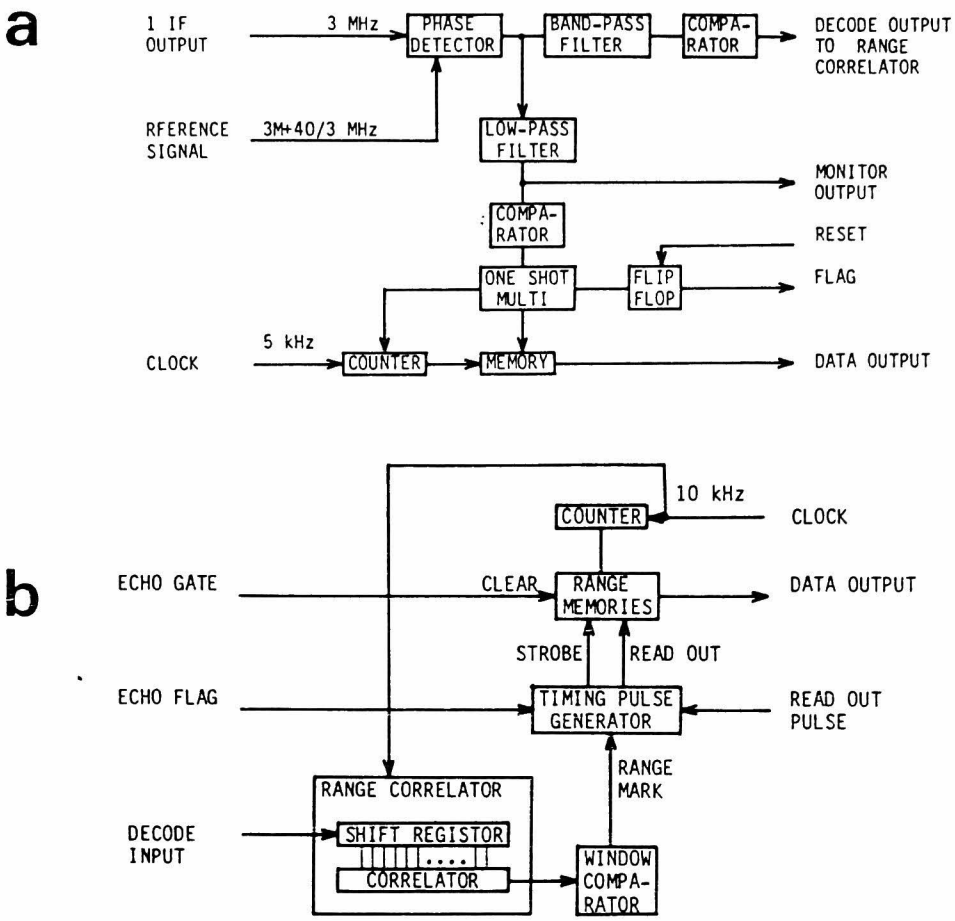

Fig. 3.12 Block diagram of the doppler measurement section (top) and the ranging section (bottom).

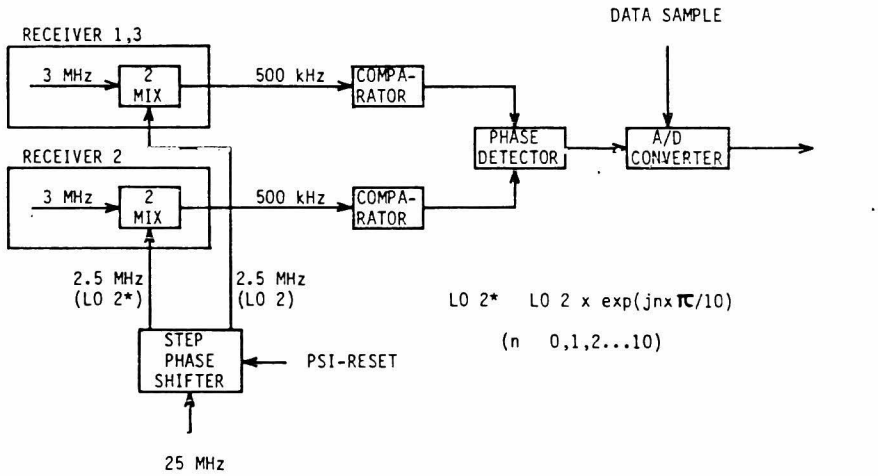

Fig. 3.13 Block diagram of the phase sequenced interferometer.

signal at a frequency of 3MHz + 40 Hz.

The output signal which is a string of samples of the doppler waveform, passes through a low pass filter and further a saturation amplifier. An interval of the phase reversal of the signal is counted with 5 kHz clock, and stored in a temporary memory.

(b) Phase Sequenced Interferometer Section

A radio interferometer technique is incorporated into the system for determining direction of arrival for a reflected echo from phase difference between the signals received at two antennae. We used especially a digitally controlled phase sequenced interferometer originally developed at University of New Hampshire [Rudman et al., 1970].

The second local signal at a frequency of 2.5 MHz for the receiver is generated by a division of the 25 MHz frequency supplied from the synthesizer subsystem as shown in Fig. 3.13. One local oscillator output L_2 has a phase delay to the basic one L_1 from 0 to π with a stepwise of $\pi/10$ as follows:

$$L_1 = \cos(\omega_g t) ,$$
$$L_2 = \cos(\omega_g t + \frac{n\pi}{10}) \; ; \quad n=0,1,2, \ldots 10 , \tag{3.3}$$

where ω_g corresponds to a frequency of 2.5 MHz. Those two local oscillator outputs are individually fed to the second mixer unit of the receivers, which gives the second intermediate outputs S_1 and S_2:

$$S_1 = |S_1|\cos(\omega' t)$$
$$S_2 = |S_2|\cos(\omega' t + \phi + \psi + \frac{11\pi}{10}) \tag{3.4}$$

where ω', ϕ and ψ are 2πx500 kHz, phase difference between the received signals and system phase delay. System phase delay is divided into ψ_1 and ψ_2 which are caused by the receivers and the antenna including a connecting cable, respectively. The phase difference $\phi + \psi + n\text{x}\,\pi/10$ is reduced to zero in a course of 11 transmissions as shown in Fig. 3.14, because n varies from 0 to 10 corresponding to a phase shift of π.

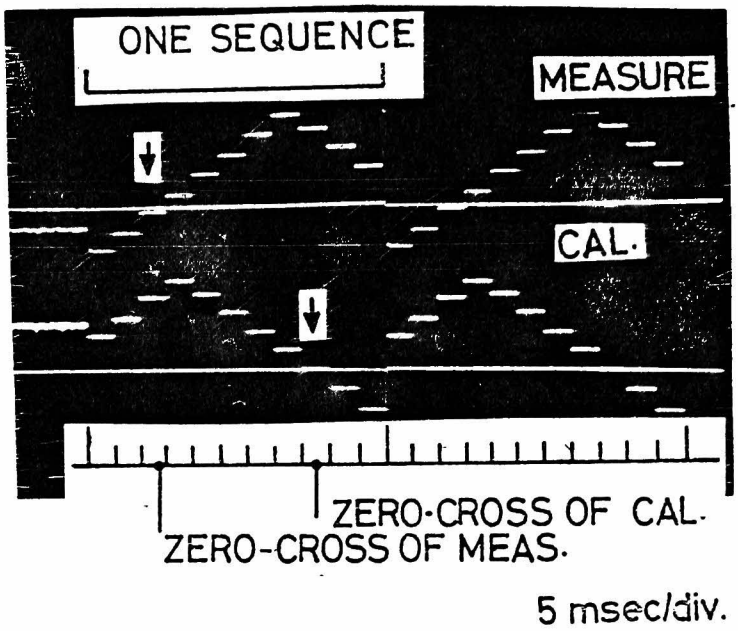

Fig. 3.14 An example of the PSI measurement for both meteor echo and calibration signal.

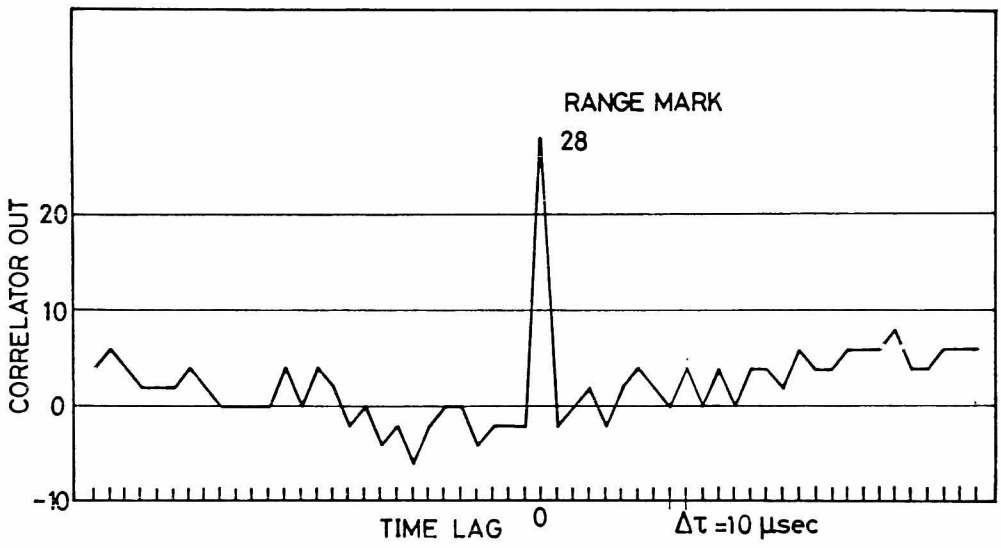

Fig. 3.15 Autocorrelation function of a 28-bit pseudo random code.

A calibration signal fed to the front-end of the receiver at the same phase between transmissions will give phase difference of $\psi_1 + n \times \pi/10$. Since the value, ψ_1, can be measured by a similar manner as mentioned above, the value ϕ due purely to path difference can be determined, when the delay, ψ_2, is measured in advance of the observation.

A timing for data sampling is provided by a rising edge of a received echo before the detection of range value. When range value is measured, the timing can be controlled by the computer.

(c) Range section

Minimum detectability of the radar for the reflected signal is proportional to a multiple of peak power and length of the transmitted pulse according to the fundamental radar equation. On the other hand, the range resolution is inversely proportional to the pulse length. A pulse compression technique, first applied to a meteor radar at Stanford University [Nowak, 1967], is incorporated into our radar, which can conserve range resolution for a long pulse with moderate peak power. The transmitted pulse is phase modulated with a pseudo random code of 28 bits with 10 sec length described as follows:

1110 0111 0000 0010 1010 0100 1001 .

The autocorrelation function of the code, shown in Fig. 3.15 has a single large peak at a time lag of zero. When the received signal is not so much distorted from the transmitted one, the running crosscorrelation between the two signals gives a similar form as that shown in Fig. 3.15.

The output of the phase detector in the doppler section is fed to a range correlator through a comparator as is already shown in Fig. 3.12. A range mark; output of the correlator larger that the threshold value, settle the present value of a range counter to a memory. The range mark is gated by the rising edge of received echo to prevent the correlator from responding spuriously due to noise.

(d) Echo intensity

The output of the logarithmic amplifier is linearly detected, and fed to a peak hold circuit. The circuit is activated during the echo gate is open so as to exclude the calibration signal.

2.7 Antenna Calibration of the PSI

Although the phase difference due to receivers can be measured by using the calibration pulse inserted between succesive echoes, calibration of a system delay from antennae to receivers is essential because the determination of the exact electrical length of the interconnecting cables is difficult. The calibration was carried out by use of a very small 31.57 MHz signal source which was raised up to around 500 m with a captive balloon moored 400 m north-east of the radar. Two trajectries of the balloon are plotted in Fig. 3.16 where a cross point shows the bore-sight of the antenna. Figure 3.17 shows the output of the phase sequenced interferometer against the electrical pass difference calculated from an optical measurements of the signal source using a surveying transit. Two results labeled SYSTEM A and B are plotted corresponding to the two interferometry baselines between antennae 1 and 2, and antennae 3 and 2 as shown in Fig. 3.10, respectively. A 95% confidence region which is defined twice the standard deviation is determined as 0.27 rad. and 0.14 rad. for SYSTEM A and B, respectively, and is plotted as a broken line in Fig. 3.17. Accuracy in measurement of elevation and azimuth angle is plotted as contour lines in Fig. 3.18 (a) and (b), respectively, where horizontal axis is an azimuth angle and vertical axis is an elevation angle. For the practical use the elevation angle can be determined with the standard deviation of 1.0° which corresponds to the representative height resolution of 1.5 km at an altitude of 95 km. As for the azimuth angle, the accuracy is worse than that for the elevation angle, it, however, does not largely affect the system ability.

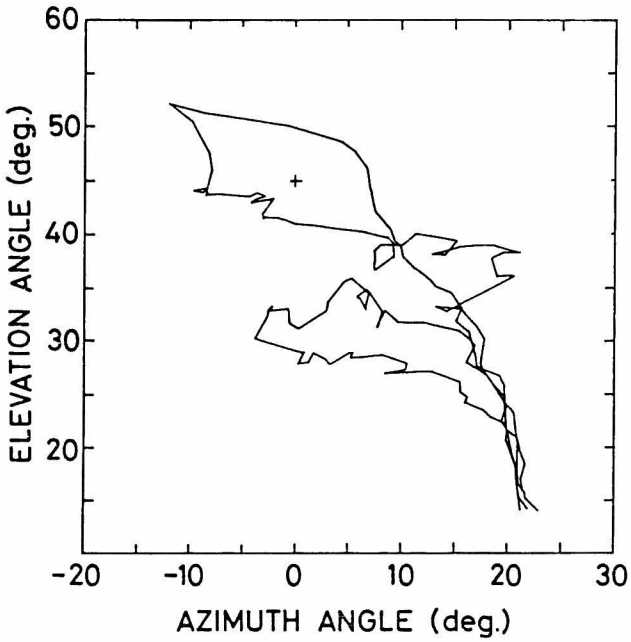

Fig. 3.16 Trajectries of a mooring balloon raised twice for the antenna calibration. A cross symbol corresponds to antenna boresight.

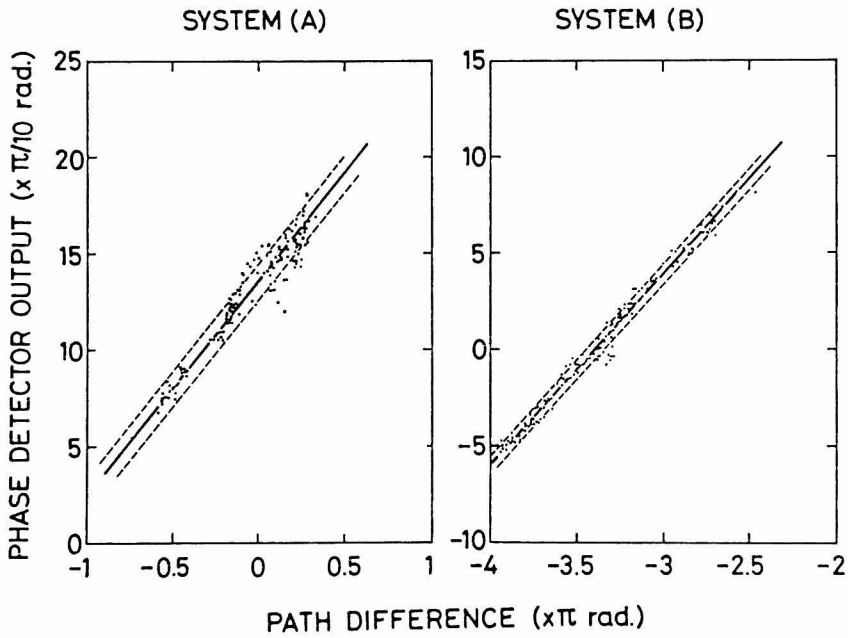

Fig. 3.17 Phase detector output of system A and system B versus electrical path differences. Linearly fitted curve (solid line) and regions of reliance (broken line) are also plotted.

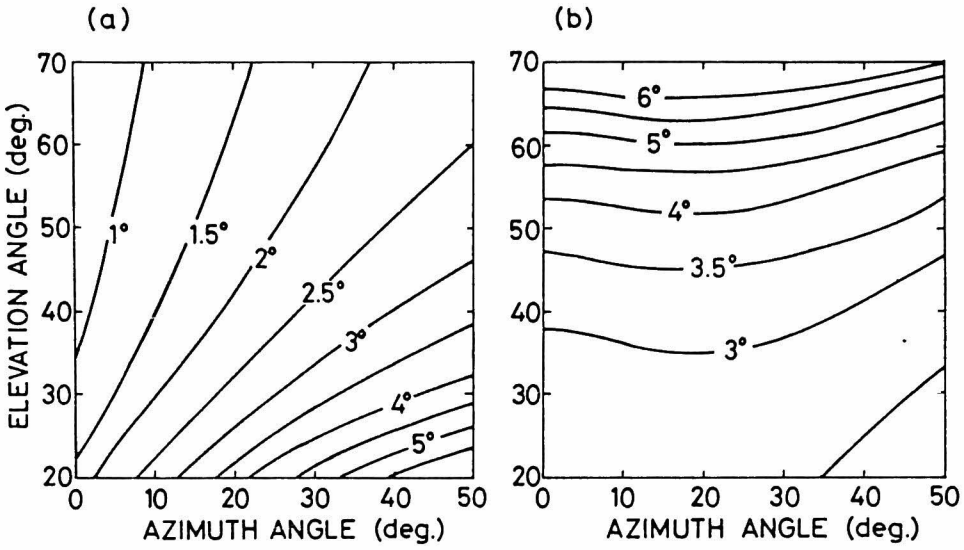

Fig. 3.18 Contour illustrations of accuracies in the measurement of (a): elevation and (b): azimuth angle.

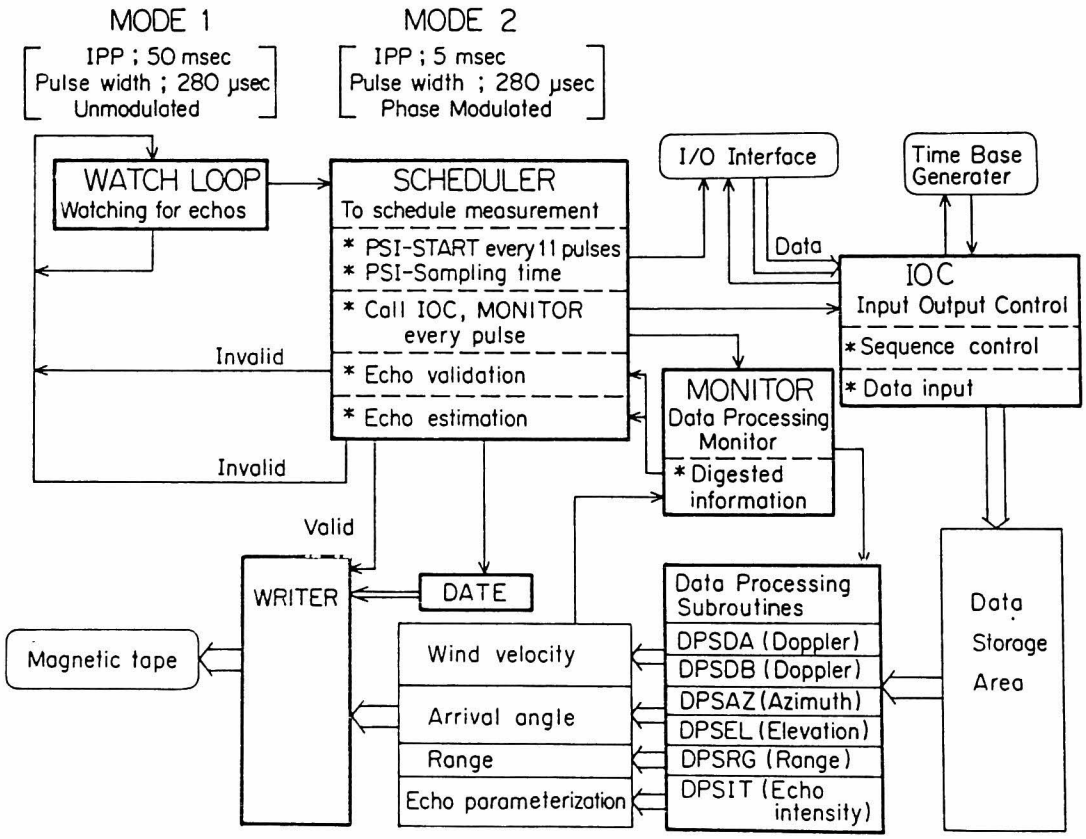

Fig. 3.19 Block diagram of the software subsystem of the Kyoto meteor radar.

Section 3 Software System of Kyoto Meteor Radar

3.1 General Description and Linkage of Programs

This section covers design of a software system for radar control and real-time data processing. The HP2108A computer incorporated into the radar performs an automatic data collection, real time data reduction, echo validation and immediate feedback to the radar operation. The presence of the computer proved of great benefit to the Kyoto meteor radar in making the system efficient and intelligent. Three main improvements are summerized below.

(i) A pulse scheme of the observation such as an inter-pulse period, a receiver gate, etc. is programmable by software, so that they can be easily changed to the purpose.

(ii) Data are collected fully automatically, and are deduced to several physically meaningful values by a real time data analysis.

(iii) Validation and discrimination of received echo are performed by software, therefore insignificant data could be removed before recording on a magnetic tape.

When we detect 5,000 meteor echoes per a day, the substantial observation time is less than one hour, because a duration time of a typical underdense meteor is about 0.5 sec. In addition to the fact, occurrence of a meteor is essentially sporadic, and could not be foreknown. The Kyoto meteor radar is operated in two different modes: mode 1 and mode 2, which correspond to WATCH LOOP and SCHEDULER, respectively. During the mode 1, the radar searchs meteor echo by use of an unmodulated 280 μsec pulse at a low pulse repetition rate (variable but nominally 40 Hz). As soon as an echo is recognized, an operation mode is changed into the mode 2 in which 200 transmissions are usually carried out for data collection with an inter-pulse period of 3.8 msec. This method preserves a transmitter from consumption.

As shown in Fig. 3.19, the software subsystem of the Kyoto meteor

radar is divided into two radar control programs (named WATCH LOOP and SCHEDULER), data collection program (named IOC), monitor program of data processing (named MONITOR), data recording programs (named WRITER and DATE) and data processing subroutines, however, all the programs are organically connected with each other. Each program is written in assembly language which is more effective than a compiler languages such as FORTRAN.

The SCHEDULER instructs IOC to perform radar control and data collection within each transmission. It transfers data from radar hardware to a storage area in the computer, and prepares them for further deduction by data processing subroutines, which calculates pertinent parameters for each echo. Real time data processing is done not only for data condensation, but utilizing reduced data for immediate feedback to radar control. The SCHEDULER is informed of quick check for each echo from MONITOR which supervises data processing subroutines, and discriminates a meteor echo from noises or an echo from an airplane. When it failed to detect a valid meteor echo, SCHEDULER returns the radar control to WATCH LOOP. Otherwise, data are recorded on a magnetic tape by WRITER with meteor occurrence date determined by DATE.

In advance of the observation, performance check of the system is carried out by the program DATE. Detector outputs for calibration signals and noise level are written in the headder record on the magnetic tape together with condition of observation such as date and system confirmations. Dating of a file on a magnetic tape is performed by DATE. In the following subsections, radar control programs and real time data processing subroutines are described individually.

3.2 Radar Control Programs

As is already shown in Fig. 3.3, the computer provides various control signals to the radar director subsystem according to a timing given by the time base generator. Figure 3.20 shows an example of observation sequence and a timing within one basic interval of WATCH LOOP. A transmitted pulse is not phase modulated, because a precise range determination is meaningless for a search of a meteor echo occurrence. Receivers are gated open for all possible echo delay. When

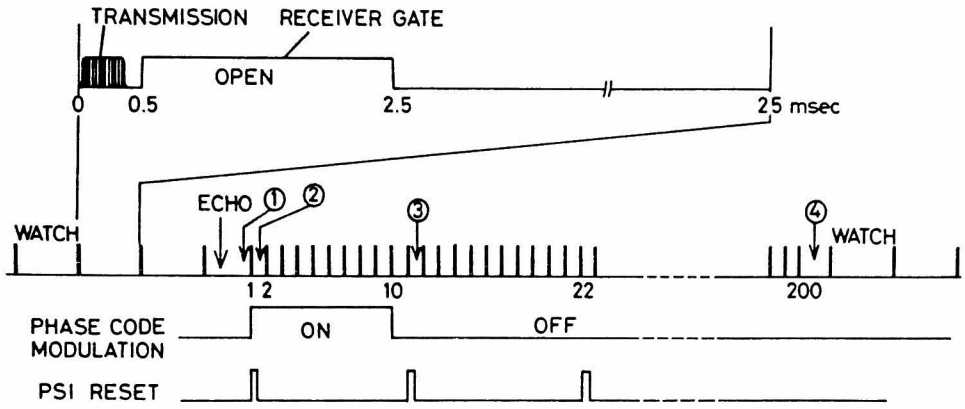

Fig. 3.20 A pulse scheme of WATCH LOOP (top) and an example of echo measurement (bottom). (1): to initialize subroutines and reserve storage area. (2): to activate MONITOR. (3): echo validation by range and echo amplitude. (4): final echo validation and recording.

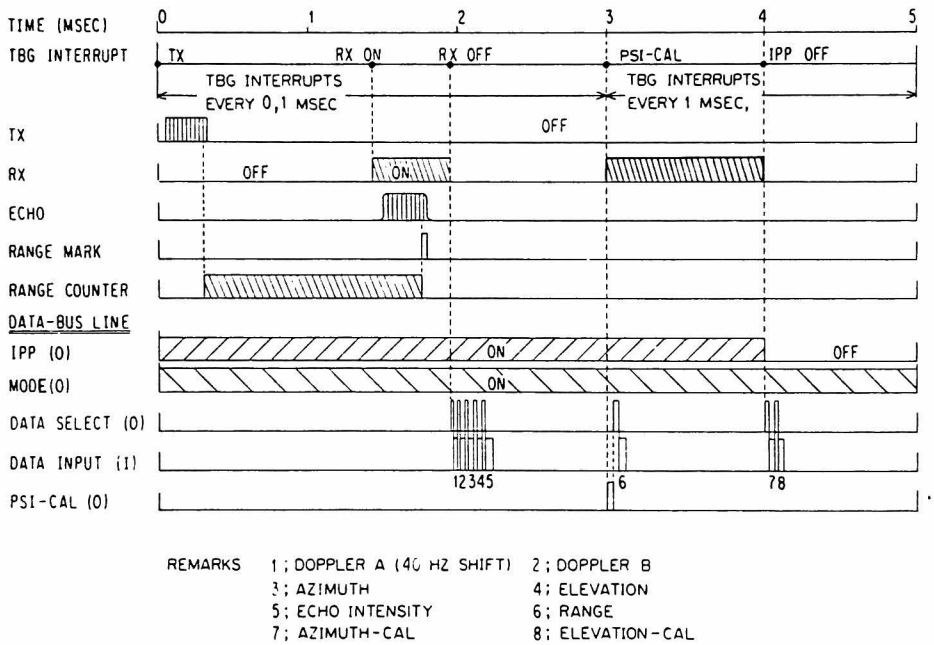

Fig. 3.21 A pulse scheme of measurement during one transmission in mode 2 controlled by IOC. Inter pulse period is variable, but is representatively set equal to 5 msec.

it failed to detect any significant echo during this interval, WATCH LOOP loops back and repeats its routine with an inter-pulse period of 25 msec. To the contrary, when a received echo intensity exceeds the threshold, WATCH LOOP hands over the radar control to SCHEDULER.

At first, SHEDULER initializes the associated programs used in the mode 2, and reserves storage area for data collection. The SCHEDULER usually transmits 200 pulses within one measurement, and the earlier ten transmissions are phase modulated by a 28-bit pseudo random code for a precise range measurement. Within one inter-pulse period, IOC controls receiver gating, calibration signal output and data acquisition as shown in Fig. 3.21. At every 11 transmissions, the PSI starts arrival angle measurement. After the first transmission, SCHEDULER activates MONITOR which searches for unprocessed data in the storage area, and assigns them to the appropriate programs when necessary. Thus, MONITOR supervises the data processing subroutines and transfers digested data to SCHEDULER for echo validation. After ten transmissions, those informations are criticised on two points: (i) if the range value is determined, and (ii) if three subsequent echoes for the earlier transmissions exceed the noise level. The measurement is continued for a valid echo, otherwise the radar control is returned to the mode 1; search mode. So that, only qualified data are recorded on a magnetic tape by the program WRITER. The recording stops observation for a few tens of mili-second.

The range value is utilized for making the receiver gate narrow enough to aim at the echo, so that the signal to noise ratio of the doppler measurement can be improved. It is also used to indicate a data sample timing at the phase detector of the PSI.

3.3 Real Time Data Processing Programs

The raw data collected by the radar are the received echo intensity, the interval of a half wave of the doppler signal counted by the 5 kHz clock, sequences of eleven phase differences for both the received signal and the calibration signal measured by the PSI and the range value counted by the 100 kHz clock. The real time data processing subroutines corresponding to those raw data execute their task concurrently with the observation. Those subroutines deduce physically meaningful data such

as the wind velocity, the elevation and azimuth angle, the range and echo morphology for each echo until the end of the measurement. Procedure done in the subroutine is described below.

Doppler Measurement: Error in the measurement is attributed to both noise and quantamization by the digital clock. Effect of the noise can be reduced by taking an average of the doppler counter outputs weighted by an echo intensity, because the signal to noise ratio rapidly decreases with time. On the other hand, the quantamization is removed by a coherent integration over prolonged period of time with eqaul weight. There is a compromise that the weighting function may be constant during large S/N, and proportional to the echo intensity for smaller signal to noise ratio echo.

Figure 3.22 shows a relation between the doppler counter output and the radial wind velocity. Because the reference frequency is shifted by 40 Hz, a plus and minus doppler frequency is converted asymmetrically as a broken line in Fig. 3.22. Without the additional frequency shift, the doppler frequency would be detected as a solid line in Fig. 3.22. For a practical use, the doppler frequency is expected to be confined within 20 Hz which corresponds to a maximum wind velocity of 100 m/sec.

Phase Sequenced Interferometer: One sequence of the PSI measurement is made of eleven data for phase difference detected by a phase comparator. Two sequences are carried out simultaneously for both received echo and calibration signal, respectively. The data sequence corresponds to half period of a triangular wave signal, and is shown, for an example, as a full circle in Fig. 3.23. Those are phase-reversed and added succeeding to the original data shown as an open circle in Fig. 3.23. Zero crosses are determined from a linearly fitted curve for the whole data, and an average of them is calculated for eighteen sequences of measurements. Taking account of the antenna configuration shown in Fig. 3.10, an azimuth angle, ϕ, and an elevation angle, θ, can be calculated from ψ_{12} and ψ_{32} which are the phase differences from the antenna 1 and 3 to the antenna 2, respectively, calculated by using the relation (3.4).

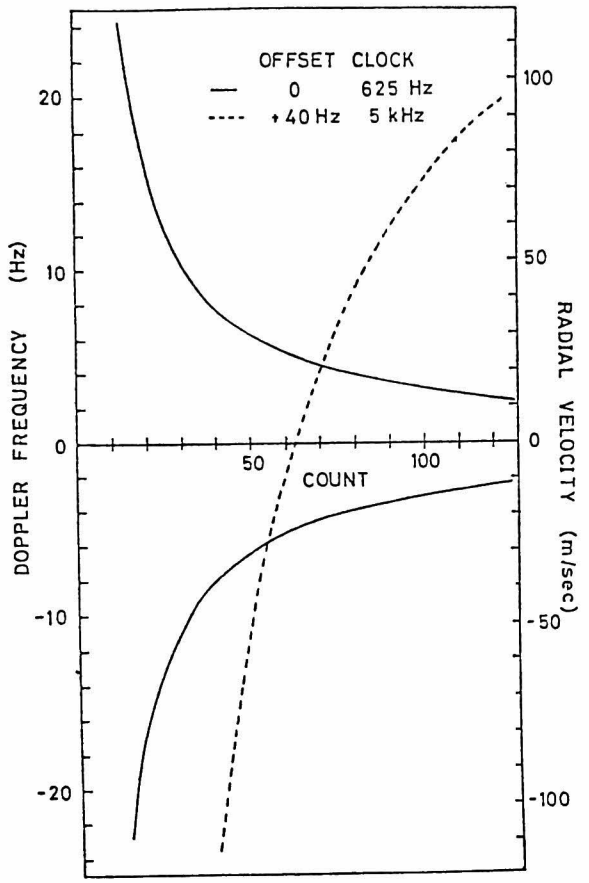

Fig. 3.22 Relation between doppler counter output and radial wind velocity. Solid and broken line corresponds to output with reference signal at 0 Hz and 40 Hz offset, respectively.

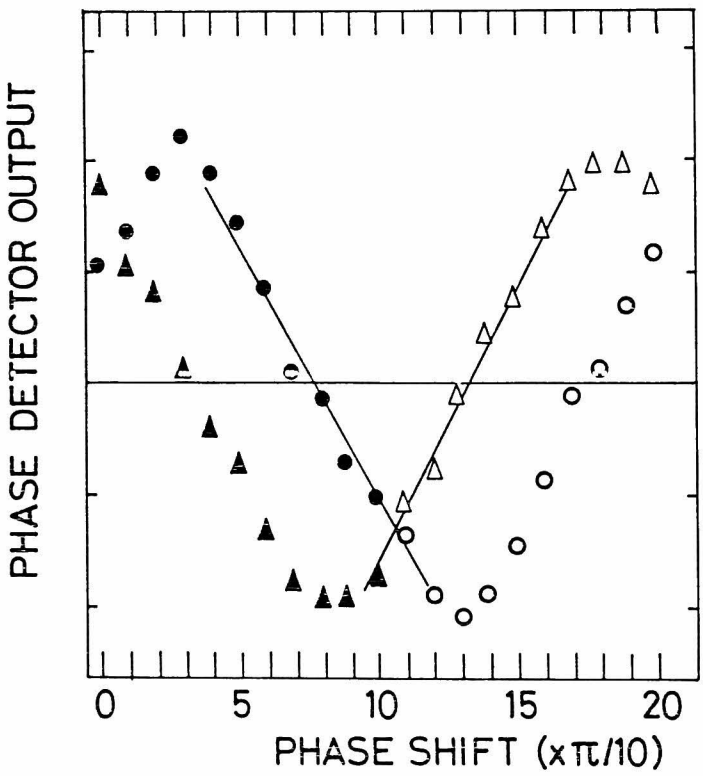

Fig. 3.23 Determination of phase difference. A full circle and a full triangle symbol corresponds to measurement and calibration, respectively. An open symbol indicates the phase reversed value of the original data. Solid lines are fitted by the least mean square method.

$$\phi = \arctan\left(\frac{-\cos a}{\frac{g_1\psi_{32}}{g_2\psi_{12}} + \sin a}\right) + b \ , \tag{3.5}$$

$$= \arccos\left(\frac{\sqrt{(g_2\psi_{12})^2 + (g_1\psi_{32})^2 + 2\sin a\, g_1 g_2 \psi_{32}\psi_{12}}}{2\pi g_1 g_2 \cos a}\right) \tag{3.6}$$

where a=1.57°, b=4.9°, g_1=1.04 and g_2=2.05.

Range Measurement: When received echo can reproduce the complete 28 bit pseudo random code, the crosscorrelation of the two has a single range mark with amplitude of 28 as shown in Fig. 3.15. Phase reversal at any one bit causes a decrease in amplitude of range mark by two, and moreover grows spurious peaks. If the noise has a constant r.m.s. value at an amplitude and a random phase, the signal at phase ϕ overwhelms the noise at probability described below

$$P_0 = \arcsin\left(\frac{2\sin\phi}{A\pi}\right) \quad ; \quad \sin\phi < A \tag{3.7}$$

$$= 1 \quad ; \quad \sin\phi > A \ ,$$

where A is the ratio between amplitude of the noise and the signal. By taking an average of P_0 with ϕ, expected value for the probability becomes

$$P_1 = \left(\frac{2}{\pi}\right)^2 \int_0^{\pi/2} \arcsin\left(\frac{\sin\phi}{A}\right) d\phi \tag{3.8}$$

Because the noise produces either code at equal chance, the phase reversal at any one bit occurs at probability of

$$P_2 = \frac{1-P_1}{2} \tag{3.9}$$

In 28 bit code, N bits of error can be brought about at probability of

$$P_3 = {}_{28}C_N(1-P_2)^{28-N}P_2{}^N \qquad (3.10)$$

Generally, the true range mark has an amplitude larger than ten, when the signal to noise ratio is 2 dB. Single trial for range measurement can determine the value, if only one range mark exceeds the threshold of range correlator. When the S/N is poor, several measurements must be repeated for integration.

Echo Inetensity: Variation of echo intensity with time is utilized to discriminate meteor echoes from noises and echoes reflected by the ground objects. Criteria for meteor echo recognition are deduced empirically with the help of theoretical investigation which will be described in the next chapter. An underdense meteor echo which is appropriate for our purpose is characterized by an abrupt increase of echo intensity during the meteor trail formation and a successive slow decrease while the trail diffuses. One of the most conspicuous feature of the underdense meteor echo is that its intensity decreases exponentially at a constant decay rate which is inversely proportional to the diffusion coefficient at the reflection point. Spurious echoes from near range objects and overdense echoes do not vary as described above, so that are easily descriminated. When a received echo suffers a fading due mainly to multiple reflection by a single trail, the echo in question is not taken into account, because the measured doppler frequency does not give a correct value. Sometimes, intense signals are refelected from the ionosphere; especially from the sporadic E layer, but those can be easily recognized because of heavy fading.

Although our morphological separation of echoes is simple, discrimination of meteor echoes is fairly well achieved. The decay rate for underdense meteor echo is calculated for an additional height determination of the altitude by using the decay height method.

CHAPTER IV

BASIC FEATURE OF OBSERVATION

Section 1. Radio Wave Scattering by Meteor Trails

Physical processes in the meteor trail formation and the radio reflection have been extensively studied by a number of authors [e.g., McKinley, 1961]. Most of optical and radio observations have been satisfactorily explained by a fairly simple theoretical models, although it is difficult to calculate the meteor echo for the general case. Characteristics of a radio meteor echo are mainly attributed to the ionization density of the meteor trail and the radio wavelength, and secondarily to some modifying effects such as meteor trail distortion, irregular distribution of electrons in the trail and a polarization of the radio wave relative to the meteor trail.

An incident meteor is heated up by an interaction with the earth's atmosphere at 80 to 110 km region, so that meteoric atoms are ablated, and ionize air molecules. Thus, a long cylindrical trail is left in the passage of the meteor. Eshleman [1957] gave a distribution of ionization electron line density q_e at height h as

$$q_e = q_{max}\, 2.25 \exp\left(\frac{h_{max} - h}{H}\right)\left[1 - \frac{1}{3}\exp\left(\frac{h_{max} - h}{H}\right)\right]^2 , \quad (4.1)$$

where q_{max} and H correspond to maximum value of q at h_{max} and the atmospheric scale height, respectively. From the viewpoint of kinetic theory, an initial radius, r_o, of a meteor trail was estimated as 14 ionic mean free paths by Manning [1958] by assuming thermal equilibrium between the meteor trail and the surrounding atmosphere. Greenhow and Hall [1960],

however, reported the initial radius is significantly larger than the value. After the formation of the trail, it expands radially by diffusion in a relatively slow manner being controlled by an diffusion equation as follows

$$\frac{dN}{dt} = \frac{D}{r}\frac{d}{dt}(r\frac{dN}{dr}) \quad , \tag{4.2}$$

where N, t, r and D are volume electron density, time, radius and ambipolar diffusion coefficient, respectively. When we assume that the trail is formed at t=0 with initial radius r_0 and electron line density q, the equation (4.2) can be solved with respect to N, whose radial distribution becomes Gaussian:

$$N(r,t) = \frac{q_e}{\pi(4Dt+r_0^2)} \exp(-\frac{r^2}{4Dt+r_0^2}) \tag{4.3}$$

It is convenient to classify meteor echoes into two types; underdense trails and overdense trails, according to that the electron line density is larger or smaller than 10^{14}/m respectively.

Overdense Echo: As for the overdense trail, the incident waves are prevented from penetration into the trail because its frequency is lower than the critical frequency of the plasma corresponding to the electron density of the trail. The radio reflection by the overdense trail can be treated as one from a metallic column with a radius r_c which is defined that dielectric constant is negative within it, so that

$$r_c = \sqrt{4Dt+r_0^2}\ \ln(\frac{q_e\lambda^2 r_e}{2\pi^2(4Dt+r_0^2)}) \quad , \tag{4.4}$$

where r_e is the classical radius of the electron. The maximum value of r_c is attained as $(q/\pi N_c e)^{1/2}$ at $t_{max} = (q\lambda^2 r_e/(\pi^2 e) - r_0^2)/4D$. By assuming the cross section $\pi R_0 r_c$ of metallic column at a range R_0,

received power at t_{max} is estimated as

$$P_r = \frac{P_t G^2}{64\pi^3} \sqrt{e}\left(\frac{\lambda}{R_0}\right)^3 \sqrt{r_e q_e}$$

$$= 1.6\times10^{-11} P_t G^2 \left(\frac{\lambda}{R_0}\right)^3 \sqrt{q_e} \quad (W) \tag{4.5}$$

Duration time T_{ov} for the overdense echo is defined as an interval up to when the radius r_c becomes zero from trail formation, and is proportional to q_e as follows:

$$T_{ov} = \frac{q_e}{4\pi N_c D} - \frac{r_0^2}{4D} = \frac{q_e}{4\pi N_c D} - \frac{q_e^2 r_e}{4\pi^2 D} \quad . \tag{4.6}$$

The electron line density does not affect largely on maximum received power, but on the duration time of echo. Manning [1953, 1963] estimated overdense echo strength by ray-path calculation which was only 0.7 of the above result.

Underdense Echo: In the case of underdense trail, the electron density is so low that the radio wave penetrates the trail, and each electron in the trail reflects incident radio wave independently at a scattering cross section of

$$\sigma_e = \frac{\mu_0^2 e^4}{16\pi^2 m^2} \quad , \tag{4.7}$$

where μ_0 and m are magnetic permeability of air and electron mass, respectively. By using a conventional radar equation, the received power by each electron is represented by a formula

$$\Delta P_r = \frac{P_t G_t}{4\pi R^2} \frac{\sigma_e}{4\pi R^2} \frac{G_r \lambda^2}{4\pi}$$

$$= \frac{P_t G_t G_r \lambda^2 \sigma_e}{64\pi^3 R^4} \quad , \tag{4.8}$$

where P_t, G_t, G_r and R are transmitted power, transmitting antenna gain, receiving antenna gain and range, respectively. By integrating equation (4.8) for all electrons in the trail, we could get the received echo. When we assume an instantaneously formed infinitely long cylindrical trail, we then obtain the expression for received power at t=0 as

$$P_r = \frac{P_t G_t G_r \lambda^3 \sigma_e}{128\pi^3 R_0^3} q_e^2 \frac{C^2+S^2}{2}$$

$$= 2.5\text{x}10^{-32} P_t G_t G_r (\frac{\lambda}{R_0})^3 q_e^2 \frac{C^2+S^2}{2} \tag{4.9}$$

The scattering of radio wave by a meteor trail can be regarded as specular reflection. The value $(C^2+S^2)/2$ may be reduced to 1, when the integration is done for a few Fresnel zones to which most of energy of reflected wave is attributed.

The echo intensity will be reduced by the radial diffusion of electrons in the trail. Reflected power from each electron whose distribution has already described in the equation (4.3) must be summed while taking proper phase relations of these contributions. The underdense echo intensity decays exponentially as

$$\frac{P_r(t)}{P_r(0)} = \exp(-\frac{32\pi^2 Dt}{\lambda^2}) \tag{4.10}$$

and, a decay time constant T_{un} is defined as $\lambda^2/(32\pi^2 D)$. Height of echo reflection point can be inferred by comparison between the measured decay

constant of the received signal and a prepared calibration curve of the ambipolar diffusion coefficient. This procedure called decay height method will give an echo height to an accuracy of several kilometers.

Considering the finite initial radius r_0 of a meteor trail, we must take into account an extra attenuation factor of $\exp(8\pi r_0^2/\lambda^2)$ to $P_r(0)$, which is equivalent to a shift in the time scale. Figure 4.1 illustrates variations of the underdense echo intensity along time for several occurrence heights, where height dependence of the ambipolar diffusion coefficient was assumed to vary with height as

$$\log_{10} D = 0.067\ h - 5.6 \quad \text{[Greenhow and Neufeld, 1955]}. \qquad (4.11)$$

Other parameters used in the calculation are as follows: $q = 10^{14}$ /m, $P_t = 10$ kW, $G = 10$, $\lambda = 9.502$ m, $\sigma_e = 9.98 \times 10^{-29}$ m^2, $R = 150$ km. The attenuation of echo intensity by the initial radius of the trail is considered [Manning, 1958].

Typical time-intensity profiles observed by the Kyoto meteor radar are shown in Fig. 4.2 for the overdense echo; (a) and (b), and for the underdense echo; (c) and (d). Vertical axis is echo intensity plotted in logarithmic scale, and the horizontal axis is time. After the formation stage of a meteor trail, the overdense echo almost maintains its initial intensity while decreasing it gradually. After this duration of intense echo, the overdense echo suddenly disappears as theoretically expected [McKinley, 1961]. As for the underdense echo, the decrease of echo intensity can be fitted by a straight line, which suggests an exponential decay of the echo. By using the relation (4.11) an altitude of the underdense meteor trail can be deduced from decay constant, and is higher for the echo in Fig. 4.2(c) than that in Fig. 4.2(d).

Although meteor echo properties can be basically understood by the simple model described above, a more detailed picture of them will be recognized by including some modifying effects. When we think better of the trail formation, a meteor trail becomes conic because of a delay in trail diffusion due to finite meteor velocity. In addition, large

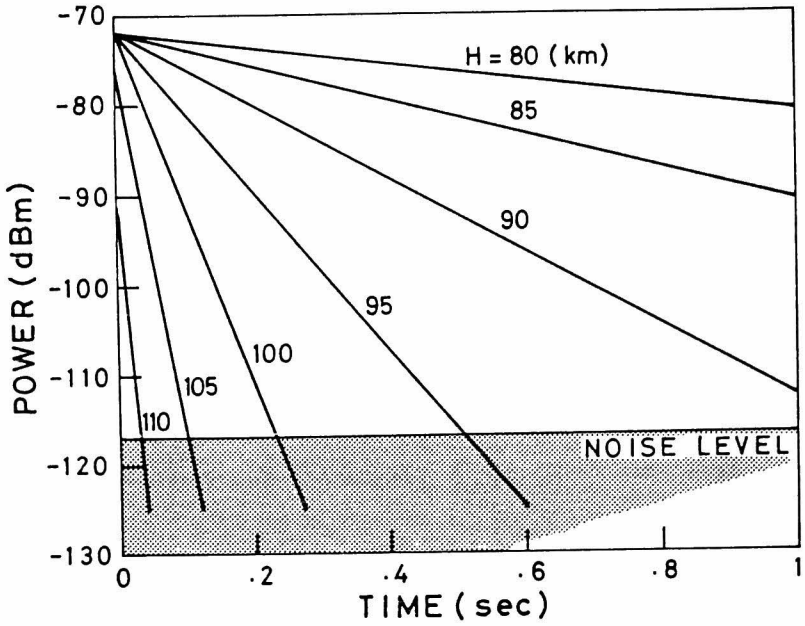

Fig. 4.1 Theoretical variation of echo power with time based on typical radar parameters as outlined in the text.

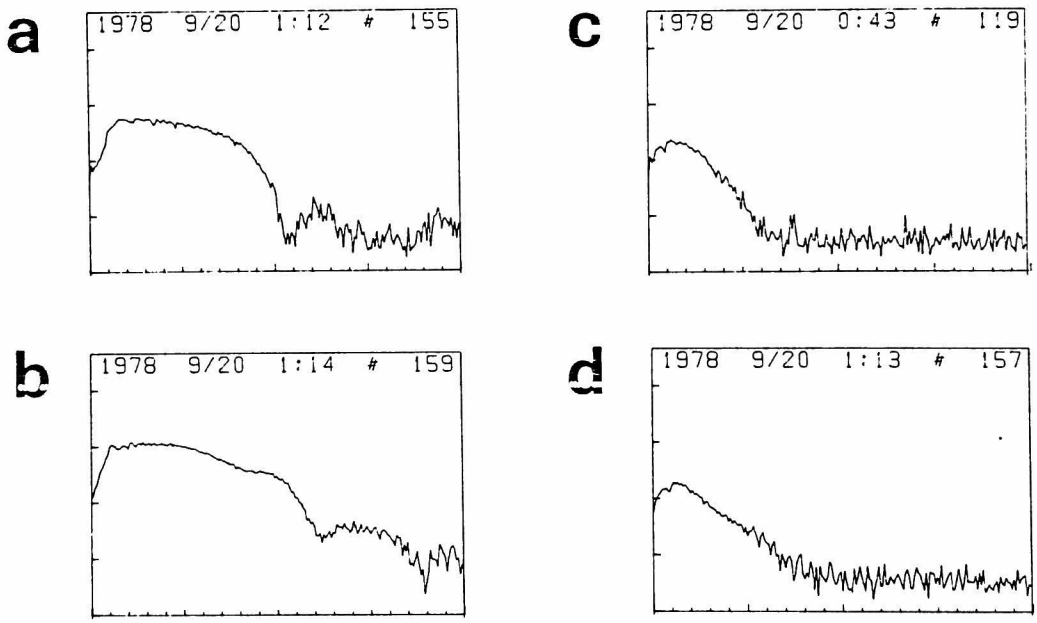

Fig. 4.2 Amplitude variation for various radar echoes. (a) and (b): overdense echo. (c) and (d): underdense echo.

altitude variation of both diffusion coefficient and initial radius of a trail will further taper off the meteor trail. These cause no large revision in received echo power from the fundamental simple model [McKinley, 1961]. Atmospheric winds inclusive of small scale wind shear and turbulence can distort the initially straight trail. Such distortions will modify the echo properties by giving rise to a superimposed fading upon the exponential decay, because another specular reflection points can be produced [McIntosh, 1969; Jones 1972a, b; Muller, 1968; Phillips, 1969]. Another cause of a scatter of decay constant from the equation (4.10) is nonuniformities of the ionization in the trail [Rice and Forsyth, 1963; Jones, 1969; Poole and Kaiser, 1967].

Section 2. Observation Period of Kyoto Meteor Radar

Kyoto meteor radar has been constructed in 1977, and started observations in December, 1977. Data have been obtained in last three years as shown in Fig. 4.3. A figure to the solid line in Fig. 4.3 shows the length of the observation period in days. Total lengths of the observations were 44, 81 and 104 days in 1978, 1979 and 1980, respectively. More than 300,000 meteor echoes have been detected during 230 days of observations.

Cooperation periods of the GRMWSP after the construction of our radar are listed in Table 4.1. Continuous observations prolonged over ten days were done seven times as in July 1978, March and August in 1979 and January, March, June and July in 1980.

The phase sequenced interferometer was set in operation in March 1979. Up to that time, only the decay height method was adopted for the determination of echo reflection height.

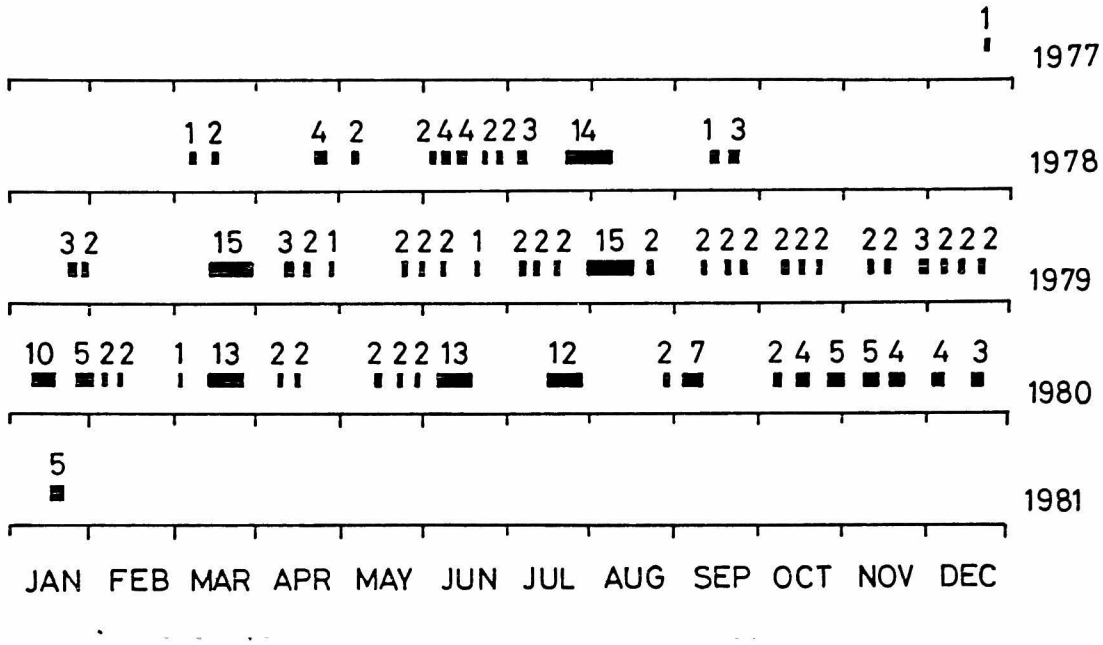

Fig. 4.3 Observation periods of the Kyoto meteor radar. A figure to the line denotes the length of the observation period in days.

Table 4.1 GRMWSP schedule in 1978 to 1980.

1978	MARCH	2	-	MARCH	15
	JUNE	1	-	JUNE	14
	JULY	27	-	AUGUST	9
1979	JANUARY	10	-	JANUARY	24
	MARCH	14	-	MARCH	28
	SEPTEMBER	12	-	SEPTEMBER	26
1980	JANUARY	10	-	JANUARY	24
	MARCH	12	-	MARCH	26
	JUNE	4	-	JUNE	18
	SEPTEMBER	3	-	SEPTEMBER	12

Section 3. Meteor Echo Distribution

3.1 Diurnal and Seasonal Variation of Meteor Echo Rate

Height-time distribution of underdense meteor echoes is plotted in Fig. 4.4 during July 24 to August 7, 1978. Each dot in the figure corresponds to one meteor echo. Note that the decay height method is used for the determination of the height of meteor trails in Fig. 4.4. Most of meteor echoes are concentrated in the thick oval region at around 6 hrs local solar time in 85 to 105 km altitude range. This subsection is devoted to describe the distribution of meteor echoes along time, while the height distribution of them will be discussed in the following subsection.

Figure 4.5 shows daily variation of underdense echo rate in 30 minutes averaged over observations done during March, April, May and June, 1978. A sinusoidal curve whose maximum occurs at 5.7 hrs solar time is well fitted for the distribution, although the echo rate from 6 to 8 hrs

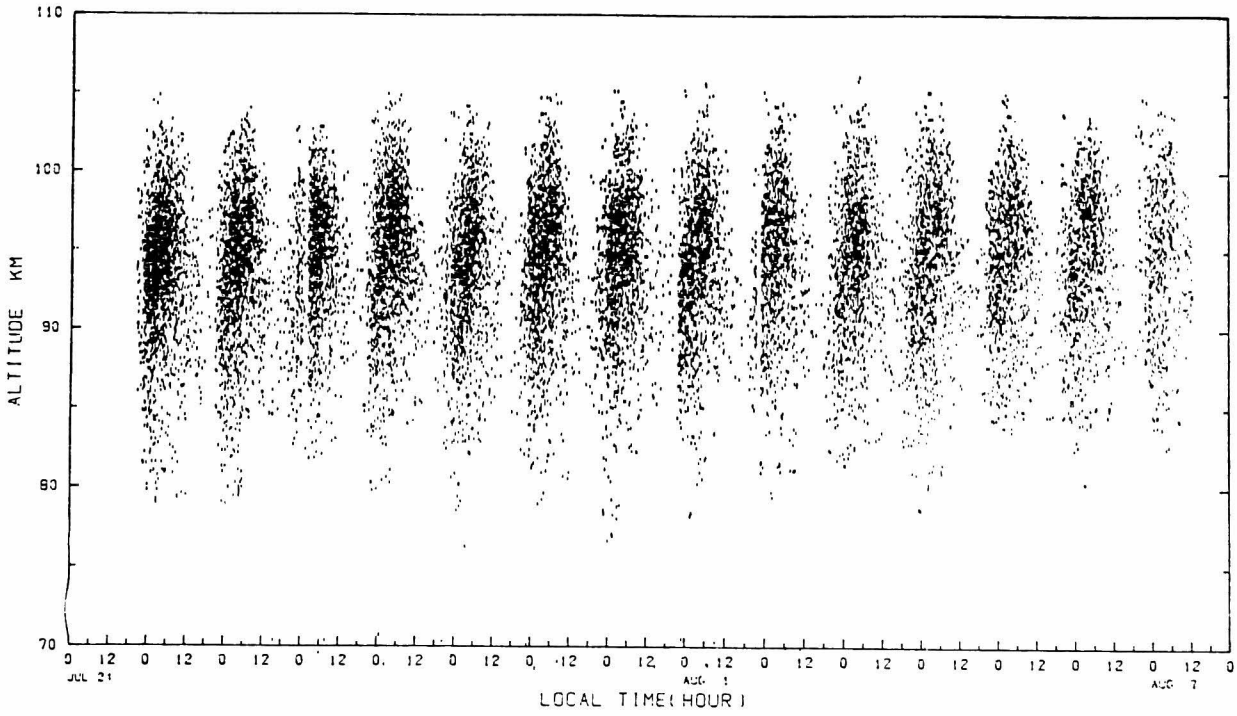

Fig. 4.4 Height-time distribution of underdense echoes during July 24 to August 7, 1978.

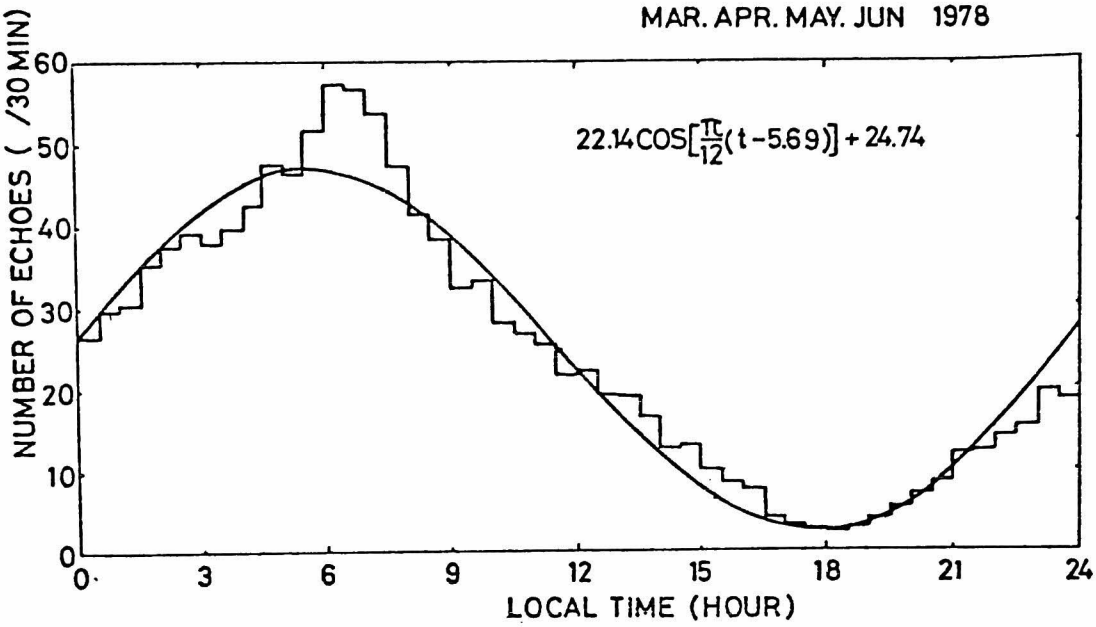

Fig. 4.5 A daily variation of underdense echo rate averaged in 30 minutes during March, April, May and June, 1978.

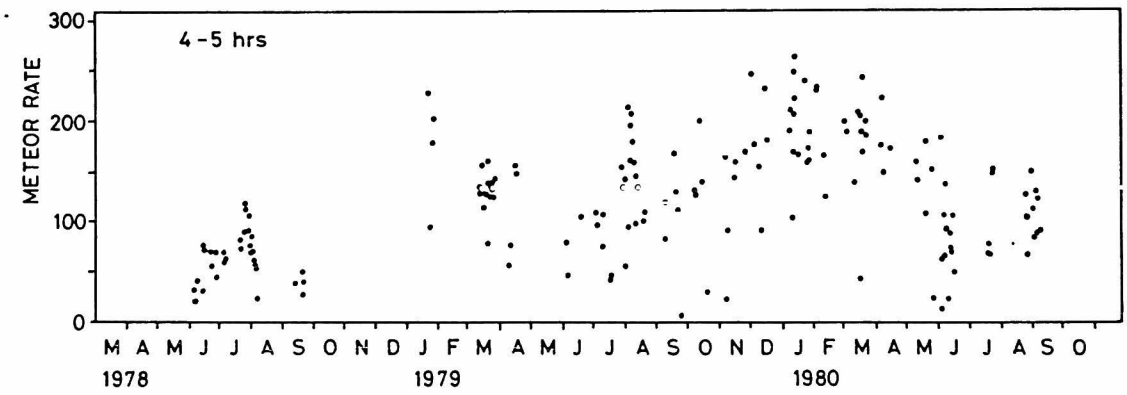

Fig. 4.6 Annual variation of meteor echo rate observed in one hour from 4 hrs to 5 hrs local time.

solar time exceeds the curve. The maximum hourly echo rate is about 110 at 6 hrs solar time in this period. The diurnal variation is fundamentally explained by the motion of the earth in its orbit around the sun while rotating itself. Anomalous increase in the early morning might be attributed to shower meteors.

In Fig. 4.6, number of meteor echoes in one hour from 4 hrs local time until 5 hrs is plotted day by day, which approximately corresponds to the maximum echo rate. One can easily imagine a sinusoidal annual variation with maximum occurring in winter, whose maximum to minimum ratio is about 3:1. McKinley [1961] discussed the annual variation of meteor echo rates observed by naked-eyes, telescopes and radars, and concluded that the meteors are low in the early months of the calendar year and high during the latter half. Because the similar variations were shown for stations in both northern and southern hemisphere, he suggested this yearly variation can not be attributed to the motion of the earth but to the change in the density and distribution of meteor radiants during the year. The maximum echo rate of our observations is delayed by three months to McKinley's estimation. Radar observations of meteor echo rates in Antarctic, however, show a similar annual variation to us [Igarashi, private communication]. Further studies are needed.

It is well known that many meteor showers occur in June, July and August [e.g. McKinley, 1961]. Among those meteor showers, Perseids is most famous, and gives a large number of meteors in a limited duration of days. In Fig. 4.7, number of underdense meteor echoes detected in 4 to 5 hrs local time is plotted during summer season. A full and an open circle corresponds to the results in 1979 and 1980, respectively. An appreciable enhancement in number of meteors is recognized from the end of July to August. Especially, meteor occurrence becomes approximately twice of the average during 7 to 11 August. This increase of meteor echoes seems to correspond to the activity of the Perseids meteor shower, although, date of peak activity of Perseids for visual meteors was forecasted to be 12 August in 1979 and 1980. It is interesting that maximum activity for visual meteors of the Perseids seemed to appear a few days after the maximum occurrence day of radio meteor echoes. Shower meteors are said to be caused by interplanetary matters scattered in the

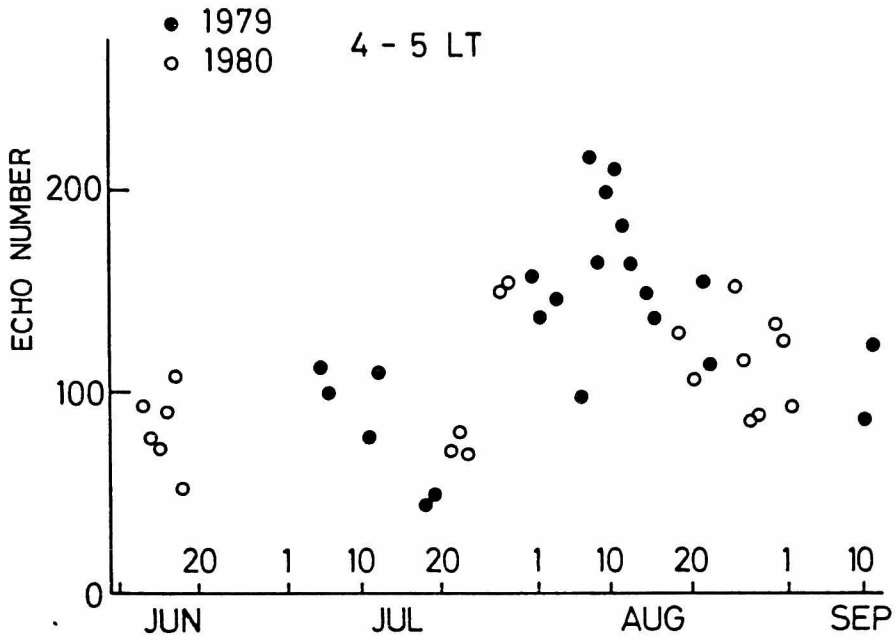

Fig. 4.7 Underdense meteor echo rate in one hour from 4 hrs to 5 hrs local time during summer months. a full circle: 1979. an open circle: 1980.

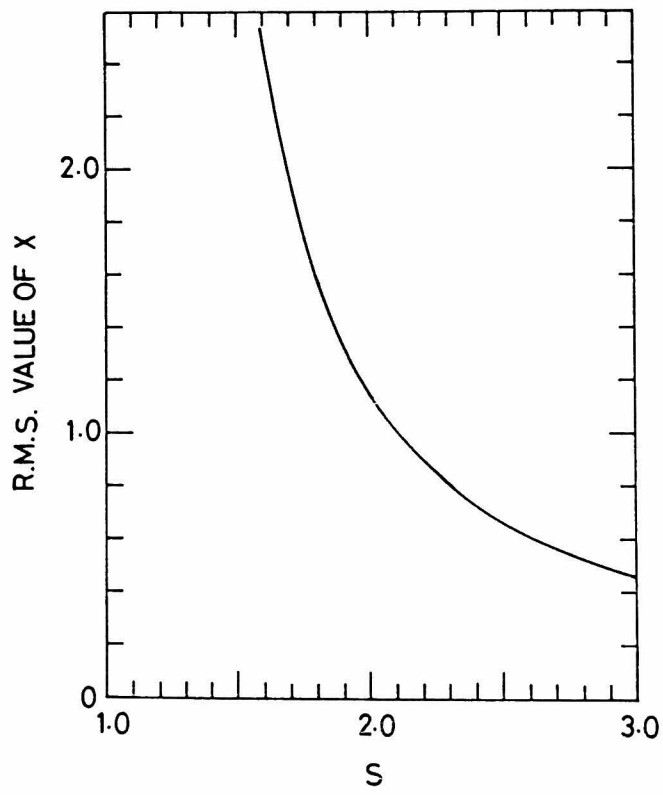

Fig. 4.8 Standard deviation of meteor echo distribution with height as a function of s.

elliptical orbit of a comet. The discrepancy of appearance date between radio faint meteors and visible vivid ones might suggest a nonuniform mass distribution of interplanetary dust in the earth's orbit.

3.2 Height Profile of Meteor Echo Distribution and Its Seasonal Variation

Kaiser [1954a, b] deduced theoretical expressions of height distribution of meteor echoes for both shower and sporadic meteors. The distribution is found to be affected by the mass-frequency distribution of the incident meteors assumed as

$$\nu_m dm_m = b m_m^{-s} dm_m \quad /m^2 sec \tag{4.12}$$

where m and b are meteor mass and a constant which defines the absolute meteor flux, respectively. The normalized height distribution observed in the limited elevation angles for meteors of the selected velocity, v, is

$$\nu_1(x) = \left(\frac{3\exp(x)}{2\exp(\frac{3x}{2})+1}\right)^{3(s-1)} , \tag{4.13}$$

where x is defined as $(h - h_0)/H$ in the case of a constant scale height H, and h_0 corresponds to a height where $\nu_1(x)$ becomes unity. Considering equipment parameters such as antenna gain patterns and minimum sensitivity, height distribution of meteors could be integrated according to the formulation deduced by Kaiser [1954a, b]. For shower meteors, the mean height, h', is close to the maximum ionization height, h_m, at which the pressure p_m is given by

$$P_m = \frac{2gl}{\Lambda A} (\cos\chi)^{2/3} \frac{1}{v_m^2} \left(\frac{9H\mu\alpha}{4\beta}\right)^{1/3} , \tag{4.14}$$

where

H; atmospheric scale height in centimeters,

μ; mean mass of a meteor atom in grams,

β; probability of ionization of evaporated meteor atoms,

χ; zenith distance of the meteor trail,

l; energy required in erg gr^{-1} to vaporize the meteoric material,

Λ; heat transfer coefficient,

A; the shape factor.

In the case of sporadic meteors, a similar relation holds for a selected velocity group of them in a narrow range of elevation angle. A discrepancy between the mean height and h_o is estimated as about a few km.

Kaiser [1954a, b] described that the r.m.s. deviation, dh, from the mean height is a function only of the atmospheric scale height and of the exponent, s, in the meteor mass distribution. In Fig. 4.8, the dependency of the r.m.s. deviation is plotted, where the antenna gain pattern given in Fig. 3.9 is taken into account. Many authors have reported on the determination of s, although a general value seems not to be established. McKinley [1961] tabulated the value of s for three showers as Quadrantids, Perseids and Geminids. The average value of his estimation was 1.66. The estimation was done for the same three showers by Kaiser [1953], and gave the average of 1.63. Jones and Collins [1974] reported the values of s as 2.17 for sporadic meteors from many radio observations, and good agreement with the theoretical estimation of 13/6 deduced by Dohnanyi [1970]. Because our observations do not discriminate shower meteors from sporadic ones, the compromise could be attained to take the mean of the two kinds of determinations, so that we assume the value of s to be 1.9. We could interpret the value of dh by the formula

$$dh = 4/3\ H\ . \qquad (4.15)$$

The relation described above can be used to derive the atmospheric scale

height from the sporadic meteor height distribution, when the meteor velocity is selected in a narrow range.

Height distribution of meteor echoes is shown in Fig. 4.9 for the observation done in January, 1980. Most of meteors are detected in the range from 80 km to 110 km. Although a slight asymmetry of the distribution with respect to the mean height is recognized, it is approximated to be Gaussian, whose mean height is 95.8 km, and the r.m.s. standard deviation is 11.3 km. The large r.m.s. value seems to be attributed to an addition of velocity variation and errors of measurement to an original value, dh, as

$$dh_m^2 = dh^2 + dh_v^2 + dh_e^2 \qquad (4.15)$$

where suffixes m, v, and e correspond to measured, velocity and error, respectively, provided the distributions are Gaussian. The values of dh_v and dh_e are roughly estimated as 5 km and 1 km, respectively, so that the expected value of dh becomes around 6 km. Mean height of meteor echo distribution observed in one hour from 4 to 5 hrs local solar time is determined daily and plotted in Fig. 4.10. Each cross point in the figure shows the mean height, and a vertical line indicate standard deviation of the distribution. A sinusoidal variation in mean height can be seen with maximum occurring in January and February. Annual mean value can be estimated from the figure as 95.5 km, and amplitude of sinusoidal variation about 2.5 km.

The height at which a meteor is illuminated depends on its mass, velocity, path inclination and the atmospheric density. Among those, an annual variation can be seen in both path inclination and atmospheric density. Although the situation is the same for the path inclination in solstices, there is a large difference in the mean height for summer and winter so that the path inclination could not be the cause of its annual variation. McKinley [1961] noticed that the velocity corrected height of the enduring radio meteor echoes show very little variation from the mean over a range of nearly eight magnitude which is closely related to meteor mass. Therefore, if the distribution of meteor incident velocity

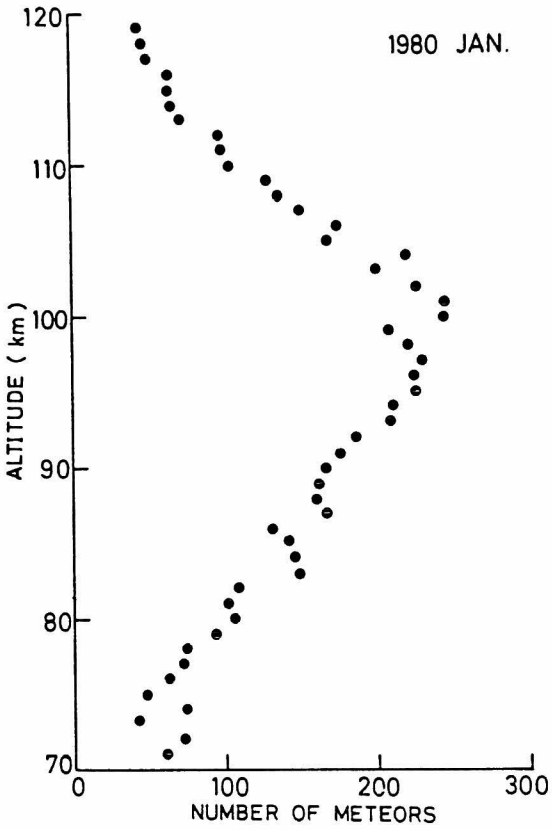

Fig. 4.9 Height distribution of meteor echoes observed in January, 1980.

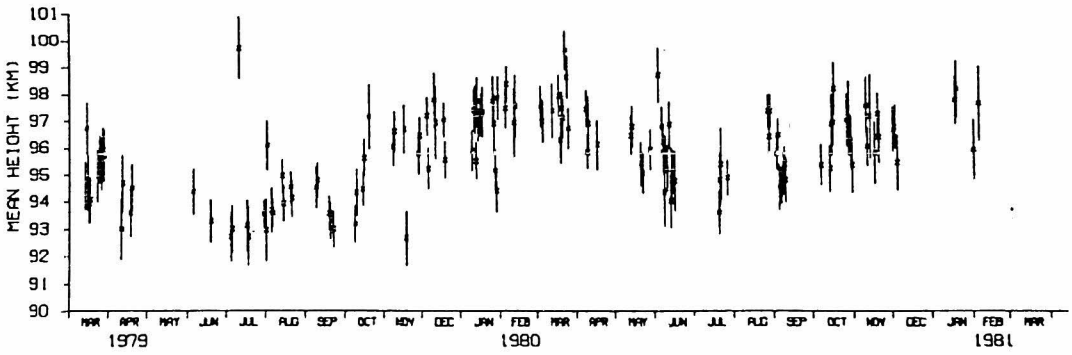

Fig. 4.10 Annual variation of mean height of meteor echo distribution observed in one hour from 4 hrs to 5 hrs local time.

KM	MEAN	JAN	FEB	MAR	APR	MAY	JUN	JUL	AUG	SEP	OCT	NOV	DEC
40 DEGREES N													
25	3.396	-020	-017	-016	-013	-009	+012	+023	+025	+017	+009	-005	-017
30	3.069	-025	-023	-021	-012	+001	+017	+029	+031	+023	+008	-010	-024
35	2.755	-032	-030	-028	-011	+005	+024	+039	+039	+028	+006	-018	-031
40	2.459	-041	-037	-032	-008	+015	+034	+044	+046	+029	+003	-027	-039
45	2.178	-046	-040	-036	-007	+021	+041	+049	+048	+031	-001	-036	-045
50	1.908	-050	-042	-038	-004	+027	+049	+052	+050	+028	-004	-041	-049
55	1.635	-052	-044	-041	-005	+033	+053	+057	+051	+029	-006	-046	-053
60	1.350	-053	-045	-042	-003	+037	+061	+061	+051	+027	-014	-049	-052
65	1.045	-047	-044	-043	+008	+041	+063	+063	+049	+014	-021	-053	-051
70	0.721	-039	-038	-034	+011	+051	+063	+053	+036	+002	-033	-054	-042
75	0.374	-027	-026	-022	+024	+052	+060	+035	+029	-007	-037	-053	-032
80	0.011	-011	-008	-004	+035	+050	+030	+005	+005	-019	-037	-045	-015
85	*1.630	+010	+013	+011	+049	+036	-005	-033	-020	-023	-026	-027	+004
90	*1.245	+035	+036	+026	+053	+012	-051	-084	-047	-025	-011	-002	+036
95	*2.868	+054	+042	+027	+042	-022	-106	-113	-048	-010	+008	+021	+061
100	*2.525	+054	+038	+024	+030	-037	-110	-106	-047	-008	+011	+037	+020
105	*2.207	+041	+033	+017	+042	-045	-104	-087	-046	-007	+028	+055	+056
110	*3.931	+022	+027	+016	+003	-036	-074	-070	-057	-015	+027	+044	+058

Fig. 4.11 Seasonal variation of atmospheric pressure at 40°N (CIRA 1972). Shaded region indicates positive enhancement.

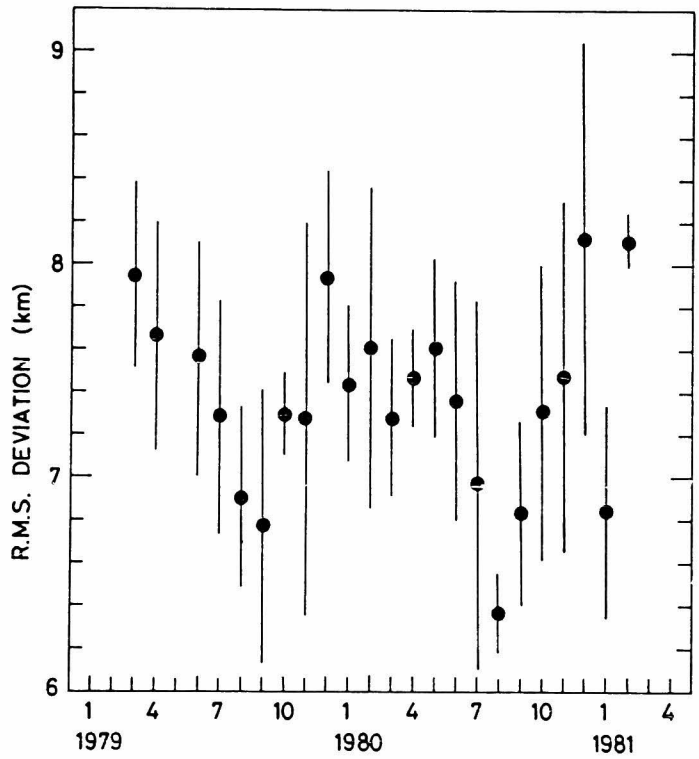

Fig. 4.12 Monthly average of r.m.s. deviation of meteor echo height.

in the limited time interval in a day is assumed to not vary around a year, the distribution of meteor echoes might be mainly affected by atmospheric parameters.

From the variation of the mean height shown in Fig. 4.10, atmospheric pressure is expected to be high in winter months, and low in summer months at meteor heights. This feature agrees well with the standard atmosphere given in CIRA 1972 which is shown in Fig. 4.11. Monthly average value of the r.m.s. deviation of meteor height distribution observed in one hour from 4 to 5 hrs is plotted in Fig. 4.12. The r.m.s. deviation ranges from 6.5 km to 8 km with minimum occurring in summer months. The seasonal variation of the width of meteor echo distribution will be discussed in terms of atmospheric temperature in later section.

Section 4. Ambipolar Diffusion Coefficient at Meteor Heights

4.1 Height Profile of Ambipolar Diffusion Coefficient

We deduced ambipolar diffusion coefficient from the decay constant of the underdense meteor echoes by using the relation (4.10). A typical result is shown in Fig. 4.13 for the observation done in August 1979. Each meteor echo corresponds to an open circle whose radius is weighted by the echo intensity. Average value and r.m.s. deviation of the diffusion coefficient in 2.5 km altitude range are also shown in Fig. 4.13 as a full circle and a horizontal line to it, respectively. The diffusion coefficient is deduced as 9.0 m^2/sec at an altitude of 100 km, 4.9 m^2/sec at 95 km and 2.7 m^2/sec at 90 km.

Although there being a considerable spread in the measurement of the diffusion coefficient, one can imagine a linear relation between altitude and logarithm of the ambipolar diffusion coefficient, which can be experimentally deduced by the least mean square method as

$$\ln D = -9.88 + h/8.28 \ . \qquad (4.17)$$

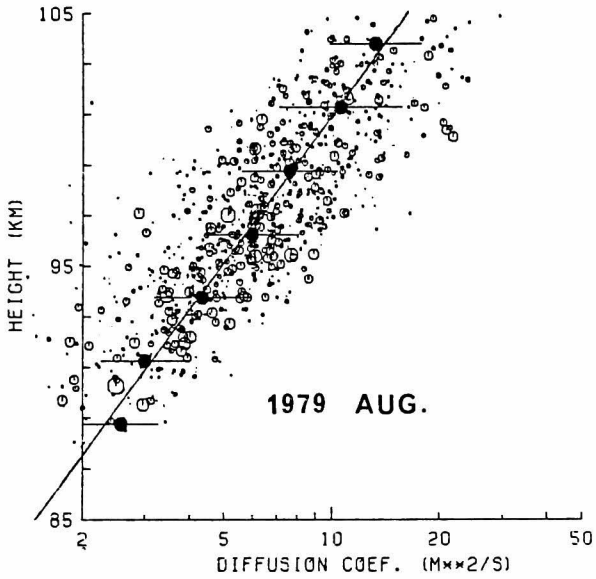

Fig. 4.13 Height profiles of ambipolar diffusion coefficient observed in August, 1979. A full circle corresponds to the average value in 2.5 km height range, and a horizontal line to it indicates the standard deviation. A straight line is the best fit curve for all data.

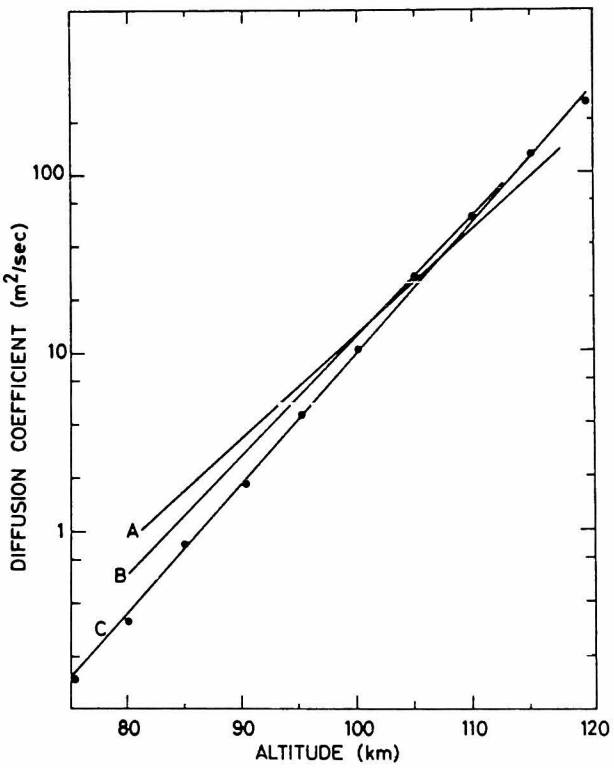

Fig. 4.14 Various estimations of height profiles of ambipolar diffusion coefficient. A full circle is the value calculated from the relation deduced by Kaiser [1953] by use of atmospheric parameters in US standard atmosphere 1962. A: Jones [1970]. B: Greenhow and Neufeld [1955]. C: best fit curve to full circles.

and is drawn in Fig. 4.13. The r.m.s. deviation of lnD is estimated as about 0.7 from the error bar shown in the figure, which indicate the deviation of 5.8 km from the relation (4.17). Thus the decay height method materially include an error of several km in altitude determination, because its basis is attributed to the relation (4.10).

A theoretical expression of the ambipolar diffusion coefficient was given by Kaiser [1953] as

$$D = \frac{8}{3} l_i \left(\frac{2kT}{\pi m}\right)^{1/2} , \tag{4.18}$$

where l_i is a mean free path of a particle, and further described as follows:

$$l_i = \frac{1}{\sqrt{2}\ \pi\sigma_i^2\ n} , \tag{4.19}$$

where n and σ_i are the atmospheric number density and the collision cross section, respectively, and the latter is estimated as 9.2×10^{-8} cm^2 for a collision between Alkari metal and molecular nytrogen and oxygen. Substituting the atmospheric temperature and density from US Standard Atmosphere 1962 to the equation (4.19), we can deduce the value of D, and plot in Fig. 4.14 as a full circle. A linear curve fitted to the estimation is drawn in Fig. 4.14, and is described as

$$\log_{10} D = 0.072h - 6.19 \tag{4.20}$$

Similar expressions were experimentally deduced by different workers similar to the relation (4.11) as follows:

$$\log_{10} D = 0.059\ h - 4.76 \qquad \text{[Jones, 1970]} \tag{4.21}$$

and are also shown in Fig. 4.16. About 3 km of spread can be recognized in the altitude deduced by various curves for a given diffusion

coefficient. Within this spread of values our result is consistent with the determinations, although the rate of increase in lnD with height is slightly smaller than others. The choice of diffusion coefficient would not be expected to affect the determination of meteor height materially, because the method essentially include a spread of determination to several km in altitude. The relation described in (4.11) is prepared for height determination of meteor echoes by the decay height method.

4.2 Daily and Seasonal Variation of Ambipolar Diffusion Coefficient

A large spread of the diffusion coefficient shown in Fig. 4.13 is seemed to be due to three reasons: daily variation of the diffusion coefficient, discrepancy of decay constant from the relation described in (4.10) and error in height measurement. Variation of the diffusion coefficient with time is examined in this subsection. In Fig. 4.15, linearly fitted curves similar to that shown in Fig. 4.13 are plotted for meteors detected in 2 hrs intervals for the observation in January and February 1980. It can be seen from Fig. 4.15 that the curves are approximately quasi-parallel with each other, and large variations in the diffusion coefficient occur at a given height at different time of a day.

The presence of a daily variation in the diffusion coefficient at 95 km altitude is illustrated in Fig. 4.16 for three seasons: August, 1979; January and February, 1980 and March and April, 1980. Because we could not obtain enough meteor echoes in the evening, no determination of the diffusion coefficient is drawn from 16 to 20 hrs local time. An error bar is representatively shown to the value observed in August in 1979. The diffusion coefficient becomes maximum at around 6 hrs local time. The amplitude of daily variation in the diffusion coefficient ranges approximately from 10 to 15 %. A diurnal variation can be seen from Fig. 4.16 in the period August in 1979 and January and February in 1980, while a semidiurnal variation seems to be dominant in the period March and April in 1980.

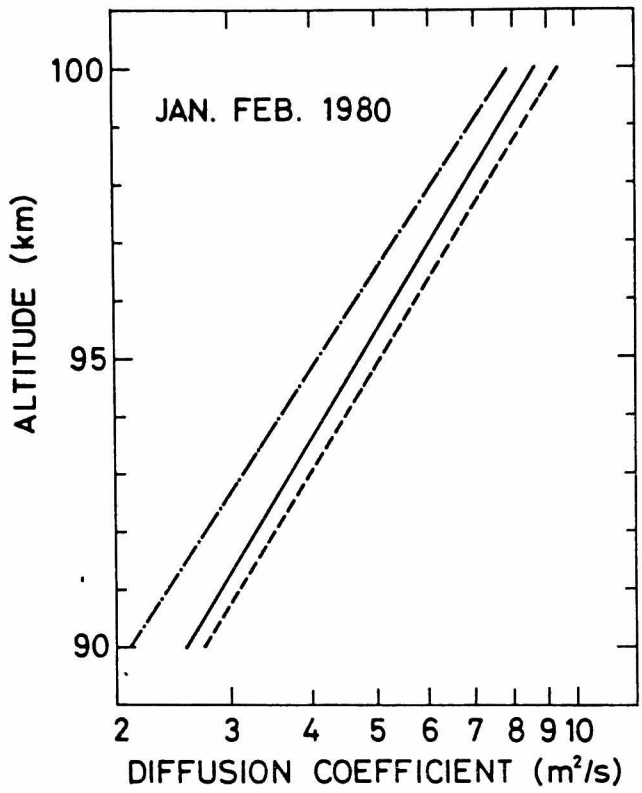

Fig. 4.15 Linearly fitted curves same as in Fig. 4.13 during 2-4 hrs and 6-8 hrs local time (solid line), 4-6 hrs (broken line) and 8-10 hrs (chained line).

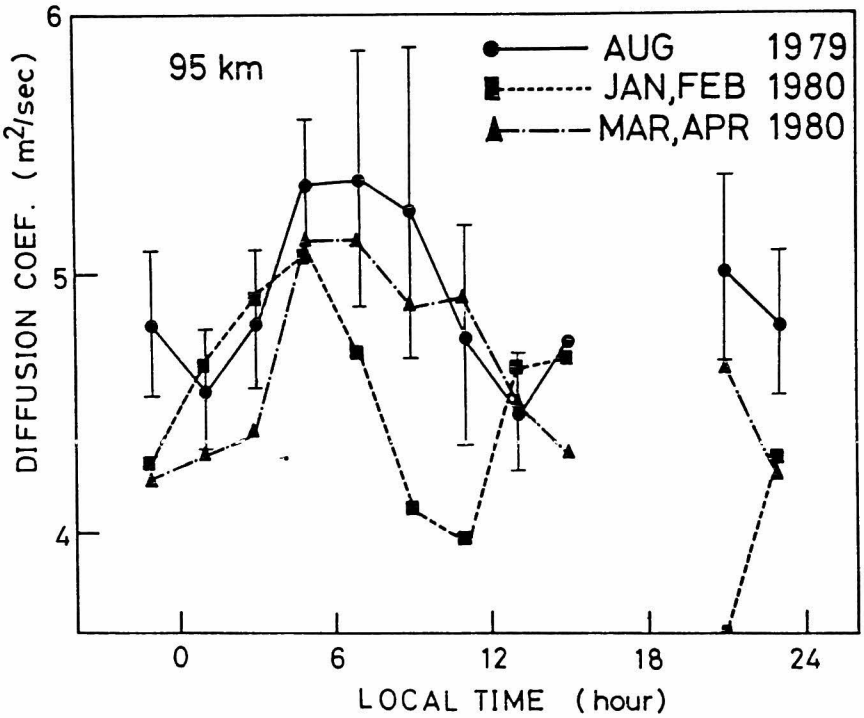

Fig. 4.16 Daily variation of diffusion coefficient at an altitude of 95 km in August 1979 (a circle), January and February, 1980 (a quadrangle) and March and April, 1980 (a triangle).

Section 5. Atmospheric Temperature Deduced from Meteor Echo Distribution and Ambipolar Diffusion Coefficient

Atmospheric temperature at meteor heights is deduced from two different quantities: (i) the r.m.s. deviation of meteor echo distribution and (ii) the ambipolar diffusion coefficient.

(i) Atmospheric scale height at meteor height can be estimated from the r.m.s. deviation of altitude distribution of meteor echoes by use of the relation (4.15). If the mean molecular weight and gravitational acceleration at meteor heights do not differ from those at ground, atmospheric temperature will be deduced by using a monthly average value of the r.m.s. deviation plotted in Fig. 4.12. The result is shown in Fig. 4.17, where model atmospheres given in CIRA 1972 and US Standard Atmosphère 1976 are also illustrated. The mean temperature and the shape of the variation around a year agree with model atmospheres, although the curve seems to proceed by about two months.

(ii) The seasonal variation of the atmospheric temperature might be estimated by use of the ambipolar diffusion coefficient. The diffusion coefficient is proportional to a square of atmospheric temperature and the inverse of the atmospheric density. If we assume that the atmospheric pressure does not vary around a year at mean height of the meteor echo distribution [Kaiser, 1953], the diffusion coefficient at that height would be decided only by the atmospheric temperature as follows

$$D \propto T^{1/2} \rho^{-1} \propto T^{3/2} . \quad \text{(when } P = \text{const)} \tag{4.22}$$

A small perturvation of the diffusion coefficient, ΔD, can be related to that of the atmospheric temperature, ΔT, as

$$\Delta D \propto 1.5 \Delta T \tag{4.23}$$

In Fig. 4.18, the diffusion coefficient at mean height of meteor echo distribution is plotted bimonthly from March 1979 to June 1980. If we

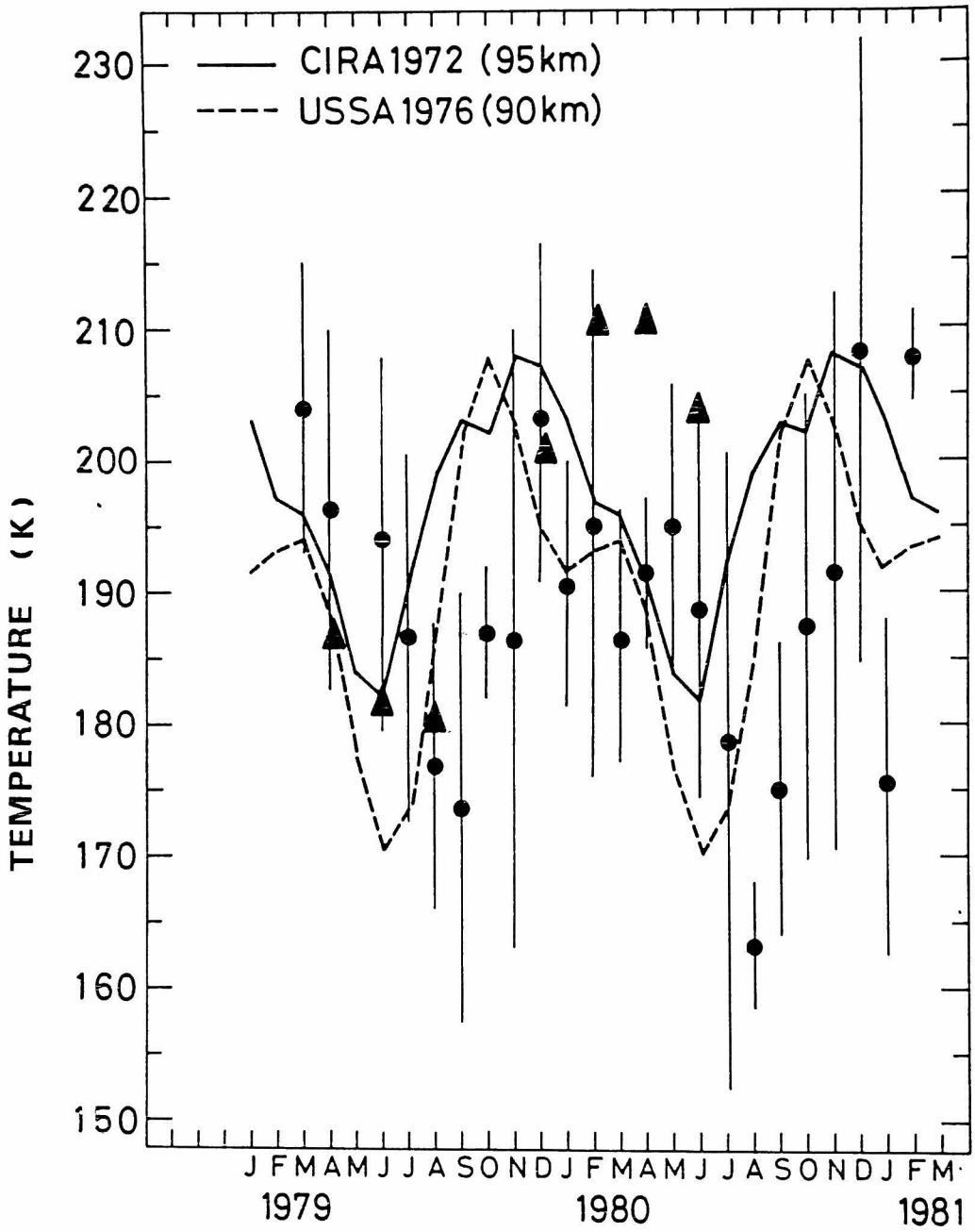

Fig. 4.17 Annual temperature variation deduced from meteor echo distribution (a full circle), and that from diffusion coefficient (a triangle).

can exclude anomalous value in September and October in 1979, a sinusoidal variation of the diffusion coefficient can be imagined whose relative amplitude of the atmospheric temperature variation is estimated as 8.7 %. Because we could not determine the annual mean atmospheric temperature, T_0, directly by this method, we assume that T_0 is 197 K from the model atmospheres. Seasonal variation of atmospheric temperature is again deduced and plotted in Fig. 4.17, and is generally agree with the result previously described during the period from July 1979 to June 1980. The range of temperature variation deduced by two different methods agree well with the model atmosphere.

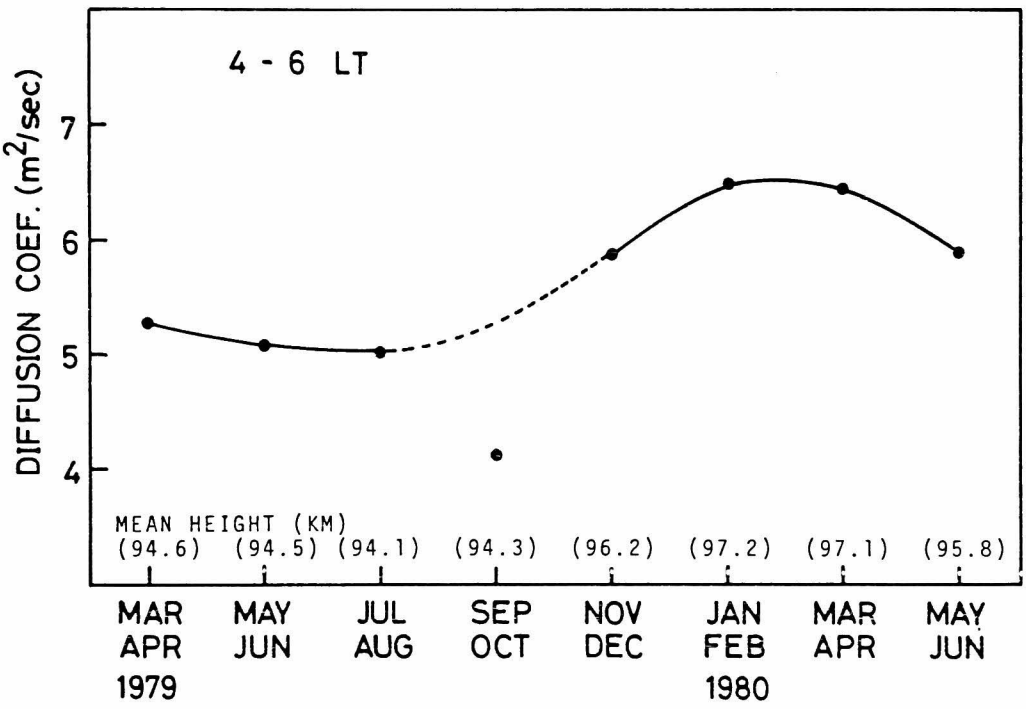

Fig. 4.18 Bimonthly average of diffusion coefficient in 4-6 hrs local time at the mean height of meteor echo distribution.

Chapter V

Observation of Solar Atmospheric Tides

Section 1. Method for Statistical Analysis of Solar Tides

1.1 Least Mean Square Method by Use of Polynomials and Sinusoidal Functions (Groves' Algorithm)

We use a statistical treatment proposed by Groves [1959] in order to obtain vertical structure of tides. He applied a statistical method to meteor wind observations to determine certain specified parameters, characterizing the tidal structure. This method consists of a linear parameter estimation on the basis of the least-squares theory.

By a single meteor echo measurement, we can obtain the following quantities:

l,m,n:		the directional cosines of the reflection point on the trail
V_r	:	the radial wind velocity in the direction of observation
R	:	the range of the reflection point
t	:	the time of observation

The velocity V_r could be expressed as follows by neglecting small vertical component of wind velocity,

$$V_r = ul + vm \tag{5.1}$$

where u and v are the northward and eastward components of wind velocity at the reflection point. The wind structure is supposed to be composed of a mean meridional and zonal wind, the diurnal tide and its harmonics.

The component of the wind velocity, e.g. u, is expressed as a function of local time t and height z:

$$
\begin{aligned}
u &= u_0(z) + u_1(z)\sin(\omega t) + u_2(z)\sin(2\omega t) + \cdots\cdots \\
&\quad + u_p \sin(p\omega t) \\
&\quad + u_1^*(z)\cos(\omega t) + u_2^*(z)\cos(2\omega t) + \cdots\cdots \\
&\quad + u_p^*(z)\cos(p\omega t) \\
&= u_0(z) + \sqrt{u_1^2(z)+u_1^{*2}(z)}\,\sin(\omega t+\arctan(u_1^*(z)/u_1(z)) + \cdots \\
&\quad + \sqrt{u_p^2(z)+u_p^{*2}(z)}\,\sin(p\omega t+\arctan(u_p^*(z)/u_p(z)) \ , \qquad (5.2)
\end{aligned}
$$

where ω is the angular velocity of the oscillation. Particularly, height variation of each coefficient u_i, or u_i^* ($i = 1,2,\ldots.p$) is expressed by polynomials. When we adopt the expression (5.2), normally distributed random fluctuation with zero mean is expected to be contained in the measured wind velocity. Parameters which determine the form of polynomials are determined so as to a sum of the square of fluctuations are minimum with respect to them. We use this method to process meteor radar data as has been done at many other stations. We investigate the validity and limitation of the Groves' algorithm by a simulation in the following subsection.

1.2 Statistical Test of The Groves' Algorithm

In this subsection, we describe a manner utilizing the algorithm to its full extent by applying it to numerically produced data.

Numerical Model: First, we reproduce a distribution of meteors whose characteristics have been described in Chapter IV as summarized below:

(1) The meteor echo rate n varies diurnally, and reaches its maximum at 0600 LT except for meteor shower epochs. An observational result at Kyoto station indicates an empirical formula [Aso et al., 1980]

$$n(t) = n_0[1+\cos(\omega(t-5.7LT))]+\Delta n \ , \qquad (5.3)$$

where specifically $n_0 = 22$ and $\Delta n = 3$.

(2) The distribution of meteor echoes with height is nearly normal with a mean height of around 95 km and a standard deviation of several km.

In addition to the above distributions attributed to physical qualities of meteors, arrival angle dependence due to antenna pattern is also taken into consideration. Artificial meteor echo distributions are produced to satisfy the characteristics specified above. Especially, those with respect to height and directional cosines are simulated by using normally distributed random numbers.

Second, we construct a model of the wind system in the meteor region which is consistent with the observation. Height-averaged power spectrum of the northward wind component are shown in Fig. 5.1 which are observed in June and July, 1978. We can see large amplitude of the diurnal and

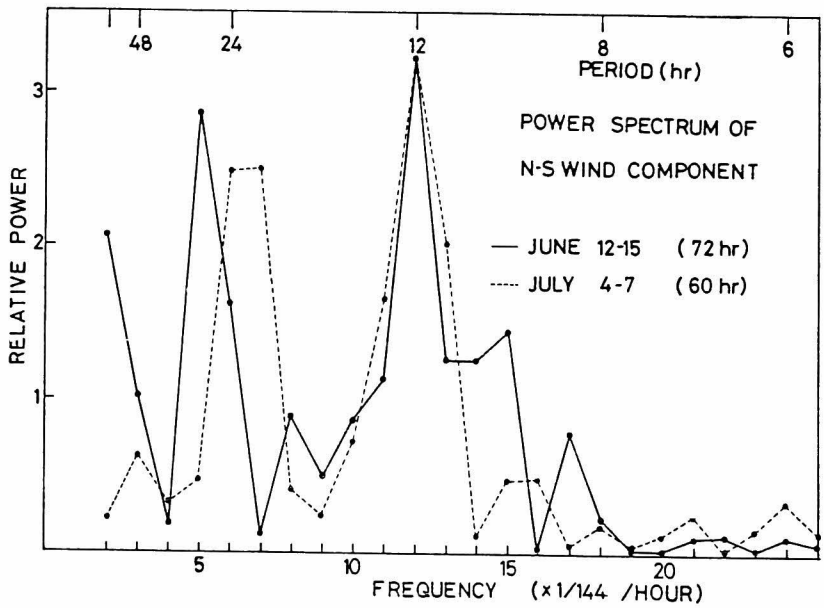

Fig. 5.1 Spectral analyses of the northward wind in 12-15 June, 1978 (a solid line) and 4-7 July, 1978 (a broken line).

semidiurnal tides, while higher harmonics are small. Figure 5.2 (a) shows measured northward radial wind velocity along with the standard deviation about the mean for each data group in two hour interval. Fitted curves by use of diurnal and semidiurnal component, and first to fourth harmonics are drawn in Fig. 5.2 (b) as a solid and a broken line,

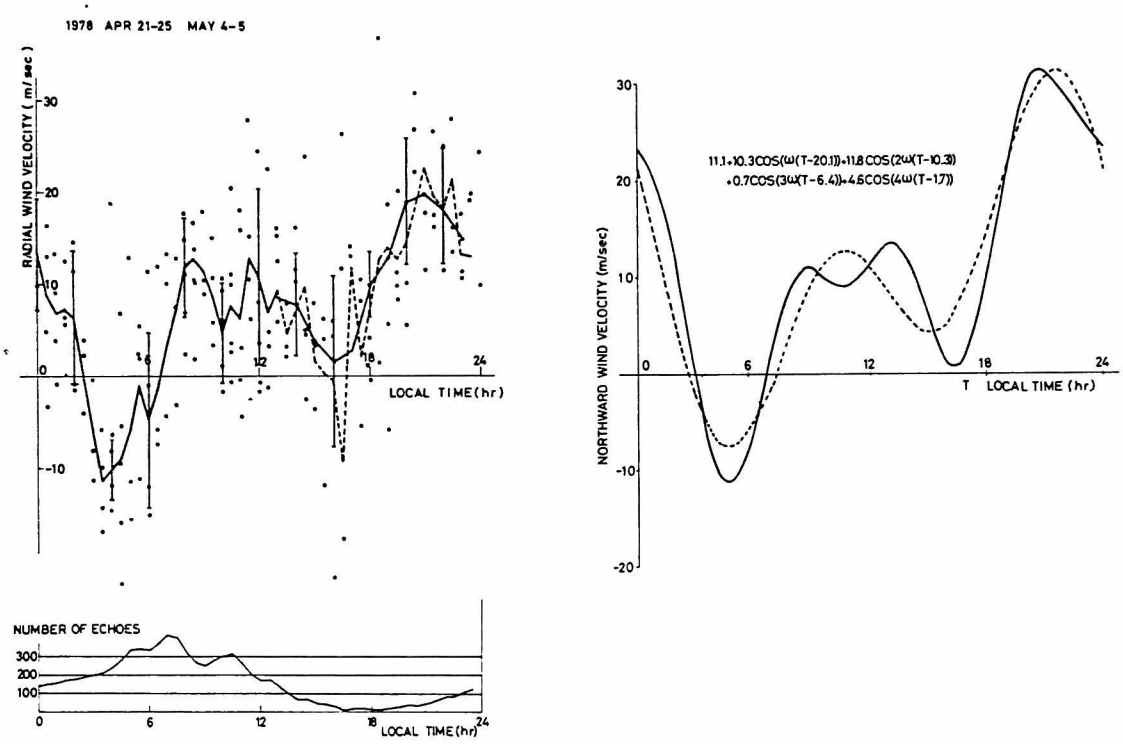

Fig. 5.2 Height-averaged radial wind velocity measured during period 21-25 April and 4-5 May, 1978. (a): Each dot corresponds to a mean value in 10 minutes. A solid line in 0-13 hrs local time and a broken line in 13-24 hrs shows variation averaged in 30 minutes. A soild line in 13-24 hrs indicates a running average in 2 hrs. Meteor echo rate is shown at the bottom. (b): A broken and solid line corresponds to the best fit curve for the northward wind velocity deduced from (a) by use of diurnal and semidiurnal component, and first to fourth harmonics, respectively.

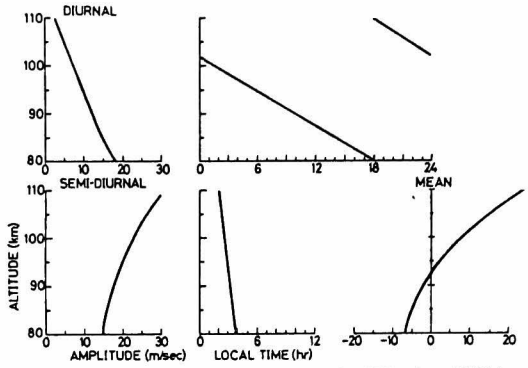

Fig. 5.3 A model of the wind structure in the meteor region for simulations.

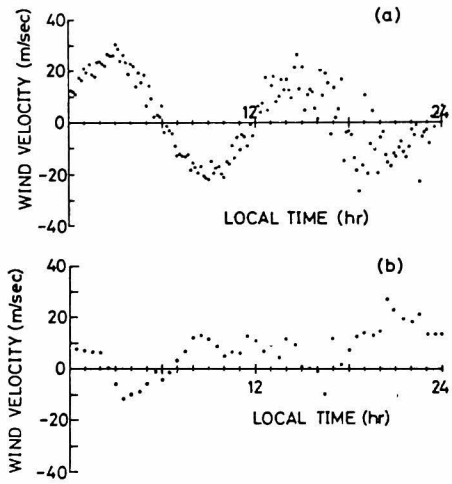

Fig. 5.4 Radial wind velocity versus local time. (a): artificially produced (averaged in every 10 minutes). (b): observed during 21-25 April, 1978 (averaged in every 30 minutes).

respectively. By an addition of third and fourth harmonics to the solid curve, a little improvement is attained in approximating the variation shown in Fig. 5.2(a). Observation again shows that higher harmonics like the ter-diurnal or quarter-diurnal tides are generally small. Hereafter we will consider only diurnal and semidiurnal tides. Figure 5.3 corresponds to a wind system composed of a mean wind and the $S_{1,1}$ and $S_{2,2}$ tidal modes. Superimposed on these basic components in a fluctuation term which is generated by a normally distributed random number in order to match the actual wind field containing gravity waves or turbulence. The fabricated wind field is shown in Fig. 5.4 (a) in comparison with an observational result during April 21-25, 1978 shown in Fig. 5.2 (b). These have a large dispersion at around 1800 LT, which

characterizes the meteor wind observation, and makes the estimate of the diurnal tide less accurate than that of the semidiurnal tide.

Parameter Estimation: Artificial data are processed through the Groves' algorithm. It is convenient to assign the number of parameters as (N_1, N_2, N_3) where N_1 means the order of harmonics, N_2 means the degree of polynomials and N_3 indicates the number of wind components which will be determined. In total, $(2xN_1+1)x(N_2+1)xN_3$ parameters must be estimatd. Numerical simulations are carried out to know (i) the optimum arrangement of parameters (ii) a reliable height range for each model and (iii) the necessary quantity of data to determine each tidal mode.

Harmonic components are orthogonal to each other, and can be estimated independently, so that N_1 is chosen as two corresponding to the present model. Because vertical wind motion is usually neglected, N_3 is set equal to two for the zonal and the meridional component, respectively. The choice of N_2 is the most important point in order to know the height variation of tides.

Amplitude and phase variations are shown in Fig. 5.5 when N_2 is chosen equal to 2, 3 and 4. Phases are well approximated in the height region 85-105 km in all three cases. Especially, that of the semidiurnal tide is almost identical to the model value. Amplitudes above and below the meteor region differ from the model. Parameters for the $S_{2,2}$ mode with long vertical wavelength can be estimated more accurately than those of the $S_{1,1}$ mode with short vertical wavelength in all three cases. It is desirable to set N_2 a little larger to estimate the waves with short vertical wavelength, although there are no appreciable discrepancies between the various cases which are examined here.

A reliable height range of the statistically treated result mainly depends on the height distribution of meteors. A standard deviation of the distribution of meteors is varied from 2 to 5 km in the simulation, while the real distribution has been described above. From the form of equation (5.2), one can recognize easily that the amplitude of the tide becomes large outside the meteor region. In contrast with the model as shown in Fig. 5.6, the result is reliable within twice the standard deviation centered at around 95 km. Therefore, we must rely on the

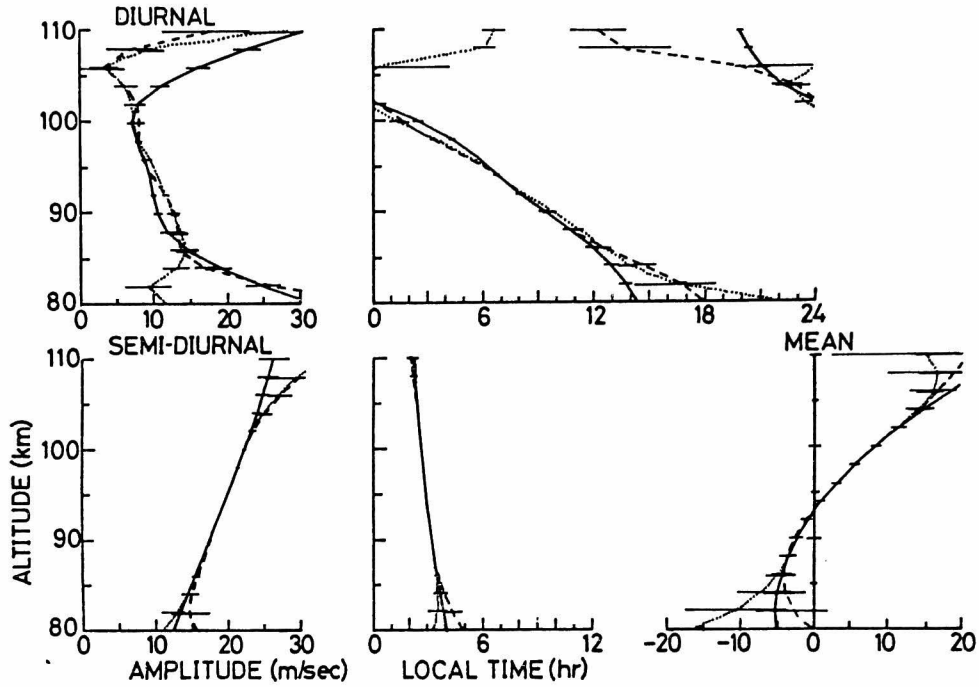

Fig. 5.5 Statistically estimated height profiles when the parameters N_2 is made equal to (a) 2 (a solid line), (b) 3 (a broken line) and (c) 4 (a dotted line).

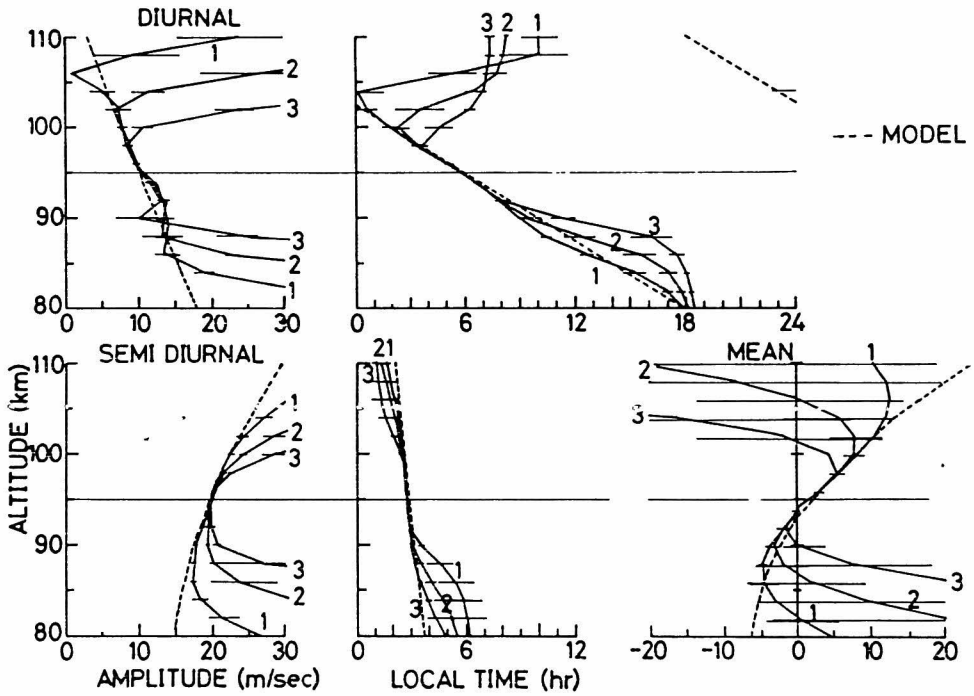

Fig. 5.6 The same as Fig. 5.5 (b) except for the standard deviations of the meteor distribution of 1; 5 km, 2; 3 km and 3; 2 km, respectively.

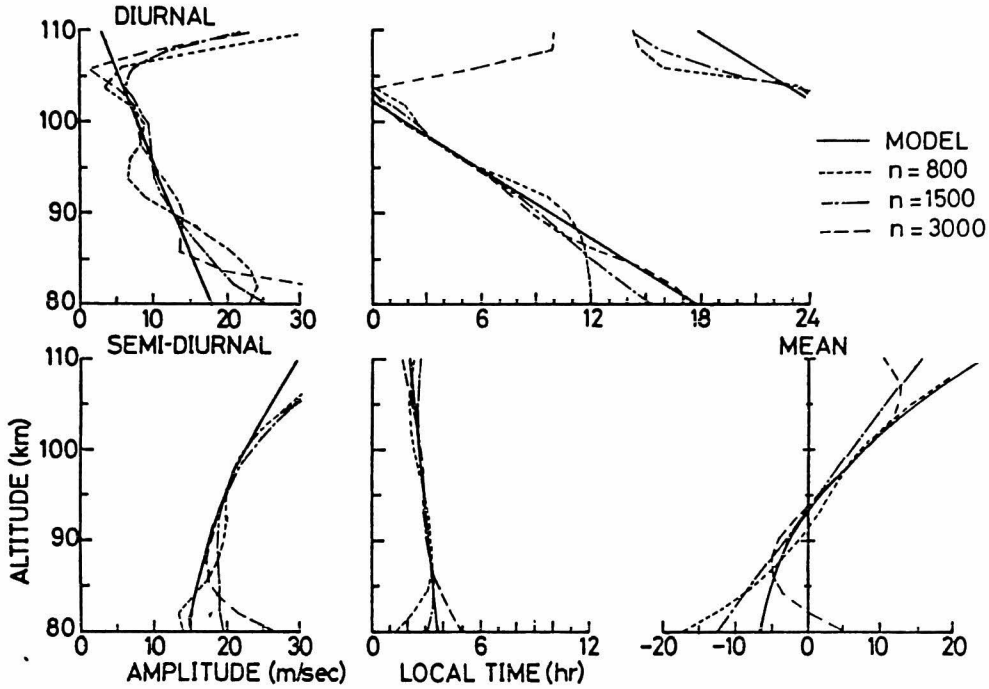

Fig. 5.7 The same as Fig. 5.5 (b) except for the number of meteors is changed.

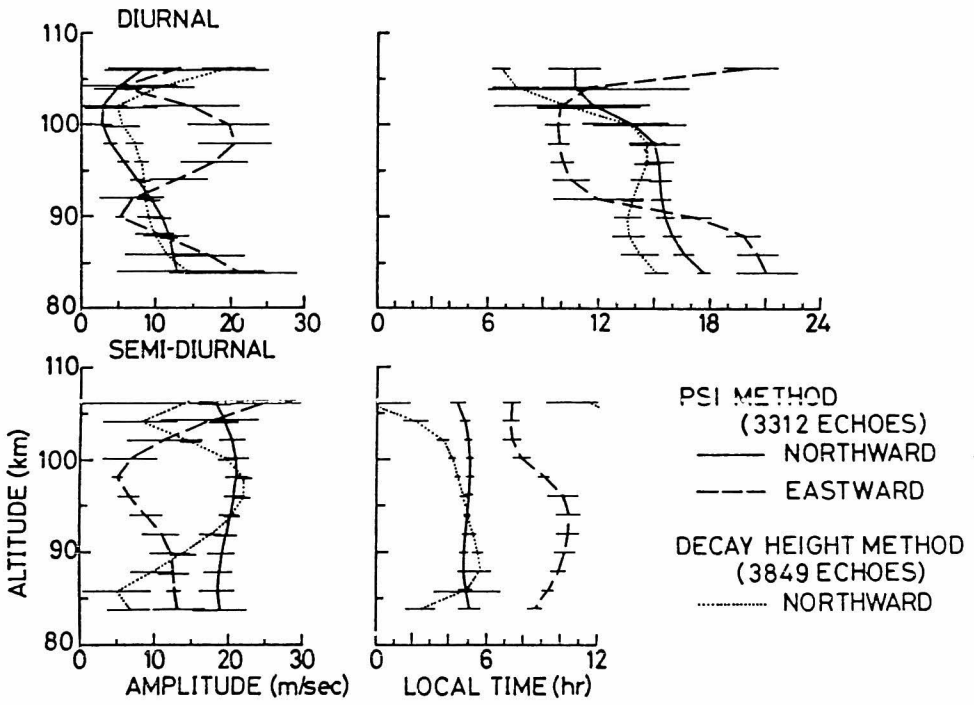

Fig. 5.8 Height profiles of diurnal and semidiurnal tidal wind. Meteor echo height is determined by either the PSI method or the decay height method.

height profile for actual observations in this altitude range.

We usually consider the observational results on a diurnal basis, but the question arises as to how many meteor echoes are needed for a correct delineation of tidal structure. The total number of meteor echoes has been set equal to 800, 1500 and 3000 respectively, and the result is shown in Fig. 5.7. We can see the height profiles of the semidiurnal tide and the mean wind to be fairly well approximated even using only 800 meteors in the 86-104 region. Though there remain small fluctuations, the vertical structure of the diurnal tide with a short vertical wavelength is well delineated by using 3000 meteors.

In summary, an acceptable way to treat the metoer radar data is to (i) set the parameter arrangement (2,3,2), (ii) use more than 3000 meteors, and (iii) extract an appropriate height region considering height distribution of meteors. Hereafter we process data in this manner. Our facility detects about 1500 meteors per day, so at least two days' observation is usually satisfactory to delineate tidal structure at meteor heights.

There are two independent methods to determine meteor echo height: the PSI method and the decay height method. Heights of meteor echoes obtained in the period from 13 to 29 May, 1980 are determined by these two method. Those are separately analysed by the Groves' algorithm, and the results are shown in Fig. 5.8. Note that data deduced from the decay height method can give only the northward component, providing an azimuth angle of the echo arrival is the same as the antenna direction. As for the PSI method, both northward and eastward component can be delineated because finite width of the antenna beam include many independent vectors. The accuracy of the determination, however, is better for the northward component, since the eastward component can be only fractionally contained in the measured radial wind velocity. From Fig. 5.8, the result by the decay height method agree with that by the PSI method at around 95 km where the largest part of data is obtained, although discrepancy becomes large in the altitude ranges below 90 km and above 100 km.

Section 2. Sesaonal Variation

2.1 Results for 1979-1980 Observations

Observations of the atmospheric tidal winds at Kyoto before March, 1979 were summerized in recent papers [Aso et al., 1979, 1980]. Height profiles at both summer solstice and vernal equinox were reported by Tsuda et al. [1980] by using data observed during CTOP campaigns.

Monthly average behaviours of the mean wind, diurnal and semidiurnal tidal wind at Kyoto are summarized in Tables 5.1 and 5.2 for the northward and eastward component, respectively. These tables contain the results in the period from March, 1979 to November 1980, however, those in May, 1979 are lacking. Groves' algorithm described in the previous section is applied by using cubic fitting curves with height.

Phases correspond to the hour of maximum wind velocity in local solar time. Errors are calculated according to Groves [1959]. Considering the reliable height ranges of the analysis, results are tabulated at altitudes from 86 to 104 km.

All the data in Talbe 5.1 are separated according to the four seasons;

spring	--	March, April;
summer	--	May, June, July, August;
autumn	--	September, October;
winter	--	November, December, January, February.

Figures 5.9 to 5.12 show the height profiles of the nothward tidal winds in four seasons. By using these results, the detailed investigation on the seasonal variation of the diurnal and semidiurnal tide will appear separately in the followings.

Table 5.1 Meridional component of the mean wind, diurnal and semidiurnal tide in the periods from March, 1979 to November, 1980.

Phase corresponds to the local time of the northward maximum wind.

Table 5.1 (a) 1979 March

ALTI-TUDE (km)	MEAN		DIURNAL				SEMIDIURNAL			
	AMP. (m/sec)	ERROR	AMP. (m/sec)	ERROR	PHASE (hr)	ERROR	AMP. (m/sec)	ERROR	PHASE (hr)	ERROR
104	2.0	1.8	12.3	0.9	3.9	0.2	6.1	1.7	6.7	0.5
102	1.9	1.4	12.3	0.7	3.9	0.2	5.2	1.2	6.9	0.5
100	2.0	1.2	11.3	0.5	3.9	0.2	4.5	1.1	6.9	0.5
98	2.3	1.0	9.8	0.5	3.9	0.2	4.0	1.0	6.6	0.5
96	2.7	0.9	7.9	0.4	3.7	0.2	3.8	1.0	6.1	0.5
94	3.1	0.8	5.9	0.5	3.5	0.3	3.9	0.9	5.6	0.4
92	3.5	0.8	4.1	0.6	3.1	0.5	4.1	0.9	5.2	0.4
90	3.7	0.9	2.8	0.8	2.6	0.9	4.1	1.0	5.0	0.4
88	3.7	1.0	2.2	0.9	2.4	1.3	3.5	1.0	4.9	0.5
86	3.4	1.2	2.3	1.0	3.4	1.0	2.1	1.3	5.0	1.1

Table 5.1 (b) 1979 April

ALTI-TUDE (km)	MEAN		DIURNAL				SEMIDIURNAL			
	AMP. (m/sec)	ERROR	AMP. (m/sec)	ERROR	PHASE (hr)	ERROR	AMP. (m/sec)	ERROR	PHASE (hr)	ERROR
104	-7.1	3.5	13.7	3.0	3.7	0.5	8.2	3.0	6.6	0.8
102	-8.8	2.3	14.6	1.8	4.2	0.3	7.3	2.3	6.5	0.6
100	-9.2	1.9	13.9	1.2	4.5	0.2	7.0	2.1	6.1	0.6
98	-8.7	1.7	12.0	0.9	4.8	0.2	7.2	1.9	5.7	0.5
96	-7.6	1.6	9.4	0.7	5.1	0.2	7.8	1.7	5.4	0.4
94	-6.1	1.5	6.7	0.5	5.6	0.2	8.5	1.6	5.2	0.3
92	-4.6	1.6	4.4	0.3	6.3	0.4	8.7	1.6	5.0	0.3
90	-3.4	1.8	3.1	0.3	7.5	1.2	8.4	1.8	5.0	0.4
88	-2.7	2.0	3.0	0.4	7.8	1.6	7.0	2.0	5.0	0.5
86	-3.0	2.5	4.4	0.7	6.9	1.0	4.4	2.6	5.3	1.1

Table 5.1 (c) 1979 June

ALTI-TUDE (km)	MEAN		DIURNAL				SEMIDIURNAL			
	AMP. (m/sec)	ERROR	AMP. (m/sec)	ERROR	PHASE (hr)	ERROR	AMP. (m/sec)	ERROR	PHASE (hr)	ERROR
104	21.7	5.8	17.8	4.6	12.0	1.0	34.8	4.2	4.4	0.2
102	19.0	4.1	18.0	2.3	10.0	0.8	31.0	3.0	4.3	0.1
100	16.3	3.6	20.3	0.8	9.1	0.6	26.4	2.5	4.2	0.1
98	13.7	3.2	21.8	0.7	8.8	0.5	21.2	2.0	4.0	0.1
96	11.4	2.8	22.2	0.3	9.0	0.5	16.1	1.5	3.9	0.1
94	9.4	2.6	22.2	1.4	9.4	0.5	11.6	1.1	3.6	0.1
92	7.8	2.7	22.5	2.2	10.0	0.5	8.3	0.6	3.2	0.1
90	6.7	3.0	23.6	2.9	10.6	0.5	6.7	0.3	2.8	0.2
88	6.2	3.2	25.6	3.7	11.0	0.6	7.0	0.4	2.7	0.2
86	6.4	3.8	28.4	5.2	11.2	0.7	9.4	0.2	2.9	0.0

Table 5.1 (d) 1979 July

ALTI-TUDE (km)	MEAN		DIURNAL				SEMIDIURNAL			
	AMP. (m/sec)	ERROR	AMP. (m/sec)	ERROR	PHASE (hr)	ERROR	AMP. (m/sec)	ERROR	PHASE (hr)	ERROR
104	5.8	3.1	10.5	1.8	9.8	1.4	19.2	2.2	4.0	0.1
102	7.0	2.5	11.4	1.9	10.2	1.0	17.9	1.8	4.1	0.1
100	7.1	2.3	11.7	2.0	10.6	0.9	16.5	1.8	4.3	0.1
98	6.2	2.1	11.6	2.0	11.1	0.9	15.3	1.7	4.6	0.2
96	4.6	1.9	11.3	2.0	11.6	0.8	14.3	1.7	4.8	0.2
94	2.5	1.9	10.8	2.1	12.1	0.7	13.5	1.9	5.1	0.2
92	0.0	2.1	10.2	2.4	12.6	0.8	12.9	2.2	5.4	0.3
90	-2.6	2.4	9.6	2.7	13.2	0.9	12.5	2.5	5.6	0.4
88	-5.2	2.6	9.1	3.0	13.8	0.9	12.1	2.8	5.7	0.4
86	-7.5	3.0	8.5	3.4	14.3	1.1	11.5	3.2	5.8	0.5

Table 5.1 (e) 1979 August

ALTI-TUDE (km)	MEAN		DIURNAL				SEMIDIURNAL			
	AMP. (m/sec)	ERROR	AMP. (m/sec)	ERROR	PHASE (hr)	ERROR	AMP. (m/sec)	ERROR	PHASE (hr)	ERROR
104	2.1	3.1	13.7	0.3	8.3	0.7	28.1	0.6	3.2	0.0
102	0.8	2.3	14.9	0.8	7.2	0.3	25.5	0.5	3.3	0.0
100	-0.1	1.9	16.1	0.6	6.6	0.2	23.3	0.6	3.4	0.0
98	-0.8	1.7	16.5	0.5	6.5	0.1	21.7	0.7	3.6	0.0
96	-1.3	1.4	16.0	0.4	6.5	0.1	20.8	0.8	3.9	0.0
94	-1.7	1.3	14.8	0.2	6.7	0.1	20.6	0.9	4.2	0.1
92	-2.0	1.4	13.3	0.3	7.1	0.2	20.8	1.1	4.4	0.1
90	-2.4	1.7	11.6	0.7	7.6	0.3	20.8	1.3	4.6	0.1
88	-2.9	1.9	9.9	1.0	8.2	0.5	20.1	1.6	4.6	0.2
86	-3.7	2.2	8.1	1.6	8.8	0.9	18.4	1.8	4.6	0.2

Table 5.1 (f) 1979 September

ALTI-TUDE (km)	MEAN		DIURNAL				SEMIDIURNAL			
	AMP. (m/sec)	ERROR	AMP. (m/sec)	ERROR	PHASE (hr)	ERROR	AMP. (m/sec)	ERROR	PHASE (hr)	ERROR
104	5.9	3.6	11.4	3.2	11.1	1.1	29.9	0.1	3.0	0.0
102	3.5	2.3	7.6	1.9	10.0	1.1	28.4	0.4	3.2	0.0
100	1.8	1.8	6.6	0.6	8.0	0.7	26.5	0.5	3.4	0.0
98	0.7	1.5	7.6	0.2	6.4	0.2	24.1	0.6	3.5	0.0
96	0.1	1.3	9.1	0.2	5.7	0.1	21.5	0.6	3.7	0.0
94	-0.1	1.3	10.2	0.4	5.4	0.1	19.0	0.7	3.8	0.1
92	0.0	1.4	10.6	0.5	5.3	0.1	16.6	0.8	4.0	0.1
90	0.3	1.7	10.1	0.8	5.1	0.2	14.7	1.0	4.1	0.1
88	0.7	2.0	8.6	1.1	4.9	0.2	13.5	1.2	4.1	0.2
86	1.1	2.5	6.1	1.9	4.1	0.5	13.1	1.5	4.1	0.2

Table 5.1 (g) 1979 October

ALTI-TUDE (km)	MEAN		DIURNAL				SEMIDIURNAL			
	AMP. (m/sec)	ERROR	AMP. (m/sec)	ERROR	PHASE (hr)	ERROR	AMP. (m/sec)	ERROR	PHASE (hr)	ERROR
104	4.2	9.4	12.3	10.9	11.2	3.8	8.7	6.3	4.8	1.2
102	0.6	5.3	7.7	4.8	9.8	3.2	7.2	4.2	4.9	0.9
100	-1.9	3.4	6.6	1.3	7.5	1.1	5.4	3.2	4.9	0.9
98	-3.2	2.8	8.3	0.2	5.9	0.1	3.5	2.6	4.8	1.1
96	-3.7	2.5	10.5	0.6	5.4	0.2	1.7	1.6	3.9	0.5
94	-3.3	2.4	12.4	0.5	5.3	0.2	1.7	1.3	1.5	2.6
92	-2.3	2.5	13.6	0.3	5.4	0.2	3.2	2.4	0.6	1.7
90	-0.9	2.9	14.1	0.2	5.7	0.1	4.5	2.9	0.4	1.4
88	0.9	3.3	13.5	0.3	6.1	0.1	5.3	3.2	0.4	1.3
86	2.9	3.7	12.0	0.4	6.7	0.4	5.3	3.5	0.5	1.4

Table 5.1 (h) 1979 November

ALTI-TUDE (km)	MEAN		DIURNAL				SEMIDIURNAL			
	AMP. (m/sec)	ERROR	AMP. (m/sec)	ERROR	PHASE (hr)	ERROR	AMP. (m/sec)	ERROR	PHASE (hr)	ERROR
104	-7.1	8.5	24.0	9.8	22.9	2.1	12.9	1.6	9.7	0.4
102	-8.9	6.1	23.1	8.2	23.7	1.4	11.8	0.7	9.8	0.4
100	-9.6	5.2	22.6	7.4	0.2	1.2	10.7	1.0	9.9	0.4
98	-9.4	4.5	21.6	6.7	0.4	1.1	9.6	0.7	9.8	0.4
96	-8.3	3.6	19.9	5.6	0.4	1.0	8.4	0.2	9.7	0.4
94	-6.6	3.0	17.8	4.6	0.0	1.0	7.1	0.3	9.6	0.4
92	-4.4	3.1	15.7	4.5	23.3	1.2	5.8	0.3	9.5	0.4
90	-1.9	3.8	14.5	4.3	22.1	1.5	4.4	0.2	9.5	0.6
88	0.8	4.4	15.2	2.8	20.7	1.4	3.0	1.4	10.0	1.6
86	3.4	5.0	18.0	0.8	19.5	0.9	2.8	4.4	11.7	3.2

Table 5.1 (i) 1979 December

ALTI-TUDE (km)	MEAN		DIURNAL				SEMIDIURNAL			
	AMP. (m/sec)	ERROR	AMP. (m/sec)	ERROR	PHASE (hr)	ERROR	AMP. (m/sec)	ERROR	PHASE (hr)	ERROR
104	6.0	4.2	17.0	5.6	1.1	1.1	6.1	2.2	10.0	0.6
102	7.6	3.3	14.5	4.3	0.8	1.1	3.9	2.6	10.4	1.1
100	7.9	2.9	12.5	3.9	0.6	1.2	2.9	3.1	11.4	2.0
98	7.2	2.7	10.9	3.6	0.4	1.2	3.1	2.8	0.4	1.8
96	5.8	2.4	9.8	3.2	0.2	1.2	4.0	2.3	0.9	1.2
94	4.0	2.2	9.3	3.1	0.2	1.3	4.9	2.2	1.0	0.9
92	2.0	2.3	9.3	3.3	0.1	1.3	5.7	2.6	1.0	0.9
90	0.2	2.6	10.0	3.6	0.1	1.4	6.3	3.0	0.8	0.9
88	-1.2	2.8	11.4	3.8	0.1	1.3	6.8	3.4	0.6	1.0
86	-1.9	3.0	13.7	4.2	0.0	1.2	7.2	3.8	0.3	1.0

Table 5.1 (j) 1980 January

ALTI-TUDE (km)	MEAN		DIURNAL				SEMIDIURNAL			
	AMP. (m/sec)	ERROR	AMP. (m/sec)	ERROR	PHASE (hr)	ERROR	AMP. (m/sec)	ERROR	PHASE (hr)	ERROR
104	8.8	2.4	4.4	2.3	22.3	2.0	18.7	0.3	8.7	0.1
102	9.5	1.7	4.3	1.7	22.4	1.5	16.7	0.2	8.6	0.1
100	9.8	1.4	4.5	1.5	22.8	1.2	14.4	0.3	8.6	0.1
98	9.8	1.2	5.0	1.4	23.4	1.0	12.0	0.3	8.5	0.1
96	9.6	1.1	5.6	1.3	23.8	0.8	9.7	0.4	8.4	0.1
94	9.3	1.1	6.3	1.2	0.1	0.8	7.5	0.5	8.1	0.2
92	9.0	1.2	6.6	1.3	0.3	0.8	5.6	0.8	7.9	0.3
90	8.7	1.3	6.5	1.5	0.3	0.9	4.2	1.1	7.5	0.6
88	8.6	1.5	5.6	1.7	0.0	1.2	3.2	1.4	7.2	0.9
86	8.7	1.7	4.1	2.1	23.1	1.8	2.5	1.6	7.3	1.4

Table 5.1 (k) 1980 February

ALTI-TUDE (km)	MEAN		DIURNAL				SEMIDIURNAL			
	AMP. (m/sec)	ERROR	AMP. (m/sec)	ERROR	PHASE (hr)	ERROR	AMP. (m/sec)	ERROR	PHASE (hr)	ERROR
104	9.8	6.6	17.4	5.1	22.3	1.6	13.2	2.6	7.9	0.5
102	8.9	4.6	17.4	4.3	22.8	1.2	11.6	2.7	7.6	0.5
100	8.5	3.5	17.1	3.8	23.1	0.9	9.4	2.8	7.2	0.6
98	8.5	2.7	16.5	3.3	23.5	0.8	6.9	2.8	6.8	0.8
96	8.6	2.3	15.4	2.9	23.8	0.7	4.8	2.8	5.9	1.1
94	8.7	2.4	13.8	2.9	0.2	0.8	4.3	2.2	4.3	0.8
92	8.7	2.8	11.6	3.4	0.8	1.1	6.2	0.7	3.2	0.1
90	8.3	3.4	9.1	4.1	1.7	1.5	9.0	0.5	2.7	0.2
88	7.5	4.4	7.0	4.4	3.6	0.5	11.7	0.6	2.4	0.3
86	5.9	6.2	7.4	2.4	6.4	1.4	14.1	1.7	2.3	0.5

Table 5.1 (l) 1980 March

ALTI-TUDE (km)	MEAN		DIURNAL				SEMIDIURNAL			
	AMP. (m/sec)	ERROR	AMP. (m/sec)	ERROR	PHASE (hr)	ERROR	AMP. (m/sec)	ERROR	PHASE (hr)	ERROR
104	1.5	2.4	12.9	2.4	0.4	0.7	10.4	1.7	4.1	0.2
102	1.3	1.7	14.5	1.7	0.9	0.4	9.6	1.5	4.4	0.2
100	0.7	1.4	15.0	1.5	1.2	0.3	9.2	1.4	4.6	0.2
98	0.0	1.3	14.5	1.3	1.5	0.3	9.1	1.3	4.9	0.2
96	-0.9	1.2	13.3	1.1	1.7	0.3	9.4	1.3	5.2	0.2
94	-1.8	1.2	11.7	1.1	1.9	0.3	9.9	1.4	5.4	0.2
92	-2.8	1.3	9.8	1.2	2.0	0.5	10.3	1.6	5.5	0.3
90	-3.7	1.5	8.0	1.5	1.8	0.7	10.5	1.9	5.6	0.3
88	-4.5	1.8	6.7	1.9	0.9	1.0	10.3	2.2	5.5	0.4
86	-5.1	2.2	7.0	2.4	23.4	1.4	9.9	2.6	5.3	0.5

Table 5.1 (m) 1980 April

ALTI-TUDE (km)	MEAN		DIURNAL				SEMIDIURNAL			
	AMP. (m/sec)	ERROR	AMP. (m/sec)	ERROR	PHASE (hr)	ERROR	AMP. (m/sec)	ERROR	PHASE (hr)	ERROR
104	-11.9	3.0	11.9	1.4	4.9	0.3	10.3	2.3	4.6	0.4
102	-11.4	2.3	9.0	0.5	5.7	0.2	11.9	2.0	4.8	0.3
100	-10.3	1.9	5.9	0.3	6.6	0.4	12.7	1.8	4.9	0.3
98	-8.8	1.7	3.2	0.8	8.4	1.5	12.9	1.7	5.1	0.3
96	-7.3	1.6	2.4	1.7	12.9	2.6	12.8	1.7	5.2	0.3
94	-6.0	1.7	4.1	1.3	15.4	0.9	12.7	1.8	5.3	0.3
92	-5.1	1.9	5.8	1.2	16.0	0.9	12.5	2.1	5.3	0.3
90	-4.9	2.2	6.5	1.5	15.9	0.6	12.7	2.4	5.2	0.4
88	-5.6	2.6	6.3	2.3	15.1	1.2	13.6	2.6	5.0	0.4
86	-7.5	3.4	6.3	4.2	13.0	2.5	15.7	3.0	4.7	0,4

Table 5.1 (n) 1989 May

ALTI-TUDE (km)	MEAN		DIURNAL				SEMIDIURNAL			
	AMP. (m/sec)	ERROR	AMP. (m/sec)	ERROR	PHASE (hr)	ERROR	AMP. (m/sec)	ERROR	PHASE (hr)	ERROR
104	9.2	3.1	4.8	3.2	10.7	1.8	19.5	2.0	4.8	0.3
102	8.8	2.3	2.8	2.3	11.7	3.1	20.6	1.8	5.0	0.2
100	8.6	1.9	2.6	1.5	14.0	2.8	21.1	1.6	5.1	0.2
98	8.4	1.6	3.9	1.0	15.1	1.4	21.1	1.4	5.1	0.1
96	8.2	1.4	5.7	0.8	15.3	0.8	20.8	1.3	5.0	0.1
94	7.8	1.5	7.7	0.9	15.4	0.6	20.3	1.4	4.9	0.1
92	7.2	1.8	9.5	1.1	15.4	0.5	19.7	1.5	4.8	0.2
90	6.2	2.1	11.0	1.2	15.6	0.5	19.2	1.8	4.8	0.2
88	4.9	2.4	11.9	1.2	16.0	0.5	18.8	2.0	4.8	0.2
86	2.9	2.9	12.4	0.2	16.7	0.6	18.7	2.4	4.9	0.3

Table 5.1 (o) 1980 June

ALTI-TUDE (km)	MEAN		DIURNAL				SEMIDIURNAL			
	AMP. (m/sec)	ERROR	AMP. (m/sec)	ERROR	PHASE (hr)	ERROR	AMP. (m/sec)	ERROR	PHASE (hr)	ERROR
104	11.6	1.9	12.2	0.8	6.6	0.2	18.0	2.1	5.2	0.2
102	11.1	1.4	11.7	0.9	7.7	0.1	17.9	1.5	5.0	0.2
100	10.4	1.2	11.4	1.0	8.9	0.3	18.1	1.3	4.9	0.1
98	9.5	1.1	11.9	1.1	10.1	0.3	18.2	1.1	4.9	0.1
96	8.4	1.0	13.0	1.1	11.1	0.3	18.3	1.1	5.0	0.1
94	7.1	1.0	14.3	1.2	11.9	0.3	18.3	1.1	5.1	0.1
92	5.6	1.2	15.4	1.4	12.5	0.3	18.0	1.3	5.1	0.1
90	3.8	1.3	15.8	1.5	12.8	0.4	17.4	1.5	5.2	0.2
88	1.7	1.5	15.1	1.8	12.9	0.5	16.3	1.7	5.1	0.2
86	-0.7	1.8	12.9	2.3	12.8	0.7	14.8	2.0	4.8	0.2

Table 5.1 (p) 1980 July

ALTI-TUDE (km)	MEAN		DIURNAL				SEMIDIURNAL			
	AMP. (m/sec)	ERROR	AMP. (m/sec)	ERROR	PHASE (hr)	ERROR	AMP. (m/sec)	ERROR	PHASE (hr)	ERROR
104	13.0	2.4	17.4	0.5	6.4	0.2	9.8	1.4	4.1	0.3
102	12.5	1.8	16.8	0.4	7.5	0.3	11.2	1.1	4.0	0.2
100	11.7	1.6	15.9	0.5	8.5	0.4	12.3	1.0	4.1	0.1
98	10.7	1.4	14.8	0.9	9.4	0.9	13.1	1.0	4.3	0.1
96	9.5	1.3	13.6	1.2	10.4	0.4	13.9	1.1	4.5	0.1
94	8.0	1.3	12.8	1.5	11.3	0.5	14.6	1.2	4.8	0.1
92	6.4	1.5	12.3	1.9	12.2	0.6	15.2	1.4	5.0	0.2
90	4.6	1.6	11.9	2.2	12.7	0.6	15.6	1.7	5.2	0.2
88	2.7	1.8	11.4	2.4	12.8	0.7	15.6	2.0	5.4	0.2
86	0.6	2.1	10.9	3.0	12.3	1.0	14.9	2.5	5.4	0.3

Table 5.1 (q) 1980 August

ALTI-TUDE (km)	MEAN		DIURNAL				SEMIDIURNAL			
	AMP. (m/sec)	ERROR	AMP. (m/sec)	ERROR	PHASE (hr)	ERROR	AMP. (m/sec)	ERROR	PHASE (hr)	ERROR
104	3.8	2.4	18.6	1.3	3.4	0.4	19.1	0.6	3.4	0.1
102	5.5	1.8	14.8	0.7	3.9	0.4	19.9	0.6	3.7	0.1
100	6.6	1.5	10.9	0.2	4.8	0.3	21.2	0.7	3.9	0.1
98	7.1	1.4	8.1	0.5	6.6	0.1	22.5	0.8	4.1	0.1
96	7.3	1.3	8.0	1.3	9.0	0.5	23.5	0.9	4.2	0.1
94	7.3	1.4	10.4	1.7	10.7	0.6	24.1	1.0	4.3	0.1
92	7.0	1.6	13.1	2.0	11.4	0.6	24.0	1.2	4.4	0.1
90	6.7	1.8	14.9	2.2	11.8	0.6	22.9	1.4	4.4	0.1
88	6.5	2.0	15.3	2.5	11.8	0.6	20.8	1.6	4.4	0.1
86	6.4	2.5	13.9	3.1	11.6	0.8	17.3	2.1	4.5	0.2

Table 5.1 (r) 1980 September

ALTI-TUDE (km)	MEAN		DIURNAL				SEMIDIURNAL			
	AMP. (m/sec)	ERROR	AMP. (m/sec)	ERROR	PHASE (hr)	ERROR	AMP. (m/sec)	ERROR	PHASE (hr)	ERROR
104	-0.2	1.7	10.2	1.5	1.7	0.5	15.3	1.0	4.1	0.1
102	-0.2	1.1	8.9	1.0	2.1	0.5	14.6	0.8	4.2	0.1
100	-0.1	1.0	7.2	0.7	2.9	0.4	13.8	0.7	4.2	0.1
98	0.1	0.9	5.8	0.4	4.1	0.3	13.1	0.6	4.2	0.1
96	0.3	0.8	5.3	0.1	5.9	0.0	12.4	0.5	4.1	0.1
94	0.5	0.8	5.7	0.4	7.6	0.2	11.8	0.5	4.0	0.1
92	0.9	0.9	6.6	0.7	8.7	0.3	11.6	0.4	3.8	0.1
90	1.4	1.0	7.2	1.0	9.4	0.4	11.6	0.4	3.6	0.1
88	1.9	1.1	7.0	1.2	10.0	0.6	12.1	0.3	3.4	0.1
86	2.6	1.4	5.8	1.5	10.4	1.0	13.1	0.2	3.2	0.0

Table 5.1 (s) 1980 October

ALTI-TUDE (km)	MEAN		DIURNAL				SEMIDIURNAL			
	AMP. (m/sec)	ERROR	AMP. (m/sec)	ERROR	PHASE (hr)	ERROR	AMP. (m/sec)	ERROR	PHASE (hr)	ERROR
104	5.7	2.8	7.5	3.0	12.6	1.6	13.1	2.8	6.5	0.6
102	5.4	2.1	6.5	2.5	11.7	1.5	11.1	1.9	6.7	0.4
100	5.2	1.7	5.8	1.9	10.4	1.4	9.3	1.6	6.7	0.4
98	5.1	1.5	6.0	1.2	8.7	0.9	7.8	1.4	6.6	0.4
96	5.0	1.3	7.1	0.5	7.4	0.4	6.5	1.4	6.3	0.5
94	5.0	1.3	8.7	0.1	6.5	0.1	5.7	1.5	5.9	0.5
92	5.1	1.4	10.1	0.0	6.1	0.0	5.3	1.7	5.5	0.5
90	5.1	1.6	10.9	0.2	5.8	0.0	4.9	1.9	5.2	0.6
88	5.1	1.9	10.9	0.3	5.7	0.0	4.3	2.1	5.0	0.7
86	5.0	2.3	9.7	0.3	5.9	0.1	3.1	2.6	5.2	1.3

Table 5.1 (t) 1980 November

ALTI-TUDE (km)	MEAN		DIURNAL				SEMIDIURNAL			
	AMP. (m/sec)	ERROR	AMP. (m/sec)	ERROR	PHASE (hr)	ERROR	AMP. (m/sec)	ERROR	PHASE (hr)	ERROR
104	4.0	7.5	7.9	2.2	17.8	1.0	6.7	2.8	10.7	1.3
102	1.1	4.4	8.8	1.1	20.1	2.0	4.8	2.1	10.4	1.1
100	-0.7	3.2	10.4	3.1	21.2	1.5	3.7	1.8	10.3	1.1
98	-1.4	3.0	11.3	3.3	21.8	1.4	3.2	1.7	10.5	1.3
96	-1.5	2.8	11.4	3.4	22.1	1.4	3.1	1.9	10.9	1.4
94	-1.1	2.7	10.7	3.6	22.3	1.5	3.5	2.4	11.3	1.4
92	-0.5	2.9	9.5	4.1	22.4	1.8	3.9	2.9	11.6	1.4
90	-0.1	3.2	8.2	4.5	22.5	2.3	4.3	3.3	11.8	1.5
88	0.0	3.5	6.9	4.8	22.5	2.9	4.2	3.5	11.9	1.6
86	-0.5	4.1	6.0	5.7	22.6	4.0	3.4	4.1	0.1	2.3

Table 5.2 The same as Table 5.1 except for zonal component.

Phase corresponds to the local time of the eastward maximum wind.

Table 5.2 (a) 1979 March

ALTI-TUDE (km)	MEAN		DIURNAL				SEMIDIURNAL			
	AMP. (m/sec)	ERROR	AMP. (m/sec)	ERROR	PHASE (hr)	ERROR	AMP. (m/sec)	ERROR	PHASE (hr)	ERROR
104	0.3	4.3	6.6	3.2	22.6	2.3	10.8	4.4	11.4	0.7
102	2.8	3.3	8.6	1.1	20.2	1.0	6.6	3.5	11.4	1.0
100	4.6	2.8	11.0	0.1	18.9	0.4	3.7	3.2	11.8	1.6
98	5.7	2.5	12.6	0.1	18.1	0.1	2.4	2.6	0.8	2.1
96	6.3	2.2	13.4	0.6	17.4	0.1	2.8	1.6	1.7	1.1
94	6.2	2.1	13.4	1.2	16.6	0.0	3.9	1.4	1.7	0.7
92	5.6	2.1	13.0	1.8	15.7	0.2	5.3	1.6	1.5	0.7
90	4.6	2.3	12.6	2.4	14.6	0.5	7.1	2.1	1.1	0.6
88	3.1	2.4	12.7	2.8	13.2	0.7	9.4	2.6	0.7	0.6
86	1.2	2.8	14.0	3.2	11.8	0.9	12.2	3.2	0.4	0.5

Table 5.2 (b) 1979 April

ALTI-TUDE (km)	MEAN		DIURNAL				SEMIDIURNAL			
	AMP. (m/sec)	ERROR	AMP. (m/sec)	ERROR	PHASE (hr)	ERROR	AMP. (m/sec)	ERROR	PHASE (hr)	ERROR
104	-6.4	10.1	24.2	6.5	8.4	1.6	27.6	8.9	12.0	0.6
102	1.0	6.7	18.2	2.7	9.9	1.6	25.9	6.6	0.2	0.5
100	6.4	5.4	15.0	5.8	11.7	1.6	23.3	5.4	0.4	0.5
98	9.7	4.8	14.0	6.0	13.5	1.1	20.0	4.6	0.6	0.5
96	11.0	4.4	13.7	5.1	14.9	0.4	16.5	3.9	0.8	0.5
94	10.5	4.2	12.3	3.8	16.0	0.6	12.9	3.5	1.0	0.6
92	8.2	4.2	9.1	2.1	17.3	0.7	9.2	3.7	0.9	0.8
90	4.2	4.4	4.8	1.1	20.7	3.7	6.5	4.6	0.1	1.4
88	-1.4	5.0	9.5	5.9	2.4	1.3	8.8	4.0	10.6	0.8
86	-8.4	6.9	22.5	6.7	3.9	0.6	16.8	3.9	10.1	0.3

Table 5.2 (c) 1979 June

ALTI-TUDE (km)	MEAN		DIURNAL				SEMIDIURNAL			
	AMP. (m/sec)	ERROR	AMP. (m/sec)	ERROR	PHASE (hr)	ERROR	AMP. (m/sec)	ERROR	PHASE (hr)	ERROR
104	10.1	9.8	61.3	0.7	6.1	0.0	31.7	6.7	10.4	0.5
102	22.7	8.0	48.4	1.5	6.6	0.2	25.4	3.2	9.8	0.3
100	29.8	7.1	34.5	1.8	7.4	0.5	21.4	1.4	9.3	0.1
98	32.6	6.4	22.6	3.2	9.0	1.1	17.8	0.5	9.0	0.0
96	32.0	5.9	18.7	6.7	11.9	1.4	13.8	0.3	9.0	0.1
94	29.1	6.0	24.4	6.9	14.1	0.7	9.5	1.2	9.2	0.2
92	24.9	6.5	31.6	6.5	15.1	0.4	6.0	4.0	9.9	0.7
90	20.4	7.0	35.7	7.9	15.3	0.4	5.3	7.5	11.4	2.6
88	16.6	7.2	34.9	5.7	15.2	0.7	6.7	8.5	0.2	2.4
86	14.5	8.5	29.2	9.6	14.2	1.4	7.2	10.2	0.5	2.6

Table 5.2 (d) 1979 July

ALTI-TUDE (km)	MEAN		DIURNAL				SEMIDIURNAL			
	AMP. (m/sec)	ERROR	AMP. (m/sec)	ERROR	PHASE (hr)	ERROR	AMP. (m/sec)	ERROR	PHASE (hr)	ERROR
104	7.2	7.7	1.8	2.4	19.2	10.1	19.9	3.8	7.7	0.7
102	14.0	6.2	3.5	7.6	13.7	6.0	17.7	4.0	7.6	0.6
100	18.7	5.5	4.9	6.9	14.1	3.6	17.6	3.7	7.6	0.5
98	21.6	5.0	5.4	5.2	15.4	1.3	18.8	3.2	7.6	0.4
96	22.9	4.5	6.4	2.1	17.3	0.8	20.9	2.8	7.8	0.3
94	22.9	4.5	8.5	1.1	18.7	0.8	23.2	2.6	7.9	0.3
92	21.8	5.0	10.9	0.6	19.5	1.1	25.0	2.5	8.0	0.3
90	20.0	5.6	12.6	1.2	19.9	1.3	25.7	2.5	8.0	0.3
88	17.6	6.1	12.7	0.2	20.0	1.5	24.4	2.6	8.0	0.4
86	14.8	7.2	10.5	2.1	19.6	2.0	20.4	3.3	8.0	0.4

Table 5.2 (e) 1979 August

ALTI-TUDE (km)	MEAN		DIURNAL				SEMIDIURNAL			
	AMP. (m/sec)	ERROR	AMP. (m/sec)	ERROR	PHASE (hr)	ERROR	AMP. (m/sec)	ERROR	PHASE (hr)	ERROR
104	-12.2	7.6	31.1	1.6	6.2	0.2	5.0	6.6	6.8	2.8
102	-0.4	5.7	26.4	1.1	8.1	0.7	8.9	5.7	5.2	1.1
100	8.1	4.9	25.8	3.3	9.6	0.8	13.0	5.1	5.4	0.7
98	13.8	4.2	25.2	4.0	10.6	0.8	16.7	4.6	5.9	0.5
96	17.2	3.6	23.2	4.0	11.4	0.7	21.0	3.9	6.4	0.4
94	18.6	3.3	19.9	3.9	12.0	0.7	25.6	3.4	6.8	0.3
92	18.7	3.5	15.9	4.1	12.8	1.0	29.6	3.3	7.2	0.2
90	17.9	3.9	12.0	4.4	13.8	1.2	31.5	3.1	7.5	0.2
88	16.6	4.4	9.4	4.5	15.0	1.2	30.1	2.9	7.8	0.2
86	15.3	5.3	8.3	4.5	16.1	0.8	24.2	2.5	8.2	0.2

Table 5.2 (f) 1979 September

ALTI-TUDE (km)	MEAN		DIURNAL				SEMIDIURNAL			
	AMP. (m/sec)	ERROR	AMP. (m/sec)	ERROR	PHASE (hr)	ERROR	AMP. (m/sec)	ERROR	PHASE (hr)	ERROR
104	-11.6	9.4	41.0	11.8	2.4	0.2	24.6	2.8	8.1	0.4
102	-2.8	6.5	29.6	7.6	2.8	0.1	23.6	3.2	7.7	0.4
100	3.3	5.0	22.0	5.3	3.3	0.2	24.8	3.3	7.5	0.3
98	7.1	4.1	17.4	3.6	3.9	0.2	27.0	3.1	7.4	0.3
96	9.0	3.5	14.7	2.4	4.5	0.2	29.4	2.8	7.5	0.2
94	9.3	3.3	12.9	1.7	4.8	0.3	31.6	2.6	7.6	0.2
92	8.4	3.5	11.1	1.7	4.9	0.3	33.2	2.5	7.7	0.2
90	6.7	4.0	8.8	2.1	4.9	0.2	33.6	2.5	7.8	0.2
88	4.6	4.6	5.3	2.4	5.1	0.8	32.2	2.6	8.0	0.2
86	2.6	5.6	1.1	6.9	10.4	27.9	28.6	3.0	8.1	0.2

Table 5.2 (g) 1979 October

ALTI-TUDE (km)	MEAN		DIURNAL				SEMIDIURNAL			
	AMP. (m/sec)	ERROR	AMP. (m/sec)	ERROR	PHASE (hr)	ERROR	AMP. (m/sec)	ERROR	PHASE (hr)	ERROR
104	6.6	14.7	22.6	3.7	18.9	0.9	1.4	3.8	8.6	7.9
102	8.2	9.5	20.3	7.3	20.0	1.1	7.6	3.0	8.6	1.1
100	10.6	8.4	17.7	8.5	20.7	1.7	8.7	1.8	8.6	0.7
98	13.3	8.2	14.2	8.8	21.2	2.6	6.1	0.9	8.8	0.6
96	16.1	7.5	9.9	8.1	21.4	3.7	1.3	4.5	10.0	4.3
94	18.5	6.8	5.6	6.9	21.4	5.7	5.6	0.5	2.3	1.3
92	20.1	6.8	2.0	5.0	20.3	10.9	11.8	2.1	2.5	0.6
90	20.6	7.5	1.2	7.6	15.0	23.3	16.8	2.4	2.6	0.4
88	19.7	8.1	1.5	6.5	15.8	16.4	19.3	2.2	2.7	0.3
86	16.9	8.3	3.7	7.3	20.6	7.7	18.0	1.3	2.9	0.2

Table 5.2 (h) 1979 November

ALTI-TUDE (km)	MEAN		DIURNAL				SEMIDIURNAL			
	AMP. (m/sec)	ERROR	AMP. (m/sec)	ERROR	PHASE (hr)	ERROR	AMP. (m/sec)	ERROR	PHASE (hr)	ERROR
104	-8.8	43.1	27.9	58.6	3.2	1.4	24.1	24.1	6.3	1.7
102	-7.1	30.7	33.0	48.6	1.6	4.1	29.5	20.5	6.8	0.9
100	-3.4	25.2	33.1	41.2	0.8	4.2	28.9	18.1	7.1	0.8
98	1.3	21.3	27.6	34.8	0.2	4.7	23.0	15.1	7.3	0.8
96	6.3	17.3	18.3	26.8	23.5	5.9	13.6	10.8	7.7	0.8
94	10.6	13.7	8.4	15.4	21.6	9.1	5.4	2.7	9.7	1.9
92	13.4	12.4	7.5	13.0	15.7	4.6	12.5	12.4	0.0	1.9
90	13.9	13.1	13.9	19.3	13.7	4.8	22.0	13.5	0.3	1.2
88	11.1	14.9	16.3	22.9	13.0	5.0	28.7	15.2	0.2	1.0
86	4.2	20.8	11.4	31.8	12.2	10.3	31.5	17.7	11.8	1.1

Table 5.2 (i) 1979 December

ALTI-TUDE (km)	MEAN		DIURNAL				SEMIDIURNAL			
	AMP. (m/sec)	ERROR	AMP. (m/sec)	ERROR	PHASE (hr)	ERROR	AMP. (m/sec)	ERROR	PHASE (hr)	ERROR
104	3.3	12.2	5.9	4.7	5.6	2.4	17.7	11.8	3.1	0.1
102	0.3	9.9	10.3	13.8	1.7	4.4	23.7	10.7	6.2	0.9
100	-1.0	8.8	12.4	12.3	0.9	3.7	23.9	9.5	6.5	0.8
98	-1.2	7.9	10.8	11.0	0.5	3.9	18.5	8.0	6.8	0.9
96	-0.7	7.2	7.0	10.4	0.2	5.7	9.7	5.6	7.5	1.3
94	-0.1	7.3	2.6	10.9	23.8	16.2	7.1	6.6	10.5	1.7
92	0.1	8.0	0.7	12.2	11.6	65.3	17.3	9.9	11.7	1.1
90	-0.6	8.9	1.7	8.8	8.6	19.2	27.3	11.1	11.9	0.8
88	-2.7	9.8	4.9	9.5	3.4	7.0	33.9	12.0	11.9	0.7
86	-6.8	11.2	15.8	14.6	2.0	3.3	35.3	13.1	11.8	0.7

Table 5.2 (j) 1980 January

ALTI-TUDE (km)	MEAN		DIURNAL				SEMIDIURNAL			
	AMP. (m/sec)	ERROR	AMP. (m/sec)	ERROR	PHASE (hr)	ERROR	AMP. (m/sec)	ERROR	PHASE (hr)	ERROR
104	-4.6	4.6	4.6	4.7	9.4	2.8	11.7	5.4	0.3	0.9
102	-4.5	3.6	2.2	3.3	8.7	3.2	13.8	4.3	0.5	0.6
100	-4.6	3.2	2.3	0.9	4.1	4.0	15.2	3.8	0.6	0.5
98	-4.9	2.9	5.0	2.0	2.8	2.2	16.0	3.3	0.8	0.4
96	-5.0	2.7	7.9	2.0	2.7	1.3	16.2	2.9	0.9	0.4
94	-5.0	2.6	10.4	1.9	2.9	0.9	15.8	2.8	1.0	0.4
92	-4.7	2.7	12.0	1.9	3.1	0.8	14.9	2.9	1.0	0.4
90	-3.9	2.9	12.0	2.0	3.4	0.8	13.6	3.1	1.1	0.5
88	-2.5	3.1	10.0	1.7	3.9	0.9	11.9	3.4	1.0	0.6
86	-0.4	3.4	5.9	0.2	5.5	0.5	9.9	4.0	0.7	0.8

Table 5.2 (k) 1980 February

ALTI-TUDE (km)	MEAN		DIURNAL				SEMIDIURNAL			
	AMP. (m/sec)	ERROR	AMP. (m/sec)	ERROR	PHASE (hr)	ERROR	AMP. (m/sec)	ERROR	PHASE (hr)	ERROR
104	-0.5	14.4	27.1	9.2	3.8	0.9	16.3	5.8	2.1	0.9
102	0.4	9.9	33.0	6.7	3.8	0.7	16.3	4.5	2.1	0.7
100	3.3	7.4	35.1	4.5	3.9	0.5	16.2	3.9	2.1	0.6
98	7.5	6.1	34.2	3.3	4.2	0.4	16.1	3.4	2.0	0.5
96	12.1	5.4	31.3	2.4	4.6	0.3	16.2	3.0	1.9	0.5
94	16.6	5.5	27.8	1.6	5.4	0.1	16.4	2.9	1.9	0.6
92	20.1	6.4	25.2	0.8	6.4	0.2	16.9	3.0	1.9	0.7
90	22.0	7.6	25.1	1.7	7.6	0.8	17.6	3.1	1.9	0.7
88	21.5	9.2	27.8	3.8	8.6	1.3	18.8	3.2	2.0	0.8
86	17.8	11.8	32.3	5.8	9.3	1.7	20.5	3.4	2.2	0.9

Table 5.2 (l) 1980 March

ALTI-TUDE (km)	MEAN AMP. (m/sec)	MEAN ERROR	DIURNAL AMP. (m/sec)	DIURNAL ERROR	DIURNAL PHASE (hr)	DIURNAL ERROR	SEMIDIURNAL AMP. (m/sec)	SEMIDIURNAL ERROR	SEMIDIURNAL PHASE (hr)	SEMIDIURNAL ERROR
104	4.1	6.4	14.4	5.9	2.0	1.3	15.5	6.8	6.2	0.9
102	4.8	4.4	10.8	3.6	3.0	0.9	18.4	5.0	6.2	0.5
100	4.8	3.6	8.9	1.6	4.9	0.1	20.1	4.1	6.3	0.4
98	4.3	3.2	9.7	0.3	6.9	0.5	20.7	3.5	6.4	0.3
96	3.4	2.8	12.0	1.5	8.2	0.6	20.5	3.1	6.6	0.3
94	2.3	2.7	14.3	2.1	9.0	0.6	19.7	2.8	6.8	0.2
92	0.9	2.9	15.4	2.8	9.6	0.7	18.2	2.8	7.0	0.4
90	-0.4	3.3	14.8	3.4.	10.2	0.9	15.9	3.0	7.1	0.5
88	-1.7	3.8	12.3	4.2	11.1	1.4	12.6	3.3	7.2	0.6
86	-2.7	4.7	9.2	5.6	13.4	2.0	8.2	4.6	7.0	1.2

Table 5.2 (m) 1980 April

ALTI-TUDE (km)	MEAN AMP. (m/sec)	MEAN ERROR	DIURNAL AMP. (m/sec)	DIURNAL ERROR	DIURNAL PHASE (hr)	DIURNAL ERROR	SEMIDIURNAL AMP. (m/sec)	SEMIDIURNAL ERROR	SEMIDIURNAL PHASE (hr)	SEMIDIURNAL ERROR
104	-8.2	9.2	21.7	4.7	7.4	1.1	3.4	6.3	7.0	4.4
102	-9.0	7.3	27.7	3.0	7.1	0.5	6.6	1.0	8.8	0.4
100	-7.4	6.1	27.9	2.7	7.3	0.5	10.3	1.1	9.2	0.2
98	-4.3	5.2	24.3	1.7	7.9	0.6	12.8	1.3	9.3	0.1
96	-0.3	4.4	19.5	2.0	9.1	0.8	13.8	1.1	9.3	0.1
94	3.7	4.1	17.3	4.3	11.1	1.1	13.4	0.7	9.2	0.0
92	7.1	4.5	19.6	5.5	13.1	0.9	11.3	0.2	9.0	0.0
90	9.0	5.1	23.3	5.9	14.2	0.6	8.1	1.7	8.4	0.4
88	8.6	5.7	24.8	6.4	14.8	0.5	6.0	5.7	6.8	1.8
86	5.4	6.9	21.2	7.7	15.0	0.8	10.6	6.8	5.1	1.2

Table 5.2 (n) 1980 May

ALTI-TUDE (km)	MEAN AMP. (m/sec)	MEAN ERROR	DIURNAL AMP. (m/sec)	DIURNAL ERROR	DIURNAL PHASE (hr)	DIURNAL ERROR	SEMIDIURNAL AMP. (m/sec)	SEMIDIURNAL ERROR	SEMIDIURNAL PHASE (hr)	SEMIDIURNAL ERROR
104	-0.4	7.1	4.9	8.2	11.5	5.5	17.5	6.7	7.2	0.4
102	0.7	5.3	14.8	6.5	9.9	1.0	11.3	5.0	7.3	0.5
100	2.5	4.5	20.0	5.6	9.8	0.7	6.7	3.7	7.8	0.4
98	4.6	4.0	20.8	5.0	9.8	0.6	4.9	0.6	9.1	0.3
96	6.9	3.5	18.1	4.5	10.0	0.6	6.6	1.4	10.1	0.8
94	9.0	3.5	13.0	4.2	10.5	1.0	9.0	2.2	10.4	0.7
92	10.8	3.9	6.8	4.4	12.0	2.4	11.0	2.6	10.4	0.6
90	11.9	4.4	5.2	0.5	17.3	0.8	12.4	2.7	10.2	0.5
88	12.1	4.8	11.1	2.9	19.9	0.9	12.9	2.0	9.9	0.4
86	11.2	5.6	17.2	5.1	20.7	1.1	12.9	1.0	9.3	0.3

Table 5.2 (o) 1980 June

ALTI-TUDE (km)	MEAN		DIURNAL				SEMIDIURNAL			
	AMP. (m/sec)	ERROR	AMP. (m/sec)	ERROR	PHASE (hr)	ERROR	AMP. (m/sec)	ERROR	PHASE (hr)	ERROR
104	-7.2	3.9	31.4	5.2	10.2	0.4	10.7	5.1	0.6	0.8
102	-0.6	3.0	30.7	4.0	10.3	0.4	8.8	3.9	11.9	0.9
100	4.2	2.6	28.9	3.4	10.6	0.4	8.6	2.6	10.9	0.7
98	7.5	2.3	26.2	3.0	10.9	0.4	10.3	1.4	10.1	0.4
96	9.4	2.1	23.0	2.8	11.2	0.4	12.8	0.8	9.7	0.2
94	10.2	2.2	19.4	2.8	11.7	0.5	15.2	0.6	9.5	0.1
92	10.1	2.3	15.7	2.9	12.3	0.7	16.8	0.7	9.4	0.1
90	9.5	2.6	11.8	3.1	13.1	1.1	17.4	1.0	9.5	0.1
88	8.4	2.9	7.7	3.1	14.0	1.7	16.9	1.7	9.8	0.2
86	7.2	3.5	3.3	2.1	16.1	2.8	16.1	3.1	10.3	0.3

Table 5.2 (p) 1980 July

ALTI-TUDE (km)	MEAN		DIURNAL				SEMIDIURNAL			
	AMP. (m/sec)	ERROR	AMP. (m/sec)	ERROR	PHASE (hr)	ERROR	AMP. (m/sec)	ERROR	PHASE (hr)	ERROR
104	-1.3	7.2	20.8	8.8	11.8	1.6	2.8	3.3	8.3	1.8
102	1.1	5.2	22.0	6.5	11.8	1.1	2.4	4.4	10.6	3.8
100	4.1	4.3	21.4	5.5	12.3	1.0	2.8	4.8	11.5	3.3
98	7.4	3.7	20.0	4.8	13.1	0.9	2.2	4.4	11.8	3.8
96	10.6	3.3	18.8	3.8	14.3	0.7	0.6	3.7	11.4	11.9
94	13.3	3.2	18.7	2.7	15.6	0.5	1.9	3.8	6.8	3.4
92	15.3	3.6	19.3	1.7	16.9	0.2	4.9	4.1	6.8	1.5
90	16.1	4.1	19.5	0.1	18.0	0.1	8.2	4.3	7.0	0.9
88	15.5	4.4	18.6	1.5	19.3	0.5	11.9	4.4	7.3	0.6
86	13.1	5.0	16.6	4.6	21.1	1.2	16.0	4.6	7.6	0.5

Table 5.2 (q) 1980 August

ALTI-TUDE (km)	MEAN		DIURNAL				SEMIDIURNAL			
	AMP. (m/sec)	ERROR	AMP. (m/sec)	ERROR	PHASE (hr)	ERROR	AMP. (m/sec)	ERROR	PHASE (hr)	ERROR
104	1.1	6.4	17.8	5.8	8.4	0.2	30.6	6.8	5.1	0.4
102	0.5	4.5	25.4	3.9	8.1	0.1	30.2	4.5	4.9	0.3
100	1.0	3.7	29.5	3.5	8.4	0.2	28.5	3.7	4.9	0.3
98	2.3	3.4	31.0	3.6	8.9	0.3	25.5	3.5	5.1	0.3
96	4.0	3.2	31.3	3.7	9.6	0.3	22.0	3.7	5.4	0.3
94	5.9	3.3	30.9	4.1	10.4	0.4	18.9	4.0	5.9	0.4
92	7.6	3.6	30.0	4.5	11.2	0.5	17.5	3.8	6.7	0.4
90	8.8	3.8	27.9	4.9	11.9	0.7	18.7	2.7	7.5	0.4
88	9.2	4.0	23.1	5.3	12.4	0.9	22.0	1.4	8.2	0.2
86	8.4	4.6	14.3	6.0	12.6	1.7	26.2	0.7	8.7	0.1

Table 5.2 (r) 1980 September

ALTI-TUDE (km)	MEAN		DIURNAL				SEMIDIURNAL			
	AMP. (m/sec)	ERROR	AMP. (m/sec)	ERROR	PHASE (hr)	ERROR	AMP. (m/sec)	ERROR	PHASE (hr)	ERROR
104	-4.5	3.8	9.8	0.3	5.9	0.1	2.6	2.6	7.8	2.0
102	-4.2	2.8	10.8	0.5	6.3	0.0	8.7	3.0	7.1	0.7
100	-3.2	2.4	10.8	1.2	7.3	0.2	13.3	2.6	7.1	0.4
98	-1.6	2.2	11.0	1.9	8.8	0.5	16.4	2.3	7.1	0.3
96	0.3	2.0	12.4	2.2	10.3	0.6	18.0	2.1	7.2	0.2
94	2.4	1.9	14.7	2.3	11.5	0.6	18.2	1.9	7.3	0.2
92	4.3	2.0	16.7	2.4	12.3	0.6	17.2	1.8	7.5	0.2
90	5.9	2.2	17.5	2.6	13.0	0.6	15.2	1.7	7.7	0.2
88	6.9	2.5	16.1	2.7	13.7	0.7	12.4	1.4	8.1	0.3
86	7.2	3.1	12.1	3.0	15.0	0.8	9.5	0.3	8.7	0.1

Table 5.2 (s) 1980 October

ALTI-TUDE (km)	MEAN		DIURNAL				SEMIDIURNAL			
	AMP. (m/sec)	ERROR	AMP. (m/sec)	ERROR	PHASE (hr)	ERROR	AMP. (m/sec)	ERROR	PHASE (hr)	ERROR
104	-1.2	6.1	5.7	8.0	1.3	4.9	10.7	6.0	10.5	0.4
102	2.6	4.9	8.9	6.3	22.9	2.9	10.5	2.9	9.7	0.2
100	6.0	4.2	11.9	5.3	22.3	1.8	10.4	1.7	9.4	0.2
98	8.8	3.7	13.4	4.7	22.2	1.4	9.4	1.4	9.3	0.2
96	11.0	3.3	13.6	4.1	22.4	1.2	7.9	1.8	9.5	0.3
94	12.4	3.2	12.5	4.0	22.7	1.3	6.5	2.8	10.1	0.2
92	12.8	3.4	10.5	4.5	23.3	1.8	6.3	3.8	11.0	0.8
90	12.2	3.8	7.9	5.4	0.3	2.5	7.5	4.4	11.7	1.0
88	10.3	4.3	5.6	5.4	2.3	3.0	9.2	4.7	0.0	1.0
86	7.1	5.1	5.5	1.3	5.7	0.6	10.4	5.5	0.0	1.0

Table 5.2 (t) 1980 November

ALTI-TUDE (km)	MEAN		DIURNAL				SEMIDIURNAL			
	AMP. (m/sec)	ERROR	AMP. (m/sec)	ERROR	PHASE (hr)	ERROR	AMP. (m/sec)	ERROR	PHASE (hr)	ERROR
104	-7.3	16.0	27.5	25.3	0.7	3.2	16.2	9.6	7.7	0.4
102	2.2	10.7	18.2	16.6	1.4	2.9	11.8	2.8	8.6	0.1
100	7.9	9.2	13.7	13.4	2.2	2.6	10.0	1.3	9.4	0.4
98	10.4	8.7	12.6	11.8	2.9	2.0	9.2	3.4	10.1	0.9
96	10.5	8.1	13.1	10.6	3.1	1.6	8.2	4.6	10.7	1.3
94	9.0	7.3	14.2	9.5	3.0	1.6	6.7	5.6	11.2	1.7
92	6.5	6.9	15.1	8.7	3.0	1.7	4.7	6.5	11.8	2.7
90	3.8	6.7	14.8	8.1	3.1	1.7	3.1	5.8	1.1	3.5
88	1.5	6.8	12.7	7.0	3.7	1.6	3.3	0.2	3.0	0.1
86	0.5	7.8	9.8	1.8	5.7	0.5	5.1	3.9	4.1	1.7

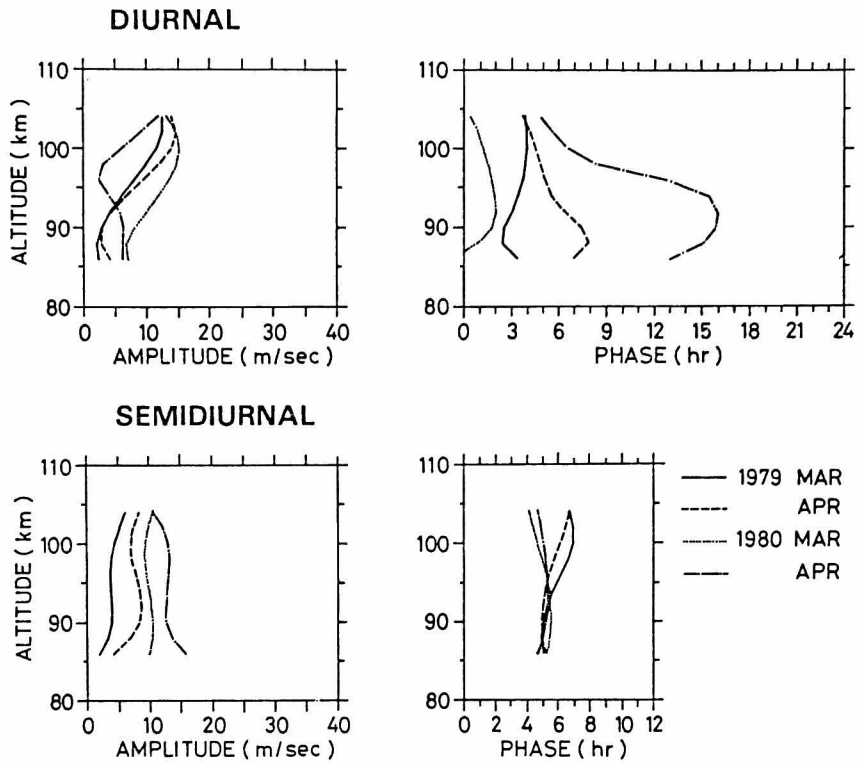

Fig. 5.9 Northward tidal wind at Kyoto in spring. top: amplitude and phase of the diurnal compoenet. Bottom: those of the semi-diurnal component.

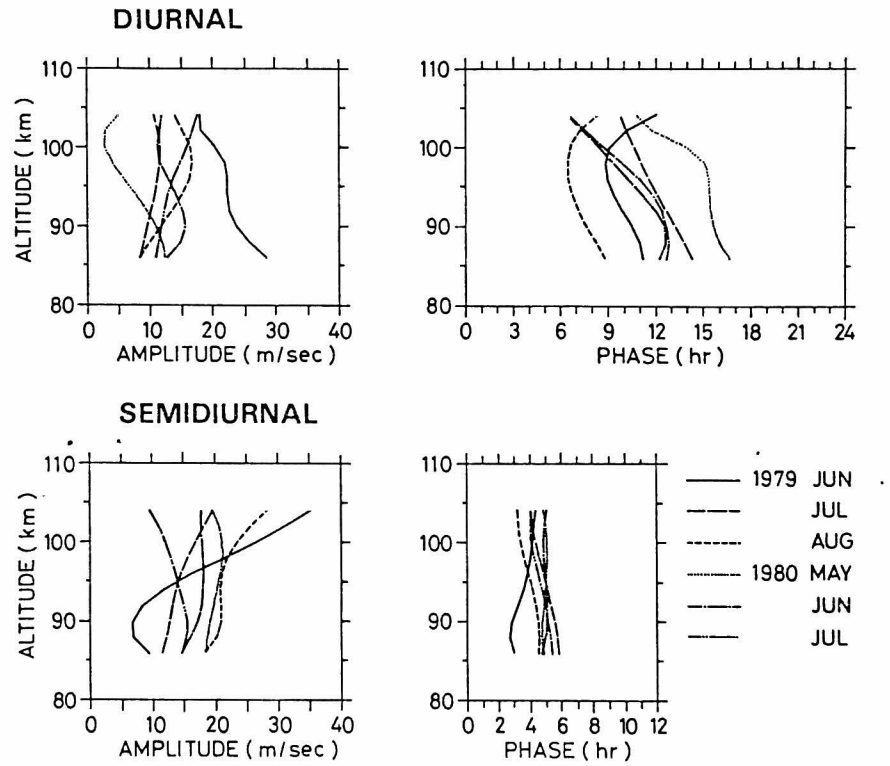

Fig. 5.10 The same as Fig. 5.9 except for summer results.

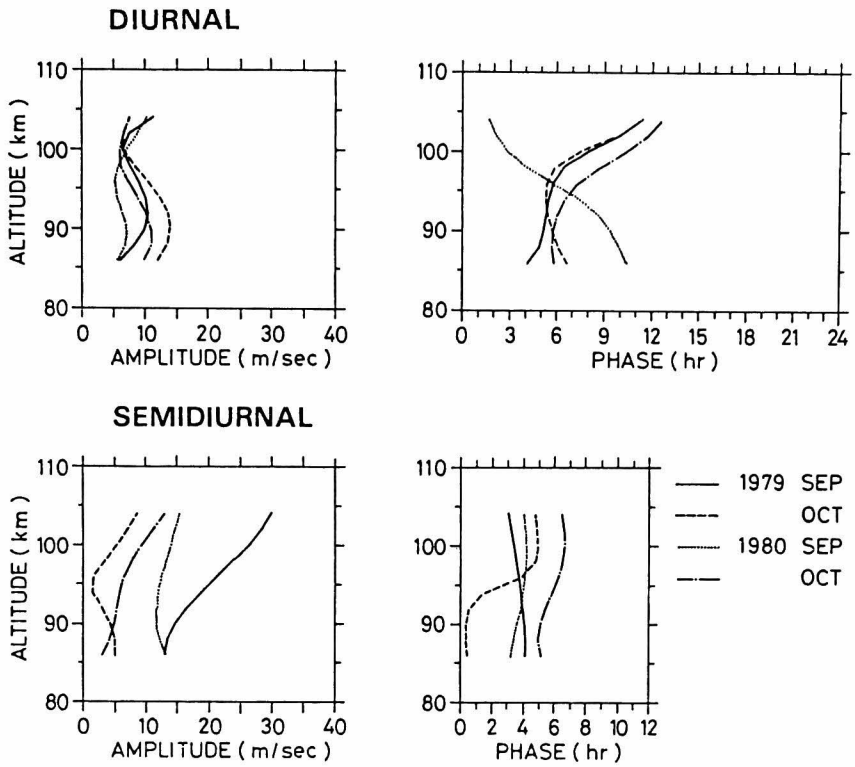

Fig. 5.11 The same as Fig. 5.9 except for autumn results.

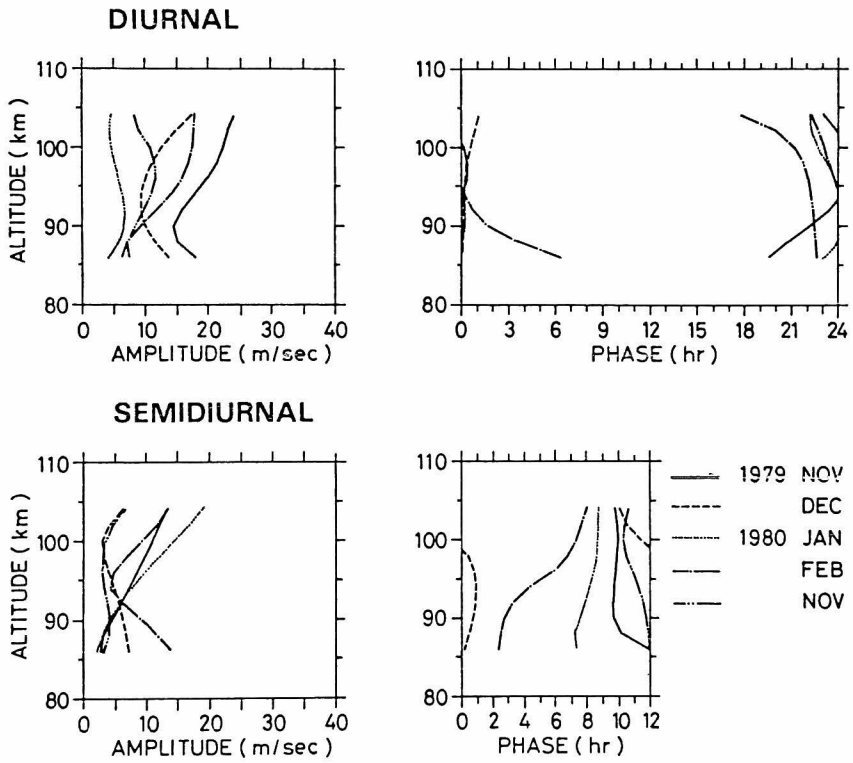

Fig. 5.12 The same as Fig. 5.9 except for winter results.

2.2 The Diurnal Tide

2.2.1 Height Profile

Time-height profiles of the amplitude of northward and eastward diurnal tidal wind are illustrated in Fig. 5.13 (a) and (b), respectively. A contour line is drawn at every 5 m/sec and 10 m/sec for the northward and eastward component, respectively. Relatively small amplitude is shown in spring in 1979, and winter in 1979 and 1980. In summer months, the amplitude is generally larger than 10 m/sec in the whole height range. There is an evidence that large amplitude accompanied with rapid change can be seen in November, 1979. As for the eastward component, large amplitude can be seen in August, 1980. The maximum amplitude is approximately twice of that for the northward component. An evidence of enhancement in the amplitude also occurs in November, 1979.

From Figs. 5.9 - 5.12, the vertical profile of the northward component of the diurnal tidal wind is characterized in each season. Except for the result in April, 1980, wind amplitude for spring varies in a similar manner such that it becomes minimum at around 90 km in altitude and increases up to 15 m/sec at 100 km. The phase varies gradually above 90 km, although it has a complicated profile below 90 km. In April, 1980, the altitude of the minimum wind velocity is shifted upward by several kilometers, and the phase is around 15 hrs local time below 95 km and changes abruptly above 95 km. Generally, the phase in April in the lower altitude region progresses toward noon in comparison with that in March. This may show the diurnal tide in spring is in a transition state. As for summer months, wind amplitude ranges widely from 5 m/sec to 25 m/sec. In May and June the amplitude generally decreases with altitude, while it gradually increases in July and August. The phase value occupies around 12 hrs local time. The phase does not vary largely in this altitude region, and generally delays with altitude. The phase variation sometimes has a positive and negative hump which corresponds to maximum and minimum value in local time, respectively. The positive hump characteristically occur in 1979, while the negative hump can be seen in 1980. These phenomena will be explained in later section in terms of a fading between an evanescent wave and a propagating

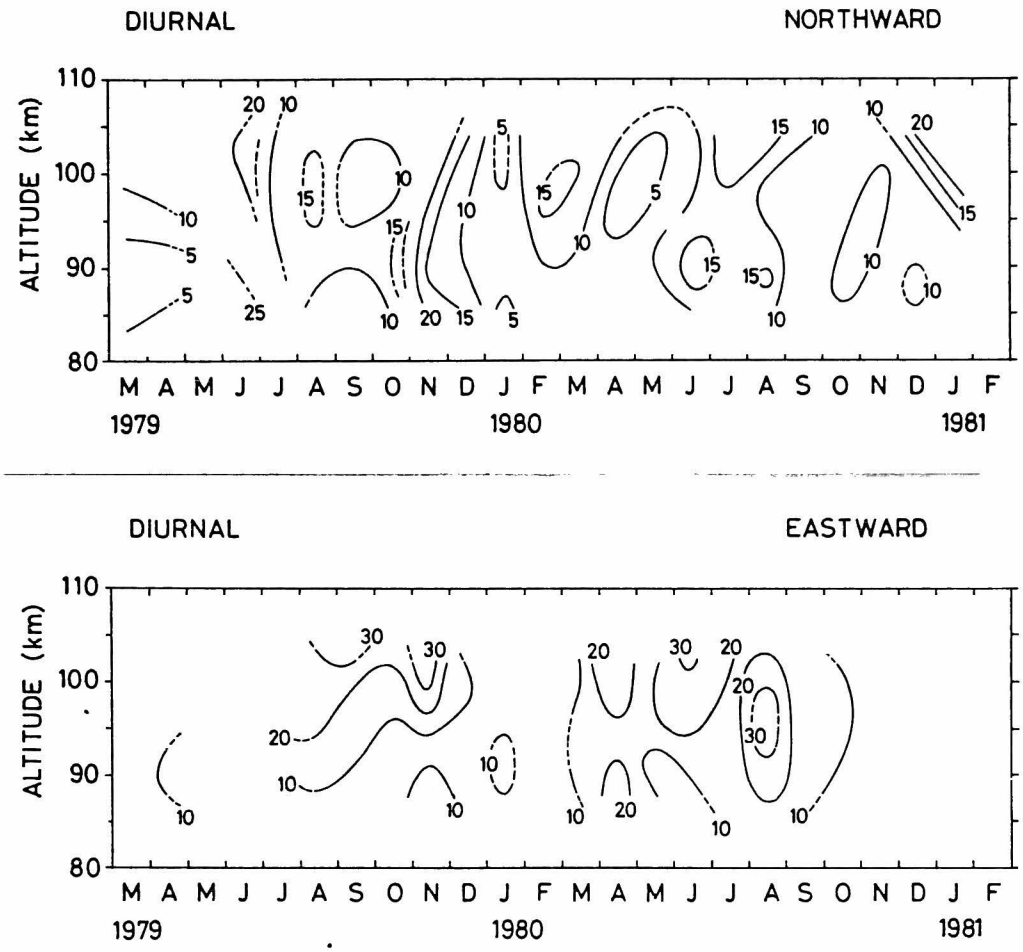

Fig. 5.13 Height time profile of the amplitude of the diurnal wind velocity. A contour line is drawn at every 5 m/sec for the northward component (top), and 10 m/sec for the eastward component (bottom).

wave. The amplitude variation for autumn is fairly well repeated in 1979 and 1980. It becomes maximum at around 90 km and minimum at around 100 km. Maximum wind velocity is 10 m/sec in average, and minimum one is 5 m/sec. The phase variation is also repeated except for the result in September, 1980. In these three cases, the phase value is about 6 hrs local time below 95 km, and progresses linearly to 12 hrs local time above 95 km. In September, 1980, the phase delays from 10 hrs to 2 hrs local time in this altitude region suffering a slight fading. In winter months, the amplitudes tends to increase with altitude, which may correspond to the behaviour of the propagating mode. The phase value lies around 0 hrs local time, and is nearly phase-reversed to those in summer. Although the altitude profile of the phase variation seems to show

gradual change, it would be attributed to cancellation of the propagating waves with short vertical wavelengths which will be shown in later section.

In summary, the amplitude is the largest in summer and the smallest in equinoxes. The phases in summer and winter solstices lies at local noon and midnight, respectively, that is, those are different from each other by 12 hrs. In equinoxical months, the phase value lies in the middle of those for solstices.

2.2.2 Harmonic Dial at 95 km

The amplitude and phase at 95 km altitude are plotted in Fig. 5.14 (a) and (b) for the northward and eastward component, respectively. Note that determinations of the northward componet by use of the decay height method are also shown only in Fig. 5.14 (a) in the period from April 1978 to January 1979. The amplitude of the northward component has a gradual annual variation with maximum in summer months. An enhancement of it, however, can be seen in November 1979. The phase is around 12 hrs local time in June, July and August in 1978 and 1980. In winter months phase becomes about 0 hrs local time, which is most clearly seen in the period from November, 1979 to March, 1980. A gradual phase decrease can be seen in late summer to autumn in each year. It seems that an annual variation can be seen more clearly in the phase than in the amplitude.

As for the eastward component, its amplitude has more distinct annual variation than that of the northward component with maximum occurring at around the June solsticial period. A maximum to minimum ratio of the annual variation is about two. The phase is around 16 hrs local time in the period from March to August, 1979, and around 12 hrs from April to September, 1980. In winter months, the phase falls around 0 hrs local time. A rapid phase reversal can be seen in September and October, 1979 and October, 1980. A gradual phase decrease is seen from January to February 1980.

Seasonal variation of the diurnal tide is replotted on a harmonic dial shown in Fig. 5.15 to investigate the repeatability of the annual variation. Each determination is separated according to four seasons and enclosed with a triangle or a quadrangle. The region of the vectorial points of the northward component is clearly separated with

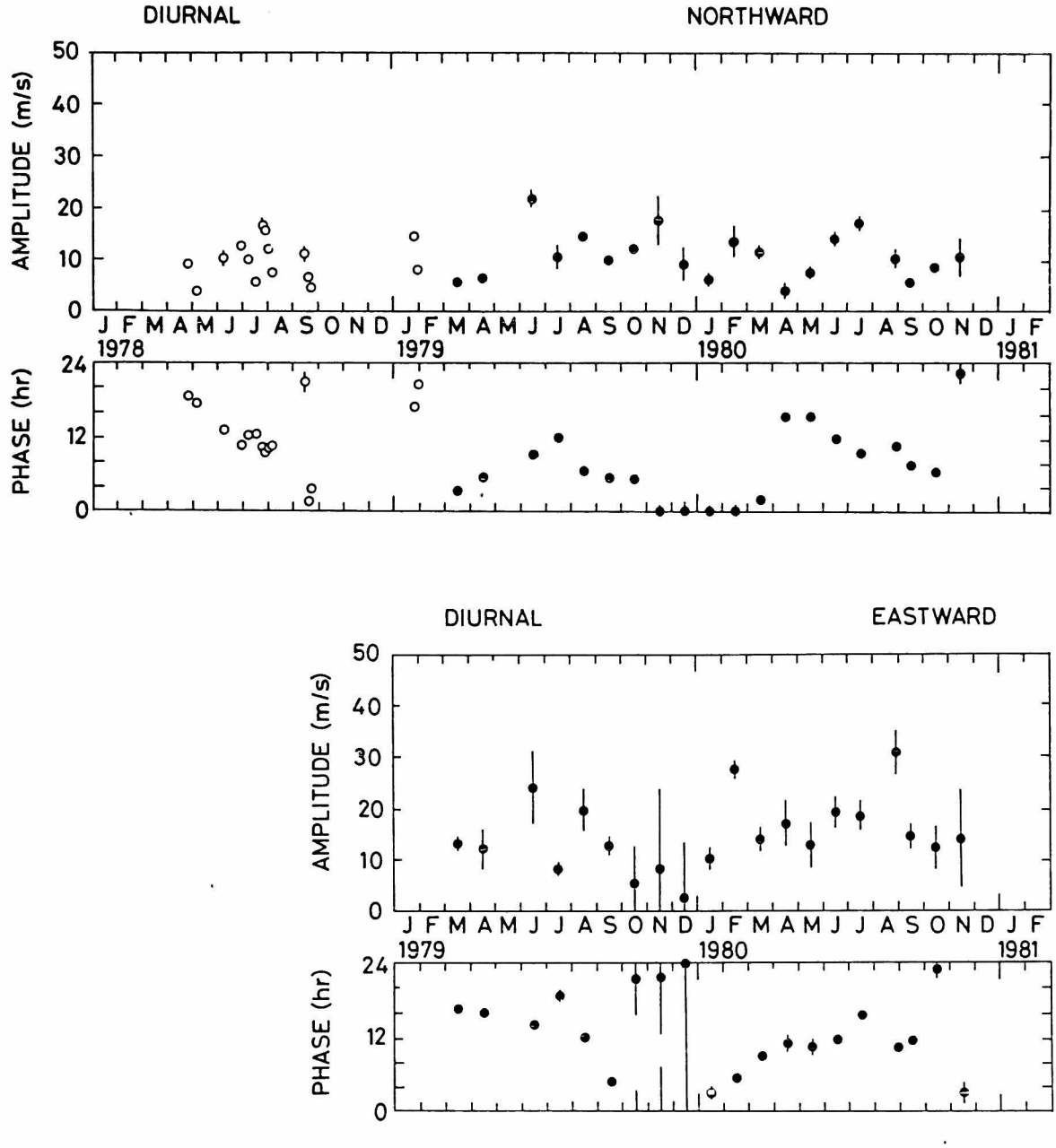

Fig. 5.14 Monthly average of the amplitude and phase of the diurnal wind velocity at an altitude of 95 km. top: the northward component. bottom: the eastward component. An open circle plotted for the northward component corresponds to the results in 1978 deduced by use of the decay height method.

each other. In spring months, the triangle includes zero point, and lies mostly in a sector from 0 to 6 hrs local time ranging up to 10 m/sec in amplitude. There is a large spread in the quadrangle for summer months: the amplitude ranges from about 10 m/sec to 20 m/sec, and the phase is widely distributed from 9.5 hrs to 15.5 hrs. The extent, however, is confined in a range from 9 hrs to 12 hrs by excluding two extremes determined in August, 1979 and May, 1980. As for the autumnal months, the quadrangle is small and has a center at coordinates of 6 hrs local time and 10 m/sec. The quadrangle for the winter months lies on the opposite site to that for the summer months, although it does not spread so wide as that for the summer months, and has a center at around 0 hrs and 10 m/sec.

As for the harmonic dial for the eastward component, considerable overlapping is seen among four areas. In spring, the average amplitude is about 10 m/sec, and the phase ranges from 9 hrs to 17 hrs. Although a large spread can be seen in the results for the summer months similar

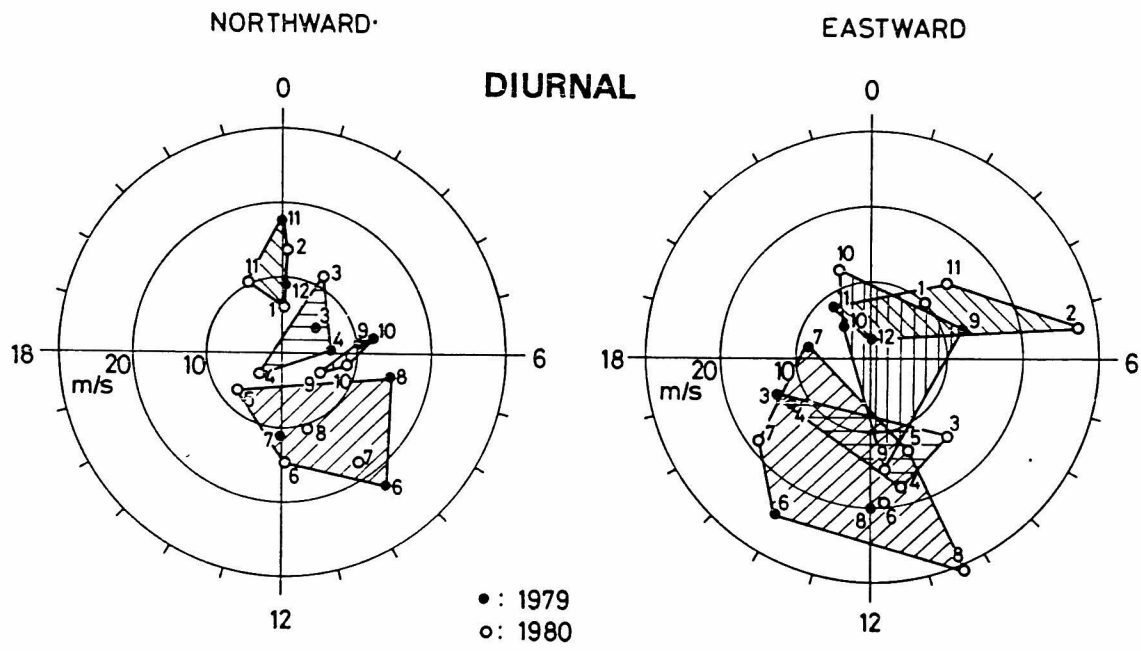

Fig. 5.15 Harmonic dial for the diurnal wind velocity at an altitude of 95 km. Data are separated into four seasons as described in the text.

to those for the northward component. The center of the polygon is estimated at 13 hrs local time and 16 m/sec. The quardrangle for the autumnal months includes the zero point, and has an average around it. In winter months, the quadrangle lies on the opposite side of that in summer months with respect to the origin. The average value of the phase is about 3 hrs local time, and that of the amplitude is approximately 10 m/sec except for that in February, 1980. Generally, average amplitude and extent of the region are larger for the eastward component than that for the northward component. The region for the winter months is in general phase-reversed to that for the summer months in both northward and eastward component.

2.3 The Semidiurnal Tide

2.3.1 Height Profile

Similar to Fig. 5.13, a time height profile of the northward and eastward component of the semidiurnal tidal wind is plotted in Fig. 5.16 (a) and (b), respectively. Northward wind becomes large in summer months, especially in June and August, 1979 and in May and August, 1980. There is an evidence of large amplitude at high altitude in January, 1980 and 1981. The amplitude, however, is generally as small as 5 m/sec in winter months. As for the eastward component, the amplitude becomes large in summer months and small in winter months similar to the case for the northward component, although the precise structure, however, seems to be different from that of the northward component. An evidence occurs in November and December, 1979 at low altitude.

Seasonal variation of the semidiurnal northward wind profile can be recognized by investigating Figs. 5.9 - 5.12. In spring, amplitude of the wind velocity ranges from 5 m/sec to 15 m/sec. It does not vary largely with altitude, however it seems to be suffuring from amplitude modulation. Below 95 km, the phase retains constant value at around 5 hrs local time. The phase ranges from 4 hrs to 7 hrs above 95 km, and shows a gradual progression or delay. As for summer months, the amplitude is the largest among four seasons, and it generally increases with altitude. In May and June, 1980, the phase value is almost constant at

5 hrs local time throughout whole altitude region. The phase profile is similar for the results in July, August, 1979 and July, 1980 such that it delays by two hours while it changes linearly from bottom to top of this altitude region. In autumn, wind amplitude shows a large spread. Specifically, those in 1979 varies abruptly from September to October. The phase variation in September rather resembles the profile in summer months. In Octover, 1979, the phase is reversed at around 95 km. In winter, the amplitude variation is classified into two types: one is that it increases monotonically with altitude and another is that it decreases below around 95 km and then increases. Phase variation does not show systematic characteristics, although its central value seems to be located at around 9 hrs local time.

2.3.2 Harmonic Dial at 95 km

Figure 5.17 shows the amplitude and phase of the semidiurnal wind at an altitude of 95 km. As for the northward component, one can easily

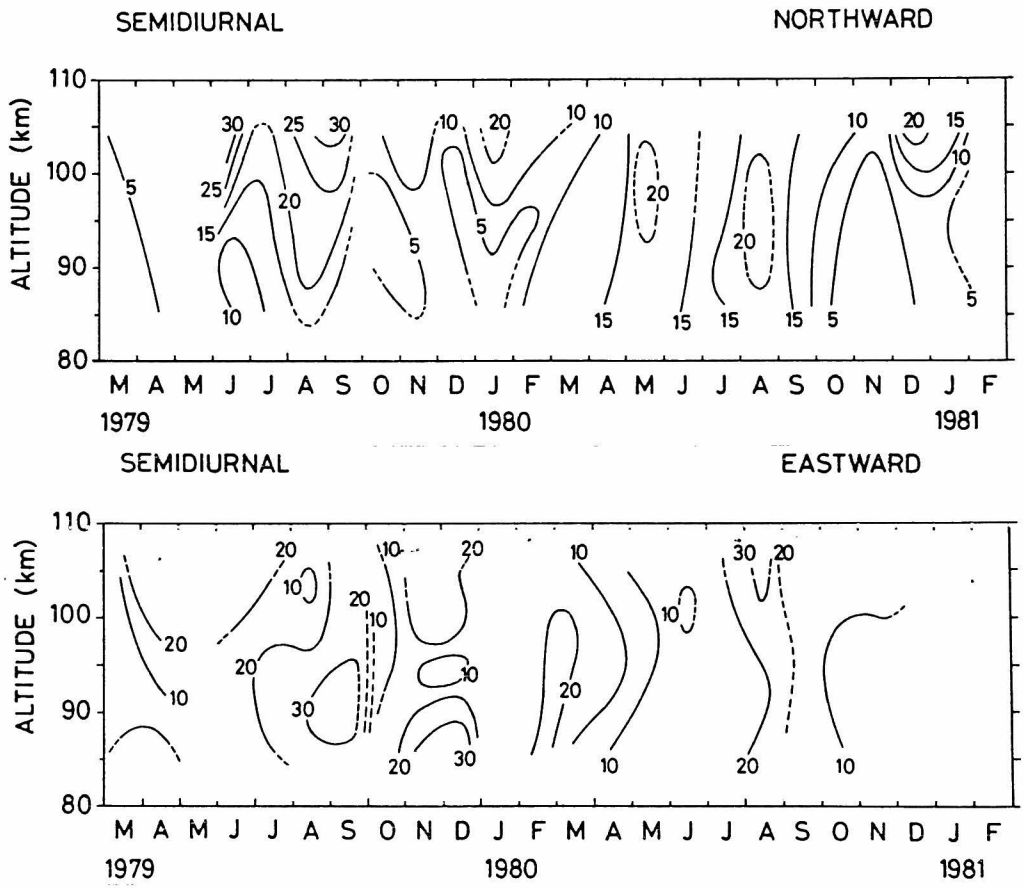

Fig. 5.16 The same as Fig. 5.13 except for the semidiurnal component.

imagine an annual variation of the amplitude with maximum occurring in summer months, which is repeated for three years. The phase value falls around 5 hrs local time during the period from late spring to early autumn. A slight increase of phase, however, is recognized from March to September in both 1979 and 1980. In other seasons, the phase is mostly determined in the range from 8 hrs to 10 hrs, although a considerable spread of the value can be recognized.

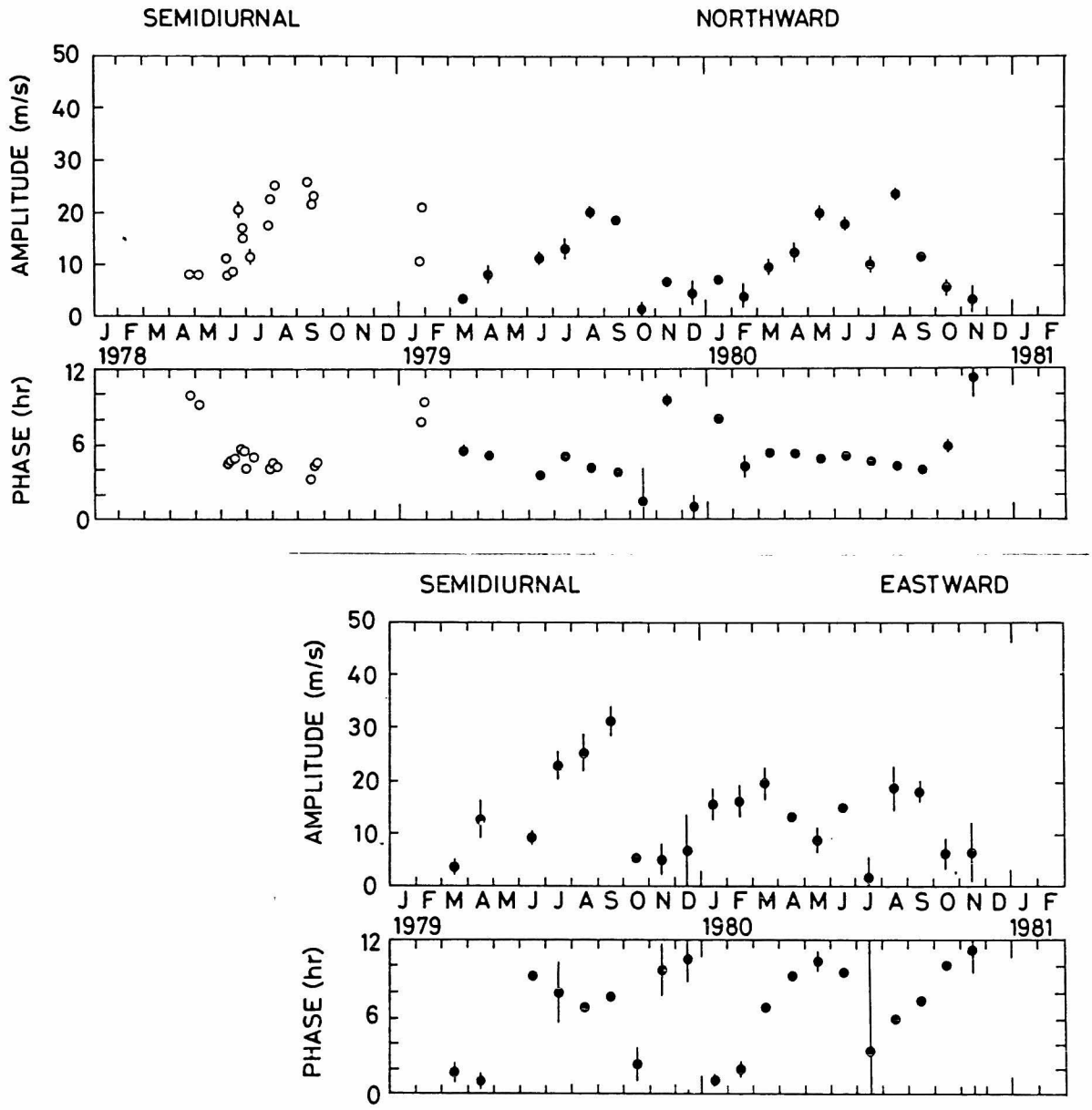

Fig. 5.17 The same as Fig. 5.14 except for the semidiurnal component.

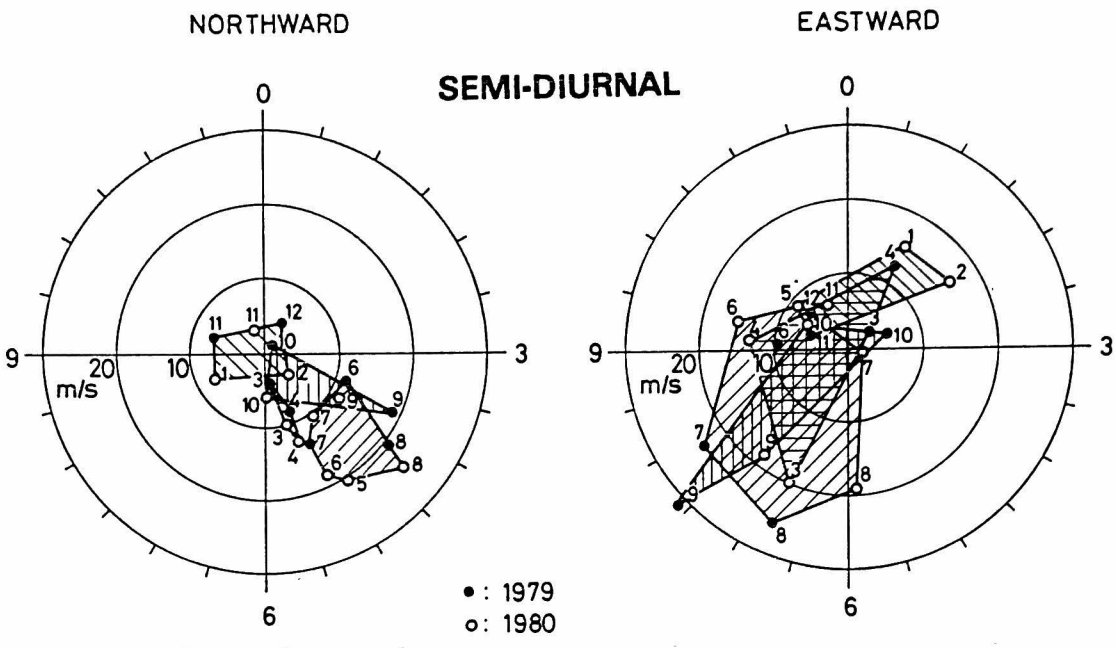

Fig. 5.18 The same as Fig. 5.15 except for the semidiurnal component.

Annual variation of the eastward component is not so distinct as that of the northward one. The variation of the amplitude in 1980 seems to contain a semiannual change with maximum occurring in both March and August. In 1979, the phase increases from 2 hrs to 7 hrs in the period from March to August, then decreases to 10 hrs in the latter half of the year. As for the results in 1980, the phase seems to decrease twice from 0 hrs to 12 hrs, which might corresponds to the semiannual variation of the amplitude mentioned above.

Harmonic dials are drawn for the northward and eastward component in Fig. 5.18(a) and (b), respectively. The dial points are separated into four polygons according to each season in a similar manner as for the diurnal tide. Generally, most of the areas is located in a sector from 3 hrs to 6 hrs. For summer months, the amplitude ranges from 10 m/sec to 25 m/sec. On the other hand, the quadrangle for the winter months includes the origin, and the amplitude does not exceed 8 m/sec. In the equinoctial period, the data fall between those in summer and winter. A smooth seasonal variation is detected in the semidiurnal tidal wind, which will be shown later. As for the eastward component, large spread and overlap of a region can be seen. When we rotate the region where

data are distributed anticlockwise by three hours, it might become analogous to that for the northward component.

Section 3. Short Period Variation

3.1 Height Profiles for Six Long Observations

Day to day variability of the tidal wind was discussed by Aso et al. [1979] for the results at Kyoto in June, 1978. They have shown an enhancement of the diurnal tidal wind in a specified period of the observation. After all many experimental and theoretical investigations, the real cause of the short period perturbations in the tidal wind field has not yet been clarified. For six observation runs, height profiles of the northward component of both diurnal and semidiurnal tidal wind are shown in Figs. 5.19 - 5.24. Their features are summerized below.

March 13 - 29, 1979: From Fig. 5.19, it is recognized that the diurnal tide shows complicated behaviour. Its amplitude increases monotonically with altitude, and is as large as 40 m/sec at 100 km. It, however, becomes less than 5 m/sec in the succeeding days; 16 - 21, March. Abrupt phase variation would indicate a severe fading among multiple waves. The semidiurnal tide seems to be a standing wave in the earlier two periods, which can be recognized from the very small amplitude at 95 - 100 km in altitude accompanied with the phase reversal. In the later two periods, height profile of the semidiurnal tide agrees with the monthly average shown in Fig. 5.9.

July 30 - August 22, 1979: The ampltiude of the diurnal tide decreases with altitude excpet for the result in 11 - 14, August as shown in Fig. 5.20. Its phase variation generally shows gradual change, although their central value varies day by day within the range of the seasonal variance. An enhancement of the diurnal wind amplitude in 11-14, August could cause the dissimillar height profile for August, 1979 shown in Fig. 5.10 to those in other months. The semidiurnal tide shows large amplitude in this period. The amplitude at an altitude of 95 km grows from about 10 m/sec in July 30 August 3 to about 30 m/sec in 11 - 14, August. The phase variation shows a fairly long vertical wavelength.

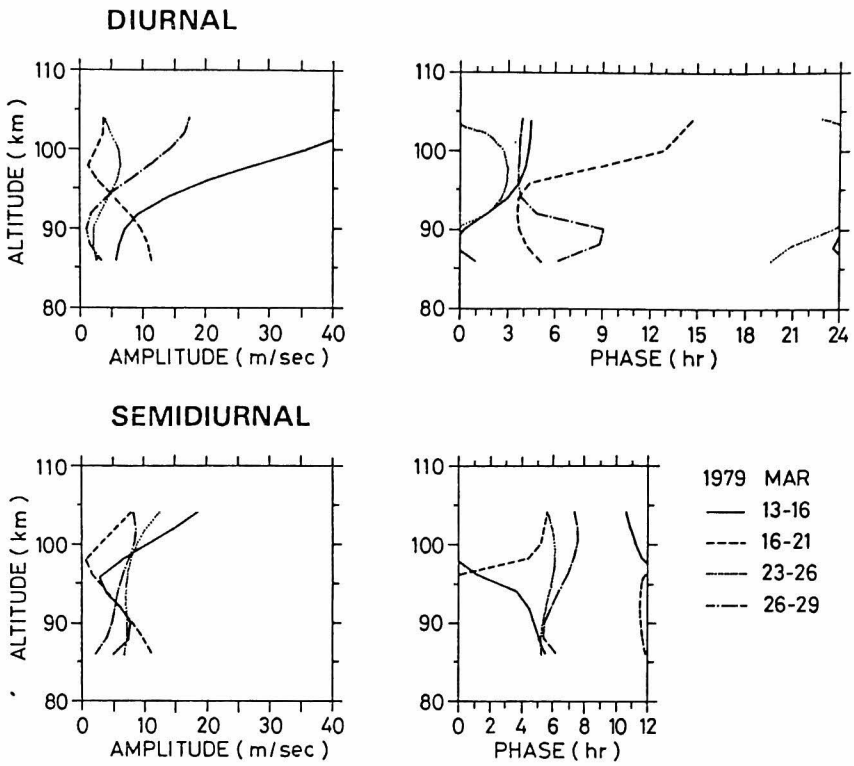

Fig. 5.19 Northward tidal wind in March, 1979.

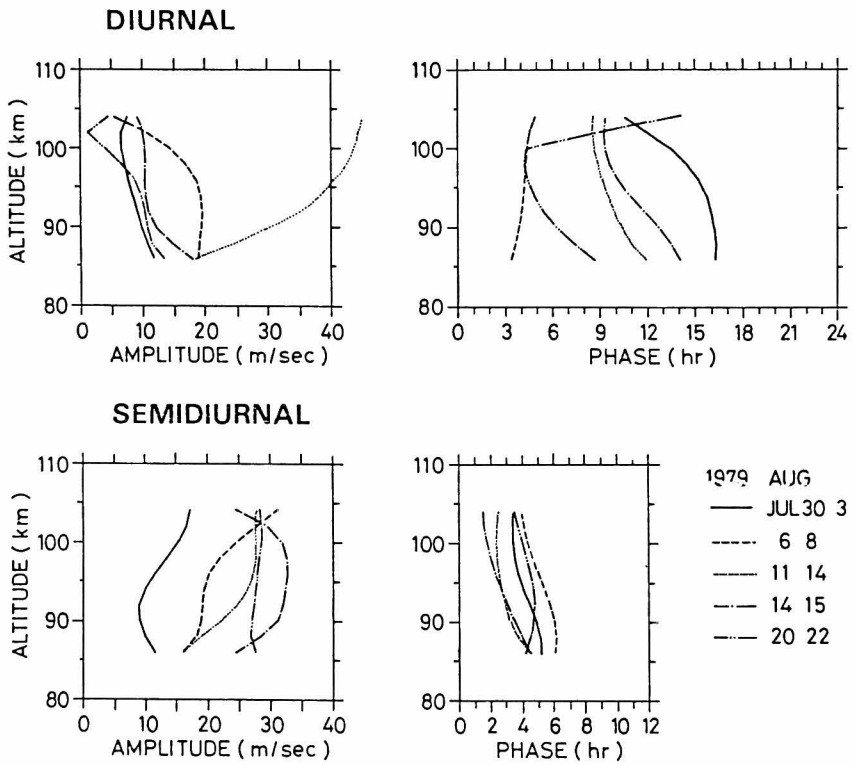

Fig. 5.20 Northward tidal wind in August, 1979.

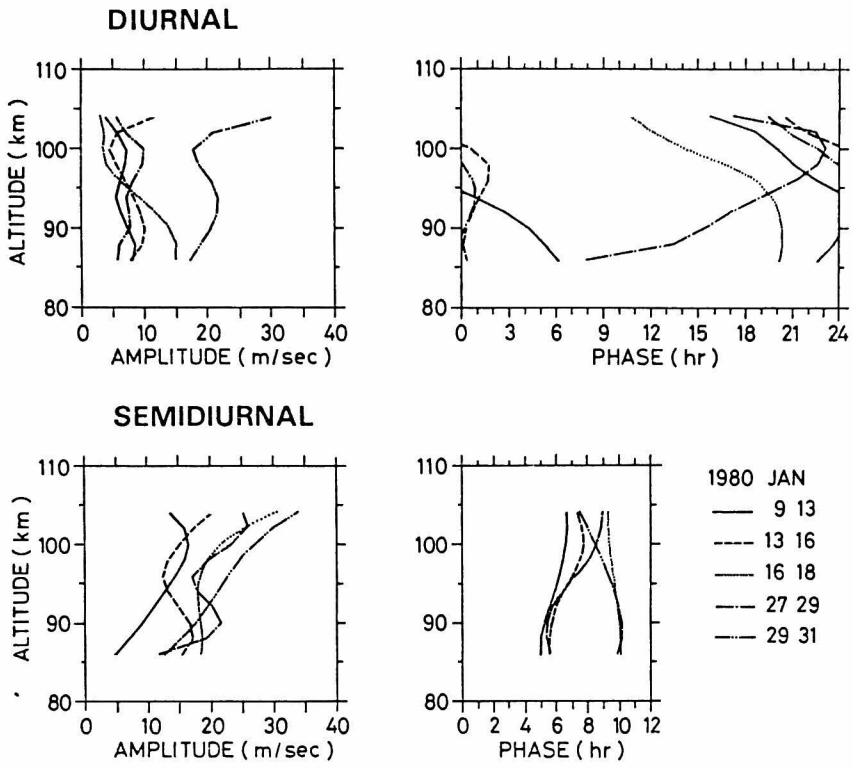

Fig. 5.21 Northward tidal wind in January, 1980.

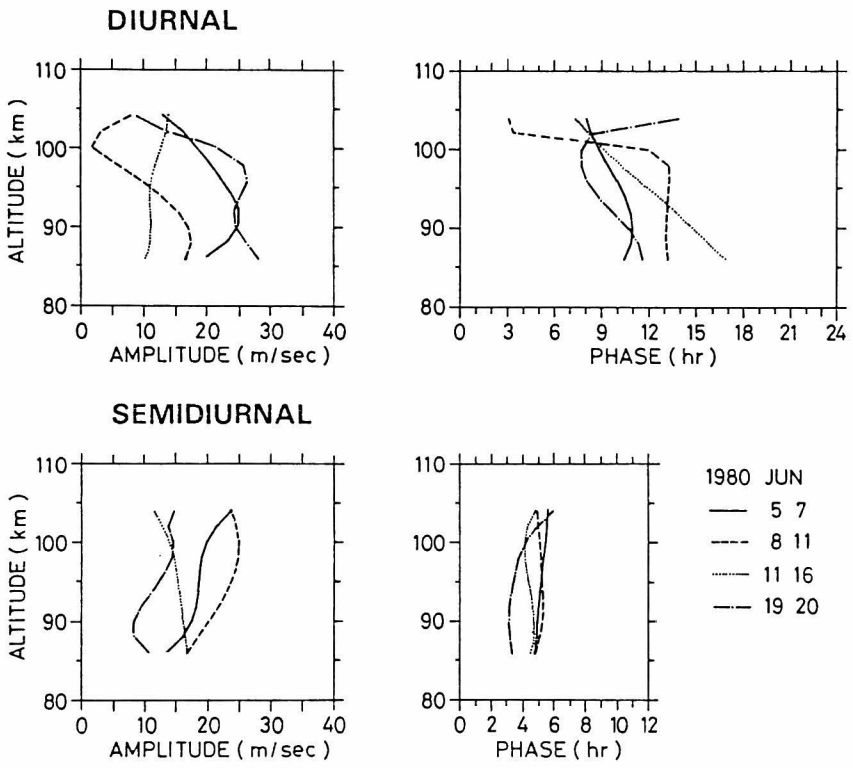

Fig. 5.22 Northward tidal wind in June, 1980.

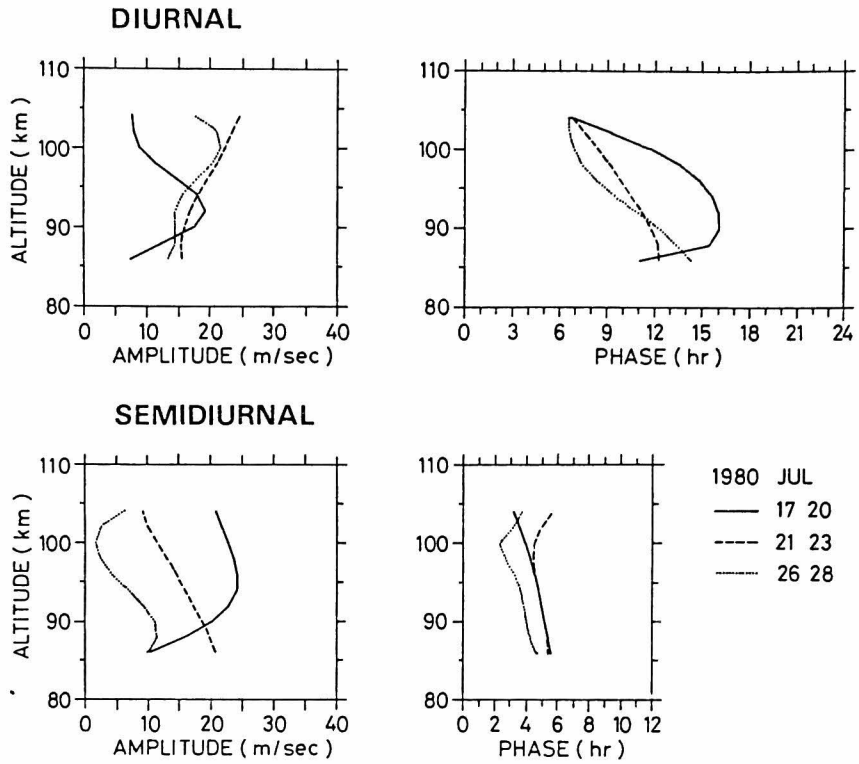

Fig. 5.23 Northward tidal wind in July, 1980.

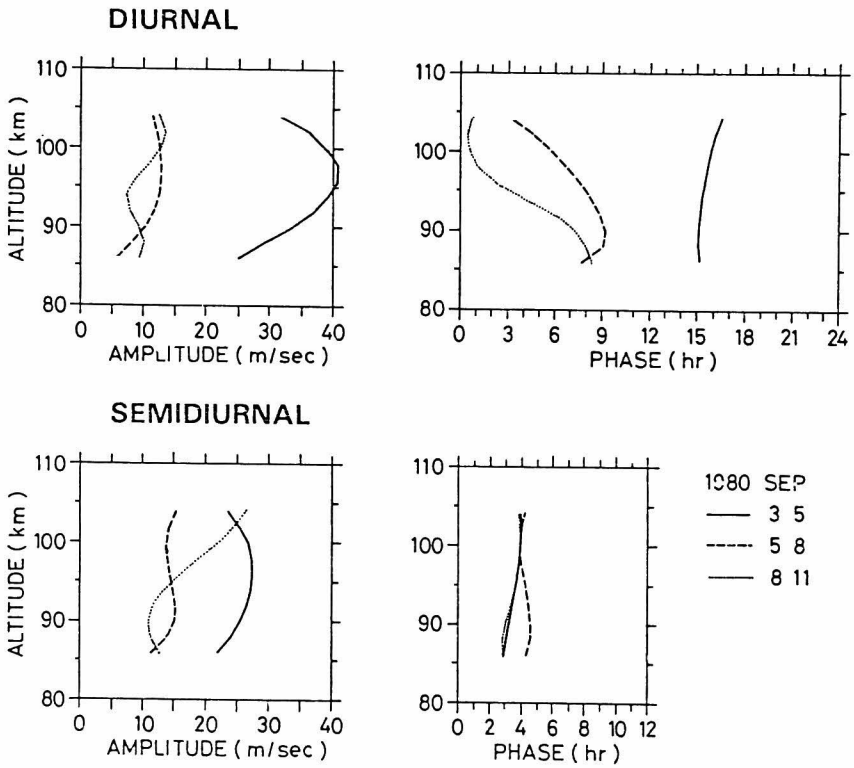

Fig. 5.24 Northward tidal wind in September, 1980.

January 9 - 31, 1980: Figure 5.21 shows small amplitude of the diurnal tide except for the result in 29-31, January. Above 95 km the phase variation is similar with each other, and indicates an appearance of the short vertical wavelength in the range from 25 km to 30 km; which corresponds to $S_{1,1}$ mode. The medium of the phase value seems to lie at around 0 hrs local time. This characteristics agree with its seasonal mean behaviour described in the preceding section. Although the monthly mean profile of the phase variation in Fig. 5.12 shows the long vertical wavelength, it seems to be caused by cancellation among the waves with short vertical wavelength at different phase value. This suggests that the $S_{1,1}$ mode is not always in phase so that it does not stable. The amplitude of the semidiurnal tide generally increases from about 10 m/sec at around 85 km to 25 m/sec at around 105 km, although amplitude modulation can be seen in the periods 13 - 16 and 27 - 29, January. The phase variation is separated into two types such that the phase progresses from 5 hrs local time to about 8 hrs with altitude and that it delays slightly from 10 hrs local time to around 9 hrs.

June 5 - 20, 1980; The profiles of both the diurnal and semidiurnal tides shown in Fig. 5.22 are analogous to those in August, 1979. Abrupt phase change can be seen for the diurnal tide in 8 - 11 and 19 - 20, August. Amplitude decreases with altitude for the diurnal tide, while it gradually increases for the semidiurnal tide. The central value of the phase in 12 hrs and 5 hrs local time for the diurnal and semidiurnal tide, respectively.

July 17 - 28, 1980; The diurnal tide suffers severe fading in the period 17 - 20, July, which is recognized from Fig. 5.23. In other two periods, the height profiles are similar with each other. As for the semidiurnal tide, the amplitdue decreases from the period 17 - 20 to 21 - 23 and 26 - 28, July.

September 3 - 11, 1980: The height profile of the diurnal tide in 3 - 5, September in Fig. 5.24 differs largely from those in other two periods such that the amplitude is enhanced three times and the phase is approximately reversed. The amplitude of the semidiurnal tide varies in the range from 10 m/sec to 20m/sec. The height profile of the phase variation is stable during these periods.

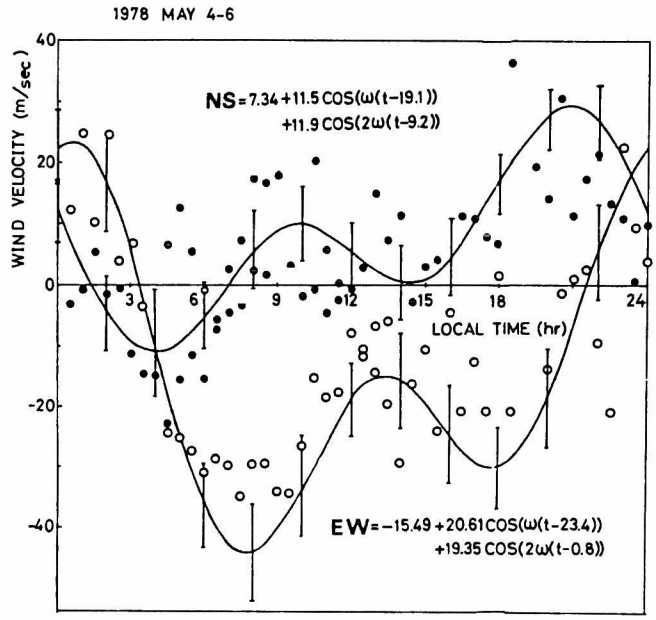

Fig. 5.25 Simultaneous plot of height-averaged northward and eastward wind velocity. a full circle: northward component observed in 4-5 May, 1978. an open circle: eastward component observed in 5-6 May, 1978.

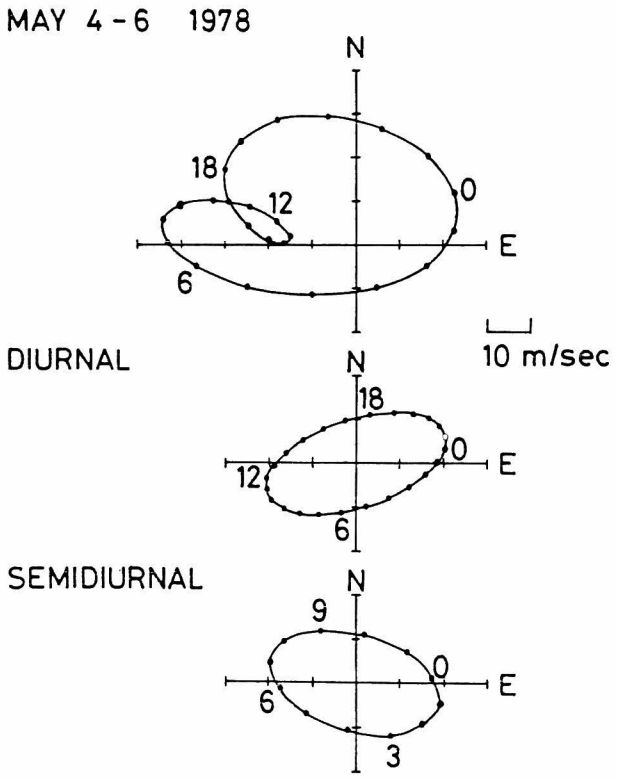

Fig. 5.26 Polar plot of the wind velocity shown in Fig. 5.25. A figure to the curve indicates local solar time. top: total wind field. middle: the diurnal component. bottom: the semidiurnal component.

3.2 Variation of Hodographs

The observation of northward wind velocity was done for one full day extended over 4 to 5 in May, 1978, and that of eastward one in the succeeding day. The height-averaged northward and eastward wind velocities are simultaneously plotted in Fig. 5.25 along with best fit curves composed of mean wind, diurnal and semidiurnal tide. Figure 5.26 (a), (b) and (c) show hodographs of the wind field in Fig. 5.25 corresponding to the total wind velocity, the diurnal wind variation and the semidiurnal wind variation, respectively. According to the classical tidal theory described in Chapter II, the eastward component is delayed by $\pi/2$ to the northward one in the cases of migrating diurnal and semidiurnal tides at a colatitude of 55°. This expect that the hodograph is an ellipse whose axis is parallel to the coordinate, and the tidal wind vector rotates clockwise on the hodograph. Observed direction of the rotation of the vector shown in Fig. 5.26 agrees with the theory for both diurnal and semidiurnal component. The delay of the phase is 4.3 hrs and 3.6 hrs for diurnal and semidiurnal component, respectively, so that the axis of the ellipse is not right parallel to the coordinate. The hodograph investigated above is one of the most comprehensible examples. In Fig. 5. 27 hodographs at altitude of 88 km, 94 km and 100 km are plotted for the monthly average of the diurnal and semidiurnal tidal wind. The hodograph shows clockwise rotation in most of cases. It, however, sometimes rotates anticlockwise, even though we exclude hodographs with large eccentricity. Day to day variation of the direction of the rotation is listed in Table 5.3 for the diurnal and semidiurnal wind field. A considerable number of anticlockwise rotation is recognized, and is abundant in diurnal component.

Section 4. Discussion

4.1 Height Profile

4.1.1 Interference due to Higher Order Modes

Height profiles of the atmospheric tides fluctuate at meteor heights as is already shown in the previous sections. Fellous et al. [1974,

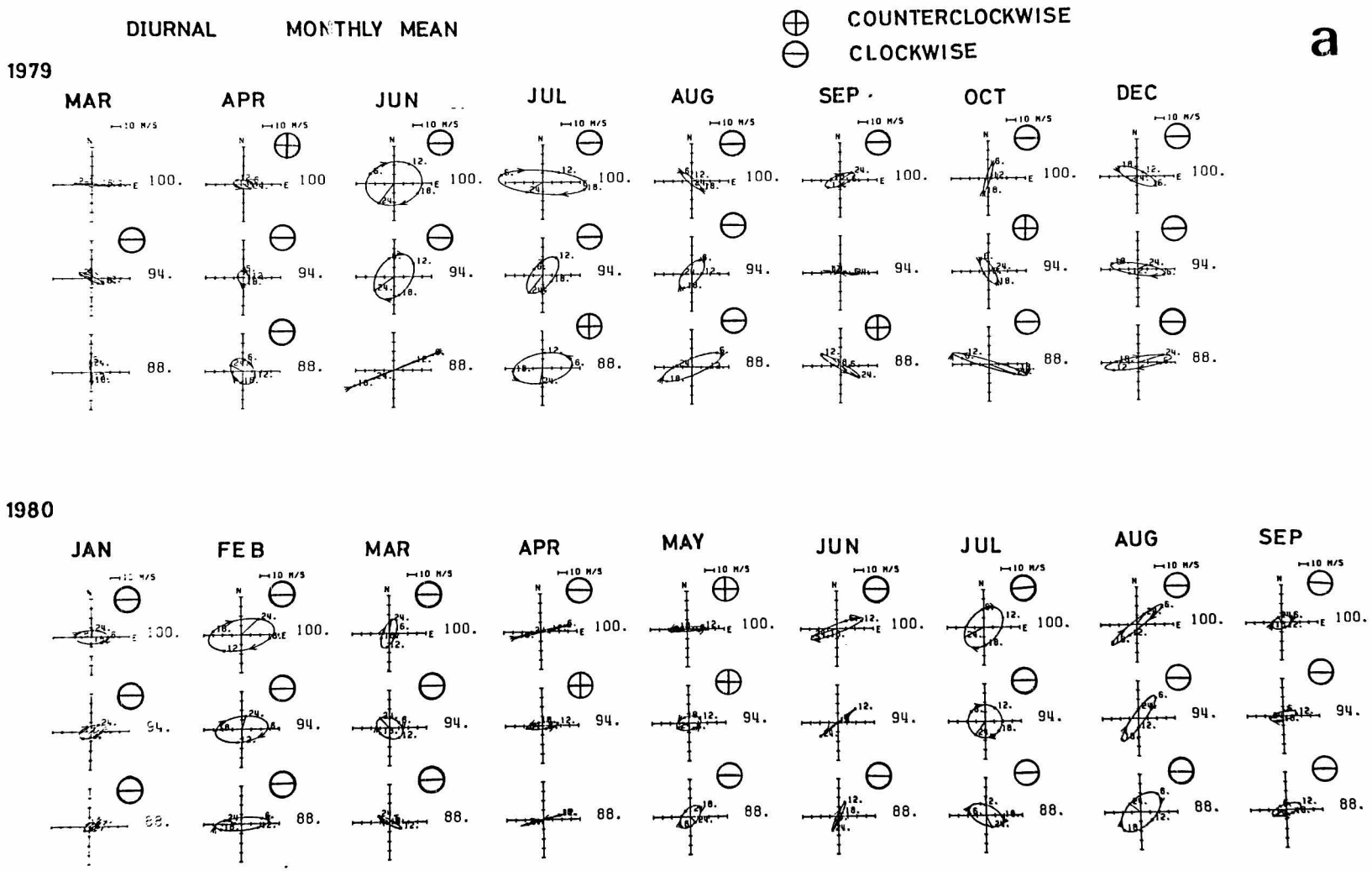

Fig. 5.27 Polar plot of the monthly averaged wind velocity at altitudes of 88, 94 and 100 km. (a): diurnal component. (b) semi-diurnal component.

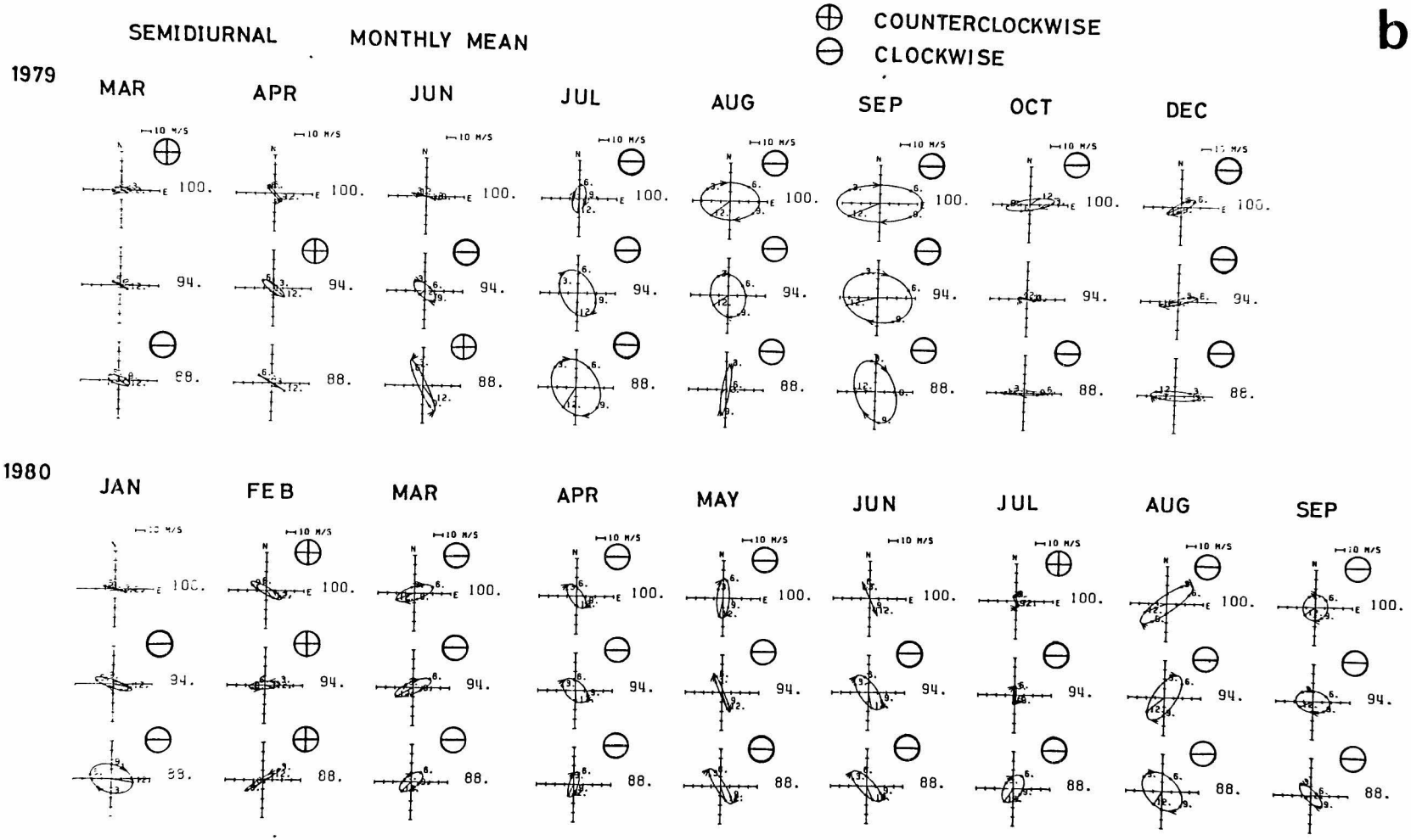

Fig. 5.27 (Continued)

Table 5.3 Rotation direction of the tidal wind

		1979																		
	ALTI-	MAR				APR		JUN	JUL		AUG					SEP			OCT	
	TUDE	14	16	24	26	10	17	19	5	17	30	6	11	14	20	9	19	22	9	15
	(km)	16	21	26	29	13	19	20	7	19	3	8	14	15	22	11	21	24	11	17
	100	+	+	-	+	-		-	-	-	-	-	-	+	-	-	-	+	+	-
DIURNAL	94	+	+	+	-	-	-	-	+	-	-	-	-		-	-	-	+	-	-
	88	+	-	+	-	+	-	-	+	-	+	-	-	-	-	-	-	+	-	+
SEMI-	100			+	+	+	+	+	-	-	-	-	+	-	-	-	-	-	-	-
DIURNAL	94	-	+	+	+	+	+	-	-	-	-	-	-	-	-	-	-	-	-	+
	88	+	-	+	+	+	-	-	-	-	-	-	-	-	-	-	-	-	-	-

		1979				1980														
	ALTI-	NOV		DEC		JAN						FEB		MAR						APR
	TUDE	8	28	11	18	9	13	16	18	27	29	5	12	4	13	17	20	23	24	8
	(km)	10	30	13	20	13	16	18	19	29	31	7	14	6	15	20	23	24	26	10
	100	-	-	-	-	-	-	-	-	-	+	-	-	-	-	-	+	-	-	
DIURNAL	94	-	-	-	+	-	-	-	-	+	+	-	-	-	-	-	+	-	-	+
	88	+	+	+		+		-	-	-	-	-	-	-	+	-	-	-	+	-
SEMI-	100	-	+		-	-		-	-	-	-	+	-	-	-	-		-	-	-
DIURNAL	94	-		+	-	-	-	-	-	-	-	+	-	-	-	-		+	-	-
	88	+	-	+	-	-	-	-	-	-	-	+	-		-	+	-	-	-	-

		1980											
	ALTI-	MAY			JUN			JUL	AUG		SEP		
	TUDE	13	21	27	5	8	11	21	26	27	3	5	8
	(km)	15	23	29	7	11	16	23	28	30	5	8	11
	100	-	+	+	-	+	-	-	-	-	+	-	+
DIURNAL	94	+	+	+	-	+		-	-		+	-	-
	88	-	-	-	-		-	-	-	-	+	-	-
SEMI-	100	-	-		-	-	+	+	+	-	-	-	-
DIURNAL	94	-		+	-	-	-	-	+	-	-	-	-
	88	-	+	-	-	-	-	-	-	-	-	-	+

+: anti-clockwise
-: clockwise

1975] studied vertical structure of the tidal winds by means of modal analysis. Kato et al. [1981] examined that these fluctuations are attributed to interference among multiple modes, although they considered only a simple case in which amplitude of each wave does not vary with altitude. In this section, their idea will be advanced one step further such that the wind amplitude increases as exp(z/2H) with height for propagating modes, and decreases exponentially for evanescent modes. As for the diurnal tide, the interference between the evanescent $S_{1,-2}$ mode and the propagating $S_{1,1}$ mode is considered:

$$v = A_1 \exp(ik_1 z) + A_2 \exp(i(k_2 z + \psi)), \tag{5.4}$$

$$\begin{aligned} A_1 &= -\exp(-z/60) \\ A_2 &= -R \exp(z/12) \\ k_1 &= 0 \\ k_2 &= -2\pi/30 \end{aligned} \tag{5.5}$$

where R and ψ are amplitude ratio and phase difference between these two modes, respectively. The evanescent mode is assumed to become maximum at noon. Amplitude and phase are plotted as functions of vertical distance in Fig. 5.28 for the cases R=0.05 and $\psi = 0, \pi/2, \pi, 3\pi/2$. As the ratio R becomes large, the minimum amplitude at around 22.5 km in vertical distance decreases, while the amplification above that point is enhanced. The phase variation shows folding feature at an altitude corresponding to minimum amplitude, although above and below that point the phase converges to the same value. The profiles are shown in Fig. 5.29 in the cases R=0.03, 0.05, 0.07 and 0.1 for a fixed value of $\psi = \pi/2$. In the range from 0 to 40 km in vertical distance, the amplitude is modulated by a wave with vertical wavelength of 30 km, and sometimes becomes very small. As the vertical distance increases from 0 km to 30 km, the fluctuation in the phase value becomes large around 12 hrs local time due to interference of the propagating mode. Above 30 km the phase tends to vary linearly at vertical wavelength of 30 km. At 30 km in vertical distance, the amplitude ratio between A_1 and A_2 becomes approximately one, so that the propagating and the evanescent mode is

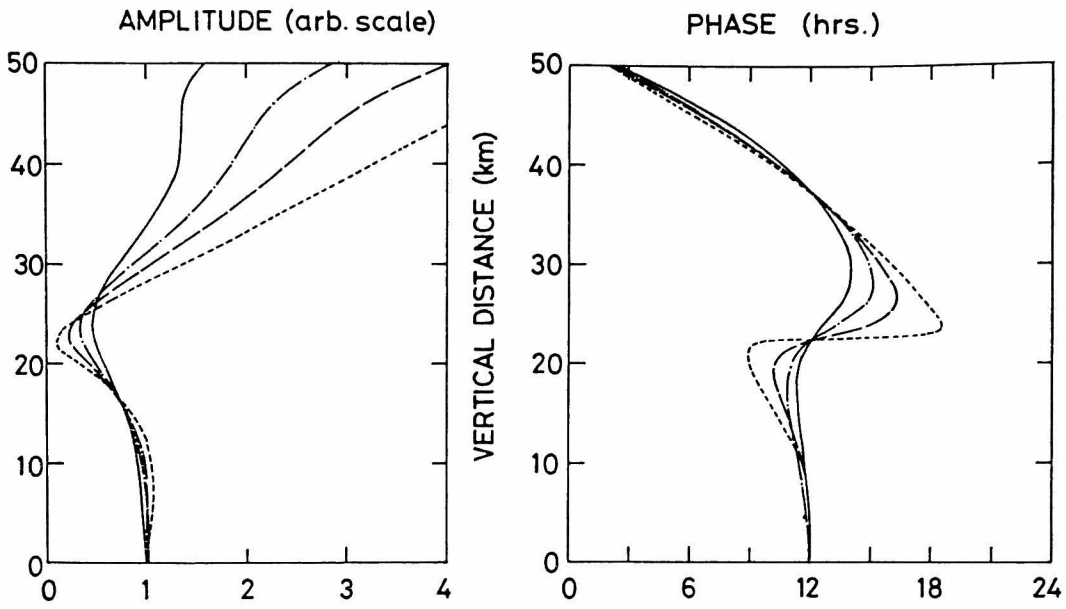

Fig. 5.28 Amplitude and phase profile of the diurnal wind velocity calculated according to a manner outlined in the text. (a): R=0.03, $\psi=\pi/2$ (solid line). (b): R=0.05, $\psi=\pi/2$ (chained line). (c): R=0.07, $\psi=\pi/2$ (long broken line). (d): R=0.1, $\psi=\pi/2$ (short broken line).

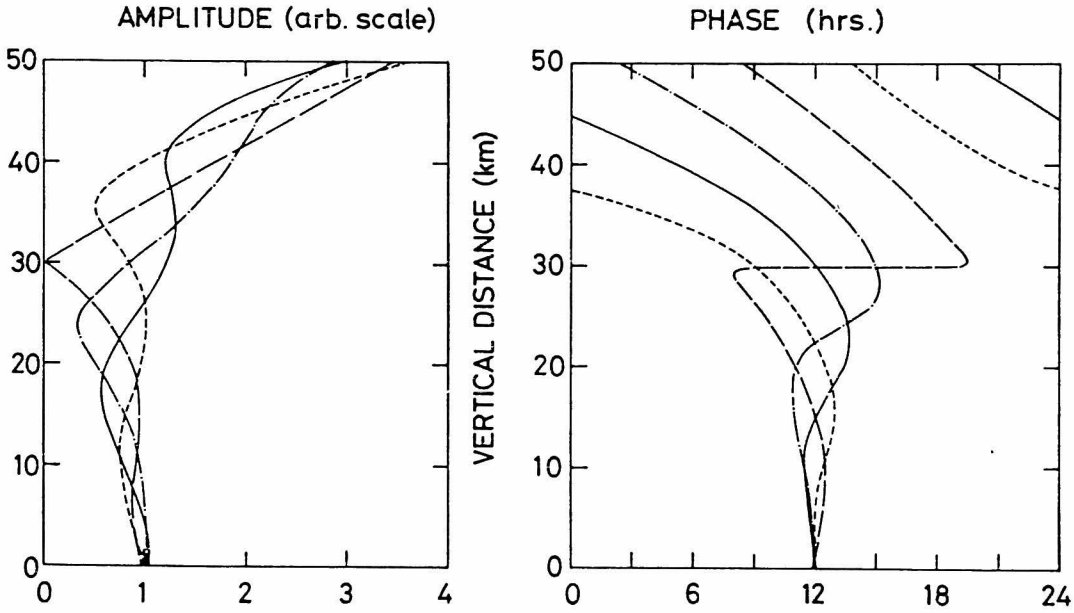

Fig. 5.29 The same as Fig. 5.28.
(a): R=0.05, $\psi=0$ (solid line). (b): R=0.05, $\psi=\pi/2$ (chained line). (c): R=0.05, $\psi=$ (long broken line). (d): R=0.05, $\psi=3\pi/2$ (short broken line).

dominant above and below this point, respectively. Note that the phase variation with height is reversed with respect to 12 hrs local time when the phase velocity of the propagating mode is inverted.

Interference for the semidiurnal tide due to $S_{2,2}$ and $S_{2,4}$ mode is investigated by the same manner for the diurnal tide, and is shown in Fig. 5.30 by adopting parameters listed below:

$$\begin{aligned} A_1 &= -\exp(z/12), \\ A_2 &= -R \exp(z/12), \\ k_1 &= -2\pi/150, \\ k_2 &= -2\pi/30. \end{aligned} \tag{5.6}$$

R is changed as 0.2, 0.5, 0.8, 1.1 and 2.0, and ψ is set equal to $3\pi/2$. As a property of the propagating mode, the amplitude increases with altitude, so that $S_{2,2}$ mode is not modulated so largely by $S_{2,4}$ mode, which is different from the case of the diurnal tide that contains an evanescent mode. The amplitude, however, fluctuates when the higher order mode is added out of phase to the fundamental modes. It especially can be seen if the amplitude ratio R is nearly equal to one as recognized from Fig. 5.30. The phase variation tends to follow the characteristics of the dominant mode when its amplitude exceeds the other by a factor of two. For the amplitude ratio from 0.5 to 2, folding or abrupt change can be seen in the phase variation.

Figure 5.31 corresponds to the cases for R=0.5, and ψ in the range from 0 to $3\pi/2$. Amplification with altitude shows different feature for the cases shown in Fig. 5.31, because the sinusoidal waves are added at various phases. Phase variation in average corresponds to the downward propagating wave with vertical wavelength of 150 km, although slight fading can be seen. The phase profiles have a variance of 1 hour in the whole height ranges. Note that the meaningful discussion can be done not on the absolute value of phase but the shape of the phase variation with altitude for Figs. 5.30 and 5.31, that is, the horizontal axis can be shifted appropriately. Interference among waves investigated above would be applied to the observed results shown in the preceding sections.

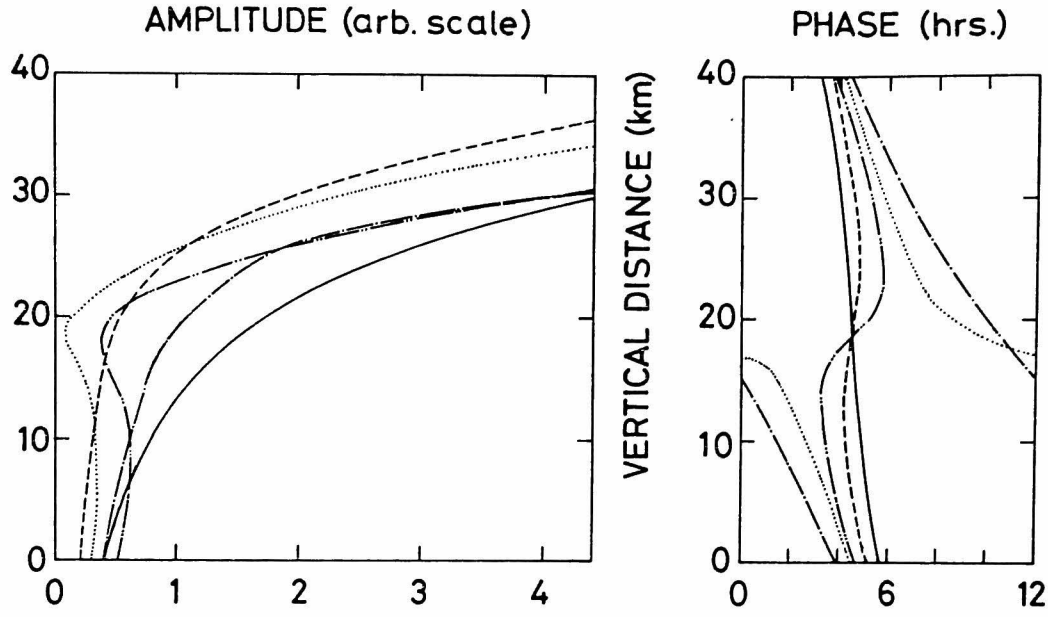

Fig. 5.30 The same as Fig. 5.28 except for the semidiurnal component. (a): R=0.2, $\psi=3\pi/2$ (solid line). (b): R=0.5, $\psi=3\pi/2$ (short broken line). (c): R=0.8, $\psi=3\pi/2$ (doubly chained line). (d): R=1.1, $\psi=3\pi/2$. (e): R=2, $\psi=3\pi/2$ (chained line).

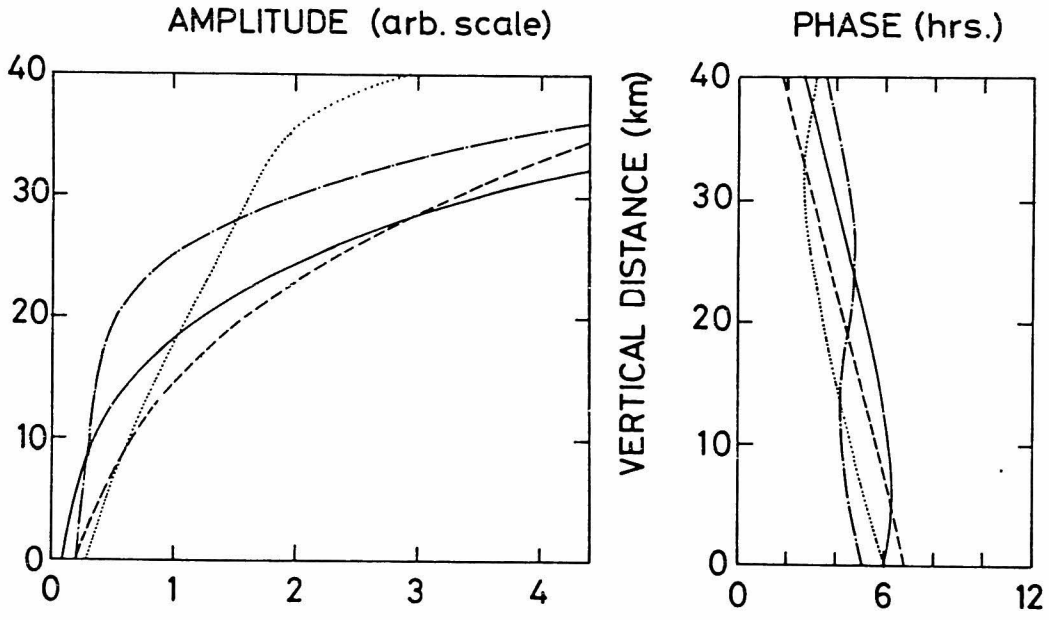

Fig. 5.31 The same as Fig. 5.30.
(a): R=0.5, $\psi=0$ (dotted line). (b): R=0.5, $\psi=\pi/2$ (broken line). (c): R=0.5, $\psi=\pi$ (solid line). (d): R = 0.5, $\psi=3\pi/2$ (chained line).

Amplitude variation in spring except for April, 1980 can be fairly well reproduced by the curve (a) in Fig. 5.29, when the altitude of 90 km in Fig. 5.9 is converted to the vertical distance of 20 km. This suggests that the amplitude of the evanescent mode exceeds that of the propagating mode below 100 km in altitude. As for summer months, both amplitude and phase variations shown in Fig. 5.10 can be explained by the curve (a), (b) or (d). The altitude of 90 km must be converted to 10-15 km in the vertical distance. Abrupt phase change of 12 hrs in 20-22 August, 1979 shown in Fig. 5.20 might corresponds to the curve (c) in Fig. 5.29. It is confirmed that the evanescent mode is dominant in the meteor ragion in summer. The height profiles in autumn resembles the curve (b) in Fig. 5.29 in the range of 10-30 km in vertical distance. Amplitude variation in winter months can be reproduced by the curves (a) and (b) in Fig. 5.29 when the altitude of 90 km is set equal to 20-25 km in vertical distance. The phase variation in January, 1980 as shown in Fig. 5.21 is similar to the curves (a) and (b) in Fig. 5.29 in the same height ranges for the amplitude profile, although the central value of the phase is shifted by 12 hrs. Above about 95 km, the propagating mode exceeds the evanescent mode in winter. It is suggested that the evanescent mode in winter corresponds to higher order modes, because the phase variation is reversed to the curves in Fig. 5.29 where the fundamental evanescent mode with maximum occurring at noon is assumed.

In summary, the meteor region includes the transition height from the evanescent mode to the propagating one for the diurnal tide. This transition height in summer would be raised by approximately 10 km with respect to that in winter. This is attributed to that the evanescent mode affects up to higher altitude in summer than in winter. The characteristics of the propagating mode are emphasized in winter, not because it is enhanced, but the evanesecnt mode becomes weak. So that, the amplitude of the diurnal tide does not becomes larger than that in summer. At the equinoctial conditions, the amplitude is the smallest, because the severe interference between the evanescent mode and the propagating mode takes place in the meteor region. These features agree with the seasonal variation of the northward wind on a harmonic dial for the diurnal tide at an altitude of 95 km shown in Fig. 5.15 (a).

The height profiles of the semidiurnal tide is examined in a similar way for the diurnal tide. As for the profiles in spring in Fig. 5.9, they can be recognized by the curves (b) and (c) in Fig. 5.30. This may suggest that the $S_{2,4}$ mode is contained in this season, and its amplitude ratio to the $S_{2,2}$ mode ranges from 0.5 to 0.8. Short period variation observed in March, 1979 which is plotted in Fig. 5.19 shows that the height profile sometimes agrees with the curve (d) in fig. 5.30. This implies that the $S_{2,4}$ mode could exceed the fundamental $S_{2,2}$ mode in spring.

Height profiles in summer shown in Figs. 5.10, 5.20 and 5.23 agree fairly well with curves (a) and (b) in Fig. 5.30. It can be concluded that the $S_{2,2}$ mode is dominant in summer. Variance of the phase values of about 1 hour could be explained by the variation in phase shift between two modes as was already described in relation to Fig. 5.31.

In autumn, curves (a) and (b) in Fig. 5.30 can be applied to the observed profiles in September, 1979, September and October, 1980. The result in October, 1979 corresponds to the intermediate state between curves (c) and (d) in Fig. 5.30. Generally, the amplitude of the $S_{2,4}$ mode is larger in October than in September. As for the result in winter, some profiles resemble to the curves in Fig. 5.30, but systematic explanation could not be done. The profile in February, 1980 might suggest that there exists a wave with upward phase velocity.

4.1.2 Comparison of Height Profiles with Other Meteor Radar Data

As is listed in Table 1.2, there are three meteor radars at around 35° in latitude: Kyoto (35°N, 135°E) and Atlanta (34°N, 84°W) in the northern hemisphere and Adelaide (35°S, 139°E) in the southern hemisphere. Height profiles of the northward tidal winds obtained at these stations are compared with each other, although the observation periods did not coincide. Figure 5.32 shows both diurnal and semidiurnal northward wind at Adelaide for the period June, 1966 - June, 1973 reported by Elford [1973]. The phase variation in summer shows that the evanescent mode is dominant, and the central value of the phase is around 0 hrs which is different from ours by 12 hrs. That for winter indicates appearance of the propagating mode, and the phase is also reversed to ours. Thus,

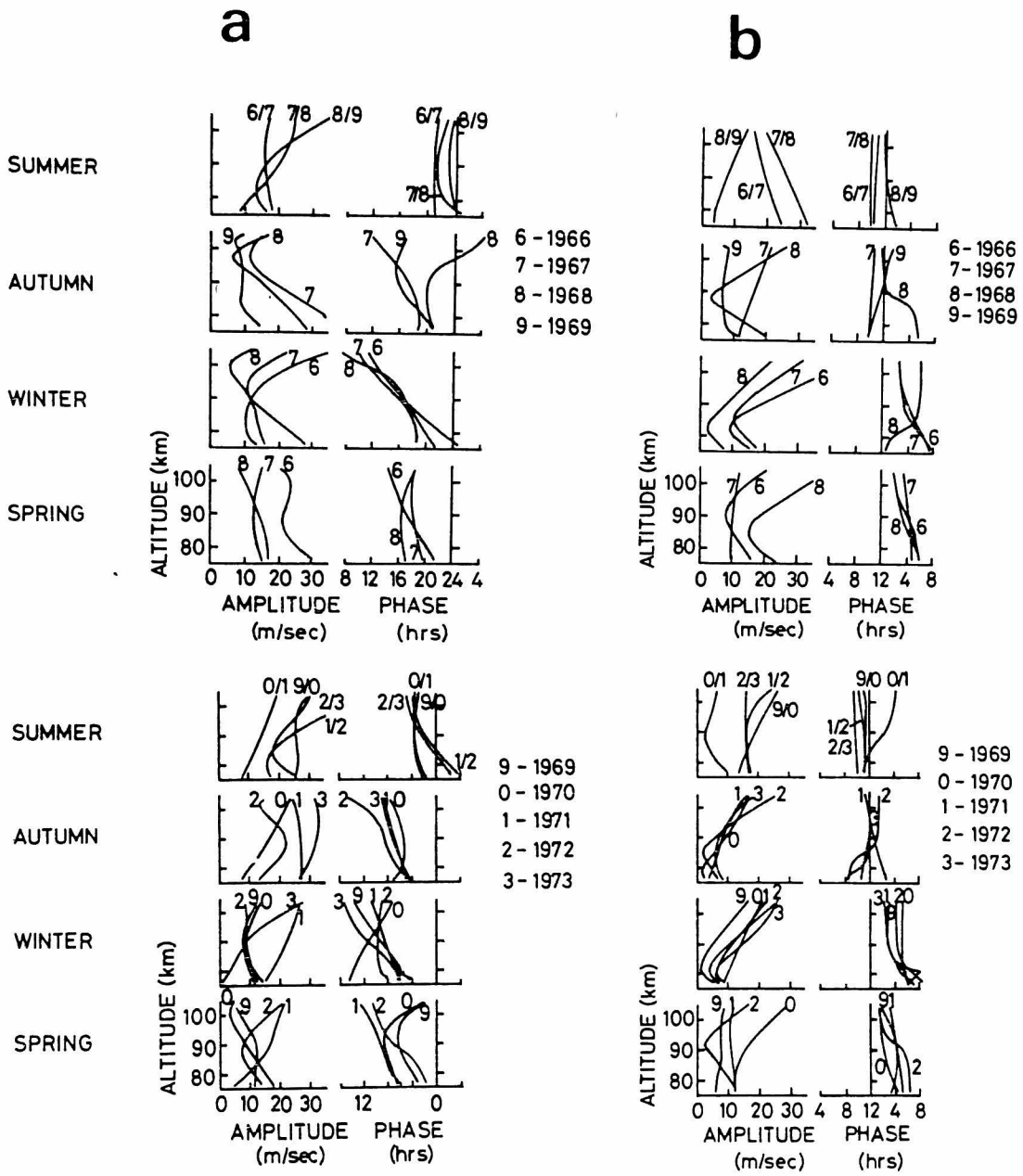

Fig. 5.32 Meridional component of the tidal wind velocity at Adelaide [Elford, 1973]. (a): diurnal component. (b): semidiurnal component.

the average behaviours of the diurnal tide in solsticial periods at two stations located oppositely with respect to the equator agrees with each other. The northward tidal wind at Atlanta observed by Roper [1978] is replotted in Fig. 5.33 for three seasons in 1974. Agreement in height profiles of the diurnal tide with our observations is poor except for the phase variation in autumn. The profile in summer indicates large discrepancy from ours such that phase variation at Atlanta corresponds to the waves with the short vertical wavelength. This disagreement might be attributed to the presence of the non-migrating tide investigated in Chapter II which can cause the longitudinal variation of the tidal wind

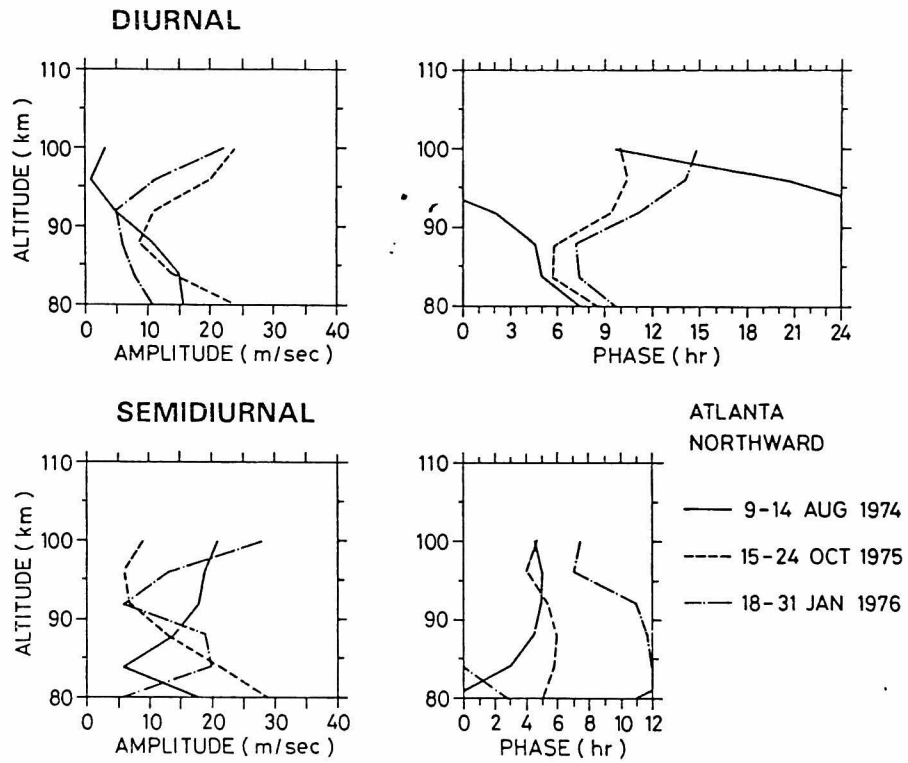

Fig. 5.33 Height profiles of tidal wind velocity observed at Atlanta [Roper, 1978].

even at the same latitude. The numerical computations done in Chapter II have shown that the non-migrating tide would not give large asymmetry with respect to the equator at higher altitudes than the heat source region. So that, the agreement between Kyoto and Adelaide would not be affected largely by the non-migrating tide.

As for the semidiurnal tide, the phase variation in summer at Adelaide corresponds to the wave with the long vertical wavelength. This characteristics is consistent with our results except for that the phase is reversed. The phase shift of 6 hrs, however, agrees with the latitudinal structure of the symmetric $S_{2,2}$ mode. The height profiles in winter show similar behaviour to ours except for the phase shift of 6 hrs. At equinoctial periods, clear correlation can not be deduced between the two. The central value of the phase in spring at Adelaide is approximately equal to that at Kyoto, which could not be explained by the symmetric modes.

4.2 Harmonic Dial for The Semidiurnal Tide

The seasonal variation of the semidiurnal tide is investigated by use of a harmonic dial at a specified altitude. Figure 5.34 shows idealized annual variation for both northward and eastward component of the semidiurnal tidal wind. A full circle in Fig. 5.34 corresponds to the bimonthly average of the northward component calculated from the results shown in Fig. 5.18 (a), while the seasonal mean for the eastward component is plotted as an open circle from Fig. 5.18 (b). Note that the coordinate is rotated anticlockwise by three hours for the eastward component. The northward wind vector rotates anti-clockwise annually on an ellipse whose major axis points at around 4.5 hrs local time. During summer months, the northward component is characterized by a stable phase and large amplitude. On the other hand, the amplitude becomes the smallest in winter. The phase in winter is reversed to that in summer. Annual variation of the eastward component generally agrees with that of the northward component, and its maximum phase is delayed by three hours being consistent with the theoretical expectation. In two equinoctial periods, the vector points are located at the opposite side on the ellipse with respect to the major axis. Considering the seasonal variation

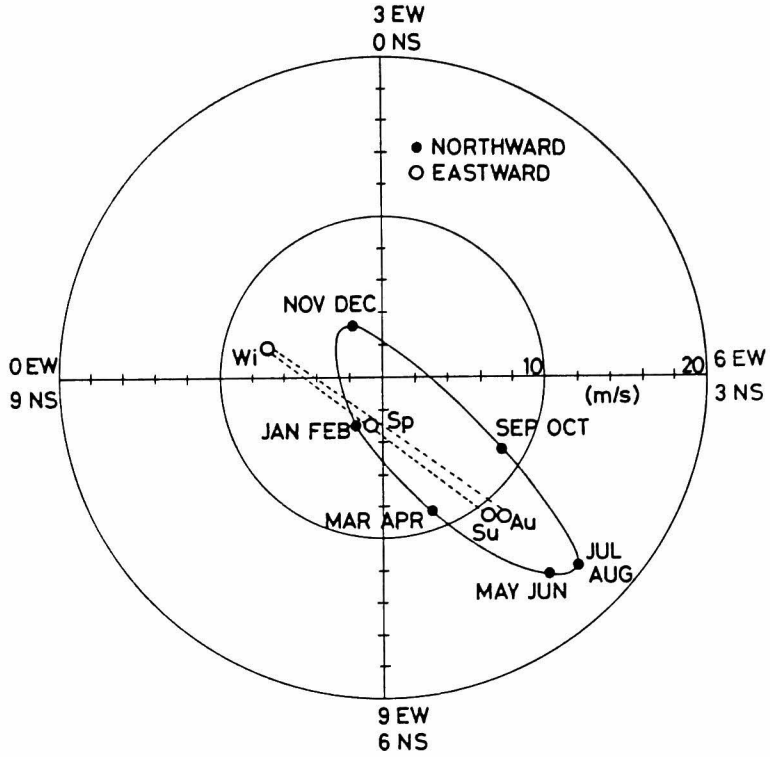

Fig. 5.34 Seasonal variation of the semidiurnal wind velocity at an altitude of 95 km observed at Kyoto in 1979-1980. a full circle: bimonthly average of the northward component. an open circle: seasonal average of the eastward component.

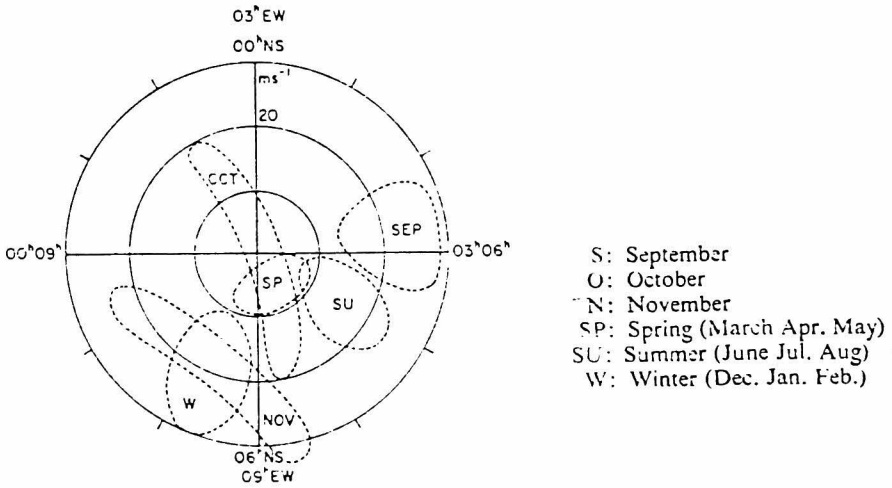

Fig. 5.35 Idealized pattern for the seasonal distribution of the semidiurnal components using results from three stations spread over 12 years [Müller]. Jodrell Bank: 1953-1957. Kharkov: 1961-1962. Scheffield: 1964-1965.

of both northward and eastward component, we could imagine a rapid change in the structure of the semidiurnal tide during winter and spring.

Müller [1966] deduced an idealized pattern for systematic seasonal variation of the semidiurnal tide as shown in Fig. 5.35 by using meteor radar data obtained at Scheffield (53°N), Kharkov (50°N) and Jodrell Bank (53°N). His result can be considered as an average in the whole meteor region, because a meteor radar in his ages could not determine a meteor echo height. Our results in summer and spring agree with the Muller's pattern very well in both amplitude and phase. Because our mean vector for autumn in Fig. 5.34 contains the results for both September and October, it corresponds to the average value of these two months in Muller's pattern. Individual monthly average shown in Fig. 5.18 (a) is included in the corresponding region in Fig. 5.35, although the amplitude detected in September at Kyoto is rather small. In November, December, January and February the amplitude is as small as a few m/sec at Kyoto, it, however, ranged from 10 m/sec to 30 m/sec at European stations. The phase in January and February at Kyoto roughly agrees with that for winter average in Fig. 5.35.

Clark [1980] reported the meteor wind observations at Durham (43°N) with the New Hampshire meteor radar system. From his determinations, the harmonic dial for the northward component of the semidiurnal wind at an altitude of 95 km is produced, and plotted in Fig. 5.36 for the period 1978-1979. General feature in spring, summer and autumn agrees with the Muller's pattern, consequently to ours. In November, the result at Durham shows a large spread similar to the Muller's result. As for the determinations in December and January, none of them is included in the region for winter in Fig. 5.34, although their amplitude sometimes becomes as large as 20 m/sec, and agrees with the characteristics of the semidiurnal tide in winter for Muller's pattern.

Another harmonic dial shown in Fig. 5.37 is deduced from the meteor radar data reported by Roper [1978] for the period 1974-1977 at Atlanta (34°N). Although it does not show a clear seasonal dependence, it is certain that the amplitude in winter is not so large as those at Durham and European stations.

These discrepancies in the behaviour of the semidiurnal tide in

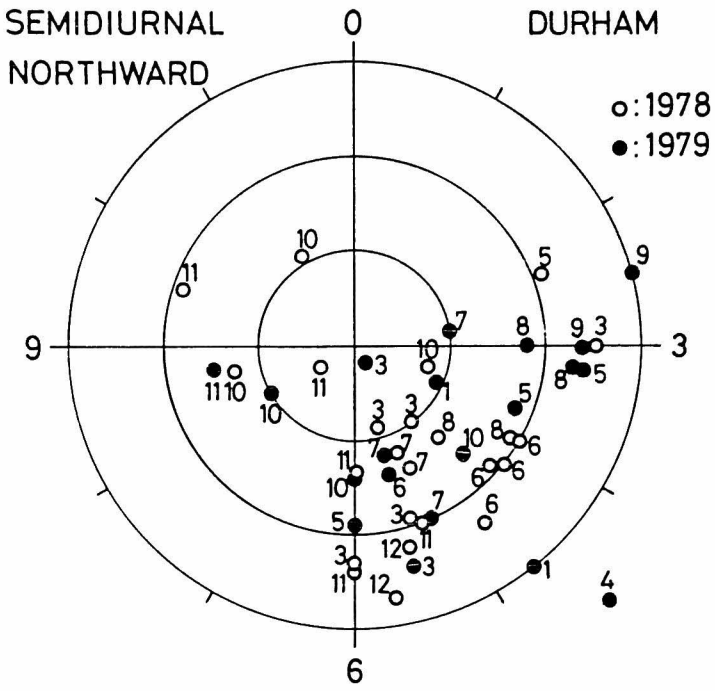

Fig. 5.36 Harmonic dial for the northward component of the semidiurnal wind velocity at an altitude of 95 km observed at Durham [Clark, 1980].

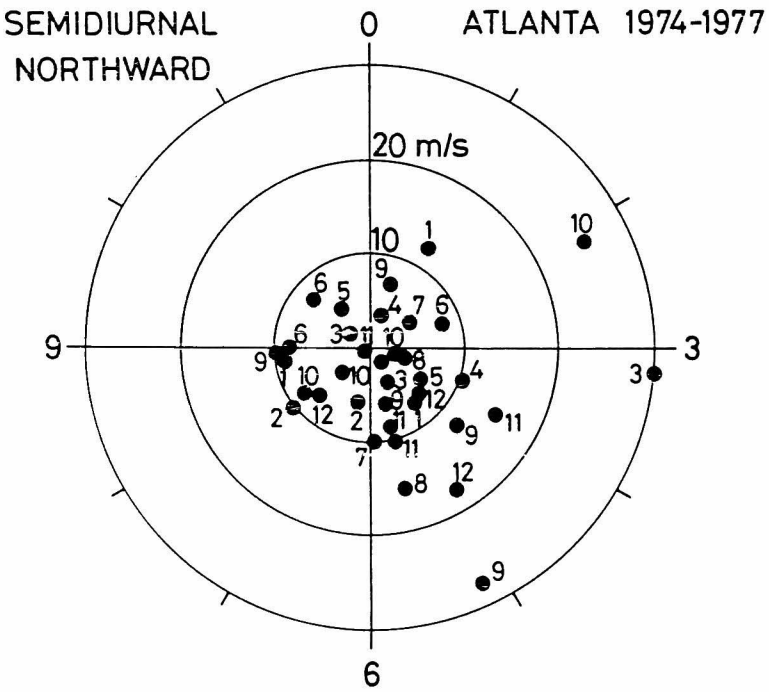

Fig. 5.37 The same as Fig. 5.36 except for the observations at Atlanta [Roper, 1978].

winter could be explained by the difference in latitude among these meteor radar stations besides the difference in observation periods. It might be suggested that the latitudinal difference of the semidiurnal tide differs from that in other stations. The higher order modes such as $S_{2,4}$ mode would be produced in winter, whose northward wind amplitude is much larger at around 50°N than that at around 35°N. A fundamental mode with a simple structure with latitude would be dominant in summer, because the harmonic dials do not differ from each other largely.

4.3 Latitudinal Structure

4.3.1 The Diurnal Tide

We have shown that the average height profiles of the atmospheric tides at meteor heights are fairly well characterized in each season when the observation period is elongated enough. So that, we could expect to obtain the fundamental horizontal structure of the atmospheric tides in each season. To investigate the latitudinal variation of the tidal wind at a specified height is one of the most certain way to identify the dominant Hough mode.

Tsuda and Kato [1980] have studied the seasonal variation of the latitudinal structure of the diurnal northward wind amplitude. They compared the theoretical expectations of the diurnal tide excited by ozone heat source with the observed results. For this comparison, used were meteor radar data which have been collected in the last two decades at many other stations. Table 5.4 shows the location and observation periods of these meteor radars. The seasonal mean is calculated by taking a vector average of the observed results especially for data in different periods. For some data whose height profiles are not known, we assume the data to represent the value at an altitude of 95 km where meteors appear most frequently. Amplitude and phase of the diurnal northward component is plotted in Fig. 5.38 (a) and (b) for summer and winter in the northern hemisphere, respectively. The theoretical curve is simultaneously drawn in the figure, which has been described in Chapter II. We attempted to fit the observed results at Kyoto station in summer to the theoretical value at June solstice. A full circle on the curve at a colatitude of 55° corresponds to the result at Kyoto in 1978.

Table 5.4 A list of meteor radar data referred to in Chapter V.

Station	Latitude	Longitude	Observed period	Reference
Heiss Island	80°N	38°E	1965-1971	Iljichev et al. [1974]
College	65°N	148°W	1968-1968	Hook [1970]
Obninsk	56°N	38°E	1964-1971	Iljichev et al. [1974]
Külungsborn	54°N	12°E	1970-1971	Lysenko and Portnyagin [1972]
Jodrell Bank	53°N	2°W	1953-1958	Greenhow and Neufeld [1961]
Scheffield	53°N	1°W	1964-1965	Müller [1966]
Kharkov	50°N	36°E	1964-1965	Kashcheyev and Lysenko [1968]
Urbana	40°N	88°W	1975-1976	Hess and Geller [1976]
Atlanta	34°N	84°W	1974-1976	Roper [1978]
Adelaide	35°S	130°E	1966-1973	Elford [1973]
Molodezhnaya	67°S	57°E	1967-1971	Iljichev et al. [1974]

An open circle is the average of the results in June and July in both 1979 and 1980 for summer, and in December, 1979 and January, 1980 for winter. Because the theoretical curves are deduced for the solsticial conditions, those in June and July are adopted for comparison with the theoretical value at June solstice, and those in December and January with that at December solstice among the recent observations in 1979 and 1980 at Kyoto. This procedure, however, did not adopted for other meteor radar data, since they sometimes did not show monthly value.

Kyoto and Adelaide stations have the same latitude in each hemisphere, so that they are convenient to check the asymmetry of the observed results with respect to the equator. As for the wind amplitude we can find a good agreement between theory and observations at these two stations in both June and December solstices. General latitudinal variation of theoretical curve is consistent with observations. Especially, in the northern mid-latitude region where many meteor radars exist, the

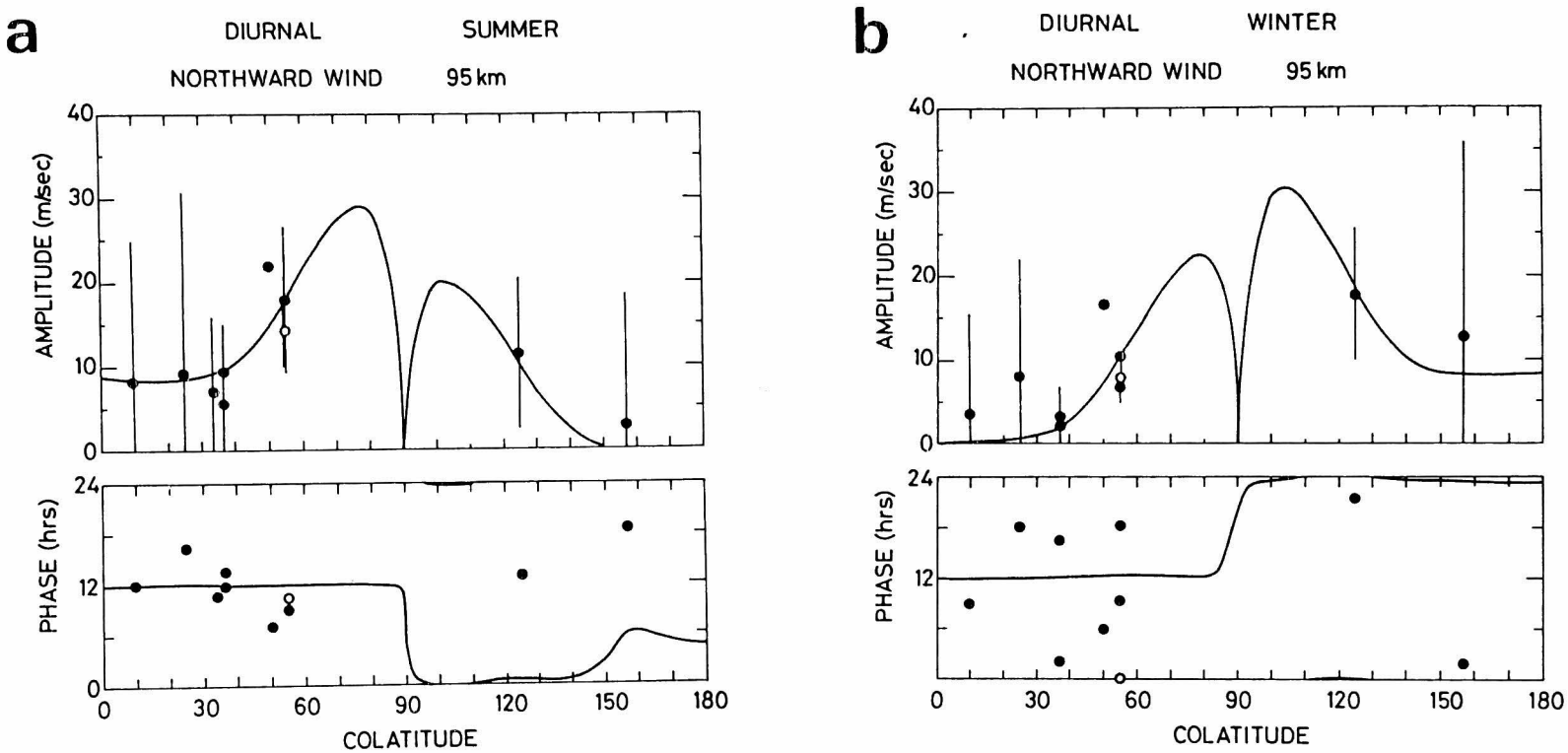

Fig. 5.38 Amplitude and phase of the northward diurnal wind velocity with colatitude. Theory (solid line) and observations (full and open circle) are simultaneously plotted for (a) summer and (b) winter, respectively.

agreement is fairly well at June solstice. An enhancement of the wind amplitude in the mid-latitude in summer is attributed to the dominance of the evanescent mode which has large amplitude outside the equatorial region as has been already described in Chapter II.

Observed phase value generally indicates 12 hrs local time in summer in the northern hemisphere, and agrees with the theoretical curve. In the case of winter results, the data spreads largely. This might be attributed to the presence of the propagating mode with short vertical wavelength whose maximum phase varies considerably in the meteor region. So that, needed are the simultaneous observations of meteor radars which can determine the height profiles appropriately.

Thus we conclude that the classical tidal theory described in Chapter II can explain the average seasonal variation of the diurnal tide in the meteor region, if we take a realistic ozone heat source distribution into account. Although water vapor near the ground is another large heat source of the diurnal tide, the propagating diurnal tides excited by water vapor reaching the meteor region do not have large amplitude outside the equatorial region as is well known. These modes can explain the asymmetry near the equator, but are doubtful to be able to explain the asymmetry in the mid-latitude.

4.3.2 The Semidiurnal Tide

The height profiles investigated previously suggest that the $S_{2,2}$ mode dominates in summer and the $S_{2,4}$ mode does in winter. Tsuda et al. [1980] examined the latitudinal structure of the northward component of the semidiurnal tide in both summer and spring in the northern hemisphere by use of meteor radar data at Kyoto in the periods up to March, 1979 together with those collected at other stations listed in Table 5.4. The results are shown in Fig. 5.39 (a) and (b) for summer and spring, respectively. A full and double circle corresponds to the determination in their study, and an open circle is the average value for the recent observations in 1979 and 1980. In summer, the additional result agrees with the previous feature, especially the phase value is fairly well consistent with the average in the northern hemisphere.

As for spring result, the phase does not agree with the idealized

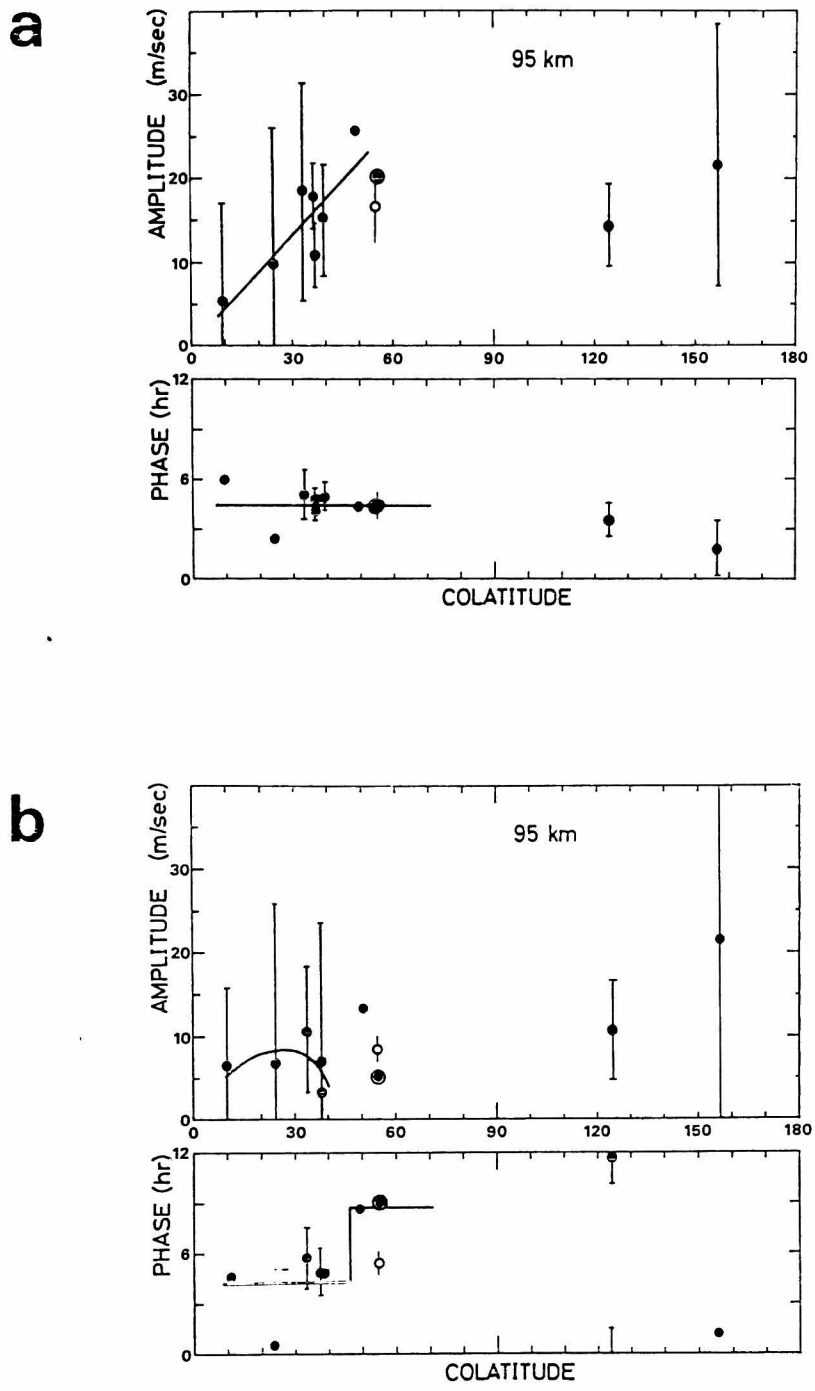

Fig. 5.39 The latitudinal variation of amplitude and phase of the northward semidiurnal wind velocity for (a) summer and (b) spring, respectively. Symbols are explained in the text.

curve drawn in Fig. 5.39, although the amplitude does not differ so much. This discrepancy might be caused year by year variation of the semidiurnal tide, because the tidal structure seems to be in transition in spring. We had better inquire the latitudinal variation of the semidiurnal tide in winter to show the dominance of the higher order modes. Figure 5.40 shows the same one as Fig. 5.39 but for the winter data. In the midlatitude, the semidiurnal tidal wind is enhanced while it becomes small at a colatitude of 55°. this latitudinal structure suggests the presence of the higher order modes in winter other than the fundamental mode.

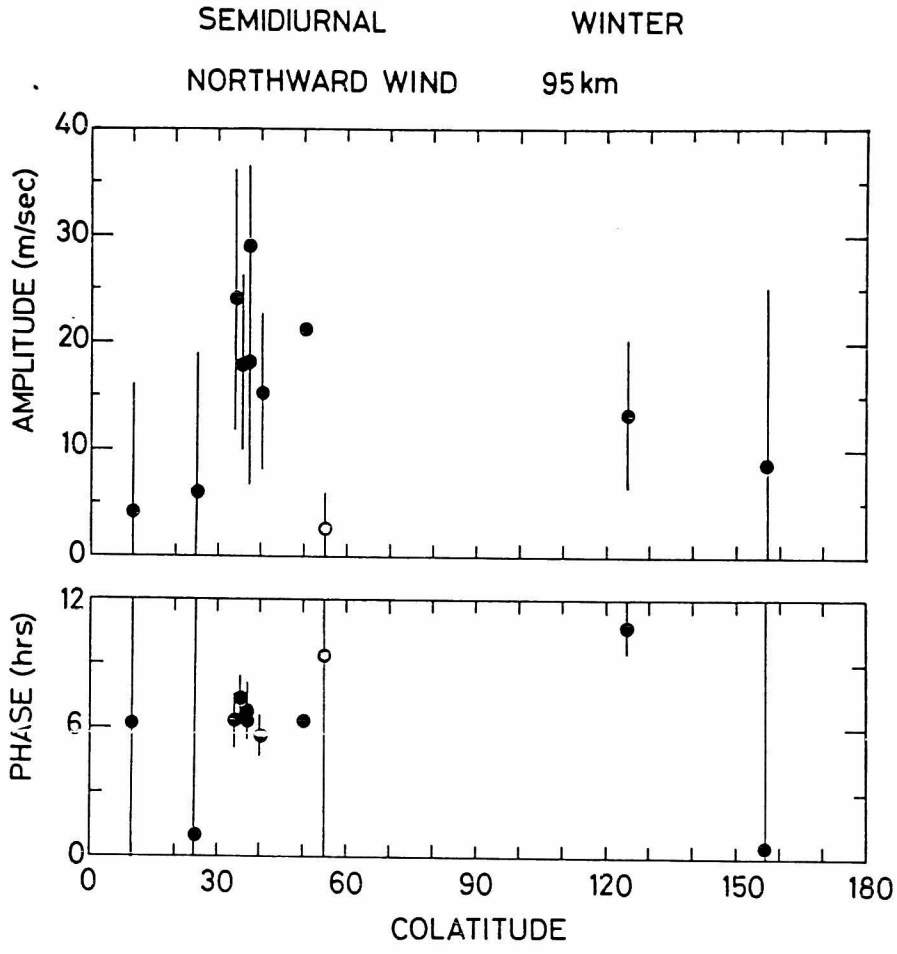

Fig. 5.40 The same as Fig. 5.39 except for winter result.

CHAPTER VI

OBSERVATION OF LUNAR ATMOSPHERIC TIDES

Section. 1 Method for Statistical Analysis of Lunar Variations

1.1 Chapman-Miller Method and Its Application to Meteor Radar Data

A variety of techniques has been used to resolve the lunar tidal component. The Chapman-Miller method [Chapman and Miller, 1940] is one of the most popular one for the analysis of lunar daily variations in geophysical data, and is used heretofore for many reliable determinations of lunar tides. Mallin and Chapman [1970a] gave a simple up-to-date account of the method for wide applications by using a computer. The application of the method to O_1 and N_2 tides has been also discussed by Mallin and Chapman [1970b].

The Chapman-Miller method is composed of three major parts; (a) the sorting of the data, (b) the harmonic analysis and (c) the estimate of the accuracy by using vector probable error, which are described below for the case of M_2 component.

(a) The value ν' is defined as the nearest integer to the Greenwich noon value of ν which is calculated as follows

$$\nu = t-\tau = 23.3827+29684.4748+0.000112\ T^2 , \qquad (6.1)$$

where τ and T are the mean lunar time and the time of measurement in Julien centuries, respectively. The ν' integer is reduced to a range 1 to 12, increasing twice in each lunation. All of the data are distributed into groups of days according to the ν' integer.

(b) Solar daily variations are calculated for data collected in days

characterized by a given values of ν'. Twelve determinations of them includes lunar variations which modifies the shape of the solar curve in a regular way with a period of half a lunar month. Lunar variations are deduced as an average of residuals calculated by subtracting the mean solar variation from each curve determined above. By the above procedure the curve for each value of ν' is added, while the solar variations are out of phase and the lunar ones are preserved to be in phase.

(c) Each twelve determinations calculated above contains both the lunar variations and errors. The end points of twelve vectors are assumed to have an isotropic two-dimensional Gaussian distribution about the end of the mean vector [Mallin and Chapman, 1970a]. An estimate of the accuracy is measured by a vector probable error whose amplitude is the radius of the circle that encloses the end points of half the measured vectors on a harmonic dial.

The grouping of the days of data is essential in the Chapman-Miller method because solar variations are canceled out when data are uniformly distributed with respect to the phase of the moon.

As for the analysis of O_1 component which is the largest of the lunar declinational diurnal constituents, data are divided into twelve groups according to the value a new daily integer 0' which is defined as the nearest integer to the Greenwich noon value of 0.

$$0 = \frac{t-\tau+s}{2} = 8.7059+30884.4500T+0.000122T^2 \qquad (6.2)$$

In applying the Chapman-Miller method to meteor radar data some modifications are added because data are not collected continuously differing from geomagnetic data. Although the number of data varies sinusoidally with maximum occurring at 6 local solar time, as described in Chapter IV that with respect to local lunar time is smoothed as shown in Fig. 6.1. This means that the harmonic analysis for the solar variations can not be done with equal weight, although that for lunar variations is performed. Thus, the procedure (b) in the Chapman-Miller method is modified as described below with the least change in significance.

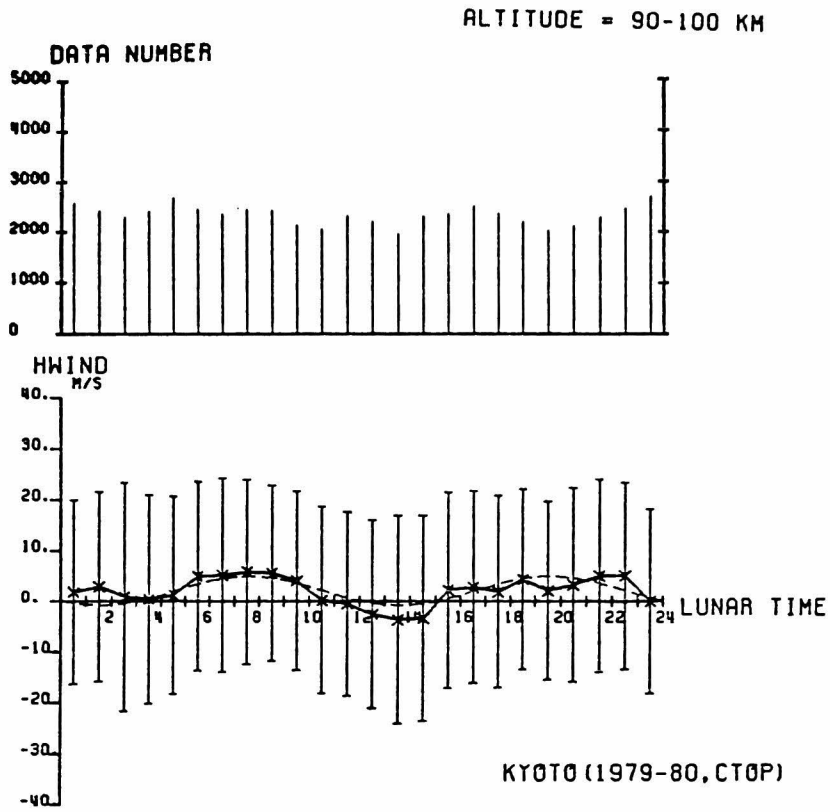

Fig. 6.1 Meteor echo distribution along lunar time (top), and average wind velocity (bottom).

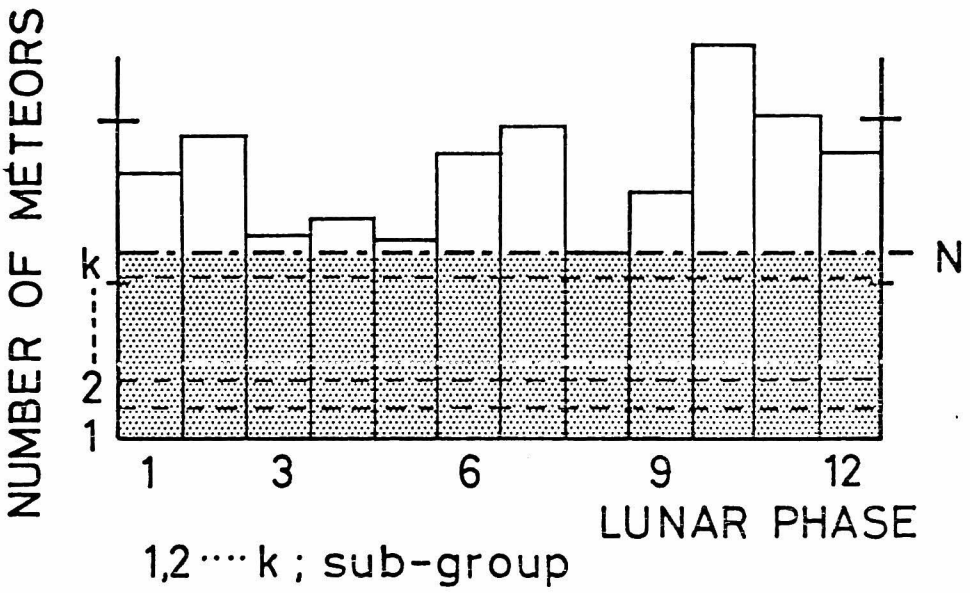

Fig. 6.2 Number of meteor echoes versus lunar phase. Lunar phase 13-24 is folded over 1-12 for the analysis of semidiurnal variaiton.

In Fig. 6.2 we show distribution of meteor echoes versus lunar phase which is used to determine the M_2 component. Meteor echoes in lunar phase 13-24 can be superimposed on those in 1-12. We use the hatched region in Fig. 6.2, because we must adopt equal number of data samples with respect to the lunar phase to avoid statistical bias. We divide the data at each lunar phase into those sub-groups each of which contains approximately four hundred samples large enough for statistical significance. We make a sub-set for harmonic analysis by picking up one of k sub-groups at each lunar phase, so that we would have a large number of sub-sets up to k^{12}. It is not necessary to use all the sub-sets for the harmonic analysis, because appropriate number of them will be clarified to be 50 in the following subsection. Solar variations could be canceled out if the number of data is equal not only to lunar phase but also to lunar time. Therefore, a sub-set which does not contain equal number of data with respect to lunar time must be discarded. Probable error ellipse [Bartels, 1932] on the harmonic dial are calculated to estimate the accuracy of the determination in addition to the conventional two-dimensional standard deviation.

1.2 Error Estimation of Analysis

The modified Chapman-Miller method described above is applied to realistic data to confirm its propriety on three points; (1) adaptation of equal number of data samples with respect to both lunar phase and lunar time, (2) necessary number of sub-sets and (3) rejection of solar tides and noises.

Analysis of O_1 component of northward wind at an altitude of 100 km is taken an example for test of (1) and (2).

Figure 6.3 shows the necessity of the procedure (1) mentioned above, because error in the results comes out when number of data in a sub-set is not equal with respect to the lunar time. Number of sub-sets N_S which corresponds to the number of determinations by harmonic analysis, must be large enough to treat the results as statistically significant ones. Variation of amplitude and phase of the mean vector against N_S is shown in Fig. 6.4 with a error bar, which indicates the constancy of the results for N_S larger than 50. The mean vectors are also plotted

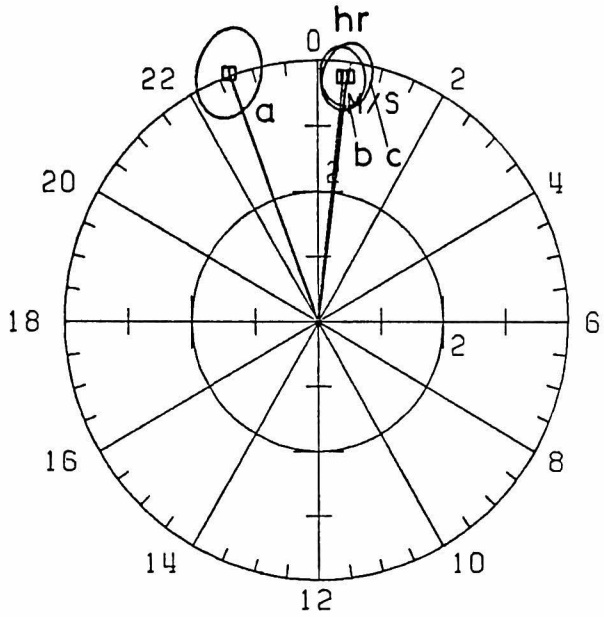

Fig. 6.3 Necessity of uniformity of number of data with respect to lunar time. Number of sub-sets is set equal to (a) 50, (b) 5000 and (c) 2000. Number of data is not made uniform for the case (c).

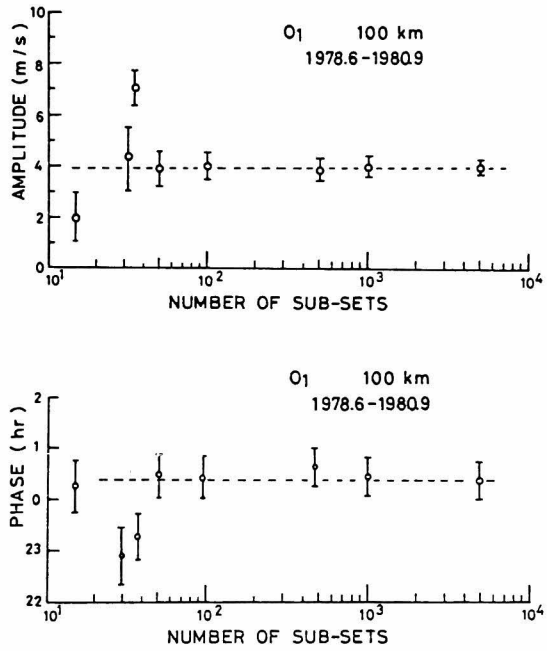

Fig. 6.4 Variation of amplitude and phase of O_1 component with number of sub-sets. True value is indicated by a broken line.

in Fig. 6.3 for the cases N_s = 50 and N_s = 5000, and agrees with each other. So that, the necessary minimum value of N_s is estimated as 50. Contamination of solar tides and noises to the determination of lunar tides is investigated for the case of M_2 component.

A realistic pseudo data set is generated by using a normally distributed random values, and its functional form is written as follows,

$$W(z,t) = S + M_2 + O_1 + R \tag{6.3}$$

where S, M_2, O_1 and R are solar variations, lunar semidiurnal component, diurnal lunar component and residuals, respectively. The amplitude and phase of M_2 component are set as 2.2 m/sec and 7.2 hrs lunar time, respectively. The S variation is composed of solar diurnal and semidiurnal tidal wind as described below:

$$S = \sum_{n=1}^{2} (S_n(z) + ds_n)\sin(nt+\phi_n(z)+d\phi_n) \tag{6.4}$$

In the expression, the values ds_n, d_n and R which distribute normally with a specified standard deviation, correspond to a day-to-day variability of amplitude and phase of solar tide and random component, respectively. Monthly mean value of solar tidal wind in 1979 and 1980 are adopted to $S_n(z)$ and $\phi_n(z)$. Daily variation of number of data is sinusoidal with its maximum occuring at 6 hrs local solar time. It is assumed that two or three days observations are repeated within five days as shown in Fig. 4.3. The analysis for M_2 component is applied to a variety of cases, and has been proved to be satisfactory, and some results are plotted in Fig. 6.5 on the harmonic dial. Random residuals with standard deviation of 40 m/sec in the amplitude does not affect the determination as shown in Fig. 6.5.(a). Even with large variations in amplitude and phase of solar tides, the determination of M_2 component is well done within the range of the error bar. Again, the necessity of the smoothing of number of data with respect to the lunar time is

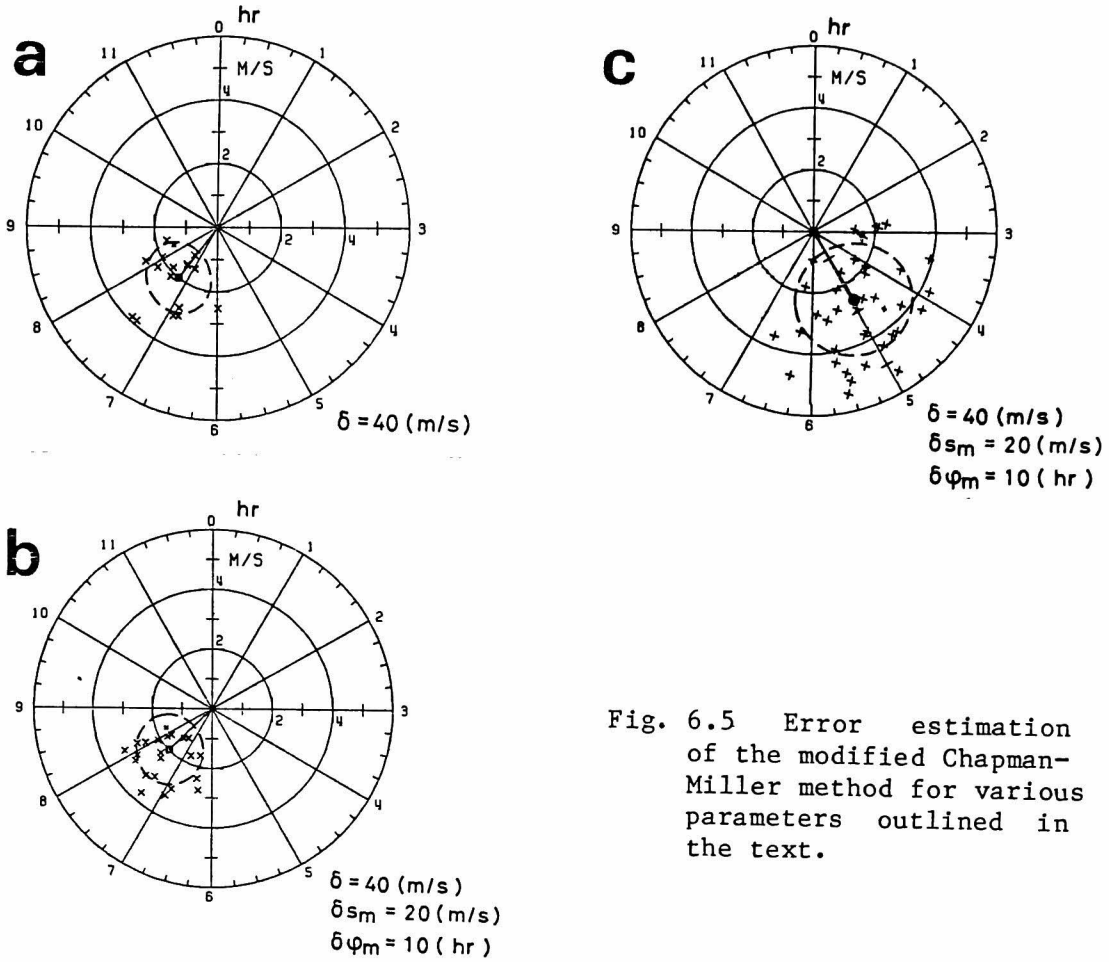

Fig. 6.5 Error estimation of the modified Chapman-Miller method for various parameters outlined in the text.

demonstrated. In Fig 6.5.(c), the analysed result without above mentioned smoothing is shown, and is very much different from the model, although random perturbations in pseudo data are the same as that for Fig 6.5.(b).

The method proposed in the preceding subsection seems to be appropriate for the analysis for lunar variations of meteor radar data, the method is applied to them in the following sections.

Section 2. Lunar Tidal Winds

An altitude profile and a seasonal variation of both M_2 and O_1 component in northward wind are determined by using the modified Chapman-

Miller method. Although the decay-height method is less reliable than the interferometer method, it is adopted to determine the altitude of a meteor, because it can supply large amount of data. Each echo is assumed to come from the direction of antenna boresight. Observation periods are again illustrated in Fig. 6.6. Analyses are done for two series of data; (a) March 1979 to July 1980 and (b) May 1978 to January 1981.

2.1 Height Profile of M_2 Component

All the data are divided into three altitude ranges as 90±2, 95±2 and 100±2 km. We have the largest number of meteor echoes in the 95±2 km region. Lunar semidiurnal component (M_2) is determined in the northward wind at three altitude ranges. The results are listed in Table 6.1 (a) and (b), and are plotted on harmonic dials in Fig. 6.7 (a) and (b) corresponding to observation period (a) and (b), respectively. A phase means the local mean lunar time of northward maximum wind velocity. The radius of the probable error circle is given in the unit of m/sec.

As for the result in the period (a), the amplitude of the M_2 wind

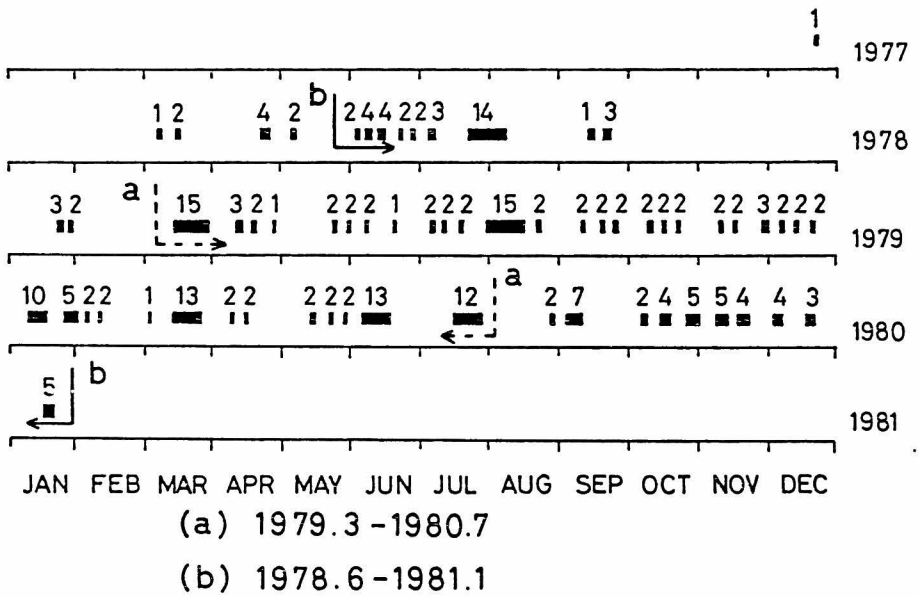

Fig. 6.6 Observation periods of the Kyoto meteor radar. Two periods are adopted for the analysis of lunar tidal winds. (a): March, 1979 - July, 1980. (b): June, 1978 - January, 1981.

ranges from 1.8 to 2.2 m/sec throughout the meteor region. Hour of northward maximum of the M_2 wind is 8.4 hrs lunar time at 90 km altitude, 6.9 hrs at 95 km and 6.1 hrs at 100 km. The M_2 component has vertical wavelength of approximately 60 km. Determinations in the period (b) show that the amplitude of M_2 wind is 2.6 m/sec at 90 km, 3.1 m/sec at 95 km and 3.6 m/sec at 100 km, indicating a slight monotonous increase of it with altitude. Phases are 8.9, 7.6 and 5.5 hrs lunar time in the 90, 95 and 100 km region, respectively. The vertical wavelength is about 35 km.

Table 6.1 Altitude variation of the M_2 component in the northward wind in (a) March, 1979 to July, 1980 and (b) June, 1978 to January, 1981.

(a) March 1979 to July 1980

ALTITUDE (km)	AMPLITUDE (m/sec)	PHASE (hr)	PROBABLE ERROR (m/sec)	NUMBER OF DATA	NUMBER OF SUB-GROUPS	NUMBER OF SUB-SETS
90 ± 2	1.8	8.4	0.3	12,000	4	64
95 ± 2	2.2	6.9	0.4	37,488	7	91
100 ± 2	2.1	6.1	0.4	24,960	5	85

(b) June 1978 to January 1981

ALTITUDE (km)	AMPLITUDE (m/sec)	PHASE (hr)	PROBABLE ERROR (m/sec)	NUMBER OF DATA	NUMBER OF SUB-GROUPS	NUMBER OF SUB-SETS
90 ± 2	2.6	8.9	0.2	21,840	4	50
95 ± 2	3.1	7.6	0.3	56,544	8	50
100 ± 2	3.6	5.5	0.4	30,360	5	50

Phase velocity in both cases is downward so as to agree with tidal theory. Amplitude is larger in period (b) than that in period (a). When the phase values for two series of data are compared with each other, differences in vertical wavelength can be seen, although the phases at 95 km agrees within the probable error. This fact suggests that the dominant mode of M_2 wind in the meteor region can be variable, and seems to be attributed to the wave propagation characteristics.

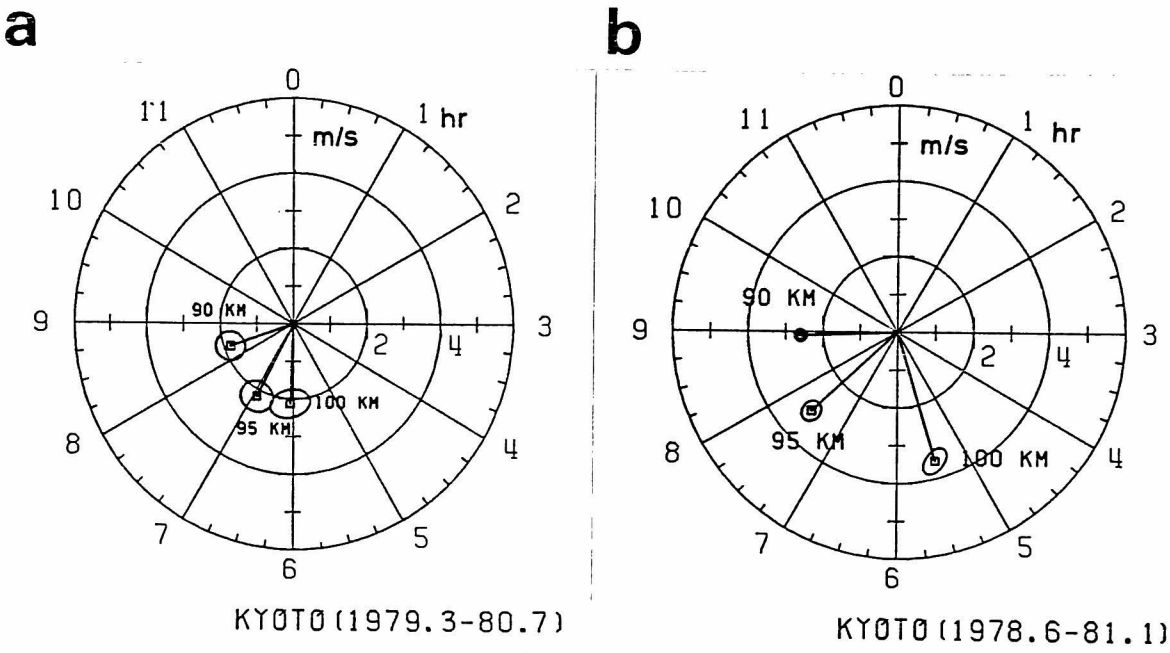

Fig. 6.7 Harmonic dial of the M_2 component in the northward wind at altitudes of 90, 95 and 100 km for the periods (a): left and (b): right, respectively.

2.2 Height Profile of O_1 Component

At three altitude regions, the O_1 component in the northward wind is detected as shown in Table 6.2 and Fig. 6.8 for the two series of data. The amplitude is 1.6 m/sec at 90 km, 1.2 m/sec at 95 km and becomes as large as 3.7 m/sec at 100 km in the period (a). Northward maximum occurs at 9.5 hrs lunar time in the 90 km region, 3.4 hrs in 95 km and 23.5 hrs in 100 km. The linear phase progression with altitude shows a downward phase velocity, and the vertical wavelength of about 25 km.

As for the results in the period (b), amplitude is 2.0 m/sec at 90 km, 1.3 m/sec at 95 km and 3.6 m/sec at 100 km. Phase is 12.0 hrs lunar

Table 6.2 The same as Table 6.1 except for O_1 component.

(a) March 1979 to July 1980

ALTITUDE (km)	AMPLITUDE (m/sec)	PHASE (hr)	PROBABLE ERROR (m/sec)	NUMBER OF DATA	NUMBER OF SUB-GROUPS	NUMBER OF SUB-SETS
90 ± 2	1.6	9.5	0.3	8,928	3	33
95 ± 2	1.2	3.4	0.5	24,768	6	60
100 + 2	3.7	23.5	0.5	17,184	4	52

(b) June 1978 to January 1981

ALTITUDE (km)	AMPLITUDE (m/sec)	PHASE (hr)	PROBABLE ERROR (m/sec)	NUMBER OF DATA	NUMBER OF SUB-GROUPS	NUMBER OF SUB-SETS
90 ± 2	2.0	12.0	0.4	15,792	4	58
95 ± 2	1.3	20.2	0.4	36,120	5	57
100 ± 2	3.6	23.7	0.5	23,880	5	56

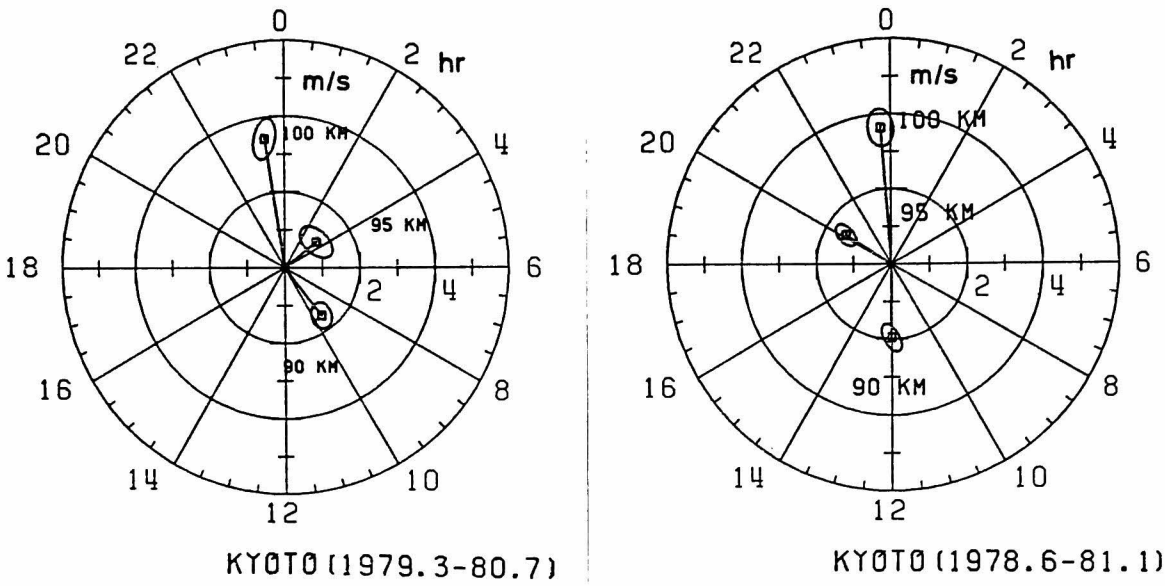

Fig. 6.8 The same as Fig. 6.7 except for the O_1 component.

time at 90 km, 20.2 hrs at 95 km and 23.7 hrs at 100 km. Phase difference between the results at 90 km and 95 km is about 8 hrs lunar time, and is twice larger than that between ones at 95 km and 100 km. Phase velocity seems to be downward by a primary calculation.

The error ellipse for determination in the 100 km region in the period (a) partly overlap with that in the period (b). The result at 90 km in the period (a) is almost reproduced if the amplitude in the period (b) is reduced by a factor of 0.8, and the phase is displaced anticlockwise by 2.5 hrs. The phase of M_2 wind at 95 km in the period (a) differs 8 hrs from that in the period (b), although the reliability of them is critical because of an small amplitude ratio between wind velocity and the radius of a probable error circle.

2.3 Seasonal Variation of M_2 Component

All the data in the altitude region 90 to 100 km in each period are separated according to the three seasons:

E - March, April, September, October;

J - May, June, July, August;

D - November, December, January, February.

The results are shown in Table 6.3 and Fig. 6.9 for the two periods.

Table 6.3 The same as Table 6.1 except for the seasonal variation.

(a) March 1979 to July 1980

SEASON	AMPLITUDE (m/sec)	PHASE (hr)	PROBABLE ERROR (m/sec)	NUMBER OF DATA	NUMBER OF SUB-GROUPS	NUMBER OF SUB-SETS
EQUINOX	4.4	5.0	0.3	23,760	5	85
JUNE SOL.	1.8	5.8	0.8	12,816	4	64
DEC. SOL.	3.6	10.1	1.0	17,604	9	90

(b) June 1978 to January 1981

SEASON	AMPLITUDE (m/sec)	PHASE (hr)	PROBABLE ERROR (m/sec)	NUMBER OF DATA	NUMBER OF SUB-GROUPS	NUMBER OF SUB-SETS
EQUINOX	3.4	7.5	0.6	34,080	5	50
JUNE SOL.	2.0	4.6	0.5	50,592	6	50
DEC. SOL.	5.7	8.3	0.7	25,216	4	50

In the period (a) at equinoctial conditions, the amplitude becomes as large as 4.4 m/sec, with maximum occurring at 5.0 hrs lunar time. In June solsticial period, the amplitude of the M_2 component is about 1.8 m/sec and northward maximum of that occurs at 5.8 hrs. As for the December solsticial period, we see the amplitude of 3.6 m/sec and northward maximum of 10.1 hrs. In the period (b), the amplitude of the M_2 wind is 3.4 m/sec, 2.0 m/sec and 5.7 m/sec in E, D and J season, respectively. Northward maximum occurs at 7.5 hrs lunar time in the E season, 4.6 hrs in J and 8.3 hrs in D.

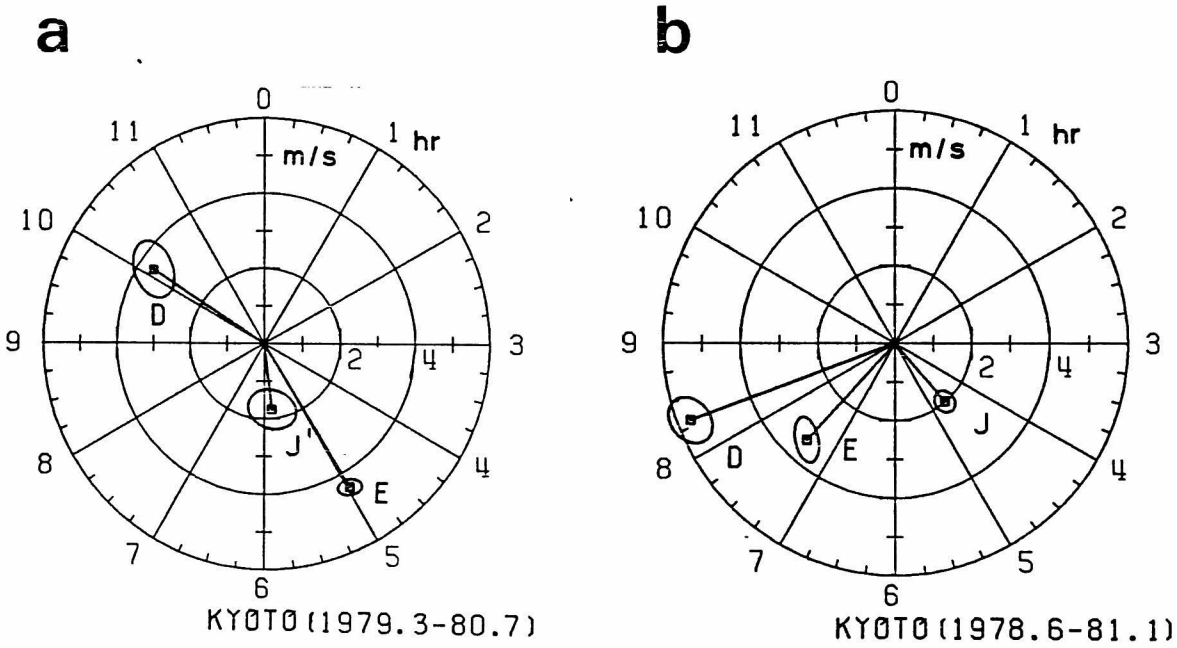

Fig. 6.9 Harmonic dials of M_2 component in the northward wind for the periods (a): left and (b): right, respectively. Capitals E, J and D in the figure denote determinations in equinoctial peiord, June solsticial period and December solsticial period, respectively.

The seasonal variation of the amplitude of M_2 wind in the meteor region can be seen that the maximum occurs during the D season, and the minimum in the J season. Phase differences between the results in the D and J seasons for the two series of data are about 4 hrs, although phase values of them in the period (a) rotate clockwise about 2 hrs from those in the period (b).

Section 3. The M_2 and O_1 Component in The Variation of Mean Height of Meteor Echo Distribution

The interferometer method is applied to a high signal-to-noise ratio meteor echo to determine its height to an accuracy of about 1.5 km. Meteor echoes approximately distribute as Gaussian along height with standard deviation of about 7 km. Mean height of meteor echoes can be known hourly during the period from 0 to 12 hrs local solar time when many meteor trails are detected.

Lunar variations have been found in the mean height of meteor echoes, and are listed in Table 6.4 for both M_2 and O_1 component. Amplitude of the M_2 variation is 0.22 km, and maximum phase of it occurs at 9.4 hrs lunar time. As for the O_1 component, amplitude and maximum phase are 0.18 km and 14.1 hrs, respectively. Fig. 6.10 shows harmonic dials for the M_2 and O_1 component of mean height variation. Probable error ellipse is also shown in Fig. 6.10.

Table 6.4 Lunar variations in the mean height of meteor echoes.

COMPONENT	AMPLITUDE (km)	PHASE (hr)	PROBABLE ERROR (km)	NUMBER OF DATA	NUMBER OF SUB-GROUPS	NUMBER OF SUB-SETS
M_2	0.22	9.4	0.03	21,300	3	105
O_1	0.18	14.1	0.05	10.464	4	64

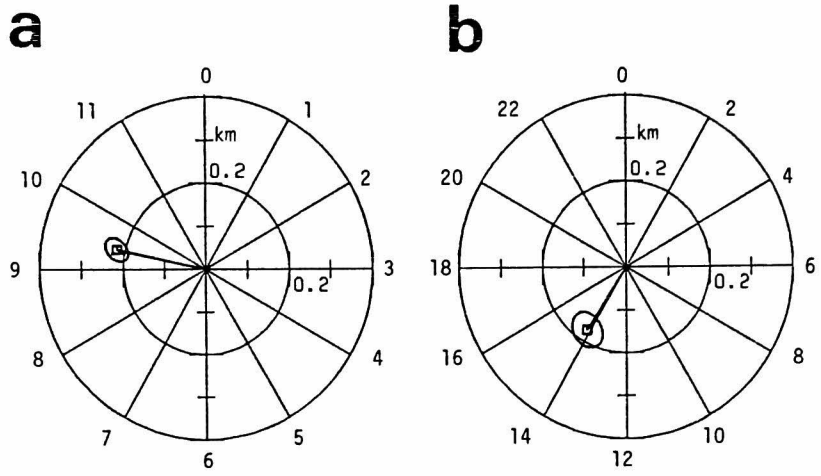

Fig. 6.10 Harmonic dials of variations in the mean height of meteor echoes; (a) M_2 and (b) O_1 component.

Section 4. Discussion

According to the classical tidal theory [Chapman and Lindzen, 1970; Kato, 1980], the equivalent depth and vertical wavelength at 90, 95 and 100 km altitude are listed in Table 6.5 for several fundamental propagating modes of the M_2 and O_1 component. Observed wavelength of the M_2 wind ranged from 40 to 75 km, and corresponded to $L_{2,3}$ or $L_{2,4}$ mode. This may show that higher modes are excited by interaction between the fundamental mode and the mean zonal wind which was first investigated by Lindzen and Hong [1974], and a number of authors [Walterscheid et al., 1980; Aso et al., 1981]. Altitude profile of the lunar semidiurnal wind

including the mean zonal wind effect was calculated by Aso et al. [1981]. The observed wind amplitude ranged within the theoretical expectations, and the observed short vertical wavelength might be explained by the mean zonal wind effect, although theoretically computed phase value differs largely from the observed results.

As for the diurnal luni-solar component, we have determined the vertical wavelength of 25±4 km which is longer than that of fundamental $L_{1,1}$ or $L_{1,2}$ modes.

The M_2 wind amplitude ranged from one-fifth to one-tenth of that of the solar semidiurnal wind [Aso et al., 1979, 1980; Tsuda et al., 1980] Ionospheric drift measurements were carried out by Chapman [1953] and

Table 6.5 Equivalent depth and vertical wavelength for fundamental modes of M_2 and O_1 component. CIRA 1972 atmosphere model is used.

	MODE	EQUIVALENT DEPTH (km)	VERTICAL WAVELENGTH (km) 90 km	95 km	100 km
	(2,2)	7.08	*	373.	159.
M_2	(2,3)	3.26	70.4	64.3	58.5
	(2,4)	1.86	44.5	41.8	39.4
	(2,5)	1.19	33.4	31.7	30.1
	(1,1)	0.512	20.6	19.7	18.9
O_1	(1,2)	0.177	11.8	11.3	10.9
	(1,3)	0.089	8.3	8.0	7.7
	(1,4)	0.054	6.4	6.2	6.0

*; EVANESCENT

Phillips [reported by Brigs and Spencer, 1953]. Their results of the M_2 wind were summerized by Matsushita [1967]. From the observations of the sporadic E, Matsushita [1962] deduced the M_2 wind in the ionospheric E region. An estimate of the lunar ionospheric wind from the dynamo theory has been made by Maeda and Fujiwara [1967]. Those determinations of the lunar semidiurnal wind are listed in Table 6.6.

As for Matsushita's estimation [1962], the amplitude is only two-fifth of ours whilst the phase is consistent with ours. Greenhow and Neufeld [1961] determined the upper limit to be 2 m/sec of the amplitude of the lunar semidiurnal component in the meteor region. Our results are

Table 6.6 Experimentally determined lunar semidiurnal wind in the ionospheric E region.

METHOD	NORTHWARD AMP. (m/s)	NORTHWARD PHASE (hr)	EASTWARD AMP. (m/s)	EASTWARD PHASE (hr)	PERIOD	STATION	STUDIED BY
PARTIAL REFLECTION	14	2.9	16	5.7	1949 - 51	52N, 0E (CAMBRIDGE)	PHILLIPS
PARTIAL REFLECTION	24	2.9	21	6.5	1950 - 51	45N, 74W (MONTREAL)	CHAPMAN
SPORADIC E	0.8	7.0	1.4	10.0		(35N)	MATSUSHITA
DYNAMO THEORY	9.5	9.5	12.9	0.5		(35N)	MAEDA & FUJIWARA
METEOR RADAR	2	0	2	3	1953 - 58	53N, 2W	GREENHOW & NEUFELD

consistent with their determination, though their result seems to be not very significant.

At meteor heights, the OI (5577A) night airglow is one of the most extensively studied phenomena on the many optical emissions. A number of authors has attempted at detecting lunar variations in the green line measurements [Nagata et al., 1961, Davidson, 1963]. The pressure variation by atmospheric waves was theoretically suggested to cause a change in the 5577 radiation [Tohmatsu and Nagata, 1963; Gadsden and Marovich, 1969; Forbes and Geller, 1972].

Mean height of meteor echo distribution is seemed to be affected by the lunar pressure variation. A displacement of 0.22 km by the M_2 component corresponds to the pressure variation of 3.6 % of the mean value, when we assume a constant scale height of 6 km. If the value is substituted into the theoretical expressions deduced by Tohmatsu and Nagata [1963], we get lunar variation in the 5577 radiation of 19 Rayleigh which is approximately twice the observations. Fukuyama [1976] examined the seasonal variation of the green line, and found a good agreement with solar semidiurnal tidal wind at meteor heights in midlatitude. He especially pointed out that the phase of the maximum emission was out of phase to that of the northward maximum of the solar semidiurnal tidal wind. Annual mean value of the phase of the M_2 wind ranges from 6 to 8 hrs lunar time as shown in Fig. 6.7. The maximum emission of the green line ocurred at 11.5 hrs lunar time and 1.8 hrs for the determinations by Nagata et al. [1961] and Davidson [1963], respectively. The phase difference between these two kind of observations falls around 6 hrs, which means the northward M_2 wind is phase-reversed to the 5577 radiation. The argument done for the solar semidiurnal tide by Fukuyama [1976] might be applicable for the correlation between lunar variation in the green line and the lunar semidiurnal wind.

Shiraki [1981] found that the seasonal variation of geomagnetic L component observed at Kakioka was very anomalous compared with that of the S variation in both amplitude and phase. A ratio of the amplitudes of the L component in the D and J season was not so large as that for the S variation. According to the ionospheric dynamo theory, the seasonal variation of the M_2 wind amplitude shown in Fig. 6.10 can explain the

characteristics in geomagnetic variation described above, which would roughly compensate for the amplification of conductivities in the dynamo region in summer. The shape of the vector diagram were similar in the J season and equinox, while that in the D season was different. This characteristics might be explained by the remarkable phase shift of the M_2 wind in these seasons.

CHAPTER VII

SUMMARY

We have designed and constructed Kyoto meteor radar which is a coherent pulse doppler radar, and applied to the observations of the atmospheric tides in the altitude ranges from 80 km to 110 km. We have determined the seasonal mean structure of both diurnal and semidiurnal tide. The diurnal tide has been found specifically to be consistent with the theoretical expectation. We have also detected height profiles of the two fundamental components of the lunar atmospheric tidal wind at meteor heights.

In Chapter II, the classical tidal theory has been applied to the two recent subjects of the diurnal tide. Firstly, the seasonal variation of the diurnal tide has been explained by the asymmetric excitation source due to ozone absorption of solar incident flux. The evanescent modes have been found to play an important role for the seasonal variation of the diurnal tide in the meteor region. Secondly, the excitation and propagation of the non-migrating diurnal tide have been studied with a view to applying it to the local effect of the observed atmospheric tides.

In Chapter III, design cnsideration on both hardware and software system of the Kyoto meteor radar has been shown. The phase sequenced interferometer incorporated into the radar can measure the height of a meteor echo to an accuracy of approximately 1.5 km. The small scale computer installed in the radar can provide radar control, data collection and quick check of the measurement. The Kyoto meteor radar would be one of the highly efficient meteor radars, although its transmitted power is moderate.

In Chapter IV, we have examined the basic feature of the meteor radar observations. Distribution of meteor echoes with both altitude

and local time has been clarified. Seasonal variation in the meteor height distribution such as meteor echo rate, maximum echoing height and the standard deviation has been investigated. We have shown the relation between the decay constant of the underdense meteor echo and the ambipolar diffusion coefficient. From these characteristics of the radio meteor echoes, the atmospheric temperature at meteor heights has been deduced, and consistent with the model atmospheres.

In Chapter V, observations of both solar diurnal and semidiurnal tidal wind have been shown. We have examined seasonal and short period variation of the solar tides. Height profiles of the solar tides has been explained in terms of the interference among multiple waves with various vertical structures. Latitudinal distribution of both diurnal and semidiurnal tides has been investigated. We have found that the theoretical expectation described in Chapter II agrees with the observed seasonal variation of the diurnal tide. Thus the classical tidal theory has been proven to be applicable to the average behaviour of the solar atmospheric tides. We hope that our comformable observations would contribute to recognize the real mechanism of the variation in the solar tides in comparison with theoretical investigations studied by many other people.

In Chapter VI, we have detected the M_2 and O_1 component of the lunar atmospheric tides in the northward wind. We have shown their height profiles and seasonal variation. Since the observations of the luanr atmospheric tidal wind at meteor heights has been scarce until now, our results would be useful for studies on lunar effects in the ionosphere.

In conclusion, the Kyoto meteor radar has been effective to observe the atmospheric tides, although the height range is limited around 95 km. Because the atmospheric tides are the global phenomena, simultaneous observations of meteor radars in the world are urgently needed. Furthermore we wish that a number of meteor radars would be constructed in the low-latitude region and in the southern hemisphere to fill up gaps among the present excellent meteor radar stations in these areas. Thus the horizontal structure of the atmospheric tides could be clarified inclusive of the local effect due to non-migrating tides.

REFERENCES

Aso, T., T. Tsuda and S. Kato, Meteor radar observations at Kyoto University, J. Atmos. Terr. Phys., 41, 517-525, 1979.

Aso, T., T. Tsuda, Y. Takashima, R. Ito and S. Kato, Observations of lower ionospheric wind by the Kyoto meteor radar, J. Geophys. Res., 85, 177-184, 1980.

Aso, T., T. Nonoyama and S. Kato, Numerical simulation of semidiurnal tides, J. Geophys. Res., 86, 1981, in press.

Bartels, J., Statistical methods for research on diurnal variations, Terr. Mag., 37, 291-302, 1932.

Bernhardt, P. A., D. A. Antoniadis and A. V. Da Rosa, Lunar perturbations in columnar electron content and their interpretation in terms of dynamo electrostatic field, J. Geophys. Res., 81, 5957-5963, 1976.

Bojkov, R., Computing the vertical ozone distribution from its relationship with total ozone amount, J. Appl. Met., 8, 284-292, 1969.

Brier, G. W. and J. Simpson, Tropical cloudiness and rainfall related to pressure and tidal variations, Quart. J. R. Met. Soc., 95, 120-147, 1969.

Briggs, B. H. and M. Spencer, Horizontal movements in the ionopshere, Rep. Prog. Phys., 17, 245-280, 1954.

Butcher, E. C. and K. Weeks, The measurements of a lunar tide in the phase height of the E region, J. Atmos. Terr. Phys., 31, 1421-1434, 1969.

Chaloner, C. P., J. R. Drummond, J. T. Houghton, R. F. Jornot and H. K. Roscoe, Stratospheric measurements of H_2O and the diurnal change of NO and NO_2, Nature, 258, 696-697, 1975.

Chapman, J. H., A study of winds in the ionosphere by radio methods, Can. J. Phys., 31, 120-131, 1953.

Chapman, S., A theory of upper-atmospheric ozone, Mem. R. Met. Soc., 3, 103-125, 1930.

Chapman, S. and C. P. Miller, The statistical determinations of lunar daily variations in geomagnetic and meteorological elements, Mon.

Not. Roy. Astr. Soc. Geophys. Supp., 4, 649-669, 1940.

Chapman, S. and R. S. Lindzen, Atmospheric Tides, D. Reidel Publ. Co., Dordrecht, 1970.

CIRA 1972, COSPAR W. G. 4, Ed. by A. C. Stickland, Academie verlag, Berlin, 1972.

Clark, R. R., Upper atmospheric winds, January, 1977 to October, 1979 UNH meteor radar system at Durham (43°N, 71°W), Tech Rep. 1, Univ. New Hampshire, 1980.

Davidson, T. W., Measurements of lunar time variations in the intensity of oxygen 5577A airglow, Planet. Space Sci., 11, 1133-1138, 1963.

Dohnanyi, J. S., On the origin and distribution of meteoroids, J. Geophys. Res., 75, 3463-3493, 1970.

Dütsch, H. U., Photochemistry of atmospheric ozone, in Advances in Geophysics, Academic Press, New York, 1971.

Elford, W. G., A 6-year synoptic study of winds between 80 and 100 km from meteor trail drifts, IAGA. Rep. to Com. VIII, 1973.

Eshleman, V. R., The theoretical length distribution of ionized meteor trails, J. Atmos. Terr. Phys., 10, 57-72, 1957.

Fellous, J. L., A. Spizzichino, M. Glass and M. Massebeuf, Vertical propagation of tides at meteor heights, J. Atmos. Terr. Phys., 36, 385-396, 1974.

Fellous, J. L., R. Bernard, M. Glass, M. Massebeuf and A. Spizzichino, A study of the variation of atmospheric tides in the meteor zone, J. Atmos. Terr. Phys., 37, 1511-1524, 1975.

Forbes, J. M. and M. A. Geller, Lunar semidiurnal variation in OI (5577A) nightglow, J. Geophys. Res., 77, 2942-2947, 1972.

Forbes, J. M. and H. B. Garrett, Solar diurnal tide in the thermosphere, J. Atmos. Sci., 33, 2226-2241, 1976.

_____, Seasonal-latitudinal structure of the diurnal thermospheric tide, J. Atmos. Sci., 35, 148-159, 1978.

_____, Theoretical studies of atmospheric tides, Rev. Geophys. Space Phys., 17, 1951-1981, 1979.

Fukuyama, K., Airglow variations and dynamics in the lower thermosphere and upper atmosphere 1. Diurnal variation and its seasonal dependency, J. Atmos. Terr. Phys., 38, 1279-1287, 1976.

Gadsden, M. and E. Marovich, 5577A nightglow and atmospheric movements, J. Atmos. Terr. Phys., 31, 817-825,1969.

Goody, R. M., The influence of radiative transfer on the propagation of a temperature wave in a stratified diffusing atmosphere, J. Fluid. Mech., 9, 445-454, 1960.

Greenhow, J. S. and J. E. Hall, The importance of initial trail radius on the apparent height and number distributions of meteor echoes, Mon. Not. R. Astr. Soc., 121, 183-196, 1960.

Greenhow, J. S. and E. L. Neufeld, The diffusion of ionized meteor trails in the upper atmosphere, J. Atmos. Terr. Phys., 6, 133-140, 1955.

_____, Winds in the upper atmosphere, Quart. J. R. Met. Soc., 87, 472-489, 1961.

Groves, G. V., A theory for determining upper-atmosphere winds from radio observations on meteor trails, J. Atmos. Terr. Phys., 16, 344-356, 1959.

Haurwitz, B., The diurnal surface-pressure oscillation, Archiv, Met. Geophys. Biokl. A14, 361-379, 1965.

Haurwitz, B. and A. D. Cowley, Lunar air tide in the Caribbean and its monthly variation, Mon. Wea. Rev., 94, 303-306, 1966.

_____, New determinations of the lunar barometric tide, Bier. Phys. Atmos., 40, 243-261, 1967.

_____, Lunar and solar barometric tides in Australia, Mon. Wea. Rev., 96, 601-605, 1968a.

_____, Lunar air winds at four American stations, Geophys. J. R. Astr. Soc., 15, 103-107, 1968b.

_____, The lunar barometric tide, Its global distribution and annual variation, Pure and Appl. Geophys., 77, 122-150, 1969a.

_____, The lunar semidiurnal wind variations at Hongkong and Uppsala, Quart. J. R. Met. Soc., 95, 766-770, 1969b.

Hays, P. B. and R. G. Roble, Observations of mesospheric ozone at low latitudes, Planet. Space Sci., 21, 273-279, 1973.

Hess, G. C. and M. A. Geller, the Urbana meteor-radar system: design, development, and first observations, Aeronomy Rep. 74, Univ. Illinois, 1976.

Hilsenrath, E. B., B. Guenther and P. Dunn, Water vapor in the lower stratosphere measured from aircraft flight, J. Geophys. Res., 82, 5453-5458, 1977.

Hook, J. L., Winds at the 75-110 km level at College, Alaska, Planet. Space Sci., 18, 1623-1638, 1970.

Hudson, R. D., Critical review of ultraviolet photoabsorption cross sections for molecules of astrophysical and aeronomic interest, Rev. Geophys. Space Phys., 9, 305-406, 1971.

Iljichev, YU. D., I. A. Lysenko, A. D. Orlyansky and YU. I. Portnyagin, Space and time variations of large-scale air motions in the lower thermosphere, J. Atmos. Terr. Phys., 36, 1841-1849, 1974.

Jones, J, The reflection of radio waves from irregularly ionized meteor trains, Planet. Space Sci., 17, 1519-1526, 1969.

_____, On the variation of the ambipolar diffusion coefficient with height, Planet. Space Sci., 18, 1836-1842, 1970.

_____, On the effects of small-scale wind shears on radio meteor echoes, Planet. Space Sci., 20, 301-312, 1972a.

_____, The effects of wind shear gradients on underdense meteor decay time, Can J. Phys., 50, 1277-1281, 1972b.

Jones, J. and G. Collins, The mass distribution of radio meteors and the full-wave scattering theory, Mon. Not. R. Astron. Soc., 166, 529-542, 1974.

Kaiser, T. R., Radio echo studies of meteor ionization, Phil. Mag. Supp., 2, 495-544, 1953.

_____, Theory of the meteor height distribution obtained from radio-echo observations, I. Shower meteors, Mon. Not. R. Astr. Soc., 114, 39-51, 1954a.

_____, Theory of the meteor height distribution obtained from radio-echo observations, II. Sporadic meteors, Mon. Not. R. Astr. Soc., 114, 52-62, 1954b.

Kashcheyev, B. L. and I. A. Lysenko, Atmospheric circulation in the meteor zone, J. Atmos. Terr. Phys., 30, 903-905, 1968.

Kato, S., Horizontal wind systems in the ionospheric E region deduced from the dynamo theory of the geomagnetic S_q variation, II. Rotating earth, J. Geomag. Geoelec., 8, 24-37, 1956.

_____, Diurnal atmospheric oscillation, 1. Eigenvalues and Hough functions, J. Geophys. Res., 71, 3201-3209, 1966.

_____, Wave dynamics in the thermosphere, I. Tidal motion, Space Sci. Rev., 12, 421-445, 1971.

_____, Dynamics of the Upper Atmosphere, D. Reidel Publ. Co., Dordrecht, 1980.

Kato, S., T. Tsuda and F. Watanabe, Thermal excitation of non-migrating tides, J. Atmos. Terr. Phys., 43, 1981, in press.

Kuo, H. L., The thermal interaction between the atmosphere and the earth and propagation of diurnal temperature waves, J. Atmos. Sci., 25, 682-706, 1968.

Lacis, A. A. and J. E. Hansen, A parameterization for the absorption of solar radiation in the earth's atmosphere, J. Atmos. Sci., 31, 118-133, 1974.

Leovy, C., Radiative equilibrium of the mesosphere, J. Atmos. Sci., 21, 238-248, 1964.

Lindzen, R. S., Thermally driven diurnal tide in the atmosphere, Quart. J. R. Met. Soc., 93, 18-42, 1967.

_____, The application of classical atmospheric tidal theory, Proc. Roy. Soc., A303, 299-316, 1968.

_____, Effect of daily cumulonimbus activity on the atmospheric semidiurnal tide, Mon. Wea. Rev., 106, 526-533, 1978.

Lindzen, R. S. and S. S. Hong, Effects of mean winds and horizontal temperature gradients on solar and lunar smeidiurnal tide in the atmosphere, J. Atmos. Sci., 31, 1421-1446, 1974.

London, J. and J. E. Fredrick, Satellite observations of the global distribution of stratospheric ozone, J. Geophys. Res., 82, 2543-2556, 1977.

Lysenko, I. A. and YU. I. Portnyagin, Results of a comparison between radar meteor wind measurements and simultaneous lower ionosphere drift measurements in the same area, J. Atmos. Terr. Phys., 34, 1435-1444, 1972.

Maeda, H and M. Fujiwara, Lunar ionospheric winds form the dynamo theory of geomagnetic variations, J. Atmos. Terr. Phys., 29, 917-936, 1967.

Mallin, S. R. C. and S. Chapman, The determination of lunar daily

geophysical variations by the Chapman-Miller method, Geophys. J. R. Astron. Soc., 19, 15-35, 1970a.

_____, Lunar tidal components N_2 and O_1 in the atmospheric pressure, Pure Appl. Geophys., 80, 309-318, 1970b.

Manning, L. A., The strength of meteoric echoes from dense columns, J. Atmos, Terr. Phys., 4, 219-255, 1953.

_____, The initial radius of meteoric ionization trails, J. Geophys. Res., 63, 181-195, 1958.

_____, Meteors in the ionosphere, Proc. IRE, 47, 186-199, 1959.

_____, Ray-path calculations of overdense meteor echo strength, J. Atmos. Terr. Phys., 25, 182-183, 1963.

Manning, L. A., O. G. Villard and A. M. Peterson, Meteoric echo study of upper atmospheric winds, Proc. IRE, 38, 877-883, 1950.

Matsushita, S., Lunar tidal variations of sporadic E, in Ionospheric Sporadic E, Ed. by E. K. Smith and S. Matsushita, 194-214, Pergamon Press, Oxford, 1962.

_____, Lunar tides in the ionosphere, Handb. Phys., 49 (2), 567-602, 1967.

McIntosh, B. A., The effects of wind shear on the decay constant of meteor echoes, Can J. Phys., 47, 1337-1341, 1969.

McKinley, D. W. R. and P. M. Millman, A phenomelogical theory of radar echoes from meteors, Proc. IRE, 37, 364-375, 1949.

McKinley, D. W. R., Meteor Science and Engineering, McGrow-Hill Book Co., New York, 1961.

Müller, H. G., Atmospheric tides in the meteor zone, Planet. Space Sci., 14, 1253-1272, 1966.

_____, Wind shears in the meteor zone, Planet. Space Sci., 16, 61-90, 1968.

Murcray, D. G., F. H. Murcray and W. J. Williams, Distribution of water vapor in the stratosphere as determined from infrared absorption measurements, J. Geophys. Res., 67, 759-767, 1962.

Nagata, T., T. Tohmatsu and E. Kaneda, Lunar time variation of the oxygen green line in the airglow, Rep. Ionos. Res. Japan, 15, 253, 1961.

Nicolet, M., Stratospheric ozone: An introduction to its study, Rev. Geophys. Space Phys., 13, 593-636, 1975.

Nitta, T and S. Esbenson, Diurnal variations in the western Atlantic trades during the BOMEX, J. Met. Soc. Japan, 52, 254-257, 1974.

Nowak, R., An integrated meteor radar system for wind and density measurements in the upper atmosphere, Tech. Rep. SEL-67-046, Stanford Univ., 1967.

Nowak, R., E. M. North and M. S. Frankel, The Stanford meteor-trails radar Mark-II, Tech. Rep. SEL-70-021, Stanford Univ., 1970.

Park, J. H. and J. London, Ozone photochemistry and radiative heating of the middle atmosphere, J. Atmos. Sci., 31, 1898-1916, 1974.

Pettit, E., The sun and stellar radiaiton in astrophysics, Ed. by J. Hynek, McGrow-Hill Book Co., New York, 703, 1951.

Phillips, E., Wind structure from the amplitude fluctuations in the present radio meteor echoes, Planet. Space Sci., 17, 553-559, 1969.

Poole, L. M. G. and T. R. Kaiser, The duration distribution of radio-echoes obtained from underdense shower-meteor, Planet. Space Sci., 15, 1131-1149, 1967.

Rice, D. W., and P. A. Forsyth, Variations in meteor radio siganl decay rates, Can. J. Phys., 41, 679-690, 1963.

Radford, H. E., M. M. Litvak, C. A. Gottlieb, E. W. Gottlieb, S. K. Rosenthal and A. E. Lilley, Mesospheric water vapor measured from ground-based microwave observations, J. Geophys. Res., 82, 472-478, 1977.

Rawcriffe, R. D., G. E., Meloy, R. M. Fiedman and E. H. Rogers, Measurement of vertical distribution of ozone from a polar orbiting satellite, J. Geophys. Res., 68, 6425-6429, 1963.

Rodgers, R. P. and E. C. Butcher, The measurements of the lunar tide in the group height of the E region on several frequencies, J. Atmos. Terr. Phys., 38, 69-75, 1976.

Roper, R. G., Winds from the Atlanta (34°N, 84°W) radio meteor wind facility, J. Atmos. Terr. Phys., 40, 891-894, 1978.

_____, Radio meteor winds measurements over Atlanta (34°N, 84°W), August, 1974 - December, 1977, Tech. Rep. E-16-668, Georgia Inst. Tech., 1978.

Rudman, R. R., F. H. Glanz, A. D. Frost and R. R. Clark, An inter-ferometer system for the measurement of radar echoes form meteor

trails, Tech. Rep. AFCRL-70-0588, Air Force Cambridge Res. Lab., 1970.

Schoeberl, M. R. and D. F. Strobel, The zonally averaged circulation of the middle atmosphere, J. Atmos. Sci., 35, 577-591, 1978.

Shiraki, M., On the daily geomagnetic variations in Japan, J. Geomag. Geoelec. 33, 1981, in press.

Siebert, M., Atmospheric tides, in Advances in Geophysics, 7, Academic Press, New York, 105-182, 1961.

Smith, W. L. and H. B. Howell, Vertical distribution of atmospheric water vapor from satellite infrared spectrometer measurements, J. Appl. Met., 10, 1026-1034, 1971.

Strobel, D. F., Parameterization of the atmospheric heating rate from 15 to 120 km due to O_2 and O_3 absorption of solar radiation, J. Geophys. Res., 83, 6225-6230, 1978.

Tarpley, J. D., The O_1 component of the geomagetic lunar daily variation, J. Geomag. Geoelec., 23, 169-179, 1971.

Tarpley, J. D. and S. Matsushita, The lunar tide in f_bE_s, Radio Sci., 6, 191-196, 1971.

_____, Lunar influence on sporadic E, Radio Sci., 7, 411-416, 1972.

Teitelbaum, H. and C. Cot, Antisymmetric tidal modes under equinoctial conditions induced by ozone heating, J. Atmos. Terr. Phys., 41, 33-41, 1979.

Tohmatsu, T. and T. Nagata, Dynamical studies on the oxygen green line in the airglow, Planet. Space Sci., 10, 103-116, 1963.

Tsuda, T., T. Aso, Y. Takashima, R. Ito and S. Kato, Meteor radar observations at Kyoto in two C.T.O.P. periods, J. Atmos. Terr. Phys., 42, 461-469, 1980.

Tsuda, T. and S. Kato, Seasonal variation of diurnal tide due to ozone heating, J. Met. Soc. Japan, 58, 292-297, 1980.

Tsuda, T., J. Tanii, T. Aso and S. Kato, Lunar tides at meteor heights, Geophys. Res. Lett., 8, 191-194, 1981.

Tuller, S. E., World distribution of mean monthly and annual precipitable water, Mon. Wea. Rev., 96, 785-797, 1968.

Upper Atmospheric Program Bulletin, NASA, Upper Atmospheric Research

Program/FAA, High Altitude Pollution Program, 79-3, 1979.

Verniani, F., An analysis of the physical parameters of 5759 faint radio meteors, J. Geophys. Res., 78, 8429-8462, 1973.

Wallace, J. M., Diurnal variations in precipitation and thunderstorm frequency over the conterminous United States, Mon. Wea. Rev., 103, 406-419, 1975.

Wallace, J. M. and R. F. Tadd, Some further results concerning the vertical structure of the atmospheric tidal motions within the lower 30 kilometers, Mon. Wea. Rev., 102, 795-803, 1974.

Walterscheid, R. L., J. G. DeVore and S. V. Venkateswaran, Influence of mean zonal motion and meridional temperature gradients on the solar semidiurnal atmospheric tide: A revised spectral study with improved heating rates, J. Atmos. Sci., 37, 455-470, 1980.

Williamson, E. J. and J. T. Houghton, Radiometric measurements of emission from stratospheric water vapor, Quart. J. R. Met. Soc., 90, 330-338, 1964.

Winch, D. E., Geomagnetic lunar partial tides, J. Geomag. Geoelec., 23, 291-328, 1970.

_____, M_2 and O_1 geomagnetic lunar tides for seasonal subdivisions of data, J. Geomag. Geoelec., 24, 33-45, 1971.

Zimmerman, S. P. and E. A. Murphy, Tropospheric stratospheric turbulence and vertical diffusivities, AFGL-TR-0020, Aeronomy Division, Air Force Geophys. Lab., 1980.